Leibniz Universität Hannover

Metamaterials with resonant silicon nanoparticles for perfect mirrors

Investigation, design, and realisation

Von der QUEST Leibniz Forschungsschule
der Gottfried Wilhelm Leibniz Universität Hannover

zur Erlangung des Grades
Doktor der Naturwissenschaften
Dr. rer. nat.

genehmigte Dissertation von

Mariia Matiushechkina

2024

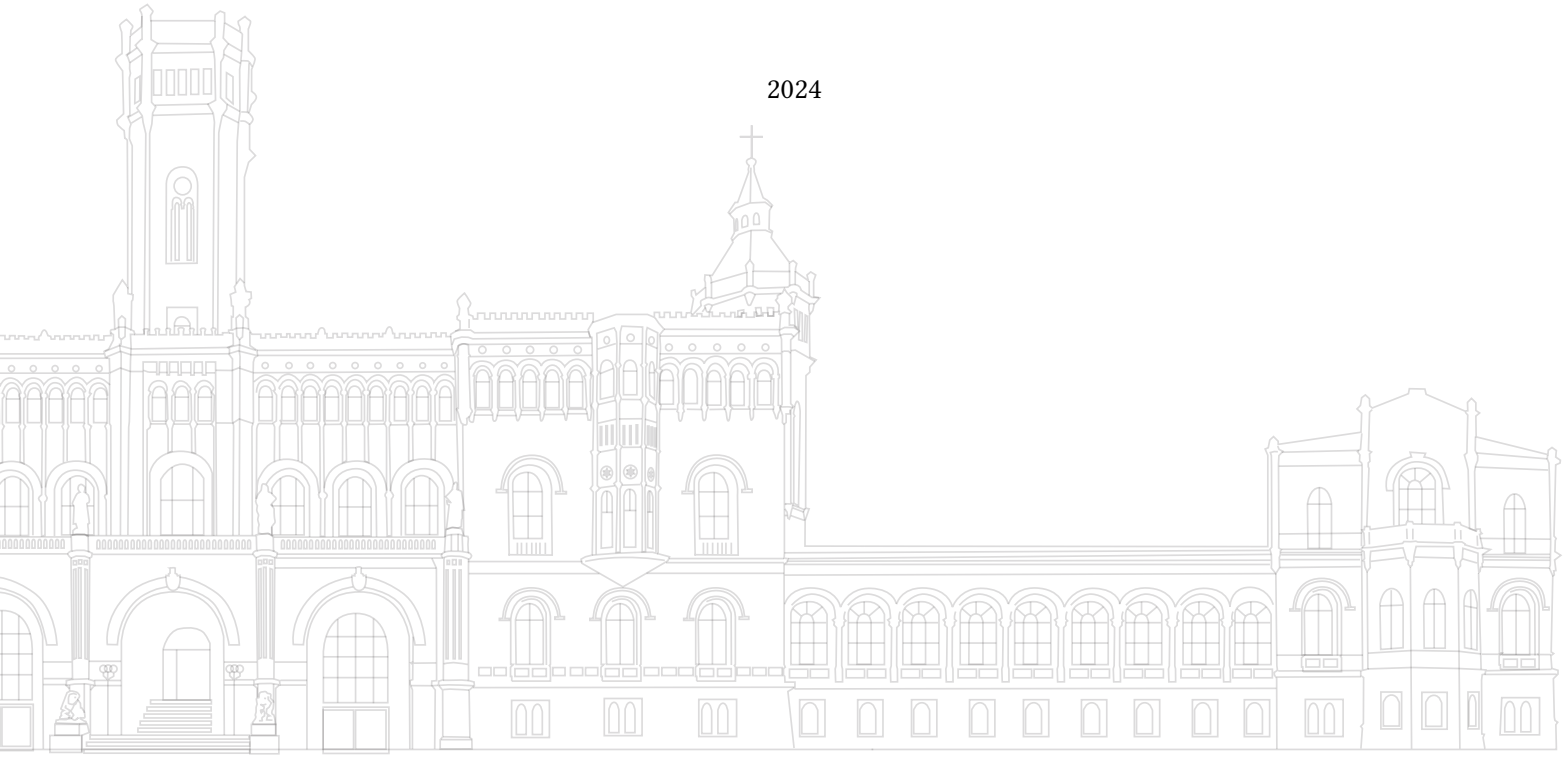

Referentin:	Prof. Dr. Michèle Heurs Institute for Gravitational Physics, Leibniz Universität Hannover
Korreferent:	Prof. Dr. Boris N. Chichkov Institute of Quantum Optics, Leibniz Universität Hannover
Korreferent:	Prof. Dr. Andrei V. Lavrinenko Department of Electrical and Photonics Engineering, Technical University of Denmark
Tag der Promotion:	29.01.2025

Abstract

A metasurface is a single-layer artificial structure composed of specially arranged particles, which can be configured in size and shape to alter the metasurface's interaction with the incident electromagnetic field. The application potential of metasurfaces is vast, as they offer flexibility in tuning their properties while maintaining an ultra-thin, lightweight coating structure optimised for specific functionalities.

Among the diverse potential applications, special attention is directed towards the field of gravitational wave physics. Gravitational wave detectors, which function as advanced Michelson interferometers, consist of highly sensitive test masses covered with reflective coatings. The next generation of detectors demands novel coating designs capable of operating at cryogenic temperatures and exhibiting minimal thermal noise. One potential alternative is a metasurface coating design that can be tailored to satisfy essential requirements.

This thesis focuses on the development of highly reflective metasurfaces and their experimental realisation. In the framework of the investigation, the target wavelengths for the high-reflectivity effect are selected to be 1064 nm and 1550 nm, as these are relevant to next-generation gravitational wave observatories. The thesis presents an analysis and description of the phenomenon of light reflection from a metasurface, originating from the resonant response of its constituent nanoparticles. Possible designs incorporating spherical and cylindrical shapes of nanoparticles are modelled and characterised through numerical simulations (Comsol Multiphysics) and a semi-analytical multipole approach. Structural optimisation, the integration of protective and supporting mediums, and their influence on performance and fabrication imperfections are considered, simulated and discussed throughout the research. On the practical side, the prototypes of the metasurface structures, composed of polycrystalline silicon cylinders on a sapphire substrate, have been realised at the selected wavelengths. The realisation process entails evaluating dimensional parameters based on the measured material properties and using a fabrication process with electron beam lithography. The characterisation of the fabricated metasurfaces demonstrates good agreement with the numerically predicted behaviour.

While the primary objective is to achieve near-perfect reflectivity across all configurations, the developed analytical and numerical methods, along with the fabrication procedure, are also applicable to the development of metasurfaces with partial reflectivity or full transmissivity. These theoretical and experimental achievements in metasurface realisation have the prospect of further development and implementation in the field of gravitational wave physics and other optical experiments.

Keywords: metamaterial, high-reflective dielectric metasurface, silicon coating, optical nanostructure, multipole resonant response, mirror effect

Contents

List of Acronyms

Al	aluminium
a-Si	amorphous silicon
BS	beam splitter
c-Si	crystalline silicon
DTU	Technical University of Denmark
e-beam	electron beam
EBL	electron beam lithography
ED	electric dipole
EQ	electric quadrupole
EO	electric octupole
ET	Einstein Telescope
ETM	end test mirror
FEM	finite element modelling
GW	gravitational wave
GWD	gravitational wave detector
ICP-RIE	inductively coupled plasma reactive ion etching
ITM	input test mirror
ISQ	International System of Quantities
LIGO	Laser Interferometer Gravitational-wave Observatory
LNQE	Laboratory of Nano and Quantum Engineering
LPCVD	low-pressure chemical vapor deposition
LSPR	localized surface plasmon resonance
MD	magnetic dipole
MQ	magnetic quadrupole
MO	magnetic octupole
PD	photodetector
PDE	partial differential equation
poly-Si	polycrystalline silicon
PRM	power recycling mirror
QCM	quartz crystal microbalance
SEM	scanning electron microscope
Si	silicon
SRM	signal recycling mirror
TD	toroidal dipole

Introduction

All materials on our planet that we observe around us are composed of chemical elements placed in the well-known Mendeleev's periodic table. The alloys and combinations of these elements have allowed humanity to develop materials with remarkable properties, such as enhanced strength, heat resistance, and transparency to the visible spectrum. With the development of technology, the demand for unique materials has only increased. This has led to the development of artificial materials, where the geometry and structure of their internal components play a key role in achieving the desired characteristics.

Even though the field of materials with periodic structures is a relatively recent development, emerging in the 20th century, nature has long demonstrated the remarkable potential of enhancing optical material properties through geometric design. An example is the wings of butterflies, which exhibit stunning diffraction effects due to nanosize scales arranged in specific patterns, or peacock feathers, whose vibrant colours result from 2D lattices made of melanin rods connected by keratin [1]. Inspired by these natural phenomena, we create materials whose architecture tailors their own complex behaviour and call them *metamaterials*.

Metamaterials are composed of elements whose position, size, and shape determine the overall behaviour of the structure. Despite the broadness of this terminology, it typically refers to periodic structures that operate on a subwavelength scale. For the visible, infrared and telecommunications wavelength ranges, both the elements and the distance between them have nanoscale dimensions, which is why metamaterials are commonly termed *nanostructures*.[1] Particular research interest among different metamaterials is given to single-layer nanostructures with unique optical properties, called *metasurfaces*. The attractiveness of the adjustable optical behaviour of a lightweight metasurface that can be applied to various quantum metrology experiments drives interest in its in-depth investigation.

This research work is a **cumulative dissertation comprising four peer-reviewed publications** on the gradual investigation of metasurfaces, supplemented by additional clarification chapters.

[1] In the thesis text, the terms 'metamaterial' and 'nanostructure' are used in a manner consistent with the definition of 'metasurface'.

Thesis outline

- **Chapter 1** explains the motivation behind the research. A target application of metasurface mirrors is directed towards an alternative design of mirror coatings for future gravitational wave detectors (GWDs), where the thermal noise of conventional multilayer coatings becomes a limiting factor. The chapter overviews gravitational wave (GW) interferometers, highlighting the specifics of new cryogenic temperature design challenges. It explores potential materials for mirror substrates and coatings, as well as the possible strategies to reduce thermal noise. The advantages of metasurfaces over other coating designs are discussed, along with the rationale for selecting specific metasurface materials.
- **Chapter 2** introduces the theoretical background on metasurface structures. The variety of metasurfaces can be categorized by dielectric and metallic behaviour based on the electromagnetic response of the structures to the incident light field. This study focuses on dielectric particles, providing detailed information on their key material parameters and scattering principles. This chapter presents a detailed analytical solution to the reflectivity effect, which begins with an explanation of the Mie scattering theory applied to a single spherical nanoparticle and culminates in the description of the contributions of generated dipole moments within the array.
- **Chapter 3** provides a detailed metasurface modelling and simulation guideline using *Comsol Multiphysics* software. Metasurfaces placed on a substrate or composed of non-spherical particles are hard to analyse analytically and require a computational numerical approach. This chapter highlights the particularities of metasurface modelling and presents the potential validation steps required to ensure the accuracy of the simulation results.
- **Chapter 4** details the steps involved in the fabrication process used to create a silicon cylindrical metasurface on a sapphire substrate. The selected realisation approach entails the exploitation of electron beam lithography (EBL) and lift-off techniques conducted at the Technical University of Denmark (DTU). This chapter also discusses the supplementary fabrication capabilities accessible at the Laboratory of Nano and Quantum Engineering (LNQE) in Hannover, which may serve as a valuable resource for future in-house fabrication procedures.
- **Chapter 5** includes all peer-reviewed publications containing all the main results of the PhD work. Each article is accompanied by an introductory section that highlights the significance of the study and outlines the logical progression of the research.
- **Chapter 6** presents the Conclusion and Outlook. This chapter summarizes the obtained results from the metasurface investigation and offers perspectives on future research directions.

Chapter 1

Research Motivation

Metasurface structures have numerous potential applications. These include optical quantum metrology [2, 3], magnetic resonance imaging [4, 5], optical invisibility [6], communication systems [7], sensing devices that respond to a light field's wavelength, polarization, and phase [8], and many others.

The particular interest in our group "QuantumControl" is directed towards the improvement of sensitivity in GWDs. The conventional multilayer coatings of future mirror designs exhibit excessive thermal noise that obscures weak GW signals, making them undetectable. An alternative design of a single-layer metasurface coating has the advantage of eliminating the friction between several layers, thereby reducing the thermal noise. This area of application for the metasurface specifies its particular configuration and material composition, including the dimensional parameters of the constituent nanoparticles.

A proper application requires, nevertheless, a comprehensive understanding of the operating principles of the structure. To ensure accurate and effective implementation, it is essential to develop a solid foundation that includes analysis of general resonant mechanisms, unconventional resonant states and potential challenges that could arise during the design and fabrication processes. The benefit of this approach is that it also allows for extending the acquired knowledge to other research fields by tailoring and adapting the structural parameters.

The discussion in this thesis starts with the initial concept, establishing the initial reference parameters, and then transitions into a thorough investigation of metasurfaces.

1.1 Design innovations for future gravitational-wave detectors

A general overview of the application field, along with recent advancements, is essential for building an effective investigation plan. It helps estimate potential advantages, disadvantages and challenges when a new idea arises. This section introduces the reader to the topic of metasurface application.

1.1.1 Gravitational waves and gravitational-wave detectors

Gravitational waves are a phenomenon of "ripples" in space-time caused by energetic processes occurring within the Universe. Their existence was first predicted in 1916 by Albert Einstein in his general theory of relativity, and only in 2015, after many years of theoretical and technical work, the first gravitational waves were detected in the Laser Interferometer Gravitational-wave Observatory (LIGO) in the USA [9]. The first signal ever detected was from a collision of two massive black holes placed 1.3 billion light-years away. In 2017, the GWs were detected from a binary of neutron stars [10], that additionally radiated a gamma-ray burst, observed by the Fermi and Integral satellites [11, 12]. Not so long ago, in 2023, a mysterious observation was made due to the merger of a neutron star with an unknown compact object that could be a potential light-weight black hole [13]. There are numerous events and unknown objects, including binary systems, individual neutron stars, and stochastic background radiation, that could be discovered due to the possibility of detecting the emitted GWs [14]. This source of information was previously beyond the reach of existing technology. The potential for detecting GWs nowadays and analysing the origins of their emergence allows us to look deeper into the Universe and build a more comprehensive picture of the world.

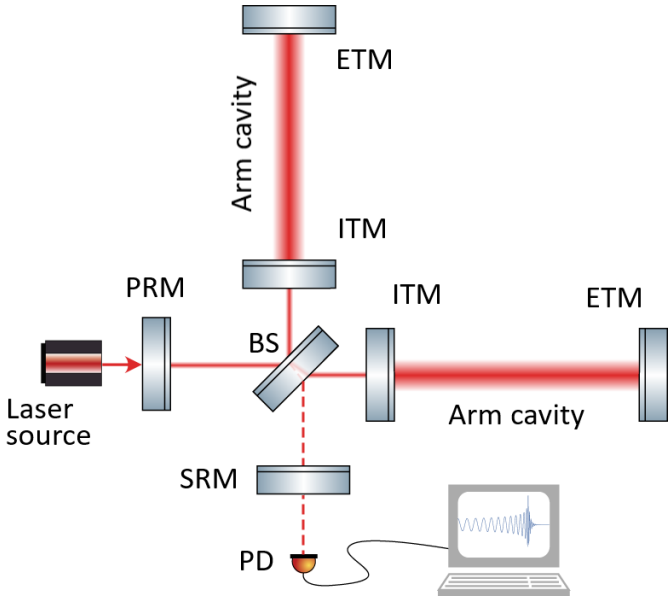

Figure 1.1.: Simplified schematic of a GW interferometer. The laser beam, after passing the power recycling mirror (PRM), is split into two arms by a 50:50 beam splitter (BS) and enters the Fabry-Perot arm cavities, which consist of input test mirrors (ITMs) and end test mirrors (ETMs). The circulating laser light reflects back and recombines at the BS, creating an interference pattern sensitive to gravitational waves. The signal then passes through the signal recycling mirror (SRM), which modulates the sensitivity band. The final transmitted signal is detected by a photodetector (PD) and processed on a computer cluster. [This figure is modified from [15]. It is licensed under a CC BY 4.0 international licence. To view a copy of this licence, visit creativecommons.org/licenses/by/4.0/.]

Telescopes used for detecting GWs are called gravitational wave detectors GWDs. A network of ground-based detectors is distributed around the globe. The amount of them helps not only

to confirm the signal with several independent observations but also more accurately to localize the source of the signal [16]. Moreover, some technical elements installed in the GWDs have different designs, allowing for a more versatile detection process [17]. Among observatories that are currently in operation, two are located in the USA, Advanced LIGO Livingston and Advanced LIGO Hanford [18], one is in Italy - Advanced Virgo Interferometer [19], and one is in Japan - KAGRA [20]. There is also a small detector, GEO600, and the 10m-PT prototype, which are used to test new technologies to be implemented for the better versions of the current detectors or for those which will be built in the future [21–23].

The fundamental principle of operation of ground-based GWDs is similar. It is an "L-shape" km-scale Michelson interferometer with enhanced sensitivity using multiple resonator techniques (Figure 1.1). Each arm of the interferometer includes a Fabry-Perot cavity. These cavities consist of two opposing large massive suspended mirrors, input test mirrors (ITMs) and end test mirrors (ETMs), that play the role of GW field probe. The generated interference pattern of the laser light coming from the two arms contains the information about the relative displacement of the mirror test masses and, therefore, has the information about the signal [24]. The additional inclusion of a power recycling mirror (PRM), which increases operational laser power circulating inside of the interferometer, and a signal recycling mirror (SRM), which tunes the frequency response, amplifies the precision of the detection process [25].

1.1.2 Noise sources

The random fluctuations in the amplitude and phase of the interference pattern, caused by the noise sources, mask the GW signal and thus decrease the sensitivity of the GWDs. The variety of the main noise sources is presented in the form of a noise budget taken from the Advanced LIGO interferometer operating at the laser power of 750 kW in the arm cavities. (Figure 1.2). The frequency spectrum is conventionally divided into three intervals in accordance with the limiting factors.

Sensitivity at high frequencies is limited predominantly by relative quantum shot noise arising from the stochastic Poisson distribution of emitted photons from the laser beam. This variation of photon number creates detection noise that can be improved with higher laser power and ultra-low-noise photodetectors in combination with quantum techniques, such as squeezed light for quadrature phase fluctuations.

The limiting noise sources at low frequencies are seismic motion of the ground, Newtonian noise and quantum radiation pressure noise. Newtonian noise refers to the random displacement of test masses caused by fluctuations in the gravity field from the influence of terrestrial sources. The seismic and Newtonian disturbances can be challenged by better seismic isolation and control, along with placing the future detectors underground as made for the interferometer of KAGRA.

Next in the line for low frequencies is quantum radiation pressure noise that also originates from stochastic photon distribution. Fluctuation in photons leads to correlated displacement or trembling of test masses, which, in return, creates back-action noise. This can be mitigated by squeezed light in the amplitude quadrature, implemented by the utilisation of filter cavities to create frequency-dependent squeezing. It has to be noted that current detectors already employ

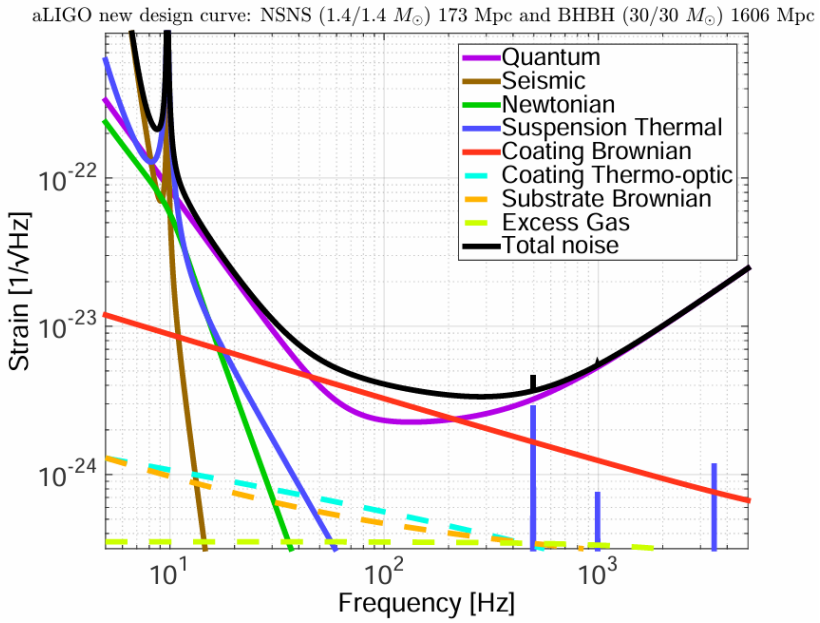

Figure 1.2.: The major noise source contribution to the sensitivity of aLIGO interferometer taken from the LSC Instrumental Science White Paper (2024) [26].

squeezing techniques around 6 dB for relative shot noise reduction since radiation pressure noise is not the dominant factor.

The middle-frequency band around a few hundred hertz, which is the most sensitive one, is limited by the thermal noise of the mirror coatings. Thermal noise is described as a coupling between mechanical degrees of freedom with stochastic thermal fluctuations of the material. It can be subdivided into Brownian noise, thermoelastic noise, thermorefractive noise, etc. The most significant influence on the coating's thermal noise is attributed to Brownian motion, which arises from the random microscopic movements of coating atoms. Initially quantified by Albert Einstein in 1905, Brownian noise is proportional to temperature [27]. Therefore, the primary strategy for reducing this type of noise is to operate future detectors at cryogenic temperatures, along with using alternative coating materials.

1.1.3 Future design of European gravitational wave observatory

All of the above-mentioned limiting noise factors are going to be mitigated in the more sensitive third generation of GWDs within the framework of such projects as Einstein Telescope (ET) in Europe and Cosmic Explorer in the USA. The forthcoming discussion will be dedicated exclusively to the ET project.

The ET will feature a novel technical design. As detailed in the design reports [29, 30], the observatory will be constructed underground and will be composed of three detectors arranged in a configuration of a triangle. Each detector will comprise two interferometers, with one maintained at room temperature and the other at cryogenic temperature (Figure 1.3). These two interferometers are supposed to target different frequency ranges. The room temperature

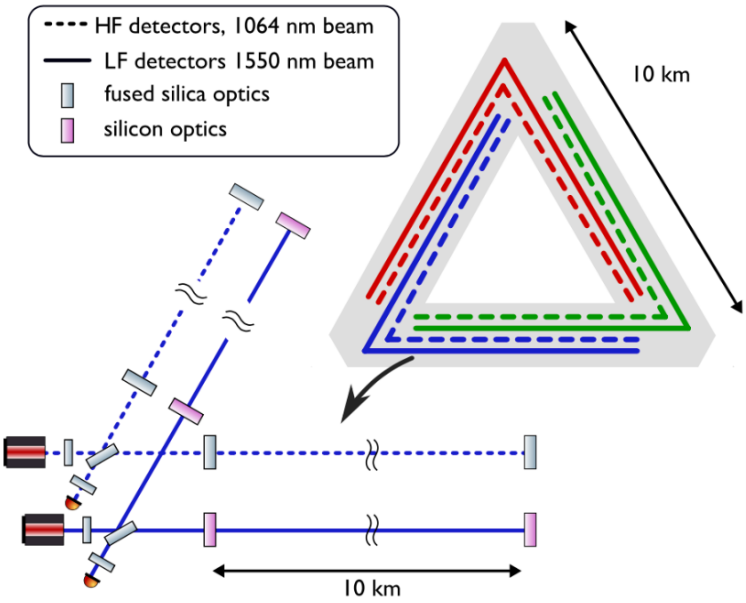

Figure 1.3.: The sketch of the ET observatory with three detectors forming an equilateral triangle, depicted in different colours (red, green, blue). Each detector consists of two interferometers: one optimised for high frequencies (HF) and the other for low frequencies (LF). [Reprinted figure with permission from: S. Rowlinson, A. Dmitriev, A. W. Jones, T. Zhang and A. Freise. 'Feasibility study of beam-expanding telescopes in the interferometer arms for the Einstein Telescope'. Physical Review D 103.2, p. 023004 (2021). Copyright (2024) by the American Physical Society. [28].]

interferometer will be optimised for high frequencies and will operate at high laser power to minimize relevant shot noise. For low frequencies, the interferometer Fabry-Perot cavities will be kept at cryogenic temperature, around 10-20 K, and will operate at low laser power with a larger beam spot on the mirrors to reduce thermal and radiation pressure noises. Additionally, the mirror mass will be increased to approximately 200 kg, and the arm length will be extended to 10 km. In comparison, the Advanced LIGO mirrors have a mass of 40 kg, and its arms measure 4 km. These technological innovations will significantly enhance detection sensitivity and broaden the frequency bandwidth, allowing for the observation of a greater number of astrophysical events.

1.1.4 Potential substrate materials in cryogenic interferometers

Cooling the optics in a cryogenic temperature interferometer helps to reduce the coating thermal noise associated with Brownian motion. However, this also impacts the mechanical properties of the currently used fused silica substrates. Fused silica mirror substrates with their exceptional properties at room temperature at 1064 nm laser wavelength exhibit excessive loss at cryogenic temperatures. A large and broad mechanical loss peak has been observed around 40 K [2]. This peak is linked to a double well potential related to the Si-O-Si bonds in the

[2] This peak contributes an excessive mechanical loss for the considered operational temperature of the interferometer, which is around 10-20 K.

amorphous structure [31]. It is, therefore, necessary to introduce a new substrate material.

The proposed potential materials for the cooled-down interferometer of the ET project are sapphire and crystalline silicon.

The current interferometer of KAGRA already uses the benefits of sapphire mirror substrates operating at 20 K at 1064 nm laser wavelength [20, 32]. Sapphire is a crystalline form of aluminium oxide (Al_2O_3) with a hexagonal structure. Having a high Young's modulus of 400 GPa, sapphire exhibits low thermal noise and low mechanical loss factor around 2×10^{-8} [33]. The high thermal conductivity, up to 40 $W/m \times K$, enables sapphire to tolerate exposure of high laser power and efficiently redistribute residual absorption. Additionally, the low thermal expansion coefficient of approximately 7.5×10^{-13} K^{-1} at 20 K [34] contributes small thermoelastic noise [35], making sapphire an excellent material candidate for use in cryogenic interferometers.

Another potential candidate is crystalline silicon (c-Si). The most remarkable property of this material is its zero thermoelastic noise at temperatures of 18 and 125 K. The thermoelastic effect can be explained as a process of volume deformation caused by temperature fluctuations. It is influenced by the temperature-dependent thermal expansion coefficient, which changes its sign or crosses the zero value at 18 and 125 K, thereby nullifying the noise [36, 37]. Moreover, c-Si has high thermal conductivity with a peak around 20 K [38], high Young's modulus of 188 GPa for [111] crystal orientation [39] and low mechanical noise around 10^{-9} for crystals at 10 K [40].

Despite the excellent mechanical and thermal properties of c-Si at cryogenic temperatures, the optical absorption of a Nd:YAG [3] laser at a wavelength of 1064 nm, due to silicon's bandgap of 1.1 eV [38], requires a shift in operation wavelength to the telecommunications range. The existing advanced laser technology based on Er-fibre [4] lasers creates a 1550 nm wavelength. At such operational laser light, c-Si absorbs < 5 ppm[5]/cm [41], making it possible to use laser power up to 3 MW without causing heating in the elements.

The new design of the detectors, low temperatures, the potential wavelength of 1550 nm and sapphire or c-Si materials for the substrate also require the improvement in the design of a reflective coating.

1.1.5 Coating materials and designs

There are several core optics in the cryogenic interferometer that necessitate modifications in their coating design. Among them are the ETMs, ITMs, PRM and SRM. The reflectivity of these mirror coatings for low-frequency interferometers in the ET project is presented in Table 1.1 [29, 30]:

[3] Nd:YAG, or neodymium-doped yttrium aluminium garnet, is a solid-state laser that typically emits light at 1064 nm.
[4] Erbium-doped fibre lasers emit at 1550 nm.
[5] The unit "ppm" stands for parts per million.

Table 1.1.: Reflectivity of different mirror coatings in the cryogenic interferometer of ET.

Mirror Type	**Reflectivity**
ETM	99.994%
ITM	99.3%
PRM	95.4%
SRM	80%

In order to achieve the required high reflectivity, especially for the ETMs, a sufficient amount of alternate dielectric coating layers of high- and low-refractive-index materials is needed. Conversely, from a noise perspective, an increase in the number of layers results in a corresponding increase in the contribution of Brownian and thermoelastic noise. Additionally, each underlying layer introduces surface fluctuations that are transitioned to the upper layers. For the increased operational wavelength to 1550 nm, the thickness of the "Bragg-type" [6] mirror coating will also proportionally increase, thereby introducing even more thermal noise to the total noise budget of the future GWDs.

The current Advanced LIGO reflective coating is composed of silicon dioxide (SiO_2) layers alternating with layers of tantalum pentoxide (Ta_2O_5) doped with 25 % titanium dioxide (TiO_2). It has ~ 25 doublets (a pair of low and high refractive index materials) for 1064 nm wavelength [43, 44]. This particular coating is not an optimal candidate for use in cryogenic temperatures, as it exhibits a peak in the mechanical loss angle at approximately 20 K [45]. There are several proposed new coating designs and optimisation techniques that are currently under investigation.

The thermal noise arising from the thickest deposited reflective coating on the ETM can be reduced by a method that employs a short Fabry-Perot cavity as an alternative to a single substrate [46]. This cavity should be tuned to antiresonance. The first mirror coating will reflect most of the incident light power and have the least thermal noise, whereas the second mirror coating will satisfy the reflection requirement but interact with the rest of the transmitted light.

Another possible way around would be to use several combinations of high- and low-index materials or change the ratio between the thickness of the layers in order to achieve the strongest interaction of the incident light field with the least lossy material. The optimisation can be performed for doping and annealing techniques. In order to inhibit material crystallisation and increase the annealing temperature, which leads to a reduction in mechanical loss, the high-index coating layer can be fabricated from a stack of nano-thick layers of two distinct materials, for instance, TiO_2 and SiO_2 [47].

Although the variety of possible materials for coating films is plentiful, there are several types that draw particular attention. Among those are amorphous silicon (a-Si), silicon nitride (SiN)

[6] Bragg mirrors are typically composed of layers, with each layer having a thickness of $\lambda/4$. The design of LIGO coatings, however, is more complex, with alternating layers having thicknesses of $3\lambda/8$, $\lambda/8$, or $(n-1)\lambda/n$, or λ/n, depending on the specific design requirements. The non-periodic coatings are designed using genetic algorithms [42].

and hafnium dioxide doped with silicon dioxide (HfO_2: SiO_2). It is important to note that all these materials belong to the category of amorphous coatings, where atoms are arranged in a disordered manner. This helps to avoid the formation of crystalline grains, which can lead to surface roughness and ensures precise thickness control.

a-Si	+ Mechanical loss is 2×10^{-5} [48]. + High refractive index allows for a thinner coating, resulting in correspondingly lower thermal noise. - High optical absorption moves the investigation towards the improvement of deposition techniques. The lowest absorption achieved corresponds to an extinction coefficient of $k = 1.2 \times 10^{-5}$ at 1550 nm [49].
SiN	+ Mechanical loss is in the order of 10^{-5} [50]. + Refractive index depends on the composition of SiN films and can vary over a large range, allowing it to be used as a replacement for both low- and high-index materials. - High thermal noise
HfO_2 : SiO_2	+ Mechanical loss is around 10^{-3} [51]. + Low optical absorption. + Replacement for low-index coating layer. - Material doping with SiO_2 is necessary due to its tendency to partially crystallise during the annealing process [52].

Instead of amorphous coatings, multilayer single-crystalline coating materials are considered as a promising alternative. The epitaxial growth of crystalline coatings results in very low mechanical and thermal losses. Extensive studies of GaAs/AlGaAs have shown the loss value as low as 5.4×10^{-6} at 20 K [53], along with low optical absorption and scattering at the 1550 nm wavelength [54]. The primary challenge for this type of coating is that it can only be grown on GaAs substrates, necessitating a reliable transfer and bonding technique. Additionally, commercially available substrate wafers on which this coating can be grown are not currently produced in the sizes required for the next-generation ET mirrors.

Another crystalline coating of interest for sapphire substrates is iron oxide or chromium oxide. These coatings can be grown directly on sapphire, making them a viable candidate for further research and investigation.

Currently, no coating type fully meets all the stringent requirements for future cryogenic interferometers, which include optical absorption of less than < 5 ppm, scattering of $< 10 - 20$ ppm, and mechanical losses not exceeding 10^{-5}. The metasurface coating investigated in this thesis can be considered as an additional player in this research field, with its own benefits in comparison to the existing reflectors.

1.2 Metasurface as an alternative coating

Metasurface, as a single-layer coating, differs significantly from traditional multilayer coating designs. Compared to a homogeneous medium layer, a metasurface has a more complex composition, consisting of particles with defined geometric shapes arranged in a specific order. The investigation of such coatings presents a number of challenges not only in regard to the required fabrication and characterisation techniques but also in terms of understanding the underlying principles involved in the interaction of particles with an electromagnetic wave.

Fortunately, despite this research field emerging relatively recently in the scientific community, it has already accumulated substantial knowledge to address the development and optimisation of metasurfaces in the frame of GWDs.

The single-layer configuration of a metasurface has the greatest advantage in avoiding the introduction of excessive thermal noise, which can be associated with the multiple-layer design of other coatings. By eliminating the friction between high and low refractive index materials, the metasurface can be optimised to be extremely light and thin while still maintaining the required optical performance.

Silicon (Si) is the state-of-the-art material for the fabrication of metasurface particles, available in various forms such as amorphous, polycrystalline, and crystalline. Independent from the GW community, silicon-based metasurfaces have gained widespread recognition due to their exceptional optical properties. Firstly, the high refractive index of Si allows for the fabrication of nanometer-sized particles across a broad range of near-infrared and telecommunications wavelengths. Secondly, the dielectric properties of Si ensure the excitation of electric and magnetic dipole resonant responses, which are key to the reflective properties of the metasurface layer. Furthermore, existing fabrication techniques are also well-developed for Si nanostructures, allowing for precise control in the production process. The initial consideration is focused on the crystalline form of Si. The thermoelastic properties of c-Si at cryogenic temperatures, combined with its extremely low optical absorption, make it an ideal material candidate for the nanoparticles in a metasurface.

The refractive indices of the metasurface and the underlying substrate must differ in order to achieve the reflective effect solely based on the metasurface's configuration. A greater difference in refractive indices between the substrate and the nanoparticles minimizes coupling between the two structures, ensuring that the interaction with incident light is concentrated predominantly on the metasurface. Concurrently, the bottom substrate should satisfy mechanical loss requirements at cryogenic temperatures. The best candidate for this purpose is sapphire, which is already used for mirror substrates in KAGRA interferometers.

Sapphire may also be interesting for consideration as a substrate due to the unique property of its C-plane (0001) surface, which exhibits piezoelectricity comparable to that of bulk piezoelectric materials [55]. The design of a metasurface sensitive to the modulation of the distance between nanoparticles can possibly lead to a change in the metasurface reflectivity. This complementary property may be applicable in devices requiring tunable reflectivity, such as a SRM.

The selected metasurface materials have the most favourable properties suitable for application in GW interferometry. However, the design optimisation, achievable optical performance,

manufacturing limitations, and the feasibility of transferring the metasurface onto mirror test masses are the biggest challenges under question.

The current research primarily addresses the first two challenges, focusing on identifying metasurface designs capable of achieving high reflectivity. This thesis also covers the first attempt at the fabrication process, demonstrating that the theoretical analysis and expectations align fairly well with the experimentally measured results.

Chapter 2

Theoretical Framework

2.1 Artificially structured materials: variety and classification

A metamaterial is an artificially structured material composed of tiny, periodically arranged components that are smaller than the wavelength of the electromagnetic waves they interact with. Metamaterials exhibit properties and behaviours that are not found in natural materials, allowing them to manipulate electromagnetic waves in unusual ways, such as bending light backwards or achieving a negative refractive index.

The concept of metamaterials has its origins in the theoretical work from the late 1960s, where the idea of materials with a negative refractive index was first proposed by Viktor Veselago [56]. However, it wasn't until 2000 that this concept was experimentally validated by a research team led by David R. Smith, who demonstrated a metamaterial with a negative refractive index at microwave frequencies [57]. Although the first years of metamaterial research were focused exclusively on negative refraction, the terminology was later expanded for all artificial materials with unique electromagnetic properties.

Metamaterials that modify light behaviour, known as *optical metamaterials*, occupy a special place among the various branches of contemporary material research. This field is actively growing, diversifying into smaller sub-disciplines, such as optical magnetic metamaterials [58, 59], materials with negative refractive index [60, 61], nonlinear optics [62, 63], imaging and microscopy [64, 65], lensing [66–68], sensing technology [69, 70], artificial chirality [71, 72], electromagnetic cloaks of invisibility[73, 74], and several more.

This huge variety of metamaterials is commonly categorized into two principal groups: *metal* and *dielectric metamaterials*. This, at first glance, simple categorization must, in fact, be perceived carefully. Unlike in electronics, where classification is based on electron conduction and governed by energy bands, the interaction of light with matter is influenced by several factors. These include the wavelength of the incident light, the size of the particles and material characteristics, such as permittivity and conductivity.

The optical properties of metal metamaterials are primarily influenced by the collective behaviour of their free electrons, which respond to the oscillating electric field of light. Having a negative real part of permittivity, metal nanoparticles made from gold, silver, or other noble elements support localized surface plasmon resonances (LSPRs) [75, 76]. These resonances are largely influenced by the particle's size, shape, composition, and dielectric environment [77]. According to the Rayleigh scattering approximation, the excitation of LSPRs does not impose

strict size limitations on particles, permitting them as an advantage to be at the subwavelength scale [78]. However, the dissipative losses in metal nanoparticles restrict their applicability in optical devices. These losses encompass Ohmic losses, where energy is dissipated as heat due to the metal's resistance to the free electron movement; radiative losses, originating from the re-radiation of energy by oscillating charges; and absorption losses. Characterised by a high imaginary part of the permittivity, these losses lead to substantial energy dissipation and heat generation, thus reducing operational efficiency in optical devices. [79].

The discovery of dielectric metamaterials has solved the problem of excessive dissipative losses and broadened the scope of potential applications. Unlike metal-based metamaterials, dielectric metamaterials don't have free-running electrons and can be selected with minimal absorption, allowing for efficient light manipulation with reduced power loss [7].

The manipulation of light by dielectric metasurfaces is more effective due to the ability of electromagnetic waves to propagate through the medium. The generation of displacement currents leads to a pronounced magnetic response, which can be comparable to or greater than the electric one [80]. In metals, generating a significant magnetic response is challenging and typically requires high-order plasmonic modes or specific geometrical configurations, such as split-ring resonators [81] [8].

The real part of permittivity in dielectric particles is positive, and the size of these particles is strictly constrained by the incident wavelength, their permittivity value and the generated mode inside of them.

In the selection of the material for dielectric nanoparticles in a metasurface, it is essential to consider a number of critical aspects. First, a high refractive index is crucial as it enables strong light-matter interaction, particularly when the nanoparticle is in a medium with a low refractive index, such as vacuum. This characteristic facilitates the fabrication of small-sized nanoparticles with sub-wavelength spacing, helping to avoid diffraction effects. Another property is low optical loss, meaning the material should exhibit minimal absorption at the operating wavelength. Additionally, the important factor is the compatibility of the material with fabrication processes, which include material deposition, etching and a process of pattern creation. Materials that meet these criteria include silicon (Si) [82], germanium (Ge) [83, 84], tellurium (Te) [85], gallium arsenide (GaAs) [86] and many others [87].

The material selected for nanoparticles in our investigation is silicon, chosen for its dual advantages in the field of GW physics as well as its benefits in metamaterial applications. From the perspective of metasurface creation, silicon offers a high refractive index [88] and low absorption at the near-infrared telecom wavelengths [41]. Additionally, its widespread use in semiconductor technology makes it an excellent candidate due to its compatibility with established fabrication processes, such as photolithography and electron beam lithography [89], along with its proven performance in existing applications.

[7] This key aspect was considered at the outset when determining the type of metasurface to be explored.

[8] Magnetic response in metal elements is not inherently strong as for dielectric elements and often requires an intricate design to achieve comparable effects.

2.2 Scattering and reflectivity principles

The unique behaviour of a dielectric metasurface is attributed to the scattering process of the constituent individual elements. This process is driven by the electromagnetic field of light, which induces electric and magnetic multipole moments in nanoparticles, leading to distinct scattering intensities and specific radiation patterns.

To understand the principles of scattering, let's consider a single particle illuminated by an electromagnetic wave. The particle has its own modes that can be excited by incident light and which can be decomposed into multipole moments. The multipole moments include electric dipole (ED), magnetic dipole (MD), electric quadrupole (EQ), magnetic quadrupole (MQ), electric octupole (EO), magnetic octupole (MO) moment, among others. These spherical harmonics form a basis. The amplitudes and phases of the excited multipole moments are influenced by the light wave's frequency and the particle's size, shape and material properties, in particular, its dielectric permittivity ϵ and magnetic permeability μ. The excited particle scatters secondary radiation in various directions, maintaining coherence with the incident wave. This coherence, along with phase and amplitude variations, leads to constructive or destructive interference, with the specific patterns of this interference dependent on the observer's direction and the particle's size, shape, and orientation.

The primary focus of this thesis is directed towards the study of perfect reflectivity effect exhibited by silicon metasurfaces. In terms of power distribution, this effect is characterised by the behaviour of light, which, after interaction with the metasurface, is completely directed backwards, with no light observed in the far-field of the transmission area.

However, looking at the scattering process of this phenomenon, particles scatter light in all directions. To achieve the desired reflectivity effect, the light scattered in the direction of the incident wave propagation must have a sufficient amplitude and a phase shift of π. This condition enables the transmitted incident light to destructively interfere with the scattered light, effectively preventing it from passing through the structure. This situation can be realised only under the resonant condition of the considered dielectric particles. Additionally, their precise positioning within the array facilitates destructive interference in the plane of the built metasurface. As a result, in accordance with the principle of energy conservation, the total light is reflected back.

The subsequent section 2.4 presents a comprehensive mathematical derivation of the high reflectivity effect observed in dielectric metasurfaces.

2.3 General concepts on light-matter interaction

The behaviour of reflective metasurfaces cannot be fully understood without first considering the fundamental principles of light-matter interaction. Before exploring the mathematical complexity of the scattering process, it is essential to introduce and consider Maxwell's equations, which describe how electric and magnetic fields interact with matter. This section also gives more details about optical material classification based on the response to the incident light field, outlines the key characterisation parameters and introduces the fundamental laws of reflection and refraction for bulk materials.

2.3.1 Maxwell's equations and material types

Nature consists of various types of material objects that interact with light, causing phenomena such as reflection, absorption, refraction, lensing, etc. The electromagnetic behaviour of light and its interaction with matter is described by Maxwell's equations, which were initially introduced in 1865 by James Clerk Maxwell [90]. Maxwell's equations in linear, homogeneous, isotropic matter can be written in the following International System of Quantities (ISQ) form [91]:

$$\nabla \times \vec{H} = \vec{j}_{\text{cond}} + \frac{\partial \vec{D}}{\partial t} \qquad \textit{Ampère's equation} \tag{2.1}$$

$$\nabla \cdot \vec{D} = \rho \qquad \textit{Gauss's law} \tag{2.2}$$

$$\nabla \times \vec{E} = -\frac{\partial \vec{B}}{\partial t} \qquad \textit{Faraday's law} \tag{2.3}$$

$$\nabla \cdot \vec{B} = 0 \qquad \textit{Gauss's law for magnetism} \tag{2.4}$$

where $\vec{E}$ and $\vec{H}$ are the electric and magnetic fields, respectively. $\vec{D}$ is the electric displacement field, $\vec{B}$ is the magnetic flux density, and ρ is the electric charge density. The conductive current density is

$$\vec{j}_{\text{cond}} = \sigma \vec{E}, \tag{2.5}$$

where σ is conductivity.

The constituent relations that provide a connection between the incident field and the corresponding dielectric and magnetic material properties, such as polarization ($\vec{P}$) and magnetization ($\vec{M}$), are:

$$\vec{D} = \epsilon_0 \vec{E} + \vec{P}, \tag{2.6}$$

$$\vec{B} = \mu_0 (\vec{H} + \vec{M}), \tag{2.7}$$

where ϵ_0 is the permittivity of free space, μ_0 is the permeability of free space.

The vectors $\vec{P}$, $\vec{M}$ characterise the response of matter to external electric and magnetic fields, respectively. Their relations to these fields are given by the equations: $\vec{P} = \chi_{\text{e}} \epsilon_0 \vec{E}$; $\vec{M} = \chi_{\text{m}} \vec{H}$, where χ_{e} is the electric susceptibility and χ_{m} is the magnetic susceptibility. These relations modify the equations for $\vec{D}$ and $\vec{B}$, resulting in:

$$\vec{D} = \epsilon_0 (1 + \chi_{\text{e}}) \vec{E} = \epsilon_0 \epsilon_{\text{r}} \vec{E} = \epsilon \vec{E}, \tag{2.8}$$

$$\vec{B} = \mu_0 (1 + \chi_{\text{m}}) \vec{H} = \mu_0 \mu_{\text{r}} \vec{H} = \mu \vec{H}. \tag{2.9}$$

Here, $\epsilon = \epsilon_0 (1 + \chi_{\text{e}})$ is the permittivity, and $\mu = \mu_0 (1 + \chi_{\text{m}})$ is the permeability of the material, ϵ_{r} and μ_{r} are relative permittivity and permeability, respectively.

Material behaviour can be attributed to one of three categories of light-medium interaction: metal, dielectric and semiconductor-type. By considering Maxwell-Ampère equation and

presenting it in a non-stationary regime as a sum of conductive $\vec{j}_{\text{cond}}$ and displacement $\vec{j}_{\text{disp}}$ currents, we get:

$$\nabla \times \vec{H} = \vec{j}_{\text{cond}} + \vec{j}_{\text{disp}} = \sigma\vec{E} + \epsilon\frac{\partial\vec{E}}{\partial t}. \tag{2.10}$$

By defining the ratio of $\beta = \frac{|\vec{j}_{cond}|}{|\vec{j}_{disp}|}$, one can distinguish three cases [91]:

- $\beta \gg 1$ (metal)
- $\beta \ll 1$ (dielectric)
- $\beta \simeq 1$ (semiconductor)

For periodically varying electric field $\vec{E} = \vec{E}_0 e^{i\omega t}$:

$$\beta = \frac{\sigma}{\epsilon\omega}. \tag{2.11}$$

It means that the same material can belong to different types depending on the frequency of the incident light field and the dispersion of its parameters [9]. In this thesis, silicon material is investigated exclusively in the near-infrared (1064 nm) and telecommunication (1550 nm) wavelength ranges, for which $\beta \ll 1$.

The equations describing the propagation of the electromagnetic waves in semiconductive material:

$$\Delta\vec{E} - \epsilon\mu\frac{\partial^2\vec{E}}{\partial t^2} = \sigma\mu\frac{\partial\vec{E}}{\partial t}, \tag{2.12}$$

$$\Delta\vec{H} - \epsilon\mu\frac{\partial^2\vec{H}}{\partial t^2} = \sigma\mu\frac{\partial\vec{H}}{\partial t}. \tag{2.13}$$

The first equation can be derived in several steps. By taking the curl of Faraday's law (2.3) and using the operation of vector Laplacian $\nabla \times (\nabla \times \vec{E}) = \nabla(\nabla \cdot \vec{E}) - \Delta\vec{E}$, we get:

$$\nabla(\nabla \cdot \vec{E}) - \Delta\vec{E} = -\mu\frac{\partial(\nabla \times \vec{H})}{\partial t}. \tag{2.14}$$

Substituting Gauss's law (2.2) for no spatial charge (ρ = 0): $\nabla \cdot \vec{D} = 0$, and Ampère's equation for the curl of the magnetic field (2.1), the second-order partial differential equation (2.12) for the electric field vector $\vec{E}$ can be obtained. The derivation of the second equation (2.13) for the magnetic field vector $\vec{H}$ follows the same logic.

[9] Permittivity ϵ and conductivity σ are frequency-dependent values.

• Dielectric-type

The electromagnetic wave propagation equations for a homogeneous, isotropic, non-dissipative and non-dispersive dielectric material, free of charge and conduction currents, take the form:

$$\Delta\vec{E} - \epsilon\mu\frac{\partial^2\vec{E}}{\partial t^2} = 0, \tag{2.15}$$

$$\Delta\vec{H} - \epsilon\mu\frac{\partial^2\vec{H}}{\partial t^2} = 0. \tag{2.16}$$

These equations resemble the wave equation: $\Delta\vec{f} - \frac{1}{v^2}\frac{\partial^2\vec{f}}{\partial t^2} = 0$, where $\vec{f}$ is the disturbance [92]. The wave equation can also be written using d'Alembert operator: $\Box\vec{f} = 0$.

The direct comparison gives the information about the speed of the propagating wave, that is equal to $v = 1/\sqrt{\epsilon\mu}$, or in vacuum $v_0 = c = 1/\sqrt{\epsilon_0\mu_0}$.

It is now possible to introduce the *refractive index* parameter - n. It is equal to the ratio between the speed of light in vacuum c and the phase velocity of light in the medium v:

$$n = \frac{c}{v} = \frac{\sqrt{\epsilon\mu}}{\sqrt{\epsilon_0\mu_0}} = \sqrt{\epsilon_\mathrm{r}\mu_\mathrm{r}}. \tag{2.17}$$

For non-magnetic medium ($\mu_\mathrm{r} = 1$): $n = \sqrt{\epsilon_\mathrm{r}}$.

• Metal-type

For the metal-type material, the displacement current is negligible in comparison with the conductive current, so the partial differential equations take the form:

$$\Delta\vec{E} - \sigma\mu\frac{\partial\vec{E}}{\partial t} = 0, \tag{2.18}$$

$$\Delta\vec{H} - \sigma\mu\frac{\partial\vec{H}}{\partial t} = 0. \tag{2.19}$$

The periodically varying electric and magnetic fields $\vec{E} = \vec{E}_0 e^{i\omega t}$, $\vec{H} = \vec{H}_0 e^{i\omega t}$ satisfy to the transformation:

$$\frac{\partial\vec{E}}{\partial t} = \frac{1}{i\omega}\frac{\partial^2\vec{E}}{\partial t^2}, \tag{2.20}$$

$$\frac{\partial\vec{H}}{\partial t} = \frac{1}{i\omega}\frac{\partial^2\vec{H}}{\partial t^2}. \tag{2.21}$$

So the same equations can be written as:

$$\Delta\vec{E} - \frac{\sigma\mu}{i\omega}\frac{\partial^2\vec{E}}{\partial t^2} = 0, \tag{2.22}$$

$$\Delta\vec{H} - \frac{\sigma\mu}{i\omega}\frac{\partial^2\vec{H}}{\partial t^2} = 0. \tag{2.23}$$

Denoting $\epsilon' = -i\sigma/\omega$, the equation can also be referred to as the wave equation, where $\tilde{v} = 1/\sqrt{\epsilon'\mu}$. An important fact is that the permittivity, in this case, is imaginary, making the phase velocity a complex number.

Accordingly, the wave number is also complex:

$$\tilde{k}^2 = \frac{\omega^2}{\tilde{v}^2} = -i\omega\sigma\mu, \tag{2.24}$$

$$\tilde{k}^2 = k_1^2 - k_2^2 + 2ik_1k_2. \tag{2.25}$$

Comparing imaginary and real parts, $k_1 = k_2 = k = \sqrt{\omega\sigma\mu/2}$. The wave number can be written as:

$$\tilde{k} = k_1 + ik_2 = k(1+i) = \frac{1+i}{\delta}, \tag{2.26}$$

$$\delta = \sqrt{\frac{2}{\omega\sigma\mu}}, \tag{2.27}$$

where δ is the *penetration depth* or *skin depth*. The skin depth quantifies how quickly the wave's amplitude decays as it travels through the conductor. It decreases with the increase in frequency, meaning that higher-frequency waves penetrate less deeply than lower-frequency waves. The skin depth also depends on material properties such as conductivity σ and permeability μ.

• Semiconductor-type

For semiconductor-type materials, the equations have the full form. Considering a monochromatic wave and previous transformations to the wave equations:

$$\Delta\vec{E} - \left(\epsilon - \frac{i\sigma}{\omega}\right)\mu\frac{\partial^2\vec{E}}{\partial t^2} = 0, \tag{2.28}$$

$$\Delta\vec{H} - \left(\epsilon - \frac{i\sigma}{\omega}\right)\mu\frac{\partial^2\vec{H}}{\partial t^2} = 0. \tag{2.29}$$

The permittivity for semiconductors is a complex number: $\tilde{\epsilon} = \epsilon + \epsilon' = \epsilon - \frac{i\sigma}{\omega}$. In this scenario, the medium exhibits both dielectric and metallic properties. The electromagnetic field propagates in a semiconductor as a plane, transverse, damped wave, with a phase delay between electric and magnetic fields.

• Anisotropic medium

There are media in nature that exhibit anisotropy, i.e. they have different properties depending on the spatial direction. For this type of material, the permittivity and permeability are tensor quantities. The constitutive relations can be written as:

$$D_i = \epsilon_{ik}E_k, \quad B_i = \mu_{ik}H_k, \quad i,k = 1,2,3. \tag{2.30}$$

2.3.2 Reflection and refraction in dielectrics

The basic laws of reflection and refraction in dielectric non-magnetic ($\mu = \mu_0$) media consist of three rules.

1. The principle of classical reflection states that the angles of incidence and reflection are equal. If the incident angle, defined as the angle between the incident ray and the normal to the surface, is θ, and the reflection angle, defined as the angle between the normal and the reflected ray, is β, then $\theta = \beta$.

2. The refraction law, also known as Snellius-Descartes law, describes the behaviour of light as it passes from one medium into another. If light travels from a medium with a refractive index n_1 to another medium with a refractive index n_2, the relation between the angle of incidence θ ($\theta \neq 0$) and the angle of refraction γ:

$$\frac{\sin\theta}{\sin\gamma} = \frac{n_2}{n_1}. \tag{2.31}$$

3. The law of total (internal) reflection tells if $n_2 < n_1$, then at the critical angle, no refraction occurs, and the incident light is completely reflected at the interface between the two media.

$$\theta > \arcsin\left(\frac{n_2}{n_1} \cdot \sin\gamma_{\text{max}}\right) = \arcsin\left(\frac{n_2}{n_1} \cdot \sin\frac{\pi}{2}\right) = \arcsin\left(\frac{n_2}{n_1}\right). \tag{2.32}$$

The behaviour of reflected and refracted components of a linearly polarized plane wave can be described by Fresnel's equations. Let's denote r and t as the complex amplitude coefficients for reflection and transmission, respectively. Linearly polarized light can be decomposed into a parallel component (p-polarization) or a perpendicular component (s-polarization) with respect to the plane of incidence.

$$t_{\text{p}} = \frac{2n_1\cos\theta}{n_1\cos\gamma + n_2\cos\theta}; \tag{2.33}$$

$$t_{\text{s}} = \frac{2n_1\cos\theta}{n_1\cos\theta + n_2\cos\gamma}; \tag{2.34}$$

$$r_{\text{p}} = \frac{n_1\cos\gamma - n_2\cos\theta}{n_1\cos\gamma + n_2\cos\theta}; \tag{2.35}$$

$$r_{\text{s}} = \frac{n_1\cos\theta - n_2\cos\gamma}{n_1\cos\theta + n_2\cos\gamma}. \tag{2.36}$$

Or using Snellius-Descartes law, the system can be written as:

$$t_{\text{p}} = \frac{2\sin\gamma\cos\theta}{\sin(\theta+\gamma)\cos(\theta-\gamma)}; \tag{2.37}$$

$$t_{\text{s}} = \frac{2\sin\gamma\cos\theta}{\sin(\theta+\gamma)}; \tag{2.38}$$

$$r_{\text{p}} = \frac{\tan(\theta-\gamma)}{\tan(\theta+\gamma)}; \tag{2.39}$$

$$r_{\text{s}} = -\frac{\sin(\theta-\gamma)}{\sin(\theta+\gamma)}. \tag{2.40}$$

Fresnel's equations are important as they describe the relation between s- and p-polarization of electromagnetic waves in reflection and refraction phenomena. Particular attention is drawn to the Brewster angle, at which p-polarized light is perfectly transmitted through a medium-separating surface, resulting in no reflected light. This occurs when the reflected

and refracted rays are at 90 degrees to each other. The Brewster angle can be found using the following relation:

$$\tan \gamma_{\mathrm{B}} = \frac{n_2}{n_1}. \tag{2.41}$$

For light incident at a normal angle of incidence ($\theta = 0$), the angle of refraction γ will also be 0 degrees. At normal incidence, the Fresnel reflection coefficients for perpendicular (s) and parallel (p) polarizations are identical because the polarization does not affect the reflection. Therefore, for both s- and p-polarizations:

$$r = \frac{n_1 - n_2}{n_1 + n_2}. \tag{2.42}$$

The amplitude transmission coefficient can be derived in the case of the absence of absorption using the equation: $t^2 n_2/n_1 = 1 - r^2$. Substituting the value r:

$$t = \frac{2n_1}{n_1 + n_2}. \tag{2.43}$$

2.3.3 Polarizability

The material properties can also be described on a much smaller scale, related to the electric field experienced by each atom or molecule within the medium. Let's consider an external electric field $\vec{E}$ applied to the material. Each atom or molecule experiences a distortion of its electric field due to contributions from both the external field and the fields generated by neighbouring atoms or molecules. This resulting field is called the local electric field, denoted as $\vec{E}_{\mathrm{loc}} = \vec{E} + \vec{P}/(3\epsilon_0)$, where $\vec{P}$ is the polarization vector. The atom or molecule becomes polarized, meaning it exhibits a separation of positive and negative charges, which is described by the microscopic electric dipole moment, $\vec{p_j}$. The relation between the microscopic electric dipole moment and the local electric field is $\vec{p_j} = \alpha_j \vec{E}_{\mathrm{loc}}$, where α_j is known as the atomic or molecular polarizability. Polarizability is an intrinsic characteristic, representing the tendency of an atom or molecule to become polarized in response to the induced local electric field.

From the previous equations, the polarization of medium can be expressed macroscopically as $\vec{P} = \chi_{\mathrm{e}} \epsilon_0 \vec{E}$, where χ_{e} is the electric susceptibility. The polarization vector can also be defined in terms of microscopic parameters: $\vec{P} = \sum_j N_j \vec{p_j} = \sum_j N_j \alpha_j \vec{E}_{\mathrm{loc}}$, where N_j is the number of polarized objects per unit volume. Equating the right-hand sides of these equations, the relation between the electric susceptibility and the atomic polarizability is:

$$\chi_{\mathrm{e}} \epsilon_0 = \sum_j N_j \alpha_j \left(1 + \frac{\chi_{\mathrm{e}}}{3}\right). \tag{2.44}$$

Or by using the relation between susceptibility and relative permittivity, $\chi_{\mathrm{e}} = \epsilon_{\mathrm{r}} - 1$, the Clausius-Mossotti relation can be derived:

$$\frac{\varepsilon_{\mathrm{r}} - 1}{\varepsilon_{\mathrm{r}} + 2} = \frac{\sum_j N_j \alpha_j}{3\varepsilon_0}. \tag{2.45}$$

The equation 2.45 can be applied to determine the effective dielectric permittivity of metamaterials consisting of individual elements [93, 94].

Polarizability of macroscopic objects is related to atomic polarizability as: $\alpha = \sum_j N_j \alpha_j$.

Moving on to a more particular case, such as the calculation of the ED moment for a macroscopic object, such as a dielectric particle of a metasurface, the local electric field $\vec{E}_{\text{loc}}$ is averaged across many atoms. This averaging leads to the approximation that the local electric field is nearly identical to the macroscopic external electric field $\vec{E}$. Therefore, the induced ED moment for a particle is described by $\vec{p} = \alpha_{\text{p}} \vec{E}$, where α_{p} is the electric dipole polarizability. Similarly, the induced MD moment is given by $\vec{m} = \alpha_{\text{m}} \vec{H}$, where α_{m} is the magnetic dipole polarizability. In this context, higher-order moments are not considered.

2.4 Reflectivity formalism based on scattering principles for metasurfaces

The interaction of a metasurface with incident light can be described using two different approaches. One of these approaches can be generalized purely based on the collective behaviour of metasurface elements. In this approach, the metasurface is treated as a standard homogeneous material characterised by its unique effective permittivity and permeability, which follow the classical laws mentioned in the previous sections (2.3.2, 2.3.3). The effective values of permittivity and permeability can be empirically determined during the metasurface experimental characterisation [95]. In practice, however, this approach is limited to revealing the essential effective parameters.

The methodology presented in the following chapters of this thesis considers the individual response of each particle to the incident light field and the resulting scattering process. Thus, the behaviour of the metasurfaces is described by the sum of all particle responses. In this approach, the optical behaviour explicitly depends on the shape, size, and position of each individual element [96].

The problem of reflection of a metasurface can be solved completely analytically if this metasurface consists of spherical particles in a homogeneous medium. For more complex particle shapes, such as cylinders, cuboids, prisms, and so on, particularly placed in a non-uniform surrounding medium, numerical techniques are commonly employed. Numerical calculations partition each geometrical figure into discrete subelements, termed *mesh elements*. For each mesh element, Maxwell's equations are solved along with appropriate boundary conditions. Then, the solutions from all mesh elements are integrated into a general solution, which details how the electric and magnetic fields are distributed inside and outside the particle.

In order to understand the principles of metasurface reflectivity and to use logical interpretation and verification of the resulting simulations for real systems, it is essential to consider an analytical approach for the simplest case. The simplest case is an infinite metasurface comprised of periodically arranged spherical particles placed in a homogeneous medium. The following subsections demonstrate the derivation of the reflectivity power coefficient of such a metasurface

using Mie theory that describes the electromagnetic plane wave scattering by a homogeneous spherical particle [97].

There are formally several steps in our approach:

1. It begins with the calculation of Mie scattering electric a_n and magnetic b_n coefficients. The incident and scattered field, as well as the field inside of a particle, can be presented as a superposition of vector spherical harmonics ($\vec{M}, \vec{N}$), weighted by the appropriate coefficients. The first step is to define the coefficients a_n and b_n responsible for the scattering process due to the excited electric and magnetic multipole moments.
2. The second step shows how to link the polarizabilities to the appropriate Mie scattering coefficients. For that purpose, we choose the consideration of only electric and magnetic dipole moments and delve into the mathematical form of the electric field representation.
3. After that, the transition from a single particle to the infinite periodic array is demonstrated. This step shows how to derive the effective polarizabilities of a metasurface, considering the identical nature of all constitutive particles.
4. Finally, the reflection and transmission coefficients are derived by integrating the information about the scattering process with the continuity condition of the electric field at the interface.

2.4.1 Scattering coefficients in Mie theory

Mie theory provides an exact solution to Maxwell's equations for spherical particles of all material types and sizes. This theory was formulated and contributed by such scientists as Alfred Clebsch (1833-72), Ludvig Lorenz (1829-91), Gustav Mie (1868-1957) and Peter Debye (1884-1966) [98]. Mie theory was originally implemented for homogeneous isotropic metallic spherical particles but was further extended for application to dielectric spherical particles and even to spheres with complex structures, such as those with outer shells [99, 100] and varying dielectric constants [98].

The general comprised formalism presented in this section is taken from the book of C. Bohren and D. Huffman [97], and several papers discussing the analytical approach [96, 101–104].

The model consists of a dielectric spherical particle with a diameter D and a complex refractive index $\tilde{n}_\mathrm{s} = n_\mathrm{s} + in'_\mathrm{s}$. The particle is embedded in a non-absorbing, homogeneous, infinite medium with a refractive index equal to n_d. The position of the sphere is at the origin of the coordinate system. A plane electromagnetic wave of frequency ν irradiates the sphere in the z-direction: $\vec{E}_\mathrm{i} = \vec{E}_0 e^{i(k_\mathrm{d} z - 2\pi\nu t)}$ [10], k_d is the wave number in the surrounding medium. The magnetic field of the incident light $\vec{H}_\mathrm{i}$ is related to the electric field $\vec{E}_\mathrm{i}$ through Maxwell's equations. The corresponding wavelength of the incident wave inside of the medium is $\lambda_\mathrm{d} = 2\pi/k_\mathrm{d} = \lambda_0/n_\mathrm{d}$, where λ_0 is the wavelength in vacuum.

Mie theory provides detailed information about the electromagnetic field distribution resulting from the interaction of incident light with a spherical particle. In particular, this theory allows

[10] Following the method used in the book of C. Bohren and D. Huffman, the exponent of the electric field is taken with a negative sign $e^{-2\pi\nu t} = e^{-\omega t}$. The imaginary part of the electric field in the previous section is positive $e^{\omega t}$.

for the analytical calculation of the scattered light field ($\vec{E}_\mathrm{r}, \vec{H}_\mathrm{r}$) and the field within the sphere ($\vec{E}_\mathrm{g}, \vec{H}_\mathrm{g}$). The scattered wave has a complex electric $\vec{E}_\mathrm{r}$ and magnetic field $\vec{H}_\mathrm{r}$, and directed along the vector $\vec{e}_\mathrm{r}$ defined by polar and azimuthal angles (θ, ϕ), respectively. The z-axis and the vector $\vec{e}_\mathrm{r}$ define the scattering plane.

The incident ($\vec{E}_\mathrm{i}, \vec{H}_\mathrm{i}$), scattered ($\vec{E}_\mathrm{r}, \vec{H}_\mathrm{r}$) and the field inside of a spherical particle ($\vec{E}_\mathrm{g}, \vec{H}_\mathrm{g}$) can be decomposed by basis vectors, that are presented as vector spherical harmonics $\vec{M}$ and $\vec{N}$, multiplied to the necessary coefficients.

The decomposition for the scattered field is:

$$\vec{E}_\mathrm{r} = \sum_{n=1}^{\infty} \vec{E}_n (i a_n \vec{N}_{en}^{(3)} - b_n \vec{M}_{on}^{(3)}), \tag{2.46}$$

$$\vec{H}_\mathrm{r} = \frac{k_\mathrm{d}}{2\pi\nu\mu_\mathrm{d}} \sum_{n=1}^{\infty} \vec{E}_n (i b_n \vec{N}_{on}^{(3)} + a_n \vec{M}_{en}^{(3)}), \tag{2.47}$$

where μ_d is the permeability of the surrounding medium. The subscripts e and o denote "even" (cos) and "odd" (sin) spherical harmonics. The superscript (3) defines the radial dependence of the vectors specified by the spherical Bessel functions of the third kind.

The functions a_n and b_n, known as Mie scattering coefficients, are the quantities we are looking for. They contain information about the particle size, optical properties and, as a consequence, define the response to the incident electromagnetic wave.

To derive explicit expressions for the scattering coefficients, we assume that the incident wave $\vec{E}_\mathrm{i}, \vec{H}_\mathrm{i}$ is fully known. Additionally, the fields must satisfy the boundary conditions at the interface between the sphere and the surrounding medium:

$$(\vec{E}_\mathrm{i} + \vec{E}_\mathrm{r} - \vec{E}_\mathrm{g}) \times \vec{e}_\mathrm{r} = (\vec{H}_\mathrm{i} + \vec{H}_\mathrm{r} - \vec{H}_\mathrm{g}) \times \vec{e}_\mathrm{r} = 0. \tag{2.48}$$

The initial condition and the boundary conditions provide all the necessary information to derive the coefficients for the scattered field and the field inside the particle. As the focus of this study is on the scattering process, the scattering coefficients are given by:

$$a_n = \frac{w\psi_n(wx)\psi_n'(x) - \psi_n(x)\psi_n'(wx)}{w\psi_n(wx)\xi_n'(x) - \xi_n(x)\psi_n'(wx)}, \tag{2.49}$$

$$b_n = \frac{\psi_n(wx)\psi_n'(x) - w\psi_n(x)\psi_n'(wx)}{\psi_n(wx)\xi_n'(x) - w\xi_n(x)\psi_n'(wx)}, \tag{2.50}$$

where

$$w = \frac{n_\mathrm{s}}{n_\mathrm{d}} + i\frac{n_\mathrm{s}'}{n_\mathrm{d}}; \qquad x = \frac{\pi D}{\lambda_\mathrm{d}} = \frac{\pi D n_\mathrm{d}}{\lambda_0}. \tag{2.51}$$

The parameter w represents the complex relative refractive index of the particle with respect to the medium, and x quantifies the relative size of the sphere compared to the wavelength. The ψ_n and ξ_n are called Riccati-Bessel functions, and their derivatives ψ_n' and ξ_n' are taken in respect to the arguments x or wx.

It is important to note that when the relative refractive index is $w = 1 + i0$, indicating that the sphere has the same refractive index as the surrounding medium, the coefficients a_n and b_n are zero for all n. Under this condition, no scattering occurs. This observation highlights that scattering is caused by differences in indexes of refraction between the particle and the medium.

The essential relations of Mie theory are also presented in terms of scattering and extinction cross-sections, designated as $\sigma_{\text{sc}}, \sigma_{\text{ex}}$, respectively. The scattering cross-section is a measure of the effective area for scattering light. The extinction cross-section quantifies the total effective area over which a particle contributes to both scattering and absorption.

$$\sigma_{\text{sc}} = \frac{2\pi}{k_{\text{d}}^2} \sum_{n=1}^{\infty} (2n+1) \left(|a_n|^2 + |b_n|^2 \right), \tag{2.52}$$

$$\sigma_{\text{ex}} = \frac{2\pi}{k_{\text{d}}^2} \sum_{n=1}^{\infty} (2n+1)\, \Re(a_n + b_n), \tag{2.53}$$

where $\Re$ denotes the real part of the argument.

In order to be independent of the size of a particle, it is common practice to sometimes use the dimensionless parameter of the efficiency. Scattering efficiency, Q_{sc}, is defined as the ratio of the scattering cross-section, σ_{sc}, to the geometric cross-sectional area of the particle, $\pi D^2/4$: $Q_{\text{sc}} = 4\sigma_{\text{sc}}/\pi D^2$. This parameter quantifies how effective a particle is at scattering light relative to its size. This concept is similarly applied to the extinction efficiency Q_{ex}.

2.4.2 Relation between scattering coefficients and polarizability

Polarizability is an intrinsic property of a particle that quantifies its response to an external electromagnetic field, leading to the generation of multipole moments. As it also depends on the particle characteristics, it is directly related to the Mie scattering coefficients.

By investigating the Mie scattering coefficients (a_n, b_n) and the decomposition of the scattered electromagnetic field $(\vec{E}_{\text{r}}, \vec{H}_{\text{r}})$ in the basis of vector spherical harmonics, it was revealed that the index n defines the multipole order. In other words, $n = 1$ corresponds to the dipole term, $n = 2$ - to the quadruple term, and so on. Moreover, it was shown that the coefficient a_n describes the electric response, while b_n - the magnetic response. As a consequence, the coefficient a_1 represents the ED moment of a spherical particle, b_1 - the MD moment, a_2 - the EQ moment, b_2 - the MQ moment, etc.

In order to establish the connection between polarizability and the Mie scattering coefficients, it is necessary to present the equation 2.46 in the spherical coordinate system [101]:

$$E_\theta^{\text{r}} = E_0 \frac{i e^{i k_{\text{d}} r}}{k_{\text{d}} r} \cos\phi \sum_n \frac{2n+1}{n(n+1)} \left(a_n \frac{dP_n^1}{d\theta} + b_n \frac{P_n^1}{\sin\theta} \right), \tag{2.54}$$

$$E_\phi^{\text{r}} = E_0 \frac{e^{i k_{\text{d}} r}}{i k_{\text{d}} r} \sin\phi \sum_n \frac{2n+1}{n(n+1)} \left(a_n \frac{P_n^1}{\sin\theta} + b_n \frac{dP_n^1}{d\theta} \right), \tag{2.55}$$

where P_n^1 is the set of associated Legendre polynomials of the first order.

If the previously discussed parameter x (Equation 2.51), which defines how small or large the particle is in comparison to the incident wavelength, is approximately equal to (π/n_s), then only a few terms of multipole decomposition are needed to accurately approximate a_n and b_n Mie coefficients. This means that the whole scattering process can be explained by ED and MD resonant responses within the nanoparticle.

Let's consider the ED moment ($n = 1$) with the Mie scattering coefficient a_1. The first associated Legendre polynomial is related to the 1st derivative of the corresponding Legendre polynomial P_n [11]:

$$P_n^1(x) = \left(1 - x^2\right)^{1/2} \frac{dP_n(x)}{dx}, \tag{2.56}$$

where $x = \cos\theta$. Then $P_1^1(\cos\theta) = \sin\theta$, $dP_1^1/d\theta = \cos\theta$. The equations for the polar (2.54) and azimuthal (2.55) components can be rewritten as:

$$E^\mathrm{r}_{\theta,n=1} = E_0 \frac{ie^{ik_\mathrm{d}r}}{k_\mathrm{d}r} \cos\phi \frac{3}{2} a_1 \cos\theta, \tag{2.57}$$

$$E^\mathrm{r}_{\phi,n=1} = E_0 \frac{e^{ik_\mathrm{d}r}}{ik_\mathrm{d}r} \sin\phi \frac{3}{2} a_1. \tag{2.58}$$

On the other hand, a general dipole representation of the radiated electric field in far-field approximation can be expressed as:

$$\vec{E}_{\vec{p}}(\vec{r}) = \frac{k_0^2}{4\pi\epsilon_0} \frac{e^{ik_\mathrm{d}r}}{r} \left[\hat{e}_\mathrm{r} \times [\vec{p} \times \hat{e}_\mathrm{r}]\right], \tag{2.59}$$

where $\hat{e}_\mathrm{r} = \vec{r}/r$ is a unit vector. In the spherical coordinate system, it is given by: $\hat{e}_\mathrm{r} = (\sin\theta\cos\phi, \sin\theta\sin\phi, \cos\theta)$. The vector of the ED is $\vec{p} = \alpha_\mathrm{p}\vec{E}_0$. For the vector $\vec{E}_0$ directed along the x-direction: $p_x = \alpha_\mathrm{p} E_0$. The wave number in the surrounding medium is related to the wave number in vacuum by relation $k_\mathrm{d}^2 = k_0^2\epsilon_\mathrm{d}$, where ϵ_d is the relative permittivity of the surrounding medium. The spherical components of this equation are [104]:

$$E^\mathrm{p}_\theta = \frac{k_\mathrm{d}^2}{4\pi\epsilon_0\epsilon_\mathrm{d}} \frac{e^{ik_\mathrm{d}r}}{r} p_x \cos\phi\cos\theta, \tag{2.60}$$

$$E^\mathrm{p}_\phi = \frac{k_\mathrm{d}^2}{4\pi\epsilon_0\epsilon_\mathrm{d}} \frac{e^{ik_\mathrm{d}r}}{r} (-p_x \sin\phi). \tag{2.61}$$

The comparison of the right sides of the equations, either for the polar or for the azimuthal component, gives the relation between the ED polarizability α_p and the electric Mie coefficient of the first order a_1:

$$\alpha_\mathrm{p} = i \frac{6\pi\epsilon_\mathrm{d}\epsilon_0}{k_\mathrm{d}^3} a_1. \tag{2.62}$$

[11] In some mathematical reference books, the first associated Legendre polynomial P_n^1 is defined with a negative sign. However, we follow the definition provided in the book of C. Bohren and D. Huffman, which uses a positive sign.

The same methodology can be applied to the derivation of the MD polarizability:

$$\alpha_{\mathrm{m}} = i\frac{6\pi}{k_{\mathrm{d}}^3} b_1. \tag{2.63}$$

It should be noted that the units of the two polarizabilities are different. The unit of ED polarizability is $[\epsilon_0 \mathrm{m}^3]$, while the unit of MD polarizability is $[\mathrm{m}^3]$. The information about polarizabilities leads to the direct calculation of the excited ED and MD moments created by the external field.

2.4.3 Electric and magnetic dipoles for a periodic structure

Having considered the behaviour of a single nanoparticle, we now turn to an examination of a periodic array of spherical particles of identical size and position relative to each other. The whole array can be simplified to one repeatable in the x- and y-direction unit cell. For this configuration, it is possible to derive the ED and MD moments for every particle in the array.

The ED moment of a single particle created by the incident plane wave $\vec{E}_{\mathrm{i}} = \vec{E}_0 e^{ik_{\mathrm{d}}z}$ is equal to $\vec{p} = \alpha_{\mathrm{p}}\vec{E}_{\mathrm{i}}$. If the particle is placed in the array, the external electric field consists not only of the falling light but also of the fields created by the EDs of the other particles. Assume that every particle has a number and the number of the particle of interest is *1*, the electromagnetic wave has a normal angle of incidence to the plane of the array and illuminates all spheres equally. Then the created ED of this particle is $\vec{p}_1 = \alpha_{\mathrm{p}}(\vec{E}_{\mathrm{i}} + \vec{E}_2 + \vec{E}_3 + ...)$.

At the same time, the fields generated by other particles can be expressed using Green's tensor $\hat{G}(\vec{r}_1, \vec{r}_j)$ that is a function of the position of the particle *number 1* relative to the others.

$$\begin{aligned} \vec{p}_1 &= \alpha_{\mathrm{p}} \left(\vec{E}_{\mathrm{i}} + \frac{k_0^2}{\epsilon_0}\hat{G}(\vec{r}_1, \vec{r}_2)\vec{p}_2 + \frac{k_0^2}{\epsilon_0}\hat{G}(\vec{r}_1, \vec{r}_3)\vec{p}_3 + \dots \right) \\ &= \alpha_{\mathrm{p}} \left(\vec{E}_0 + \frac{k_0^2}{\epsilon_0}\sum_{j\neq 1}^{\infty} \hat{G}(\vec{r}_1, \vec{r}_j)\vec{p}_j \right). \end{aligned} \tag{2.64}$$

For the infinite metasurface, where all particles are illuminated equally, the dipoles induced in each particle are the same: $\vec{p}_1 = \vec{p}_2 = ... = \vec{p}$.

If the incident plane wave $\vec{E}_0$ is polarized in the x-direction, the created dipoles and the contributing parts of the radiated fields are also oriented along the x-axis. Moreover, the impact of nearby dipoles oriented in the x-direction to a certain distance can be neglected, allowing for an approximation of Green's function:

$$\begin{aligned} S_{\mathrm{pp}} &= \frac{k_0^2}{\epsilon_0}\sum_{j\neq 1} G_{xx}^j \\ &= \frac{k_0^2}{4\pi\epsilon_0}\sum_{j\neq 1} \frac{e^{ik_{\mathrm{d}}r_j}}{r_j}\left(1 + \frac{i}{k_{\mathrm{d}}r_j} - \frac{1}{k_{\mathrm{d}}^2 r_j^2} - \frac{x_j^2}{r_j^2} - \frac{i3x_j^2}{k_{\mathrm{d}}r_j^3} + \frac{3x_j^2}{k_{\mathrm{d}}^2 r_j^4}\right). \end{aligned} \tag{2.65}$$

Then, the ED moment created in particle *number 1* can be rewritten as:

$$\vec{p} = \alpha_{\mathrm{p}} \vec{E}_{\mathrm{i}} + \alpha_{\mathrm{p}} S_{\mathrm{pp}} \vec{p}, \tag{2.66}$$

$$\vec{p} = \alpha_{\mathrm{p}}^{\mathrm{eff}} \vec{E}_{\mathrm{i}}. \tag{2.67}$$

The coefficient $\alpha_{\mathrm{p}}^{\mathrm{eff}} = \alpha_{\mathrm{p}}/(1 - \alpha_{\mathrm{p}} S_{\mathrm{pp}})$ is called effective electric dipole polarizability of the array. The same is applicable for the magnetic dipole moment:

$$\vec{m} = \alpha_{\mathrm{m}}^{\mathrm{eff}} \vec{H}_{\mathrm{i}}, \tag{2.68}$$

where $\alpha_{\mathrm{m}}^{\mathrm{eff}} = \alpha_{\mathrm{m}}/(1 - \alpha_{\mathrm{m}} S_{\mathrm{mm}})$ is the effective magnetic dipole polarizability of the array, S_{mm} is the sum of Green's functions in y-direction for magnetic dipole moments. Note that due to the symmetrical properties of the metasurface and irradiation conditions, the MDs do not interact with the EDs of the particles.

2.4.4 Reflectivity and transmissivity of a metasurface made of spheres

The electric field at distance $\vec{r}$ from the particle array is considered in the far zone and has a contribution from both electric $\vec{p}$ and magnetic $\vec{m}$ dipole moments. The incident plane wave E_{i} propagates along the z-axis and has polarization along the x-axis [12]. The particle array is oriented in xy-plane and positioned at the point of $z = 0$. The total electric field at any point outside of the array is:

$$E_{\mathrm{tot}} = E_{\mathrm{i}} + E^{\mathrm{p}} + E^{\mathrm{m}} = E_0 \left[e^{ik_{\mathrm{d}} z} + \alpha_{\mathrm{p}}^{\mathrm{eff}} \frac{k_0^2}{\epsilon_0} G_{xx}^r - i \alpha_{\mathrm{m}}^{\mathrm{eff}} k_{\mathrm{d}} g_z^r \right], \tag{2.69}$$

$$G_{xx}^r = \frac{i}{2 S_{\mathrm{L}} k_{\mathrm{d}}} e^{\mp i k_{\mathrm{d}} z}; \qquad g_z^r = \frac{\pm 1}{2 S_{\mathrm{L}}} e^{\mp i k_{\mathrm{d}} z}, \tag{2.70}$$

where S_{L} is the area of the array unit cell; E^{p} and E^{m} are the electric fields of the waves radiated by the ED and MD moments, respectively. The upper sign of g_z^r corresponds to $z < 0$ and refers to the reflected field. The lower sign to $z > 0$ is the transmitted field.

For the normal angle of incidence of the electromagnetic wave, the condition of continuity for the electric field at the metasurface plane requires:

$$E_{\mathrm{i}} + E^r = E^t, \tag{2.71}$$

where $E^r = E_0 r e^{-ik_{\mathrm{d}} z}$ is the reflected electric field and $E^t = E_0 t e^{ik_{\mathrm{d}} z}$ is the transmitted electric field. The contributing parameters r and t are the electric field amplitude reflection and transmission coefficients.

For $z < 0$: $E_{\mathrm{i}} + E^r = E_{\mathrm{tot}}$, which, after substituting E_{tot}, results in $E^r = E^{\mathrm{p}} + E^{\mathrm{m}}$. The expression for the amplitude reflection coefficient is then:

$$\begin{aligned} r = \frac{E^{\mathrm{p}}(z<0) + E^{\mathrm{m}}(z<0)}{E_0 e^{-ik_{\mathrm{d}} z}} &= i \alpha_{\mathrm{p}}^{\mathrm{eff}} \frac{k_0^2}{\epsilon_0} \frac{1}{2 S_{\mathrm{L}} k_{\mathrm{d}}} - i \alpha_{\mathrm{m}}^{\mathrm{eff}} \frac{k_{\mathrm{d}}}{2 S_{\mathrm{L}}} \\ &= \frac{i k_{\mathrm{d}}}{2 S_{\mathrm{L}}} \left[\frac{1}{\epsilon_{\mathrm{d}} \epsilon_0} \alpha_{\mathrm{p}}^{\mathrm{eff}} - \alpha_{\mathrm{m}}^{\mathrm{eff}} \right]. \end{aligned} \tag{2.72}$$

[12] The vector sign is omitted to simplify the calculations.

For $z > 0$: $E^t = E_{\text{tot}}$, or $E^t = E_{\text{i}} + E^{\text{p}} + E^{\text{m}}$. The amplitude transmission coefficient can be found as follows:

$$\begin{aligned} t = \frac{E_{\text{i}}(z>0) + E^{\text{p}}(z>0) + E^{\text{m}}(z>0)}{E_0 e^{ik_{\text{d}}z}} &= 1 + i\alpha_{\text{p}}^{\text{eff}} \frac{k_0^2}{\epsilon_0} \frac{1}{2S_{\text{L}}k_{\text{d}}} + i\alpha_{\text{m}}^{\text{eff}} \frac{k_{\text{d}}}{2S_{\text{L}}} \\ &= 1 + \frac{ik_{\text{d}}}{2S_{\text{L}}} \left[\frac{1}{\epsilon_{\text{d}}\epsilon_0} \alpha_{\text{p}}^{\text{eff}} + \alpha_{\text{m}}^{\text{eff}} \right]. \end{aligned} \tag{2.73}$$

The effective polarizabilities in the following equations can be replaced by the corresponding dipole moments: $p_x = \alpha_{\text{p}}^{\text{eff}} E_0, m_y = \alpha_{\text{m}}^{\text{eff}} E_0$. In order to replace, let's remember the relation of the magnetic and electric field: $H_{\text{r}} = (\epsilon_{\text{d}}\epsilon_0/\mu_0)^{1/2} E_{\text{r}}$, and the speed of electromagnetic wave in surrounding nonmagnetic medium: the $\upsilon_{\text{d}} = 1/\sqrt{\epsilon_{\text{d}}\epsilon_0\mu_0}$. Then, one can obtain:

$$r = \frac{ik_{\text{d}}}{E_0 2S_{\text{L}}\epsilon_{\text{d}}\epsilon_0} \left[p_x - \frac{1}{\upsilon_{\text{d}}} m_y \right], \tag{2.74}$$

$$t = 1 + \frac{ik_{\text{d}}}{E_0 2S_{\text{L}}\epsilon_{\text{d}}\epsilon_0} \left[p_x + \frac{1}{\upsilon_{\text{d}}} m_y \right]. \tag{2.75}$$

The reflection and transmission power coefficients are the square of the corresponding amplitude coefficients: $R = |r|^2, T = |t|^2$. Absorption coefficient $A = 1 - R - T$.

Following this logical consequence, the reflectivity and transmissivity of an array of spherical particles embedded in a homogeneous medium can be derived using purely analytical calculations. This step-by-step investigation clarifies the mechanism of reflectivity and establishes a robust framework for comparing the numerical simulations to the analytical solutions.

2.5 Unconventional resonant states

Investigating the effect of metasurface reflectivity, it is unavoidable to acknowledge two unique phenomena: the *Kerker effect* and the *Anapole state*. The Kerker effect is the phenomenon of high transmissivity, which plays the inverse role in the desired reflectivity search. In contrast, the anapole state is defined as a non-radiative state and can be manipulated to observe reflection at a single multipole moment. The following section provides a comprehensive examination of both states.

2.5.1 Kerker effect

The Kerker effect refers to a specific condition, where the electric and magnetic dipole responses of a particle destructively interfere in the direction of backscattering, enhancing scattering in the forward direction. In the context of a metasurface, this phenomenon leads to a high transmissivity of the incident light field with an accumulated phase shift $(0; 2\pi)$.

The mathematical description of the Kerker effect can be demonstrated through the equations for the reflectivity and transmissivity coefficients, as referenced in equations (2.72),(2.73). The suppression of back-scattered light occurs when the effective electric and magnetic polarizabilities are equal, implying that both their real and imaginary parts coincide: $\Re(\alpha_{\text{p}}^{\text{eff}}/\epsilon_{\text{d}}\epsilon_0) = \Re(\alpha_{\text{m}}^{\text{eff}})$

and $\Im(\alpha_{\mathrm{p}}^{\mathrm{eff}}/\epsilon_{\mathrm{d}}\epsilon_0) = \Im(\alpha_{\mathrm{m}}^{\mathrm{eff}})$. At this operational point, the amplitude reflection coefficient r is nullified, resulting in total transmission of the metasurface. The phase information of the transmitted light field is contained in the imaginary part of the amplitude transmission coefficient and can vary within the range $(0, 2\pi)$.

This mathematical equality is illustrated in Figure 2.1 by black arrows [102]. The graph shows the behaviour of the electric and magnetic effective polarizabilities of a spherical Si nanoparticle as a function of wavelength. The nanoparticle is part of an infinite array of identical spheres symmetrically arranged along the x- and y-axes, with each sphere positioned in a square unit cell. The blue lines represent the imaginary component of the effective polarizabilities, while the red lines represent the real component. From the graph, it can be observed that the real and imaginary parts of the electric and magnetic effective polarizabilities coincide at the point indicated by the black arrows, marking the Kerker effect.

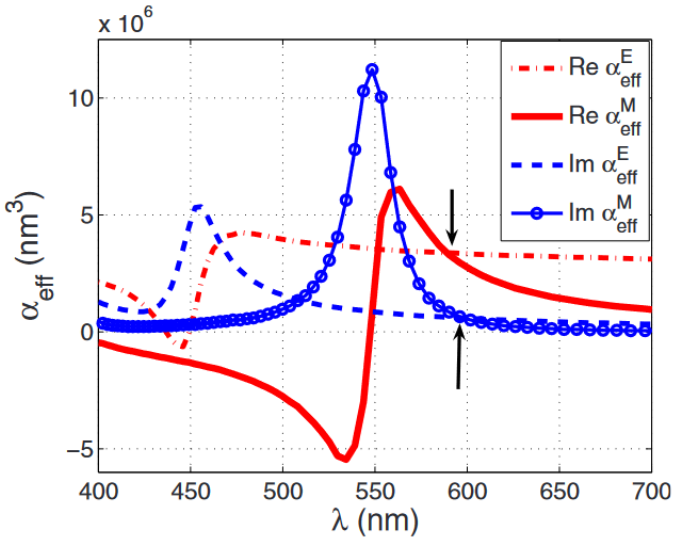

Figure 2.1.: Effective polarizability spectra of the infinite metasurface made of spherical Si nanoparticles. [Reprinted figure with permission from: A. B. Evlyukhin, C. Reinhardt, A. Seidel, B. S. Luk'yanchuk and B. N. Chichkov. 'Optical response features of Si-nanoparticle arrays'. Physical Review B—Condensed Matter and Materials Physics 82.4, p. 045404 (2010). Copyright (2024) by the American Physical Society. [102].]

The full counterbalance of effective polarizabilities for a spherical nanoparticle placed in a square unit cell is always achieved at a non-resonant regime. This happens due to the spectrally separated electric and magnetic dipole resonant responses. The resonant Kerker effect was shown for the spheres placed in the rectangular unit cell, which allows manipulation of the spectral position of resonances, bringing them into a state of overlap.

The full counterbalance of the effective polarizabilities for a spherical nanoparticle placed in a square unit cell is always achieved in a non-resonant regime due to the spectral separation of the electric and magnetic dipole resonant responses. However, the resonant Kerker effect has been demonstrated for a metasurface composed of spheres placed in rectangular unit cells. Varying the distance between nanoparticles in the direction perpendicular to the electric field

of the incident light can lead to the spectral overlap of the particle responses. The details of this investigation are presented in the following paper [105].

Another way to achieve the resonant Kerker effect is to use a cylindrical configuration of nanoparticles [106]. While the unit cell of such nanoparticles can be square, the additional geometrical parameter, such as the height of the cylinders, allows overlapping of the resonant responses of the ED and MD moments.

It is interesting to note that the transmitted light field at the resonant Kerker effect has a phase shift of π, while off-resonance, it can take values within the range $(0;\pi)\cup(\pi;2\pi)$, excluding the values of 0 and π [96]. This implies that even when creating a perfect optical cloaking effect, where the light is fully transmitted, the presence of the metasurface can still be detected by measuring the phase information.

The Kerker effect created by the ED and MD moments is mentioned and discussed in the research papers of this thesis. Particularly, it was considered for the metasurfaces with a cylindrical configuration of nanoparticles, where avoiding a specific cylindrical height allows for achieving the desired reflectivity.

2.5.2 Anapole state

The anapole state is a non-radiating effect that, despite the excitation of multipole moments and the existence of the corresponding currents inside of the nanoparticle, does not exhibit any backward or forward scattering. This unique state can be achieved for the scattering processes with comparable strength and the same distribution pattern in the far field. However, the phases of the scattered light from the multipoles must be opposite to destructively interfere in order to make the excitation invisible.

A single spherical particle can have the anapole state for the exact electric dipole moment, which in the multipole decomposition of radiation fields can be expressed as the sum of the electric dipole ED and toroidal dipole (TD) moments. TD moment corresponds to currents flowing around the surface of a sphere, also known as poloidal currents. ED and TD modes have identical scattering patterns at the far field, which, in the case of their spatial overlap and opposite phase, can cancel each other (Figure 2.2). The near-field, though, as well as the field inside of the sphere, is strongly pronounced, having the electric and magnetic currents within it. Such a state can be achieved by a careful geometrical design and material choice of the particle, and it is attractive due to its unique properties of a long lifetime and high-quality factor [107].

Particles in the anapole state can be periodically arranged to form a metasurface so that the distance between them is sufficient not to deteriorate the anapole effect [13]. This metasurface can be tuned to exhibit either high transmission or high reflection behaviour, depending on the additional excited multipole moments. When the anapole state is spectrally isolated from the other multipole moments, the metasurface can function with high transmissivity. The transmitted light undergoes a phase accumulation of 2π, indicating that the metasurface is effectively invisible even by the detection of phase information. Alternatively, if the metasurface is tuned to a resonant response of the MD, it can achieve total reflection, which is characterised

[13] Particles are placed so far apart that the near field does not interact.

exceptionally by the MD particularities. The magnetic mirror effect aligned with the anapole state is investigated in detail in one of our papers.

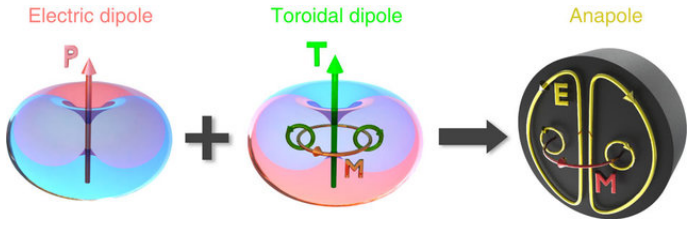

Figure 2.2.: The schematic of anapole excitation. Destructive interference between the far-field radiation of the electric dipole (ED) and toroidal dipole (TD) moments leads to the cancellation of the scattering process, resulting in the formation of the anapole state. In the near-field, the excitation is non-zero and includes the circulating magnetic field $\vec{M}$ associated with the TD moment. [This figure is adapted from [107]. It is licensed under a CC BY 4.0 international licence. To view a copy of this licence, visit creativecommons.org/licenses/by/4.0/.]

The anapole effect also exists as a collective lattice behaviour and is referred to as the lattice anapole state [96, 103, 108]. In lattice structures, the compensation of scattered light at this state should occur only in the directions of transmission and reflection to achieve "lattice invisibility." This compensation happens only among multipole moments that share the same inversion symmetry.

The terminology of inversion symmetry can be explained in the following way. The multipoles that are unaffected by a change in the spatial vector, or in other words, are symmetric under inversion, are called *even*. Among them are the MD, EQ, MO moments. The multipole moments that are asymmetric under inversion are called *odd* and include the ED, MQ, and EO moments. The simultaneous excitation of multipole moments with the same inversion symmetry can result in destructive interference of scattered light in the far field.

The investigation of the lattice anapole state is not addressed in this thesis, although it represents an avenue worthy of further research in the future, particularly in the context of the functionality of metasurfaces.

Chapter 3

Simulation of Metasurfaces using Comsol Multiphysics

Computational simulation is a powerful tool that serves as a bridge between theoretical predictions and experimental validations. Real-world systems are often highly complex and cannot be predicted analytically with sufficient accuracy. In addition, most systems cannot be easily replicated and studied experimentally without proper planning. Simulation tools are ideal for this purpose, modelling scenarios that closely resemble realistic cases, helping to prepare for experiments, and minimising potential failures. It is also important to ensure that all three methods - analytical calculation, simulation and experiment - deliver consistent results and do not contradict each other. This increases the reliability of the conducted research and supports a comprehensive investigation.

The current system of interest is investigated using the Comsol Multiphysics program that supports the finite element modelling (FEM) approach. FEM is a numerical technique used to find an approximate solution to a complex problem described by partial differential equations (PDEs) over a defined domain. In FEM, the investigated domain is split down or discretized into smaller, simpler pieces called finite elements. These elements are interconnected at points called nodes. The real solution to a problem is approximated by solving the PDEs within each finite element, by ensuring that the solutions at the nodes of these elements are continuous. After that, the technique assembles these local solutions to form a final global solution.

Domain discretization is a fundamental step in the FEM process. The accuracy of the chosen finite elements influences the correctness of the solution and optimises the required computational effort. Additionally, each of the finite elements has to be approximated with the same shape functions as the one used for the solution. This means that if the problem contains PDEs with the second derivative term, each of the finite elements has to be approximated with the second-order (quadratic) function (Figure 3.1).

The package to investigate the interaction between electromagnetic wave fields and structures in Comsol Multiphysics is called the *Electromagnetic Waves, Frequency Domain* package. This package employs Maxwell's equations in the frequency domain to model and analyse how electromagnetic waves propagate, interact with materials, and affect the structure within a given domain. Its features are perfectly suited for the investigation of metamaterial structures.

[14] For a comprehensive understanding of the "Simulation" chapter, it is recommended to read it in conjunction with the running Comsol Multiphysics program.

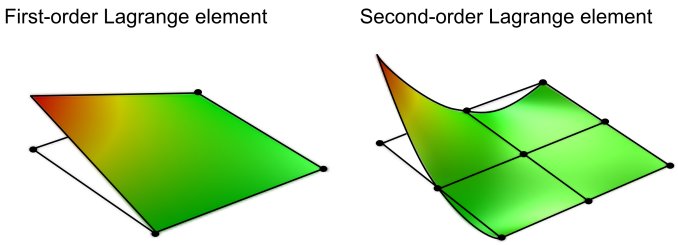

Figure 3.1.: The approximation functions of the first order (linear) and of the second order (quadratic) for a finite element. [Adapted from https://www.comsol.com/blogs/keeping-track-of-element-order-in-multiphysics-models.]

To demonstrate and explain the particularities of metasurface simulation, it is essential to present the main steps involved in building the model using Comsol Multiphysics.

- **Geometry creation**
- **Material assignment**
- **Physics initialization**
- **Mesh generation**
- **Study and Solver settings**
- **Post-processing**
- **Validation alalysis**

3.1 Geometry creation

As a first step in simulating a metasurface structure using Comsol Multiphysics, it is necessary to define the model. The model can be 2D or 3D, depending on the objective of the simulation. Some tasks may require a 2D approach due to symmetrical behaviour, which simplifies the model and reduces computational load. For instance, if the metasurface exhibits rotational or planar symmetry, a 2D model can efficiently capture the essential physics while saving time and resources. On the other hand, some tasks must be simulated as 3D objects to accurately represent the complexity of the metasurface structure, particularly when interactions occur in all three spatial dimensions. The ED and MD moments generated within the dielectric nanoparticle are perpendicular to each other. Therefore, to extract both types of information, it is essential to use a 3D representation.

In the process of building the structure, fundamental geometric shapes are directly employed at the Comsol interface. Specifically, for the initial and simplest iteration of the metasurface model constructed from nanospheres periodically arranged in a homogeneous medium, a sphere and a rectangular are selected as the primary geometrical entities. The dimensional parameters, including size and position, can be conveniently specified directly within the settings dedicated to the geometric figure. Alternatively and more preferably, these geometric parameters can also be defined in a separate "Parameters" section (Figure 3.2a), which is detached from the

core model construction interface. This substitute parameter setting offers better flexibility and control over the model configuration, especially when the geometry comprises multiple elements that require modifications.

To model an infinite metasurface configuration in the x- and y-directions, it is sufficient to construct only a single geometrical unit that symmetrically repeats with the appropriate boundary conditions. In our case, this geometrical unit consists of one sphere placed within a repeating area corresponding to the periodicity length. An alternative modelling approach that reduces even more computational load and saves time is the construction of a quarter of the previously mentioned unit cell. This approach includes the reflection symmetry along both the x- and y-cuts passing through the nanoparticle figure. This can be done by adding a "Cross section" node in the "Work Plane", "Geometry" sequence. Furthermore, the rest of the quarters of the unit cell can be removed by using "Partition Objects" and "Delete Entities" nodes (Figure 3.2b). The visualization of various unit cells for the metasurface simulation within the Comsol interface is shown in Figure 3.3a.

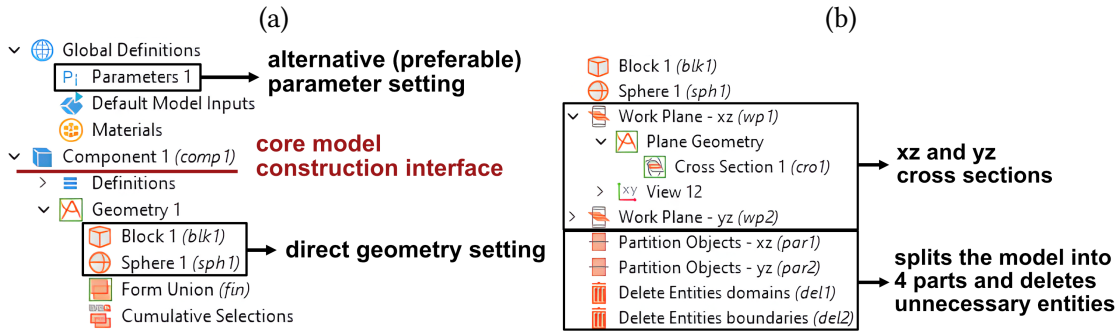

Figure 3.2.: Geometry settings in Comsol Multiphysics. (a) Direct value assignment and using the "Parameters" feature. (b) Construction of a quarter of the nanoparticle in the medium.

The height of the intermediate medium block surrounding the nanoparticle is a critical parameter for obtaining accurate simulation results. It has to be sufficient to capture the full electromagnetic interaction around the nanoparticle, including any near-field effects. A general rule of thumb is to make the height above and below the nanoparticle not less than half of the wavelength of the incident electromagnetic wave $(\lambda/2)$. In the current simulations, given the available computational power, the block height is typically set to 2λ to ensure that boundary effects do not interfere with the particle's interaction with the wave.

For the unit cell that consists of a quarter of a nanoparticle, the implementation of the "Cumulative Selection" node can simplify the process of operations. This node helps to group geometric entities and further use these entities for material or physics settings. Another beneficial property is that the entity retains the same label during parameter changes. In other words, each domain, boundary, or point is assigned to a specific number (label). When changing the geometry or some physics settings, these numbers can be shuffled and reassigned to other elements, potentially causing errors in the simulation. The application of cumulative selection maintains the assignments in the correct order, ensuring that all settings remain consistent and accurate. The "Cumulative Selection" node is shown in Figure 3.3b and can be directly assigned in the "Settings" for each geometric figure.

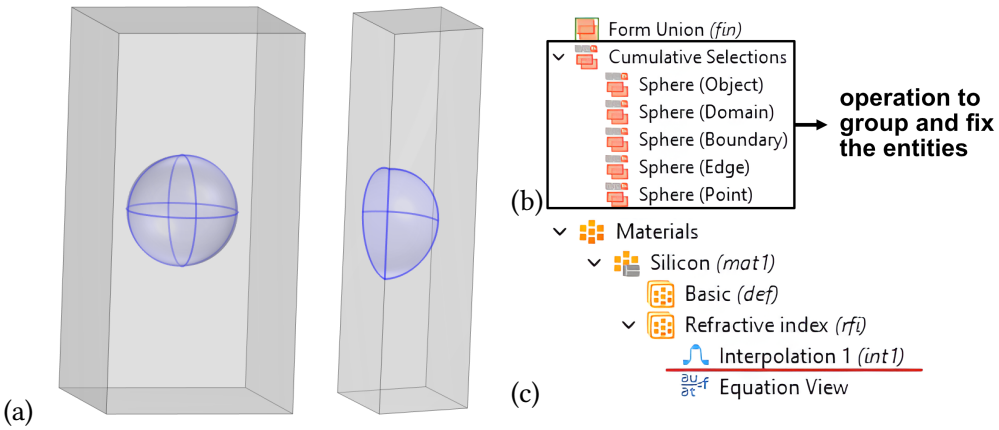

Figure 3.3.: a) A unit cell with a full nanoparticle and a symmetrically recurring quarter of a nanoparticle. b) "Cumulative Selections" node in Geometry settings. c) "Interpolation" function in Material settings for introducing the dispersion behaviour.

3.2 Material assignment

The material settings specify the material-dependent quantities for the selected physics package. In the Electromagnetic Waves, Frequency Domain package, this includes the refractive index of the structure, both its real and imaginary parts. The material can be chosen either from the existing Comsol library by clicking on the "Add Material" node or added manually - the "Blank Material" node.

Most material refractive indices selected from the library include dispersion behaviour, which is the variation of real and imaginary parts of refractive index with wavelength. When experimentally measured dispersion data needs to be included in the Comsol simulation, it can be incorporated by selecting the "Interpolation" function in the "Refractive Index" extension node of the material (Figure 3.3c).

In the settings of the "Interpolation" function in the Comsol, several methods can be used to upload data. The most common method is using the "Local table" under the "Definition, Data Source" section (Figure 3.4). For example, an arbitrary function named *nSi* can be defined to represent the real part of the refractive index of silicon (Si). The measured data, in the form of a matrix where the refractive index depends on frequency, is then uploaded. In this context, the variable *t* represents the wavelength, and *f(t)* represents the real part of the refractive index.

The data values can be interpolated using a linear function and extrapolated using the nearest function for wavelengths not included in the table. Additionally, the settings require the manual input of units for both the argument (wavelength - nm) and the function (refractive index - 1). After configuring these settings, the value of the refractive index in "Material Contents" should be written in the form of a function $n\left(\frac{c}{\nu}\right)$, where n is the refractive index, and the wavelength is denoted as the ratio of the speed of light to frequency, $\frac{c}{\nu}$. For the example given in Figure 3.4, this function looks like *nSi(c_const/freq)*, where *c_const* and *freq* are reserved variables in Comsol Multiphysics.

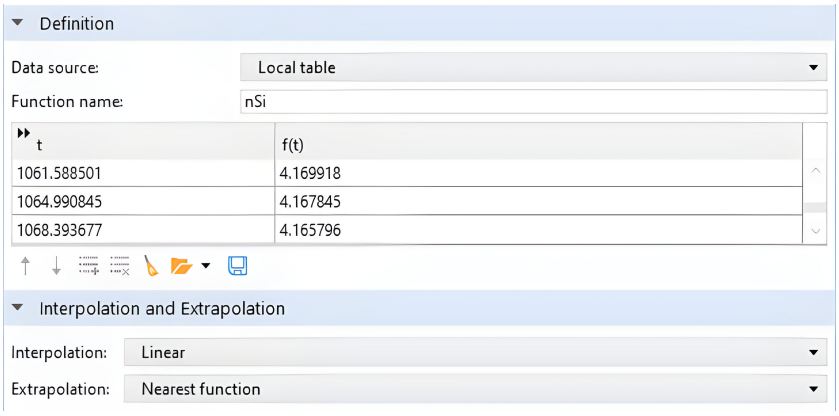

Figure 3.4.: Settings of the "Interpolation" function.

3.3 Physics of the "Electromagnetic Waves" package

The *Electromagnetic Waves, Frequency Domain* physics interface in Comsol Multiphysics is designed to solve Maxwell's equations for a time-harmonic electromagnetic field. The electric and magnetic components of such waves vary sinusoidally with time. This simplifies Maxwell's equations by factoring out the time dependency, leaving a set of equations that depend only on spatial coordinates and the frequency of the wave. This is particularly useful for analyzing steady-state behaviours of electromagnetic waves at specific frequencies, where amplitude and phase do not change over time. Such equations are implemented in the investigation of metasurfaces.

The full form of the Helmholtz equation that describes the interaction of the electromagnetic wave with the medium is integrated into the Comsol Multiphysics software and shown in Figure 3.5. The wave is considered as a harmonic electromagnetic wave $\vec{E} = E_0 e^{j\omega t}$ in the frequency domain, where j is the imaginary unit and ω is the angular frequency.

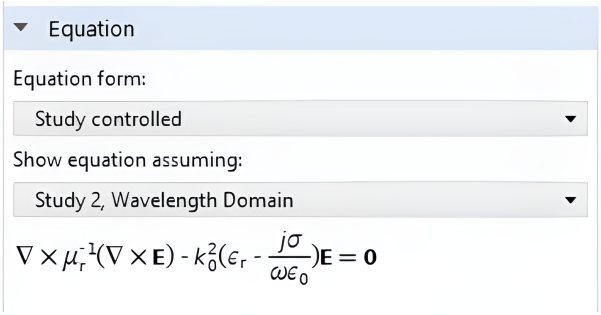

Figure 3.5.: Helmholtz equation integrated in the Comsol Physics interface.

The Faraday's Law (Equation 2.3) and Ampère's Law (Equation 2.1) take the form:

$$\nabla \times \vec{E} = -j\omega\vec{B}, \tag{3.1}$$

$$\nabla \times \vec{H} = \vec{J} + j\omega\vec{D}. \tag{3.2}$$

Substitution of the constitutive equation for the magnetic flux density (Equation 2.9) in Faraday's Law gives:

$$\nabla \times \vec{E} = -j\omega\mu_0\mu_r\vec{H}. \tag{3.3}$$

Whereas the substitution of the current density (Equation 2.5) and the electric displacement field (Equation 2.8) in Ampère's Law gives:

$$\begin{aligned} \nabla \times \vec{H} &= \sigma\vec{E} + j\omega\epsilon_0\epsilon_r\vec{E} \\ &= (\sigma + j\omega\epsilon_0\epsilon_r)\vec{E}. \end{aligned} \tag{3.4}$$

Let's take the curl of Faraday's Law:

$$\nabla \times (\nabla \times \vec{E}) = -j\omega\mu_0\mu_r(\nabla \times \vec{H}). \tag{3.5}$$

And substitute Ampère's Law in it:

$$\nabla \times (\nabla \times \vec{E}) = -j\omega\mu_0\mu_r(\sigma + j\omega\epsilon_0\epsilon_r)\vec{E}. \tag{3.6}$$

Simplifying the right-hand side and introducing the square of the wave number in free space $k_0^2 = \omega^2\mu_0\epsilon_0$, we get:

$$\begin{aligned} \nabla \times (\nabla \times \vec{E}) &= \omega^2\mu_0\mu_r\epsilon_0\epsilon_r\vec{E} - j\omega\mu_0\mu_r\sigma\vec{E} \\ &= k_0^2\mu_r\epsilon_r\vec{E} - jk_0^2\frac{\sigma\mu_r}{\omega\epsilon_0}\vec{E} \\ &= k_0^2\left(\mu_r\epsilon_r - j\frac{\sigma\mu_r}{\omega\epsilon_0}\right)\vec{E}. \end{aligned} \tag{3.7}$$

Dividing the equation to μ_r and transferring the right-hand side to the left, the final equation corresponds to the one presented in Comsol:

$$\nabla \times \mu_r^{-1}(\nabla \times \vec{E}) - k_0^2\left(\epsilon_r - \frac{j\sigma}{\omega\epsilon_0}\right)\vec{E} = 0. \tag{3.8}$$

The part denoted by $\epsilon_r - \frac{j\sigma}{\omega\epsilon_0}$ defines the complex relative permittivity, which includes both dielectric and conductive properties.

The investigated Si material of nanoparticles belongs to the category of semiconductors. It is considered to be a non-magnetic material, characterised by a relative permeability μ_r of 1.0. This indicates that Si neither enhances nor diminishes the magnetic field applied to it.

The electrical conductivity (σ) of intrinsic pure Si at room temperature (297 K) is approximately 10^{-3} S/cm according to A. Wold's "Solid State Chemistry" [109] and 4×10^{-6} S/m as reported in C. Kittel's "Introduction to Solid State Physics" [110]. In comparison, highly conductive materials like aluminium have electrical conductivity around 3.5×10^7 S/m. Consequently, the conductive properties of undoped Si are minimal and can be neglected in metasurface simulations.

The simplified version of the equation for Si can be presented in the following form and mentioned in Comsol in the "Wave Equation, Electric 1" node:

$$\nabla \times (\nabla \times \vec{E}) - k_0^2 \epsilon_r \vec{E} = 0. \tag{3.9}$$

There are several configuration steps of light-matter interaction in the Electromagnetic Waves, Frequency Domain physics interface that must be taken into account. First, regardless of the unit cell type, the "Full field" option under "Formulation" must be selected in order to simulate the reflective properties of metamaterials. Next, it is important to select two ports to indicate where the electromagnetic wave enters and exits the simulation domain (Figure 3.7). For metasurface structures, the "Type of port" should be set to "Periodic" in order to use the same parameters of the incident electromagnetic wave for all repeated unit cells. In the "Port" node, we also specify the "Input power", which can be a fixed value of 1 W or defined by the equation $P_{in} = I \times P^2$, where I is the intensity of the incident electromagnetic wave and P represents the periodicity of the unit cell.

In the electromagnetic wave simulation, it is possible to define the components of the electric or magnetic field. By selecting "Electric field" in the "Input quantity" of the "Port Mode Settings", the "Electric mode field amplitude" components can be specified. If the electric field is uniform with only one component in the y-direction, without variations in x or z-directions, this value should be assigned to the "y" component to represent the magnitude and direction of the field, while the values for the x and z components should be set to 0 [V/m]. However, the more accurate assignment of the electric field contains the wave vector components, designated in the software as 'ewfd.nx', 'ewfd.ny' and 'ewfd.nz' (Figure 3.6a). In this example, the electric field has an amplitude of 1[V/m] directed along the y-axis. The additional inclusion of the wave vector parameters helps accurately to model the direction and phase of the electromagnetic wave as it propagates through different media. The electric field with the magnitude of 1[V/m] in the y-direction in a full form has the following formulation:

$$\begin{aligned} E_x &= -\text{ewfd.nx} \times (1) \times \text{ewfd.nx} \times 2, \\ E_y &= 1 - \text{ewfd.ny} \times (1) \times \text{ewfd.nx} \times 2, \\ E_z &= -\text{ewfd.nz} \times (1) \times \text{ewfd.nx} \times 2. \end{aligned} \tag{3.10}$$

This input method not only defines a linearly polarized plane wave but also offers a more precise depiction of wave behaviour, reducing computational inaccuracies.

Moreover, the incident electromagnetic wave can impinge upon the structure at a specific angle, which is characterised within the simulation software by parameters such as the "Elevation angle of incidence" and "Azimuth angle of incidence". These angles define the orientation of the incoming wave relative to the structure. Additionally, when the distance between the centres of the nanoparticles within the structure exceeds the wavelength of the incident wave, it becomes crucial to include "Automatic Diffraction Order Calculation" in the simulation. This feature enables the software to compute multiple orders of diffraction that influence the resonant response of the metasurface.

Having modelled only one unit cell, it is necessary to apply periodic boundary conditions to its lateral surfaces to replicate this unit cell infinitely in both the x- and y-directions. For a unit

cell with a full nanoparticle and a full periodicity distance, the appropriate boundary condition to apply is "Periodic Condition". In "Periodicity settings", the type of periodicity selected should be "Floquet periodicity", used for frequency domain problems with a spatial periodicity of the geometry and solution (Comsol Multiphysics documentation). The choice of "k-vector for Floquet periodicity" (k_F) should be set to "From periodic port" (Figure 3.6b).

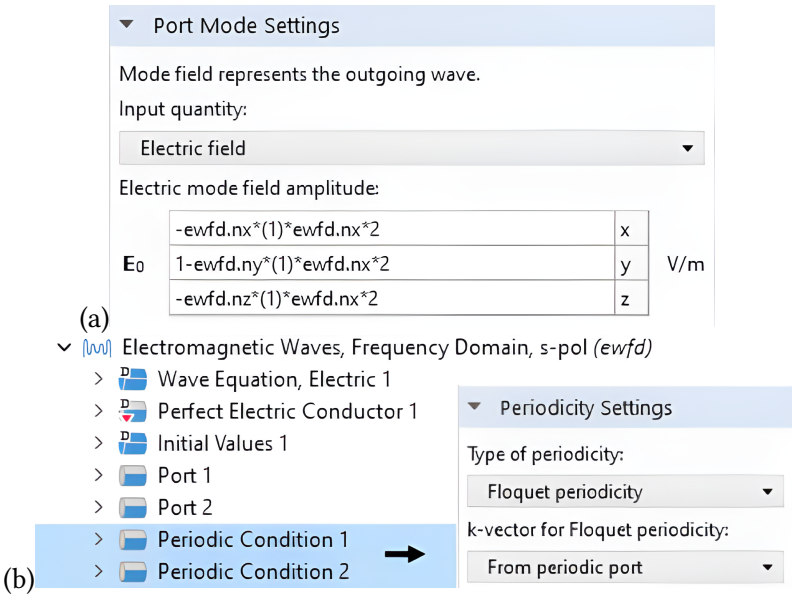

Figure 3.6.: a) Amplitude specifications for the incident electromagnetic wave. b) Floquet periodic boundary conditions applied to a unit cell with a full nanoparticle. (1) corresponds to the x-direction, (2) - to the y-direction.

The Floquet boundary condition states that the fields on one side of a periodic structure are related to the fields on the other side by a phase shift. This mathematically can be written as:

$$\psi(x + L) = e^{jk_F L}\psi(x), \tag{3.11}$$

where $\psi(x)$ is the wave function, L is the periodicity of the structure, k_F is the Bloch wave number, and j is the imaginary unit. This expression ensures that the wave function is phase-shifted but not altered in form as it translates across each period of the structure. By applying this boundary condition, Comsol considers a periodic nanoparticle structure where the field of each unit cell influences the field of the nearby unit cell but has the same interaction with the incident light field.

The modelling of a quarter of a nanoparticle has the same procedure for material assignment and incident wave settings. The boundary conditions, though, are different. In order to create an infinite repeating structure, the selected nodes are "Perfect Electric Conductor" and "Perfect Magnetic Conductor". These options are applied if the electric field of the electromagnetic wave is directed in x- or y-directions (perpendicularly to the boundaries of the unit cell). The equations describing the boundary conditions are $\vec{n_1} \times \vec{E} = 0$ and $\vec{n_2} \times \vec{H} = 0$, respectively, where $\vec{n_1}$ and $\vec{n_2}$ are normalization vectors to the selected surfaces. If the cross product of two vectors is equal to zero, it indicates that the vectors are parallel and have the same orientation.

These boundary conditions in electromagnetic simulation define how the electric and magnetic fields are oriented relative to the boundaries of the unit cell, enabling the internal reproduction of the same periodic structure across the simulation domain.

3.4 Mesh generation

The accurate simulation results can only be achieved by correct discretization of the investigated object into smaller finite mesh elements. This step has its significance due to the implementation of PDEs to each mesh element, where the general solution is compiled from all the results.

By simulating the interaction of the electromagnetic wave with a metasurface, each medium, whether it is a nanoparticle, substrate or air from where the electromagnetic wave comes from, the maximum mesh element satisfies the following equation: $S_{max} = \lambda/(n \times 10)$, where λ is the wavelength of the incident electromagnetic wave, n is the refractive index of the medium. If the size of the element is too big, it doesn't capture the shape or small features of the area, at the same time extremely small mesh elements require a huge computational time.

Another point to address is the symmetric distribution of mesh elements at the boundaries (Figure 3.7). (The mesh size has been scaled up to clearly illustrate the symmetric distribution.) Implementing the periodic boundary condition also requires symmetry in nodal points on the boundary surfaces for the integrity of the solution. The asymmetric distribution leads to numerical artefacts.

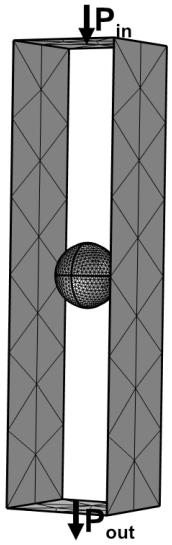

Figure 3.7.: Symmetric distribution of mesh elements and nodal points on the boundaries with applied Floquet periodicity. In order to enhance the visual representation, the height of the block has been reduced, while the size of the mesh element has been increased. The arrows P_{in} and P_{out} indicate the boundaries or ports where the electromagnetic wave enters and exits the simulation domain.

Most of the time, using the "Physics-controlled mesh" option, Comsol builds the mesh correctly based on the implemented geometry, material, and physics sequences. However, in areas

where accuracy has to be improved or neglected, the manual ("User-controlled mesh") gives an advantage in controlling the simulation process. Mesh modification is also a part of the validation process of the obtained results.

3.5 Study and solver settings, post-processing

When the model is built, the study setting is the step to define the value to be searched. It can be one number, a range of numbers depending on the parameter or a colourful representation of the physics process.

In the model tree in the "Study" sequence, the "Step1: Wavelength Domain" line allows to enter the wavelength or the frequency of the incident wave. Choosing additionally the "Parametric Sweep" option makes the result dependent on the parameter, such as diameter or periodicity of nanoparticles. It calculates a massive of data dependent on the changed parameter with the specified step.

The Solver or the computational algorithm is selected by Comsol by default and doesn't require manual customisation. However, it can be changed manually based on the complexity of the task or computational resources. There are two fundamental classes of algorithms: direct and iterative methods.

The direct method is used to achieve the most accurate and robust solution. However, it requires a sufficient amount of memory. Comsol Multiphysics supports direct solvers such as Multifrontal massively parallel sparse direct solver (MUMPS), Parallel direct solver (PARDISO) and Sparse object-oriented linear equations solver (SPOOLES). All the solvers are based on lower-upper (LU) decomposition. The returned solution by all these solvers is the same. The primary difference between them is their relative computational speed. The fastest solver is PARDISO, used for the simulations of metasurfaces, that can use out-of-core storage to offload some of the computations onto the hard disk. The SPOOLES solver is the slowest but also tends to use the least memory. The advantage of MUMPS is the capability of using cluster computing, which allows for the use of more memory than what is available on a single machine.

The iterative solver requires less computational memory than a direct solver, and so is implemented for large physics problems. It approaches the solution gradually, rather than in one computational step. With each iteration, the system returns an error estimate that decreases monotonically with the number of iterations. The oscillatory behaviour of the error estimate indicates that the problem formulation, including the boundary conditions, may be incorrect. By default, the model is considered to be converged when the error estimate is below 10^{-3}. This number is defined in the "Relative tolerance" of the solver settings and can be made looser for faster solutions or tighter for greater accuracy. The minimum tolerance number is restricted by the machine precision (2.22×10^{-16}) and, most of the time, much greater due to the strong relation to the chosen mesh size.

When the Study step is completed, the computation process can be started.

The Post-processing step aims to extract the necessary data after the computation process that is not directly visualized. The data about metasurface reflectivity at a specific wavelength can be presented in the form of a table by using the "Global Evaluation" in the "Derived Values"

sequence. The other parameters, such as transmittance, absorption, total energy, etc., can also be found by clicking on the cross in the "Expression" line (Figure 3.8). The post-processing capabilities in Comsol Multiphysics are huge and can be accessed via the software's official website.

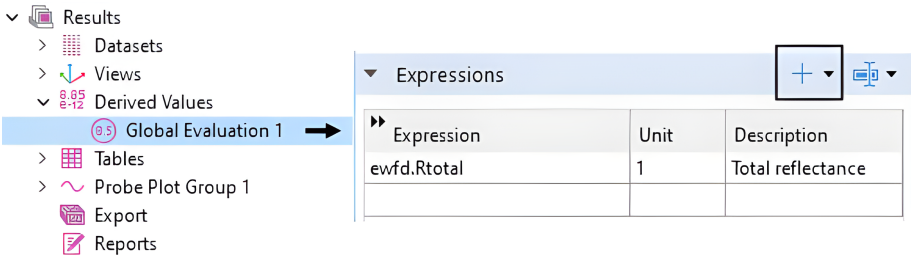

Figure 3.8.: "Global Evaluation" node to extract information about the optical properties of the metasurface, such as reflectivity, transmissivity, etc.

One particularly useful feature in data representation is the implementation of "Global Variable Probe" in the "Definition" section above "Geometry". This diagnostic tool allows prematurely setting the expression whose value is being extracted for results analysis. The table is generated directly after the computation and doesn't require additional setup.

3.6 Validation analysis

The simulated results may not always correspond to the real solution. Several approaches can be used to check and validate the obtained results.

- Comparison with an analytical solution

The simulation model can be simplified to a form where the results can be verified analytically. Complex problems often begin with a simple case that is progressively modified. At the beginning of the task, when the model is defined with its initial geometry, material properties, and boundary conditions, the simulation results should be compared with the corresponding analytical solutions.

- Mesh convergence

Finite element modelling is highly dependent on the size of the finite elements, or mesh, selected. Too large mesh will fail to capture the intricate details of the model. Performing a mesh refinement study ensures that the results are independent of the mesh size. Starting with a coarse mesh and gradually refining it gives the observation of how the solution changes. If the results stabilise as the mesh is refined, it indicates that the solution is mesh-independent.

- Parameter sensitivity analysis

Depending on the model, various parameters have different levels of impact on the result. For instance, a block of medium above the nanoparticle with a height less than $\lambda/2$ (where λ is the wavelength of the incident electromagnetic wave), might result in incorrect simulation outcome. It is crucial to verify the stability of the solution by altering the height of this medium. In contrast, changes in the diameter of the nanoparticle should produce corresponding changes in

the results. If the results remain unchanged despite modifications to the nanoparticle's diameter, this indicates potential errors in the model.

- Physical Consistency

This validation approach ensures the conservation of mass, momentum, and energy. The initial electromagnetic wave energy interacting with the nanoparticle is conserved and redistributed among absorption, transmission, and reflection. In other words, the sum of these values must equal 1.

- Error estimate of iterative solver

The direct and iterative solvers may differ in their calculation approaches, but they should give the same results (with the accepted error). The gradual search for the solution using the iterative solver also provides information about the error estimate, which should decrease smoothly. The oscillation behaviour of this solver indicates the uncertainties in the built model.

- Validation with the experimental data or another software results

The final and most challenging approach involves the comparison of the simulation results with experimental data or results obtained using other software, such as Matlab or Ansys. Experimental and simulation data can also be sourced from articles, reviews, or books. Officially published data serves as a reference to validate the accuracy of the obtained results.

Chapter 4

Fabrication Techniques

The fabrication of metasurfaces can be achieved through a variety of techniques, depending on the available machinery, chemicals, materials, and the required precision of the structures [111]. In this thesis, we focus on the fabrication approach developed at DTU for the realisation of cylindrical Si metasurfaces on substrates. The details of the metasurface realisation process are presented in this chapter, as well as in the last published paper, entitled "Design and experimental demonstration of wavelength selective metamirrors on sapphire substrates".

The initially considered reflective metasurfaces consist of Si nanoparticles with a spherical shape. Spheres are challenging for fabrication due to the absence of flat surfaces but can be realised using femtosecond laser printing technology [112]. The process involves the ultrafast heating of a donor Si layer by a single tightly-focused Gaussian femtosecond laser pulse, that forms a spherical droplet. This droplet, propelled by potential energy, progresses towards the receiver substrate and subsequently solidifies on it in the form of a sphere. By employing pulses of the same energy, a metasurface consisting of similar spherical nanoparticles can be fabricated. This fabrication method is discussed in the first published paper, entitled "Lightweight metasurface mirror of silicon nanospheres". However, it is not subsequently employed in the realisation process of reflective metasurfaces due to the consideration of the cylindrical shape of nanoparticles.

The investigated and subsequently fabricated highly reflective metasurfaces consist of cylindrical nanoparticles placed on a substrate. The selected wavelengths for reflectivity are 1064 and 1550 nm, with polycrystalline silicon (poly-Si) used for the cylinders and sapphire for the substrate. The main steps of the fabrication process were conducted in collaboration with the Department of Electrical and Photonics Engineering at DTU.

The fundamental fabrication idea involves the creation of a mask on the poly-Si layer and the subsequent etching of the unmasked area. To accurately resolve mask patterns with nanometer-sized features, the fabrication process includes electron beam lithography EBL, which uses a focused electron beam (e-beam) to expose electron-sensitive material (resist).

It should be noted that the discussion suggests the approach implemented for the realised structures, which can be modified or adapted for the fabrication of future metasurfaces. Additionally, the last section of this chapter explores a potential fabrication method that could be carried out at the LNQE of Hannover, which may serve as a potential site in the future.

4.1 Preparation of the samples

The samples with the planned metasurfaces must be prepared prior to the manufacturing process. It means that the poly-Si material of the nanoparticles has to be deposited on the substrate, and the substrate needs to be sized in accordance with the specifications of the technical machinery. Moreover, the numerically estimated dimensional parameters of the cylinders, such as diameter (D) and periodicity (P), must be recalculated based on the measured height (H) and refractive index of the deposited poly-Si layers.

4.1.1 Deposition of poly-silicon layers

The process commences with the ordering of sapphire wafers with the C-plane (0001) orientation, selected as the bottom substrate for the metasurfaces. The wafers, ordered from "Siegert Wafer Company", have a diameter of 100 mm, a thickness of 650 µm, a purity of 99.998%, and are polished on both sides.

The wafers are coated with poly-Si layers of varying thicknesses using the low-pressure chemical vapor deposition (LPCVD) technique, realised in the horizontal cluster system (Centrotherm 2000) at the LNQE (Figure 4.1).

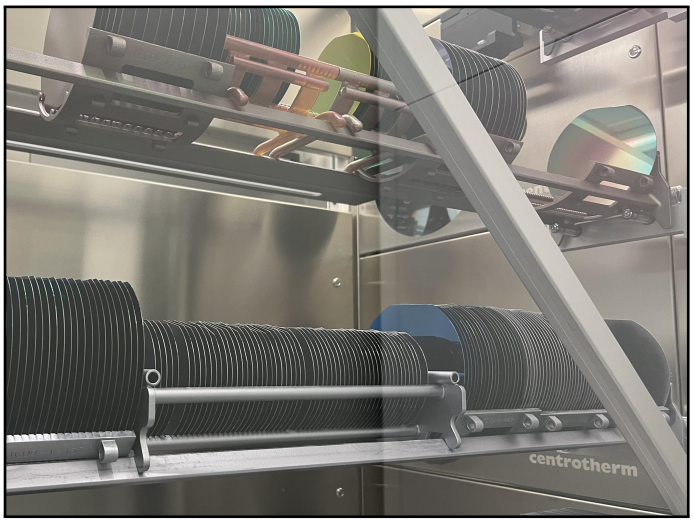

Figure 4.1.: Photo of the horizontal cluster system (Centrotherm 2000) that deposits poly-Si layers on wafers using the LPCVD technique.

The LPCVD technique is a precise deposition method that uses chemical precursors, such as gases or vapours, that contain the elements needed to form a solid layer. These precursors are introduced into a chamber, where they react on the surface of a heated substrate, creating a thin film. The "low-pressure" setting reduces the chances of the gases colliding with each other, which helps to ensure that the film is deposited evenly across a large surface area.

The temperature of the LPCVD process plays an important role in determining how much silicon crystallizes and transitions from an amorphous to a poly-crystalline state. Temperatures $\sim 500 - 600°\mathrm{C}$ often result in a-Si, whereas higher temperatures, typically above $600°\mathrm{C}$,

initiate the formation of poly-Si, as the atoms gain enough thermal energy to form crystalline grains.

The deposition machine (Figure 4.1) has a wafer boat with dozens of vertically placed 'dummy' wafers, some of which are replaced with sapphire samples that need to be coated. A dummy wafer is typically a silicon wafer coated with a silicon dioxide layer (Si/SiO_2). The use of dummy wafers is an integral part of the process, ensuring uniform chemical deposition of poly-Si layers on both sides of the wafers. They are also additionally used to measure the thickness of the deposited layers, protecting the sapphire wafers intended for future utilisation from unnecessary handling.

4.1.2 Ellipsometry measurements

The deposited poly-Si layers must be characterised to ensure that their thicknesses correspond to the intended values and to measure the actual refractive indices of these poly-Si layers. The characterisation is conducted via ellipsometry. The measurement process uses dummy wafers that were included in the LPCVD process, protecting the sapphire wafers with the poly-Si coating from potential scratches and dust. Moreover, measuring the thin poly-Si layer on sapphire is challenging. Due to the transparent nature of sapphire wafers and their double-sided polishing, the ellipsometric measurement light is additionally reflected from the back side of the wafers, contributing to the detected signal. In contrast, the Si dummy wafers are polished on one side, making the unpolished side a good scatterer. This particularity helps to avoid the additional reflected signal in the detection, making the dummy wafers ideal monitor samples for accurate examination.

Ellipsometry is a non-destructive optical technique, which provides precise data on the thickness and refractive index of a thin film. It works shortly in the following way [113]. The polarized light of the ellipsometer falls at an oblique angle onto the sample surface. As the light reflects, its polarization state is altered due to interactions with the thin film, resulting in changes to both the amplitude and phase of the reflected polarized light. These changes are quantified by measuring two parameters: ψ, which represents the amplitude ratio of the p- and s-polarization components, and Δ, which captures the phase difference between the p- and s-polarizations. These two values allow to calculate the reflectivity ratio:

$$\tan \psi e^{i\Delta} = \frac{r_p}{r_s}, \tag{4.1}$$

where r_p and r_s are the amplitude reflection coefficients for p- and s-polarized light, respectively.

The coating properties can't be extracted directly from the measured parameters ψ and Δ alone, as they do not account for variations introduced by the underlying materials. To address this, the ellipsometer software constructs an optical model of light interaction with all interfaces within the multi-layer structure, based on Fresnel's Equations (2.33 - 2.40). Through an iterative fitting process, optimisation algorithms adjust the model to minimize the difference between the measured and predicted ellipsometric data. This comparison results in the accurate calculation of such parameters as film thickness and refractive index.

The ellipsometry measurements of the produced poly-Si layers were conducted at DTU for the wavelength range of $[210; 1688]$ nm. The data on thicknesses and refractive indices at wavelengths of 1064 and 1550 nm are subsequently used in reflectivity simulations to refine the dimensional parameters of cylinders for fabrication, including the diameter (D) and periodicity (P).

4.1.3 Metasurface area and cutting process

The final preparation step involves choosing the dimensions for the metasurface area and cutting the sapphire wafers into smaller samples.

The metasurface area for fabrication is selected to be 100×100 µm^2. The fabrication of this area size is time-efficient when using EBL, and the resulting area is sufficiently large for the characterisation setup. Moreover, in order to confirm the effect of metasurface reflectivity in the initial fabrication attempt, it is also important to select the appropriate area size at which the EBL stage with the mounted sample would remain stationary. The movement of the stage may result in misalignment of the exposure pattern, which is considered undesirable. The maximum writing field for the operational EBL machine at DTU is $1000 \times 1000\,\mu$m^2, which is larger than the selected metasurface area.

The wafers are cut into squares of 15×15 mm^2 using metal bond blades (B1A-Serie Disco) that are capable of cutting sapphire. The size is selected to accommodate efficiently several metasurface areas and to ensure that the samples are compatible with the equipment used throughout the manufacturing process. For the cutting process, the surface of the samples is additionally protected with available photoresist (MICROPOSIT S1813).

After these preparation steps, the samples are ready for the metasurface fabrication process.

4.2 Fabrication process details at DTU

This section details the fabrication steps conducted at DTU. To assist the reader in navigating the process, the fabrication steps are presented in the accompanying Figure 4.2.

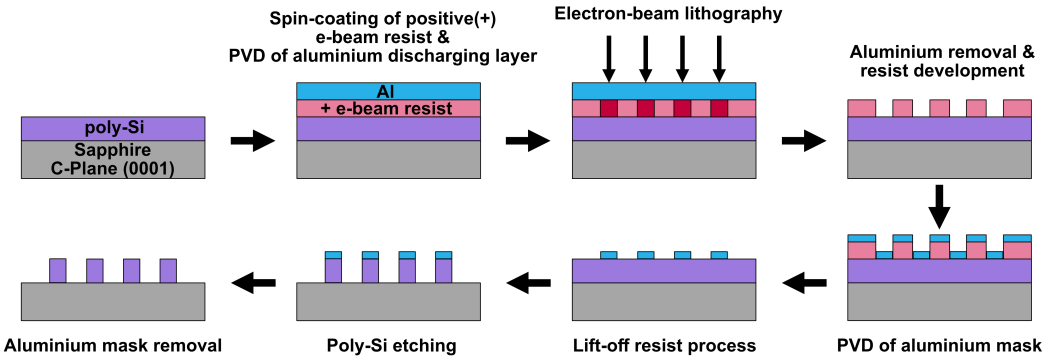

Figure 4.2.: Fabrication process at DTU.

4.2.1 Resist spin-coating

The deposition of electron-sensitive resist on a poly-Si layer is an essential step in the creation of a pattern or mask with EBL. The e-beam resist influences the fabrication accuracy and defines the subsequent stages of production.

Before applying the e-beam resist, the prepared samples must be thoroughly cleaned, and the protective photoresist must be removed. For the samples used in the production, the cleaning procedure involves the Piranha method (4:1), in which four parts of sulfuric acid (H_2SO_4) are mixed with one part of hydrogen peroxide (H_2O_2). The samples are immersed in the Piranha solution for 10 minutes and then thoroughly rinsed with distilled water.

The positive e-beam resist (Csar AR-P 6200) is deposited onto the poly-Si surface through spin-coating (Figure 4.3). This process involves centrifugal force and high-speed rotation to distribute the liquid resist evenly across the sample. The positive e-beam resist is spin-coated to a thickness of 150 nm. Following this, the samples are baked for two minutes at a temperature of 180°C and then left to cool. The baking process helps evaporate the solvent, transforming the resist from a liquid to a solid, making it ready for e-beam exposure.

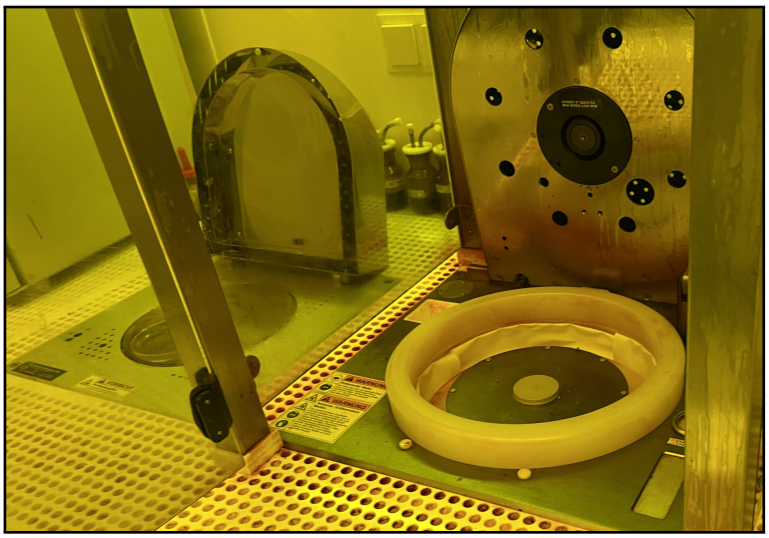

Figure 4.3.: The spin-coating machine (right) and the oven for the baking process (left). The photo is taken at the LNQE.

The discharging layer of aluminium (Al) is additionally thermally evaporated on top of the resist. This procedure is necessary to prevent charge accumulation during the EBL process. Due to the dielectric nature of sapphire and since we do not know the doping level of poly-Si, some electrons can become trapped inside the material. The presence of this charge can deflect the electron beam, deteriorating patterning precision by causing unwanted exposure in nearby areas. Therefore, the Al layer serves as a 'ground' for the sample, helping to dissipate the excess charge.

The deposition of the Al layer takes place in a thermal evaporator, which is pumped down to a pressure of 6×10^{-6} Pa. The sample is mounted on a rotating substrate holder, spinning at a speed of 10 RPM to ensure uniform film thickness across the surface. At the base of the

vacuum chamber, the Al boat is loaded with Al pellets, which are subjected to a gradual heating process. Upon reaching a temperature of $\sim 2000°C$, Al begins to vaporise. The vaporised atoms travel towards the substrate, where they condense onto the surface, in this case, onto the resist. The deposition thickness is continuously monitored in real-time using a quartz crystal microbalance (QCM). The final Al thickness reached in the thermal evaporator is around 20 nm.

4.2.2 Electron beam lithography

The fabrication of nanometer-scale structures requires the use of EBL. Unlike photolithography, which is limited to ~ 1 µm due to the wavelength of the exposure light and is more suitable for micrometre-scale structures, EBL offers significantly higher resolution, enabling the fabrication of extremely small, precise patterns down to a few nanometers [111].

EBL works by directing a focused beam of electrons onto a substrate coated with an electron-sensitive resist, which alters its chemical structure in the exposed areas. At the core of the EBL machine is the electron gun that generates a high-energy e-beam, typically between 10 and 100 keV. The process occurs inside a vacuum chamber, which is important to prevent electrons from being scattered by air molecules. The substrate, coated with the resist, is mounted on a precisely controlled stage that moves the sample while the e-beam scans the surface to write the desired pattern.

There are several important parameters that define the performance of the EBL machine: *dose*, *beam current (intensity)*, *spot size*, and *exposure time*. The dose is the amount of electron energy delivered per unit area and depends on factors such as the resist material and the size of the structures to be produced. The optimal dose is often determined by experience and experimentation. The beam current is proportional to the dose, meaning that a higher dose requires either more electrons (higher beam current) or longer exposure time to achieve the desired pattern resolution. The spot size, which refers to the diameter of the focused electron beam, plays a crucial role in determining the resolution of fine features. Optimising the spot size involves balancing resolution, exposure time, and beam current. In particular, a smaller spot size requires more exposure time to illuminate the same area due to the increased number of e-beam shots. Finding the "golden point" for all these parameters can be challenging and requires careful tuning in the software of the EBL machine.

The dose factor for the fabricated structures is initially set to $325\mu C/cm^2$. Since the setting up of the EBL process takes a considerable amount of time, including pumping the system into vacuum, several metasurfaces with different doses are produced on each sample. The first variation is taken with a dose of $325\mu C/cm^2$, while the second is created with a dose that is increased by 10% and the third with a dose that is increased by 20%. In the software, this is achieved by implementing multiplication coefficients of 1, 1.1, and 1.2 to different areas.

The electron beam energy is set to 100 keV, with a spot size of 7.75 nm and a step size of 5 nm. The beam current is measured precisely at settings, and the exposure time is recalculated automatically.

The patterns for the exposure are uploaded to the EBL machine as GDSII files [15], which can be created in any computer-aided design software, for instance 'KLayout'. Each circle of the metasurface pattern is divided by the EBL software into multiple sections. The e-beam, with specified parameters, scans through each section in a particular order, as shown in Figure 4.4. Notably, the e-beam spots overlap in order to achieve an even distribution of resist exposure.

Figure 4.4 also illustrates that the beam covers the area of the circle that is slightly larger than the area depicted in the schematic. Furthermore, the forward and backward electron scattering (proximity effect) results in the broadening of the exposed area. In order to achieve the intended dimensions, the diameter of the circles in the schematic must be reduced to compensate for this effect. For the fabricated structures, the increase in the exposed area is estimated to be $\sim 15 - 20\,\text{nm}$. The deviation of periodicity is considerably less and estimated to be $\sim 0.1 - 0.5\,\text{nm}$.

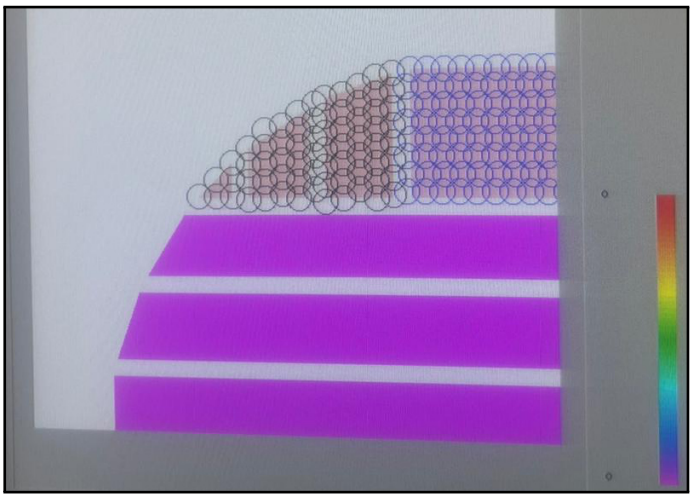

Figure 4.4.: The software of the EBL machine displays the exposure pattern with the selected parameters of the e-beam.

The manufactured metasurface structure consists of cylinders, which offer the advantage of having no corners. Corners are challenging to resolve in the EBL process, and a standard uniform dose distribution can lead to inaccuracies. For structures with corners, a Monte Carlo method is used to generate an approximate dose distribution pattern for the 2D geometry, ensuring better accuracy in fabricating the corners.

4.2.3 Development

The layer of the positive e-beam resist is exposed as a pattern of cylinders. Due to the positive nature of this resist, the electrons make the polymer structure more soluble for the developer solution. This means that the development stage leaves behind the unexposed regions as a final pattern. Since the exposed area corresponds to circles representing the diameters of the future cylinders, the development results in the production of holes within the resist layer.

[15] GDSII files stand for "Graphic Design System II" files, a standard format for layout data of integrated circuits.

The exact fabrication steps involve the removal of the discharging Al layer using phosphoric acid (H_2PO_4) solution diluted with water in a 4:1 ratio. The samples are then rinsed with distilled water. The developer solution used is AR600-546. The samples are immersed in the developer solution for two minutes, followed by a one-minute rinse in isopropanol.

The developed holes in the resist could be observed in the optical microscope (Figure 4.5), which also allowed us to check the clearance of the developed structures.

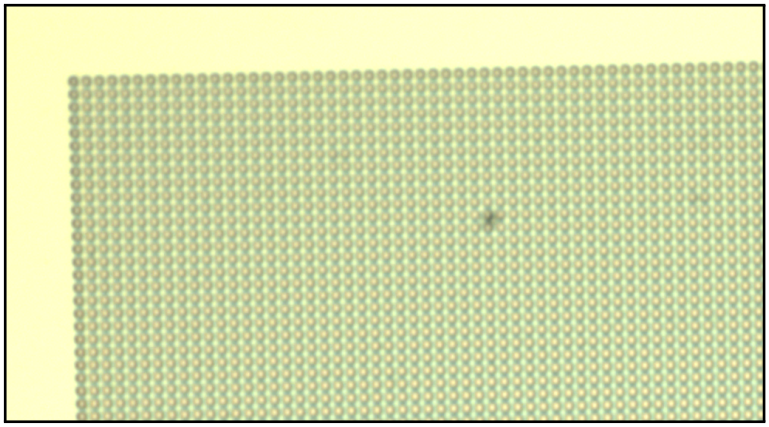

Figure 4.5.: Image of the developed resist structure made with an optical microscope.

4.2.4 Lift-off process

The lift-off process involves the deposition of an additional layer that, by removing ("lifting off") the remaining positive resist, creates an inverse mask. The material for this additional layer is Al.

The Al deposition is carried out using an e-beam evaporator, which works in a similar way to a thermal evaporator, but, in this case, with the help of the high-energy e-beam directed at the melting material. This beam causes localized heating, allowing the Al to evaporate and condense onto the substrate to form a thin layer.

The thickness of the Al layer must be small enough to avoid the merger or intersection of the deposited layer in the holes with the layer above the resist. Otherwise, the resist cannot be properly removed or lifted off with a chemical. A common rule of thumb is to keep the Al thickness to less than one-third of the resist's thickness. If the resist has a thickness of 150 nm, the Al mask should be less than 50 nm. In the fabrication process, the Al thickness is set to 25 nm. The Al pattern is also observed using the scanning electron microscope (SEM) (Figure 4.6), revealing the typical effect of Al growth at the edges.

The remaining resist is removed using chemical 1165 (a pyrrolidinone compound) for 25 minutes. Following this, the samples are rinsed with isopropanol and distilled water.

The obtained Al mask on top of the poly-Si layer is observed in the SEM (Figure 4.7).

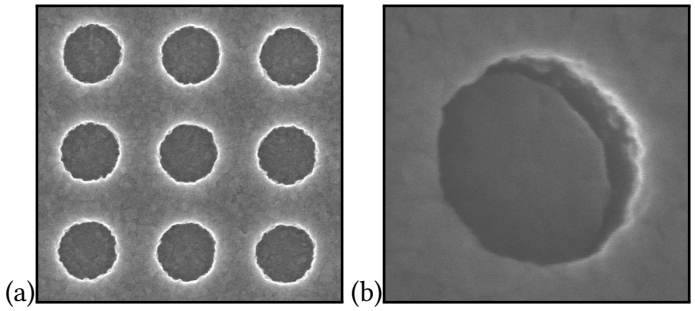

Figure 4.6.: SEM images of the Al layer covering the resist pattern and the area inside of the holes. a) An array of holes. The periphery of the circles has crystalline irregularities. b) The view at an angle to one of the holes.

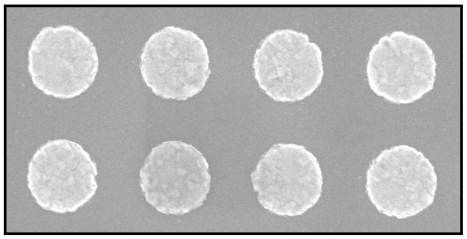

Figure 4.7.: SEM image of the Al mask on the poly-Si layer.

4.2.5 Reactive ion etching of poly-Si

The created Al mask acts as a shield, protecting certain areas of the poly-Si layer from the etching process. The method used to etch the poly-Si layer is classified as "dry" etching, which removes material using gases or plasma, unlike the liquid chemicals of "wet" etching.

The technique, called inductively coupled plasma reactive ion etching (ICP-RIE), is a widely employed method in nanometer-scale structure fabrication. It involves two mechanisms of etching, defined as a chemical and physical interaction. Chemical etching tends to be isotropic, meaning it removes material uniformly in all directions. This also includes the material under the mask, leading to a more spherical removal profile. This can cause "undercutting" beneath the mask. On the other hand, physical etching can be visualized as ion bombardment of the substrate, where ions physically knock off the material. This process is highly directional, typically resulting in anisotropic etching concentrated on the central region of the etched wells. It limits lateral removal, which requires vertical features.

The combination of chemical and physical etching in ICP-RIE results in the creation of structures with vertical, almost perpendicular sidewalls, which is important in the fabrication of cylinders.

The process of poly-Si ICP-RIE often involves cycles. Each cycle starts with a phase of mixed etching types (both chemical and physical), during which reactive species, such as fluorine radicals (F*), are generated. These radicals form a protective layer, preventing the further process of etching. Once the sidewalls are passivated, a short phase of purely physical etching follows. It removes the F*-cover from the bottom horizontal surface without affecting the

protected sidewalls. Once the bottom is cleared, the process repeats in the next cycle, allowing for controlled deep etching while maintaining verticality and precision.

The number of etching cycles required for various thicknesses of poly-Si layers is the following: a 72 nm thickness requires 6 cycles, 132 nm - 10, 211 nm - 17, and 297 nm - 24 [16].

The gases typically used in this process are octafluorocyclobutane (C_4F_8) for passivation and sulfur hexafluoride (SF_6) for etching, as they provide the necessary reactive species for the chemical and physical etching mechanisms.

To maintain a temperature difference between the substrate and plasma for better process control, the sample is placed on a droplet of a liquid resist to establish thermal contact between the sample and the bottom plate, which is maintained at a temperature of $-19°C$. The temperature of the plasma during the etching process rises up to $+120°C$. The image of the sample placed on the holder of the ICP-RIE machine is shown in Figure 4.8.

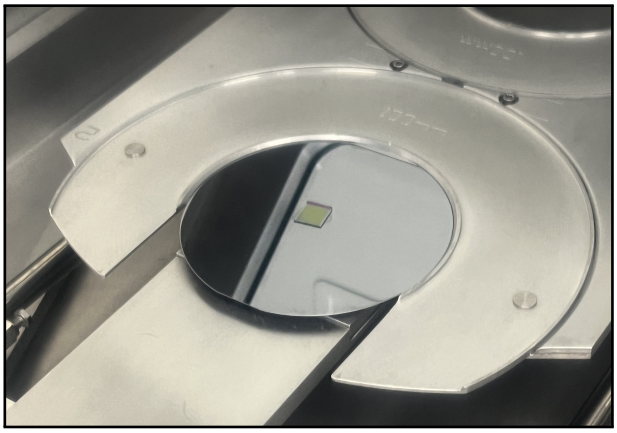

Figure 4.8.: The sample placed on the holder of the ICP-RIE machine.

Before and after the etching process, the structure undergoes cleaning with oxygen plasma. This cleaning step is integrated into the etching system and helps to remove any residues for the accurate handling. Additionally, the resist used for the thermal contact is cleaned with acetone (10 minutes) and isopropanol (10 minutes).

4.2.6 Back-side etching and removal of Al mask

The final preparation of the metasurface structures includes the ICP-RIE of the back-side of the samples covered with poly-Si layer and removal of the Al mask. The ICP-RIE of the back-side is made by placing the samples upside-down onto the resist and undergoing the same etching process described in the previous chapter. The removal of the Al mask is done by phosphoric acid (H_2PO_4) diluted in water in a ratio of 4:1.

The fabricated metasurfaces are observed in the SEM (Figure 4.9) and are further characterised to reveal their reflectivity. The characterisation results and simulation details of the realisation

[16] The average etching rate is estimated ~ 13.5 nm/cycle. However, it slightly decreases when the number of cycles exceeds 10.

process are presented in the last paper, entitled "Design and experimental demonstration of wavelength-selective metamirrors on sapphire substrates".

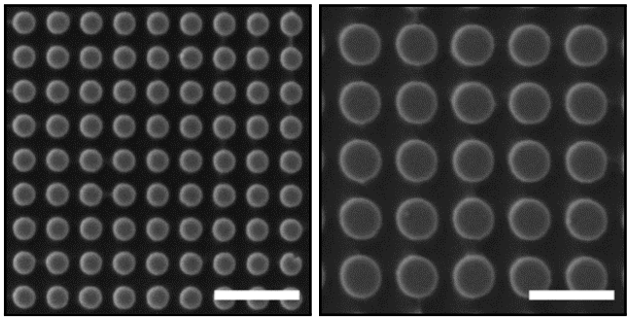

Figure 4.9.: SEM images of the fabricated metasurfaces.

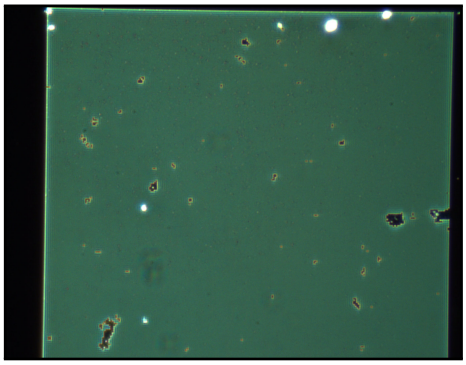

Figure 4.10.: The damaged structure after undertaking a too-long process of cleaning.

The process of the metasurfaces fabrication had some challenges based on the unconventional behaviour of Al with the bottom sapphire substrate. This effect was mostly observed for the structures with the thinnest poly-Si layers, namely for 72 and 132 nm. The removal of the discharging Al layer caused for several samples the disposal of the positive resist that had to be implemented for the further EBL process. The final cleaning process of the Al mask also had a certain degree of difficulty, as it required a longer period of time using the phosphoric acid and the utilisation of an ultrasonic bath. The overly lengthy cleaning process could also lead to damage to the structure, potentially resulting in the loss of some cylinders (Figure 4.10). The fabrication process for the future silicon metasurfaces on sapphire substrates requires further investigation and optimisation in order to achieve the highest possible quality and precision.

4.3 Alternative fabrication at the LNQE

The fabrication process presented in the previous chapter is adapted for the facilities available at DTU. The process of metasurface fabrication is also possible within the facilities of the LNQE, described in detail in the Master Thesis of Shan Song. In this section, I describe the main differences between the two fabrication approaches.

The fabrication stages are presented in Figure 4.11. The sapphire sample with a poly-Si layer

is initially spin-coated with the negative e-beam resist (SX AR-N 8200) [17]. The exposure of the sample in the process of the EBL leads to the hardening of the resist, thereby reducing its solubility in the developer solution (AR 300-44). Following development, the remaining structure configures a mask that covers the area of the metasurface cylinders. The subsequent poly-Si ICP-RIE creates the required 3D pattern. The removal of the resist with buffered oxide etch (NH_4F and HF in a ratio of 5:1) leaves the developed cylindrical structure ready for further characterisation.

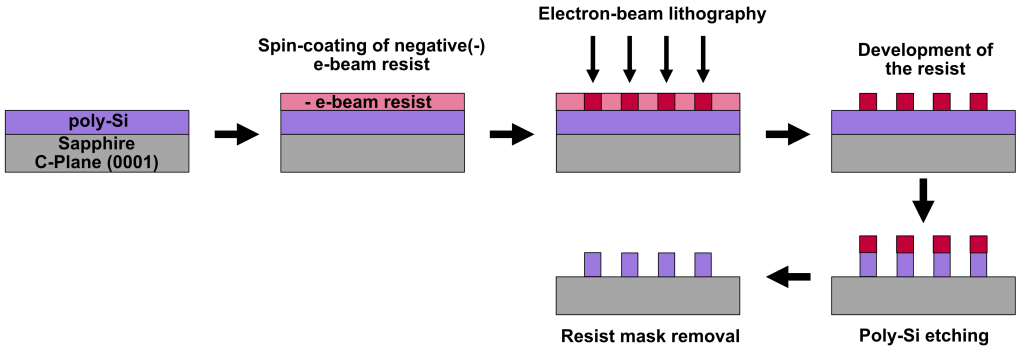

Figure 4.11.: Metasurface fabrication steps at the LNQE.

In comparison to the process described in the previous chapter, this fabrication process involves fewer steps due to the implementation of the negative e-beam resist, which, after the exposure, creates the desired mask. Nevertheless, the selection of the resist also depends on the required precision of the fabricated nanostructures. For instance, the negative e-beam resist (SX AR-N 8200) is used for the metasurfaces with nanoparticles, whose dimensional parameters don't require resolution of less than 10 nm. The positive e-beam resist (Csar AR-P 6200) can be preferential for the structures with the resolution of around 6 nm.

The selection of the resist, as well as the precision of the nanostructures, also depend on the EBL machine employed in the fabrication process. The higher acceleration voltage of the EBL machine reduces the electron scattering, maximizing finer resolution in the patterned structures. For the comparison, the EBL machine at DTU could resolve nanocylinders with the spacing of ~ 100 nm and less, while at the LNQE a spacing of ~ 150 nm could have a potential challenge. This limitation on the selection of dimensional parameters of nanoparticles must be taken into account in the realisation process of metasurfaces.

The manufacturing facilities of the LNQE are extremely broad and improving every year. The fabrication technology of future metasurfaces with alternative substrates or with different nanoparticle configurations can be tested and developed there.

[17] The following fabrication sequence was previously conducted at the LNQE and did not include the deposition of the discharging layer after spin-coating of the resist. Therefore, the details of this step are not presented here. Nevertheless, the deposition of the discharging layer must be taken into account in the future fabrication process within the LNQE facilities.

Chapter 5

Publications - Main Results

The research findings are presented across four publications in peer-reviewed journals, each offering a comprehensive analysis of the system under investigation and the results obtained. These papers are organized chronologically, with each subsequent paper addressing progressively more complex aspects of the study, culminating in the development and fabrication of a metasurface prototype.

5.1 Research objectives

At the beginning of the research process, it is important to consider the reflectivity effect of the simplest metasurface design. For this purpose, a metasurface structure composed of spherical c-Si nanoparticles is chosen, symmetrically and periodically arranged in a homogeneous polymer medium. The impinging wave is a plane monochromatic light wave at a normal angle of incidence. Taking into account the technologies used in the current GWDs, the selected wavelength of light is 1064 nm.

The reflectivity effect can be achieved through resonant excitation of multipole moments in the nanoparticles. The most practical case involves the excitation of ED and MD moments, which depends on the geometrical parameters of the spheres and their arrangement, as well as material parameters, such as the refractive index of the spheres and the surrounding medium. Theoretical justification of this process, including the corresponding equations, is an important initial step.

The periodic metasurface can exhibit total reflection (100%) in the case of the absence of losses and ideal structure, meaning that all nanoparticles, as well as the distance between them, are identical. To investigate the reflective behaviour, we use two approaches: analytical calculations based on the coupled dipole approximation and numerical simulations using Comsol Multiphysics software. The validated numerical simulations can later be applied to more complicated scenarios, such as cases where nanoparticles are embedded in a finite layer of polymer, which is closer to realistic conditions. Additionally, the system can be made more complex and supplemented by introducing nanoparticles with varying diameters and periodicity distributions. All results from this research are presented in the first published paper (Section 5.2):

Publication 1

Andrey B. Evlyukhin, Mariia Matiushechkina, Vladimir A. Zenin, Michèle Heurs, and Boris N. Chichkov, **"Lightweight metasurface mirror of silicon nanospheres [Invited]"**, Opt. Mater. Express 10, 2706-2716 (2020). DOI: 10.1364/OME.409311.

In the next stage of the research, it is essential to consider the metasurface on a substrate to enable fabrication using the laser-printing technique. The substrate material must exhibit low mechanical losses and low optical absorption at near-infrared and telecommunications wavelengths. Based on these requirements, sapphire has been selected as a suitable candidate due to its favourable properties. Since the spherical nanoparticles make contact with the substrate at only a single point, an additional intermediate protective layer is required. The optical impact of this intermediate material on the metasurface must be negligible. Therefore, materials such as polymers (e.g., PDMS) or amorphous substances (e.g., fused silica) are appropriate choices.

The proposed configuration still ensures perfect reflectivity in the absence of losses at the ED and MD resonant responses of nanoparticles. The wavelength chosen for the investigation is 1550 nm. The primary objective of the multi-layer configuration is to study the influence introduced by the contribution of the substrate and the protective layer materials. For this purpose, we vary the refractive index of the substrate and the protective layer and examine how dimensional parameters, such as periodicity, must be adjusted to achieve perfect reflection. The results demonstrate that the contribution of the substrate in the optical response of spherical nanoparticles is negligible. However, even with a relatively low refractive index of around 1.4, the protective layer has a significant impact that leads to adjustments to the metasurface's dimensional parameters.

Additional numerical simulations focus on investigating how random small variations in the diameter and periodicity of the metasurface on a substrate with a protective layer affect its reflectivity. The simulations target the excitation of the (MD) moment, revealing that changes in diameter have a more significant impact than fluctuations in periodicity. Slight variations in the thickness of the protective layer are also considered, though these can be treated as negligible in the first approximation.

The reflectivity of the metasurface becomes polarization-dependent when the incident light deviates from a perfectly perpendicular angle of incidence. The research indicates that s-polarization is more robust in achieving full reflection compared to p-polarization. All these findings, along with more detailed discussions, are presented in the second publication (Section 5.3):

Publication 2

Mariia Matiushechkina, Andrey B. Evlyukhin, Vladimir A. Zenin, Michèle Heurs, Boris N. Chichkov, **"High-efficiency silicon metasurface mirror on a sapphire substrate"**, Optical Materials 138, 113618 (2023). DOI: 10.1016/j.optmat.2023.113618.

An alternative method for fabricating metasurfaces is electron beam lithography (EBL). This technique, however, requires that the top and bottom surfaces of the nanoparticles be flat. Among potential shapes, cylinders offer a significant advantage, as they do not have sharp

corners that are difficult to produce with high resolution. Thus, as an alternative configuration, a metasurface composed of cylindrical nanoparticles on a substrate can be fabricated using the EBL technique. In this case, an intermediate protective layer is unnecessary due to the larger contact area between the nanoparticles and the substrate.

Before addressing this configuration, it is necessary to first consider the simpler case, where nanocylinders are embedded in a homogeneous medium [18]. This simplification is important due to the additional geometric parameter of cylinders — their height.

Cylinders offer a distinctive feature compared to spheres: the ratio between the height and radius of a cylinder allows for manipulation of the relative spectral position of the ED and MD resonances. In contrast, for spheres in the array with a square elementary cell, the relative spectral positions of these resonances are fixed. This spectral manipulation of the ED and MD resonances provides broader flexibility in selecting fabrication parameters and allows control over the phase of the reflected light field.

Two specific states deserve special attention: the resonant Kerker effect and the anapole state. The resonant Kerker effect occurs when the ED and MD resonant peaks overlap, resulting in high transmissivity of the metasurface rather than its reflectivity. For the realisation of high reflectivity, this state must be avoided, and the undesirable ratio between height and radius that leads to this effect must be calculated. The anapole state, in contrast, is an interesting state that provides the suppression of ED scattering. By aligning the MD resonance at the anapole state, it is possible to create a metasurface magnetic mirror effect.

The design optimisation process for a specific wavelength (for instance, 1550 nm) can be constructively divided into several steps. To create a metasurface operating at the MD resonance aligned to the anapole state (magnetic mirror effect), the initial step involves the consideration of a single nanoparticle. Tuning the aspect ratio between height and radius while keeping the radius fixed allows for positioning the MD resonance at the anapole state. Then, by changing the radius while maintaining the aspect ratio, the spectral positions of the dipoles can be tuned to the desired wavelength of 1550 nm. As a final step, transitioning from the analysis of a single particle to the metasurface structure, we select the periodicity parameter.

Following a similar procedure, it is possible to create the electric metasurface mirror that operates at the ED resonant response with the minimum contribution from the MD moment. The electric and magnetic metasurface mirrors differ in the phase of the reflected light field, with the relative phase shift equal to π. This research, including the consideration of the mirror effects at higher-order modes, is presented in the following publication (Section 5.4):

Publication 3

Mariia Matiushechkina, Andrey B. Evlyukhin, Vladimir A. Zenin, Boris N. Chichkov, Michèle Heurs, **"Perfect mirror effects in metasurfaces of silicon nanodisks at telecom wavelength"**, Adv. Opt. Mater. 12, 2400191 (2024). DOI: 10.1002/adom.202400191.

After a detailed theoretical analysis of cylindrical metasurfaces, the focus shifts to their practical realisation. The structure consists of an array of cylinders on top of a substrate. The materials chosen for the metasurface structure are poly-Si and sapphire, respectively. The nanoparticle

[18] For reasons of simplicity, the decision was taken to use vacuum in numerical simulations.

material of poly-Si is used in preference to c-Si for the first realisation attempt due to the flexibility to deposit via LPCVD any selected cylinder height.

Simulations in the initial phase provide approximate values for cylinder height that should be feasible to fabricate in order to avoid the Kerker effect. This data is approximate because the material parameters, such as refractive index, are sourced from external databases. The actual refractive index can be measured only after the deposition process of poly-Si layers. Measuring additionally the exact height after LPCVD, we can determine through simulations the more accurate values of diameter and periodicity of cylinders needed to achieve high reflectivity at specific target wavelengths (1064 nm or 1550 nm).

The fabrication process involves EBL, which creates a pattern of nanometer-scale circles [19]. The stages of metasurface fabrication may vary depending on the type of resist used in the EBL process, the required level of fabrication precision, and the presence of additional materials utilised for discharging or cleaning. The fabrication sequence employed in our metasurface development is referred to as the "lift-off" technique, which incorporates the use of an aluminium mask.

The fabricated metasurfaces must be characterised for their reflectivity at specific wavelengths. It is reasonable to conduct measurements across a wide frequency range to determine if the maximum reflectivity aligns with the desired frequency. For this purpose, a white light source is applied in the near-infrared and telecommunications wavelength range to observe spectral reflectivity and the width of the excited resonances.

The experimental behaviour of the metasurfaces is in good agreement with the predictions obtained from the simulations. The methodology presented in the development of the first prototype of a metasurface mirror, along with the obtained results, are detailed in the fourth publication (Section 5.5):

Publication 4

Mariia Matiushechkina, Andrey B. Evlyukhin, Radu Malureanu, Vladimir A. Zenin, Torgom Yezekyan, Andrei Lavrinenko, Sergey I. Bozhevolnyi, Boris N. Chichkov, Michèle Heurs, **"Design and experimental demonstration of wavelength-selective metamirrors on sapphire substrates"**, Advanced Photonics Res. 2400116 (2024). DOI: 10.1002/adpr.202400116.

[19] A pattern of circles becomes a cylindrical array after the etching process.

5.2 Lightweight metasurface mirror of silicon nanospheres

Authors: Andrey B. Evlyukhin, Mariia Matiushechkina, Vladimir A. Zenin, Michèle Heurs, and Boris N. Chichkov

Journal: Optical Materials Express

Article Number: 10, 2706-2716 (2020)

DOI: 10.1364/OME.409311

Author contribution: All authors contributed to the development of the concept for the lightweight metasurface mirror composed of silicon spherical nanoparticles. M.M., under the supervision of A.B.E., delved into the theoretical analysis and assisted A.B.E. in preparing the theoretical framework for the manuscript. A.B.E. performed the analytical calculations. V.A.Z. and M.M. worked on the numerical simulations. M.H. and B.N.C. supervised the project. A.B.E., M.M., and V.A.Z drafted the initial manuscript, while M.H. and B.N.C. verified the results and contributed to the final version of the manuscript. All authors participated in the review process, discussions and critical analysis of the obtained results.

Research Article | Vol. 10, No. 10 / 1 October 2020 / Optical Materials Express 2706
Optical Materials EXPRESS

Lightweight metasurface mirror of silicon nanospheres [Invited]

ANDREY B. EVLYUKHIN,[1] MARIIA MATIUSHECHKINA,[2] VLADIMIR A. ZENIN,[3] MICHÈLE HEURS,[2] AND BORIS N. CHICHKOV[1,*]

[1] Institute of Quantum Optics, Leibniz Universität Hannover, Welfengarten 1, 30167 Hannover, Germany
[2] Institut for Gravitational Physics, Leibniz Universität Hannover, Callinstr. 38, 30167 Hannover, Germany
[3] Center for Nano Optics, University of Southern Denmark, Campusvej 55, 5230 Odense, Denmark
[*] chichkov@iqo.uni-hannover.de

Abstract: Many experiments in modern quantum optics require the implementation of lightweight and near-perfect reflectors for noise reduction and high sensitivity. Another important application of low mass and high reflectivity mirrors is related to the development of solar or laser-driven light sails for acceleration of ultra-light spacecrafts to relativistic velocities. Here, we present numerical results and theoretical analysis of a metasurface mirror consisting of periodically arranged silicon nanospheres embedded in a polymer. In the absence of material losses or disorder, this mirror demonstrates absolute 100% reflection at a single wavelength, which can be tuned by changing nanosphere dimensions or periodicity (for example, by mechanical stretching). We show that high reflectivity can be reached due to electric or magnetic dipole resonant responses of Si nanoparticles in the metasurface. Dependence of mirror reflectivity on surrounding conditions, nanoparticle sizes, and the disorder in the array is studied and discussed. The optimization and simulation procedures presented in this work can be used for the development of other optical devices with functional characteristics determined by the resonant interaction of light with metasurfaces made of nanospheres.

1. Introduction

The growing interest in the ability to create small sensitive detectors of weak mechanical forces and vibrations has stimulated investigations in the fields of optomechanical sensors, cavity optomechanics, and quantum noise reduction devices [1,2]. One of the main optical components in such systems is a low mass and high reflectivity mirror which can be used as a suspended mirror in optical resonators and interferometers. Low mass and high reflectivity mirrors are also required for the realization of solar or laser-driven light sails for acceleration of nano-satellites to relativistic velocities and their exploratory missions to nearby stars and exoplanets [3–5].

For the design and fabrication of such mirrors different optical configurations and materials have been investigated during the last years. One of the approaches in the field of optomechanics is related to the application of artificial metamaterials [6] composed of specially designed building blocks (meta-atoms) determining optical and mechanical properties of the total system and its functional characteristics. In contrast to three-dimensional (3D) metamaterials, which are used for control and manipulation of light in spectral, spatial, and temporal domains, two-dimensional (2D) single layer artificial structures, called metasurfaces, provide unique possibilities for light management and control at the subwavelength scale. In this case, strong light-matter interaction is reached due to resonant optical responses of meta-atoms building the metasurface [7]. For minimisation of light absorption in artificial structures, dielectric high-refractive index nanoparticles are used as building blocks, for example, crystalline silicon nanoparticles with negligibly small absorption in near-infrared. Due to the high refractive index ($n_{\mathrm{Si}} = 3.56$ at $\lambda = 1064$ nm), the sizes of Si nanoparticles supporting the optical resonant response can be n_{Si}-times smaller than the free-space wavelength of light [8]. All these properties

#409311 https://doi.org/10.1364/OME.409311
Journal © 2020 Received 2 Sep 2020; accepted 11 Sep 2020; published 30 Sep 2020

Optical Materials EXPRESS

of silicon nanoparticles make them very promising candidates for the development of ultra-thin metasurfaces with different optical functionalities [9,10].

In this article, we suggest a straightforward design and numerical optimization procedure for a low mass mirror based on the spherical nanoparticle structure that allows to achieve extremely high incident-light reflectivity. This mirror is specially designed for optomechanical applications and the detection of weak physical forces. Note that the same metasurface mirror concept can be used for the realization of light sails. For practical realization of low mass, high reflectivity metasurface mirrors, laser printing of Si nanoparticles is discussed as a promising technology.

The proposed mirror consists of silicon nanoparticles arranged in a 2D subwavelength periodic array embedded in a polymer elastomer layer of polydimethylsiloxane (PDMS). The size of the particles and the distance between them are optimized to achieve maximum reflectivity of the normally incident plane-wave at the near-infrared wavelength of 1064 nm. In this spectral range, silicon and PDMS exhibit negligibly low absorption which allows to use this mirror in experiments where light-induced material heating is undesirable [11,12]. Our metasurface design with only a single layer of nanoparticles allows realization of a thin and lightweight mirror, which is beneficial over multilayer mirrors usually implemented in mechanical resonators [13,14].

The reflection and transmission of the metasurface is analyzed in the framework of excited nanoparticle multipole resonances [15]. It is important to note that the suppression of light transmission is not related to the light absorption, but rather to the destructive interference between incident and resonantly scattered light in the forward direction. Dielectric nanospheres support Mie resonances corresponding to the excitation of their different multipole moments. As will be shown in this article, resonant electric or magnetic dipole scattering can completely cancel the transmission and provide the near-unity reflection for the light at the target wavelength of 1064 nm. How to reach high reflectivity in all-dielectric metamaterial structures has recently been investigated using the effective medium approach (EMA) [16]. In our work we apply a completely different approach, namely direct multipole analysis, which provides an intuitive understanding, a rather good match to the simulations, and simplifies the design optimization for the desired wavelength.

The modelling approach presented in this work is based on full-wave numerical simulations and semi-analytical calculations developed in the framework of the coupled dipole approximation [10]. We show that by tuning the array periodicity, it is always possible to get a near-unity reflectance at a desired light wavelength for any particle diameter within a reasonable range. An estimate of the metasurface mirror robustness to possible imperfections in terms of deviations of nanoparticle sizes and their positions is obtained by numerical simulations. The simulated perfect reflection and suppressed transmission effect by our metasurface mirror agrees well with the coupled dipole model.

In the sections below, basic parameters of the considered mirror system and applied calculation approaches are discussed. Then, the obtained results are demonstrated and analysed. Finally, a short summary of our research is given.

2. Physical model and calculation methods

2.1. Physical system and parameters

Schematic presentation of metasurface considered in this paper is shown in Fig. 1. A periodic 2D array of spherical silicon nanoparticles is placed in a surrounding dielectric matrix with the refractive index n_{d}. The light beam, considered as a monochromatic plane wave with linear polarization, is normally incident along the z-axis of the Cartesian coordinate system illuminating all nanoparticles in the metasurface. The electric field of the incident wave is $\mathbf{E} = (E_x, 0, 0)\exp(ik_{\mathrm{d}}z - i\omega t)$, where k_{d} is the wave number in the surrounding matrix, ω is the angular frequency. In the following, the time dependence $\exp(-i\omega t)$ will be omitted. In our investigations we consider three different surrounding conditions: i) the array is placed in an

Optical Materials EXPRESS

infinite surrounding PDMS matrix with $n_d = 1.45$; ii) the surrounding PDMS matrix occupies only semi-infinite space with the other half-space being air; iii) the nanoparticle array is placed inside a finite size PDMS membrane suspended in air. The refractive index of silicon in the considered near-infrared region (around the target wavelength of 1064 nm) is assumed to be constant $n_{Si} = 3.56$ without any absorption losses [17]. All wavelengths correspond to free space.

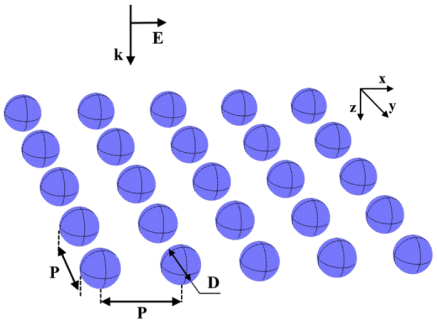

Fig. 1. Schematic view of the considered metasurface, composed of nanospheres, arranged in a square lattice, and definition of basic parameters. The metasurface is irradiated by a plane monochromatic light wave at normal incidence.

2.2. Calculation approaches

In our numerical simulations, the total electric fields and corresponding reflection and transmission spectra in the considered system with spherical nanoparticles, building an infinite-size metasurface, and embedded in a PDMS matrix, are calculated using the finite element method, implemented in the commercial software COMSOL Multiphysics.

For analytical calculations, the coupled dipole approximation (CDA) with the inclusion of only electric and magnetic dipoles is used. Details of this approach are presented elsewhere [10]. Briefly, every particle in the array is considered as a combination of point electric and magnetic dipoles, located at the particle's center. The electric $\mathbf{p}_j$ and magnetic $\mathbf{m}_j$ dipole moments of the j-th particle in the array are determined by the following equations

$$\mathbf{p}_j = \alpha_p \mathbf{E}_{loc}\,, \qquad \mathbf{m}_j = \alpha_m \mathbf{H}_{loc} \tag{1}$$

where $\mathbf{E}_{loc}$ and $\mathbf{H}_{loc}$ are the local electric and magnetic fields, respectively, acting on the particle, including fields of the incident external wave and fields generated by all other particles in the array. The dipole polarizabilities α_p and α_m of a spherical particle can be found from Mie theory [18]. In our case we can write [10]

$$\alpha_p = i\frac{6\pi\varepsilon_0\varepsilon_d}{k_d^3}a_1, \quad \alpha_m = i\frac{6\pi}{k_d^3}b_1,$$

where i is the imaginary unit, ε_0 and $\varepsilon_d = n_d^2$ are the vacuum dielectric constant and the relative dielectric constant of the surrounding matrix, a_1 and b_1 are the corresponding scattering coefficients [18].

Due to the periodicity of the geometry and the external field, all particles in the array have the same electric and magnetic dipole moments. In this case the field reflection r and transmission t coefficients are determined only by the elementary cell area $S_L = P^2$ containing one particle, the incident light wavelength, and the effective electric α_p^{eff} and magnetic α_m^{eff} dipole polarizabilities

Optical Materials EXPRESS

[10]:

$$r = \frac{ik_{\mathrm{d}}}{2S_L}\left[\alpha_p^{\mathrm{eff}} - \alpha_m^{\mathrm{eff}}\right], \tag{2}$$

$$t = 1 + \frac{ik_{\mathrm{d}}}{2S_L}\left[\alpha_p^{\mathrm{eff}} + \alpha_m^{\mathrm{eff}}\right]. \tag{3}$$

The above equations are applicable when the array periods are smaller than the light wavelength in the surrounding matrix and, therefore, light diffraction is absent [10]. It should be noted that when the particle size becomes large, such that higher-order multipole moments are no longer negligible, or when higher accuracy is required, one should include higher-order terms into the above equations [19]. The effective particle polarizabilities are determined by the single particle dipole polarizabilities and interparticle electromagnetic interactions:

$$\alpha_p^{\mathrm{eff}} = \left(\frac{\varepsilon_0\varepsilon_{\mathrm{d}}}{\alpha_p} - S_p\right)^{-1}, \qquad \alpha_m^{\mathrm{eff}} = \left(\frac{1}{\alpha_m} - S_m\right)^{-1}, \tag{4}$$

where S_p and S_m are the lattice dipole sums for electric-electric dipole and magnetic-magnetic dipole interactions, respectively. For arrays with a square elementary cell, $S_m = S_p$ (analytical expressions for S_p and S_m can be found, for example, in [19]).

The intensity reflection R and transmission T coefficients are determined as

$$R = |r|^2, \qquad T = |t|^2. \tag{5}$$

As follows from Eqs. (3) and (5), the necessary (but not sufficient) condition for $T \to 0$ is given by

$$\mathrm{Re}(\alpha_p^{\mathrm{eff}}) = -\mathrm{Re}(\alpha_m^{\mathrm{eff}}). \tag{6}$$

When $\alpha_p^{\mathrm{eff}} = \alpha_m^{\mathrm{eff}}$, the lattice Kerker effect is realized [10,20] and, as follows from Eq. (2), the reflection is absent.

3. Results and discussion

3.1. Basic configurations

The final goal of our investigations is the realization of a metasurface mirror with strong reflection at a certain incident wavelength $\lambda = 1064$ nm (in vacuum), chosen due to the availability of powerful and ultra-stable lasers at this wavelength. Using facilities of COMSOL Multiphysics, the intensity reflection and transmission coefficients for infinite Si-nanoparticle arrays embedded in surrounding PDMS ($n_{\mathrm{d}} = 1.45$) are calculated as a function of the particle diameter D and the array period P (the array geometry is shown in Fig. 1). Results of the full-wave simulations are demonstrated in Fig. 2.

In Fig. 2(a) one can see that the reflection coefficient R can approach unity for almost any particle diameter D, when the array period P is optimum. Since there are no absorption losses in the system, meaning $R + T = 1$, the proximity of R to 1 can be derived from the proximity of T to 0. Moreover, the absence of losses allows reaching absolute 0 and 1 for R and T at the desired wavelength (Fig. 2).

Even though the system is quite simple (dielectric spheres, arranged in a square lattice), it allows different operation regimes, among which we highlighted two [see circles in Fig. 2(a,b) and corresponding spectra in Fig. 2(c)]. When the particle diameter is $D = 248$ nm and periodicity $P = 719$ nm (point #1), there is a close spectral proximity between suppressed reflection and suppressed transmission. Therefore, one can exploit such a configuration for modulation applications, for example, by stretching the array, heating it, or changing the incident wavelength. Another interesting point (point #2) is selected where the change of the sphere diameter does not

Optical Materials EXPRESS

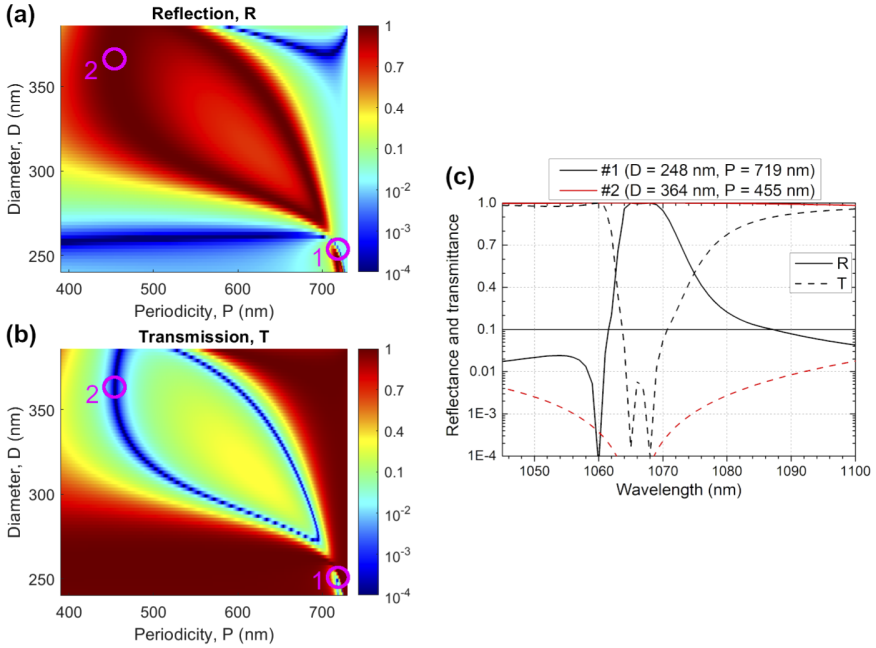

Fig. 2. (a) Reflection and (b) transmission coefficients of metasurfaces calculated as a function of the particle diameter and the array period. The surrounding matrix is PDMS with the refractive index 1.45. Irradiation conditions are the same as shown in Fig. 1, with the free-space wavelength of 1064 nm. Note hybrid colormap scale, used to enhance the perception of values near zero and 1. (c) Reflection and transmission spectra of metasurfaces for two selected sets of parameters (P and D), particularly promising for modulation (black, point #1), broadband reflector (red, point #2).

influence the reflection and transmission. It appeared that for this configuration our metasurface behaves as a broadband near-perfect reflector.

Even though broadband operation (point #2) could be advantageous for our goal, the realistic fabrication of such structures might be extremely difficult due to the proximity of particle diameter to the periodicity. Therefore, we have chosen realistic configurations with a particle diameter of $D = 290$ nm and two array periodicities: $P = 602$ nm and $P = 686$ nm, both featuring complete reflection at the free-space wavelength of 1064 nm (Fig. 3).

In order to clarify physical mechanisms responsible for such high reflection, we apply the CDA described above. The silicon nanoparticles in metasurface arrays are considered as point electric and magnetic dipoles with moments defined by the corresponding polarizabilities. In Fig. 3, the reflection and transmission spectra calculated by analytical and numerical methods are presented. One can see that the CDA provides reasonably good agreement in the reflection and transmission spectra with the numerical simulations. In both cases, high reflection is reached at the same wavelength of 1064 nm. In the CDA the reflection and transmission coefficients [Eqs. (2) and (3)] are determined by the effective polarizabilities [Eq. (4)]. Their spectral behaviour is shown in Fig. 4. For the period $P = 602$ nm [see Fig. 4(a)], the magnetic dipole effective polarizability α_m^{eff} has a broad resonance at the wavelength $\lambda \approx 1075$ nm. As a result, α_m^{eff} gives the main contribution into the coefficients r and t and is responsible for the transmission suppression. The non-resonant contribution of α_p^{eff} only provides an additional small spectral tuning of the reflection maximum to $\lambda \approx 1064$ nm, owing to the necessary condition of Eq. (6). For better visualization, the $\text{Re}(\alpha_m^{\text{eff}})$ is plotted with a negative sign, and the crossing with $\text{Re}(\alpha_e^{\text{eff}})$, highlighted with a

Optical Materials EXPRESS

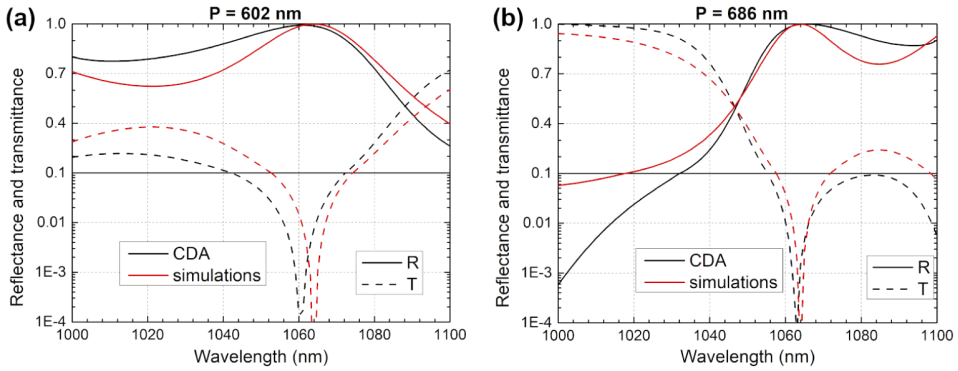

Fig. 3. Comparison between the coupled dipole approximation (CDA) and full-wave numerical simulations, applied to calculate the reflection and transmission spectra for the metasurface with diameter of silicon nanospheres D = 290 nm and periodicity (a) P = 602 nm and (b) P = 686 nm. Irradiation conditions are shown in Fig. 1.

green circle in Fig. 4(a), indicates where this condition is satisfied. It should be noted that the condition of Eq. (6) is also satisfied in another point (at $\lambda \approx 1025$ nm), but there is no total suppression of the transmission at this point, because, as mentioned before, the condition of Eq. (6) is not sufficient.

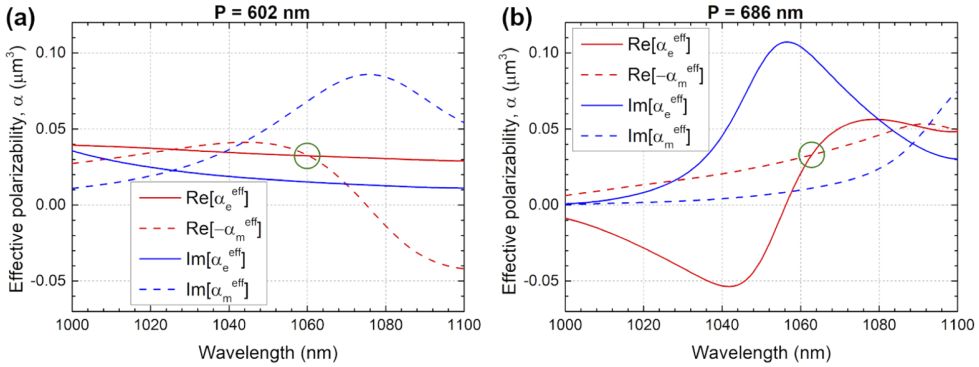

Fig. 4. Effective electric and magnetic dipole polarizabilities, calculated using the coupled dipole approximation for the metasurface arrays with the periods (a) P = 602 nm and (b) P = 686 nm, assuming the nanoparticle diameter D = 290 nm. Green circles indicate the points, where the condition for the complete suppression of transmission [Eq. (6)] is fulfilled.

For the larger period P = 686 nm [see Fig. 4(b)], the electric dipole effective polarizability α_p^{eff} has a resonance at $\lambda \approx 1055$ nm and provides the main contribution into the reflection, whereas the non-resonant contribution of α_m^{eff} slightly corrects the spectral position of the reflection maximum according to the condition of Eq. (6). The green circle in Fig. 3(b) indicates where $\text{Re}(\alpha_p^{\text{eff}}) = -\text{Re}(\alpha_m^{\text{eff}})$. Thus, both magnetic and electric dipole moments, being resonantly excited, can be responsible for the total suppression of the transmission through the metasurfaces. Moreover, each region with the suppressed transmission in Fig. 2(b) can be associated to either electric or magnetic dipole near-resonant excitation. When these two curves are expected to cross (at $D \approx 260$ nm and $P \approx 710$ nm), the perfect reflection is lost and replaced with the perfect transmission. Explanation of this reflection suppression follows from the lattice Kerker effect [10,20]: when the effective electric and magnetic dipole polarizabilities of nanoparticles are

Optical Materials EXPRESS

equal to each other, the reflection is significantly suppressed, because every nanoparticle in the array does not scatter the incident wave into the backward direction [21]. Directly it can be seen from Eq. (2): when $\alpha_p^{\text{eff}} = \alpha_m^{\text{eff}}$, the reflection coefficient $r = 0$. Note that, despite transparency of the metasurface, the polarizabilities of each particle is not zero in this case, but rather resonant, which could be beneficial for non-invasive sensing or non-linear optical applications.

So far we considered that the metasurfaces are embedded in an infinite homogeneous medium (PDMS) with the refractive index of 1.45. However, the near-unity reflection can be also realized when the PDMS surrounding is limited from one or both sides (Fig. 5). Similar to a homogeneous environment (Fig. 2), strong reflection is realized for certain values of the nanoparticle diameter and the array period. Due to the high refractive index contrast of particles relative to the PDMS and air, the partial substitution of PDMS with air does not significantly influence the reflection and transmission, which can be compensated by slightly changing the periodicity of the array in order to reach perfect reflection at 1064 nm. Thus, our perfect metasurface mirror can be extremely lightweight, when Si nanospheres are embedded in thin PDMS membrane [Fig. 5(b)]. When the mirror of the same weight is realized as a silver mirror, its thickness is as low as 30 nm. Since this is close to the skin depth of silver (which is ≈ 24 nm at the wavelength of 1064 nm), the expected reflectivity of such mirror is only ~ 95%.

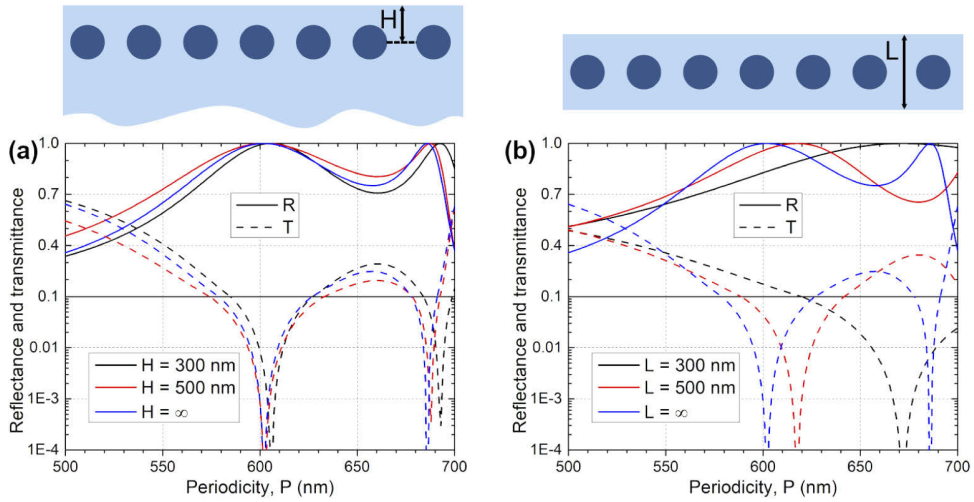

Fig. 5. Reflection and transmission coefficients of metasurface arrays, embedded in PDMS (a) semi-infinite space at different depths H and (b) membrane of finite thickness T (see inserts) as a function of periodicity. All nanoparticles have the same diameter of 290 nm. Irradiation conditions are shown in Fig. 1 and the vacuum wavelength of incident light is 1064 nm.

3.2. *Influence of imperfections*

In real experimental situations arrays of nanoparticles include some structural imperfections related to deviations of the particle sizes and their positions from certain average values. In order to investigate the sensitivity of the reflection coefficient to this type of imperfections we simulate reflection from the infinite metasurface arrays with an elementary cell containing four nanoparicles (Fig. 6). The sizes of the nanoparticles can randomly deviate from the average diameter D = 290 nm [Fig. 6(a)]. Additionally, the positions of the nanoparticles in the cell can also randomly deviate from the positions corresponding to perfect periodicity in an ideal array [Fig. 6(b)].

Optical Materials EXPRESS

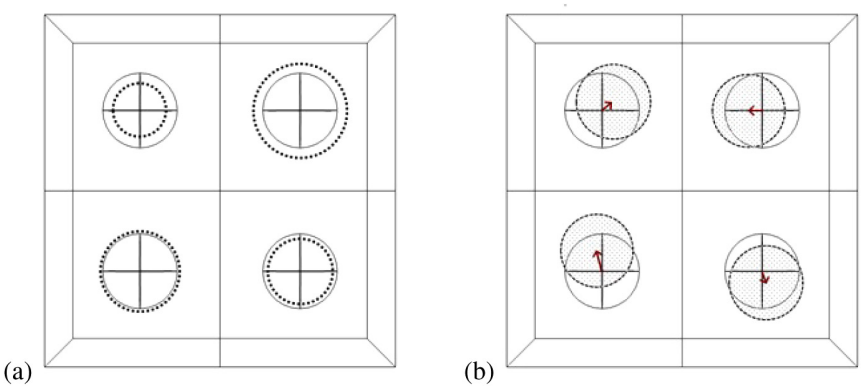

Fig. 6. Schematic presentation of the considered metasurface imperfections. Single elementary cell of periodic arrays with deviations of (a) particle sizes and (b) particle positions from perfect values.

To estimate the decrease in reflectivity, the metasurface structure with an elementary cell consisting of 4 nanoparticles was modelled and simulated using the software COMSOL Multiphysics in combination with Java code. The implementation of two programs allowed to generate random geometry and accumulate the required statistics. Our simulations show that for the maximal random deviation $\Delta D = 5$ nm from the diameter $D = 290$ nm the average value of the reflection coefficient R is equal to 0.9831 which corresponds to a 1.7% deviation from the ideal case. The random position deviations lead to a reduction of the reflection coefficient which is strongly dependent on the value of the maximum deviation. If the maximum position deviation is 20 nm (3.3% of the period of the ideal array) the reflection coefficient is reduced by 1.5% from the ideal

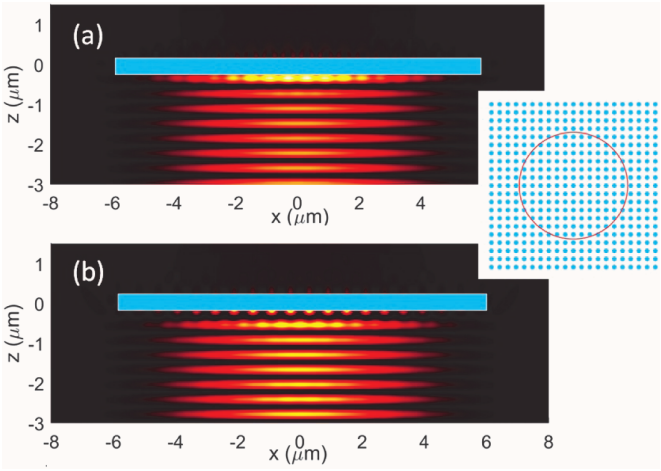

Fig. 7. Strong reflection effect for a Gaussian beam impinging on the finite-size Si nanoparticle metasurface. (a) Intensity of the total electric and (b) magnetic fields calculated in the framework of the CDA [10]. The Gaussian beam (radius of waist is 5 μm) propagates along the z-axis with E-polarization along the x-axis. Position of the metasurface is schematically shown by the blue blocks in (a) and (b). Insert picture demonstrates the nanoparticle structure, and the region inside the red circle is irradiated by the light beam. Parameters: $\lambda = 1064$ nm; $n_{\mathrm{d}} = 1.45$; $P = 600$ nm; $D = 290$ nm.

Optical Materials EXPRESS

case. However, increasing the maximum deviation up to 6.7% from the period of the ideal array, the reflection coefficient decreases by 18%.

The obtained results and additional simulations carried out in the CDA for a finite-size metasurface structure are shown in Fig. 7. They demonstrate good practical potential of the silicon nanoparticle arrays for the development of ultra-thin and ultra-low mass optical mirrors for optomechanical applications.

4. Practical realization

For practical realization of metasurface mirrors made of Si nanospheres, we plan to apply laser printing technology [22] schematically illustrated in Fig. 8. By illumination of a 50 nm crystalline Si donor layer coated on a glass substrate with a single tightly-focused Gaussian femtosecond laser pulse, absorption in the Si layer leads to ultrafast heating and local melting of this layer. At sufficiently high laser pulse energies, the 50 nm Si layer melts completely, forming a nanodroplet, induced by the surface tension. This nanodroplet formation is accompanied by the motion of its centre-of-mass, driving this droplet towards the PDMS layer on the receiver substrate. During the flight and later contact with the receiver substrate, the nanodroplet will be cooled down and crystallized in the form of spherical nanoparticles. One can vary the nanoparticle diameter by simply changing the laser pulse energy [22]. Due to our preliminary experiments we know that laser printed nanoparticles will be embedded in the PDMS layer. The described process will be performed in air at atmospheric pressure and the distance between the receiver and donor substrates will be set at approximately 10 micrometers. After all nanoparticles are printed, the PDMS layer with the laser printed nanoparticles will be detached from the glass substrate, producing the desired stretchable membrane, acting as a low mass and high reflectivity metasurface mirror.

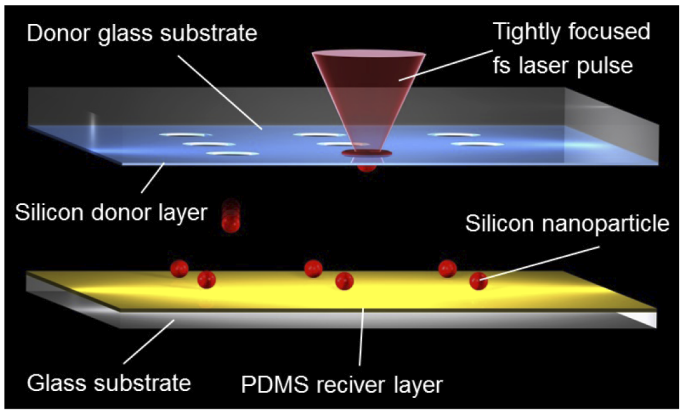

Fig. 8. Schematic illustration of femtosecond laser printing of Si nanoparticles. A 50 nm crystalline Si layer on donor glass substrate wafer is used as a target (irradiated by single laser pulses) to generate and transfer spherical Si nanoparticles onto the PDMS layer.

For fabrication of large mirror arrays, the Si donor layer can be lithographically pre-patterned in the form of periodic circular islands at the required distance between them. In this case many such islands can be melted and transferred by a single laser pulse. This technique has been tested and described in our previous publications [23,24].

Optical Materials EXPRESS

5. Conclusion

In this paper, numerical and analytical calculation methods have been applied for investigations of reflection properties of 2D metasurface arrays, composed of spherical silicon nanoparticles, arranged in a square lattice. Using numerical simulations we have found certain particle sizes and array periods, for which a near-unity reflectivity is achieved for the target near-infrared light wavelength of 1064 nm. It has been shown that the optical response of our metasurface mirror is only weakly influenced by the surrounding conditions, and this influence can be compensated by small adjustments of the periodicity in order to reach perfect reflection at the target wavelength. This allows for realization of perfect and extremely lightweight metasurface mirrors in the form of Si nanoparticles embedded into a polymer membrane. The optical response of the metasurface is explained with analytical coupled dipole approximation, whose results agree well with numerical simulations. Finally, we complited our study by checking the robustness of the real metasurface to possible disorder in terms of random variation in particle size and position.

These mirrors can also be applied as solar or laser-driven light sails for acceleration of ultra-light space craft to relativistic velocities. Practical realization of such metasurface mirrors by laser printing of Si nanoparticles [22] has been discussed.

Funding

Villum Fonden (16498); Deutsche Forschungsgemeinschaft (EXC 2122, Project ID 390833453, EXC 2123, Project ID 390837967).

Acknowledgments

The authors acknowledge financial support from the Deutsche Forschungsgemeinschaft (DFG, German Research Foundation) under Germany's Excellence Strategy within the Cluster of Excellence PhoenixD (EXC 2122, Project ID 390833453) and the Cluster of Excellence QuantumFrontiers (EXC 2123, Project ID 390837967). V.A.Z. acknowledges financial support from Villum Fonden (Grant No. 16498). The analytical analysis has been supported by the Russian Science Foundation Grant No. 20-12-00343.

Disclosures

The authors declare that there are no conflicts of interest related to this article.

References

1. M. Aspelmeyer, T. J. Kippenberg, and F. Marquardt, "Cavity Optomechanics," Rev. Mod. Phys. **86**(4), 1391–1452 (2014).
2. J. Rui, D. Wei, A. Rubio-Abadal, S. Hollerith, J. Zeiher, D. M. Stamper-Kurn, C. Gross, and I. Bloch, "A subradiant optical mirror formed by a single structured atomic layer," Nature **583**(7816), 369–374 (2020).
3. H. A. Atwater, A. R. Davoyan, O. Ilic, D. Jariwala, M. C. Sherrott, C. M. Went, W. S. Whitney, and J. Wong, "Materials challenges for the Starshot lightsail," Nat. Mater. **17**(10), 861–867 (2018).
4. O. Ilic and H. A. Atwater, "Self-stabilizing photonic levitation and propulsion of nanostructured macroscopic objects," Nat. Photonics **13**(4), 289–295 (2019).
5. M. M. Salary and H. Mosallaei, "Photonic metasurfaces as relativistic light sails for Doppler-broadened stable beam-riding and radiative cooling," Laser Photonics Rev. **14**(8), 1900311 (2020).
6. M. A. Noginov and V. A. Podolskiy, *Tutorials in Metamaterials* (CRC Press, 2011).
7. A. E. Minovich, A. E. Miroshnichenko, A. Y. Bykov, T. V. Murzina, D. N. Neshev, and Y. S. Kivshar, "Functional and nonlinear optical metasurfaces," Laser Photonics Rev. **9**(2), 195–213 (2015).
8. A. B. Evlyukhin, S. M. Novikov, U. Zywietz, R. L. Eriksen, C. Reinhardt, S. I. Bozhevolnyi, and B. N. Chichkov, "Demonstration of magnetic dipole resonances of dielectric nanospheres in the visible region," Nano Lett. **12**(7), 3749–3755 (2012).
9. I. Staude and J. Schilling, "Metamaterial-inspired silicon nanophotonics," Nat. Photonics **11**(5), 274–284 (2017).
10. A. B. Evlyukhin, C. Reinhardt, A. Seidel, B. S. Luk'yanchuk, and B. N. Chichkov, "Optical response features of Si-nanoparticle arrays," Phys. Rev. B **82**(4), 045404 (2010).

Optical Materials EXPRESS

11. S. Mancini, V. I. Man'ko, and P. Tombesi, "Ponderomotive control of quantum macroscopic coherence," Phys. Rev. A **55**(4), 3042–3050 (1997).
12. J. D. Thompson, B. M. Zwickl, A. M. Jayich, F. Marquardt, S. M. Girvin, and J. G. E. Harris, "Strong dispersive coupling of a high-finesse cavity to a micromechanical membrane," Nature **452**(7183), 72–75 (2008).
13. J. Steinlechner, I. W. Martin, A. S. Bell, J. Hough, M. Fletcher, P. G. Murray, R. Robie, S. Rowan, and R. Schnabel, "Silicon-based optical mirror coatings for ultrahigh precision metrology and sensing," Phys. Rev. Lett. **120**(26), 263602 (2018).
14. S. Reid and I. W. Martin, "Development of mirror coatings for Gravitational wave detectors," Coatings **6**(4), 61 (2016).
15. V. E. Babicheva and A. B. Evlyukhin, "Resonant suppression of light transmission in high-refractive-index nanoparticle metasurfaces," Opt. Lett. **43**(21), 5186–5189 (2018).
16. B. Slovick, Z. G. Yu, M. Berding, and S. Krishnamurthy, "Perfect dielectric-metamaterial reflector," Phys. Rev. B **88**(16), 165116 (2013).
17. E. Palik, *Handbook of Optical Constant of Solids* (Academic, 1985).
18. C. F. Bohren and D. R. Huffman, *Absorption and Scattering of Light by Small Particles* (Wiley, 1983).
19. V. E. Babicheva and A. B. Evlyukhin, "Analytical model of resonant electromagnetic dipole-quadrupole coupling in nanoparticle arrays," Phys. Rev. B **99**(19), 195444 (2019).
20. V. E. Babicheva and A. B. Evlyukhin, "Resonant lattice Kerker effect in metasurfaces with electric and magnetic optical responses," Laser Photonics Rev. **11**(6), 1700132 (2017).
21. M. Kerker, D. Wang, and C. Giles, "Electromagnetic scattering by magnetic spheres," J. Opt. Soc. Am. **73**(6), 765–767 (1983).
22. U. Zywietz, A. B. Evlyukhin, C. Reinhardt, and B. N. Chichkov, "Laser printing of silicon nanoparticles with resonant optical electric and magnetic responses," Nat. Commun. **5**(1), 3402 (2014).
23. A. I. Kuznetsov, A. B. Evlyukhin, M. R. Gonçalves, C. Reinhardt, A. Koroleva, M. L. Arnedillo, R. Kiyan, O. Marti, and B. N. Chichkov, "Laser fabrication of large-scale nanoparticle arrays for sensing applications," ACS Nano **5**(6), 4843–4849 (2011).
24. A. I. Aristov, U. Zywietz, A. B. Evlyukhin, C. Reinhardt, B. N. Chichkov, and A. V. Kabashin, "Laser-ablative engineering of phase singularities in plasmonic metamaterial arrays for biosensing applications," Appl. Phys. Lett. **104**(7), 071101 (2014).

5.3 High-efficiency silicon metasurface mirror on a sapphire substrate

Authors: Mariia Matiushechkina, Andrey B. Evlyukhin, Vladimir A. Zenin, Michèle Heurs, Boris N. Chichkov

Journal: Optical Materials

Article Number: 138, 113618 (2023)

DOI: 10.1016/j.optmat.2023.113618

Author contribution: All authors devised the conceptual idea. M.M., V.A.Z., A.B.E. build up, performed and analysed computational research. M.H. and B.N.C. supervised and assisted the project. M.M. created the figures. M.M., A.B.E, and V.A.Z. drafted the initial manuscript, while M.H. and B.N.C. reviewed and provided feedback on the content. All authors actively participated in discussions, offered feedback, and contributed to the preparation of the manuscript.

Optical Materials 138 (2023) 113618

Contents lists available at ScienceDirect

Optical Materials

journal homepage: www.elsevier.com/locate/optmat

Research article

High-efficiency silicon metasurface mirror on a sapphire substrate

Mariia Matiushechkina [a,c,*], Andrey B. Evlyukhin [b,c,**], Vladimir A. Zenin [d], Michèle Heurs [a,c], Boris N. Chichkov [b,c]

[a] Institute for Gravitational Physics, Leibniz University Hannover, Callinstr. 38, Hannover 30167, Germany
[b] Institute of Quantum Optics, Leibniz University Hannover, Welfengarten 1, Hannover 30167, Germany
[c] Cluster of Excellence PhoenixD, Leibniz University Hannover, Welfengarten 1A, Hannover 30167, Germany
[d] Center for Nano Optics, University of Southern Denmark, Campusvej 55, Odense 5230, Denmark

ARTICLE INFO

Keywords:
Metasurface
Silicon nano-coating for telecom wavelength
Optics in gravitational wave interferometers

ABSTRACT

For a possible implementation of high-efficiency Si-nanosphere metasurface mirrors functioning at telecom wavelengths in future gravitational wave detectors, exact dimensional and configuration parameters of the total system, including substrate and protective coating, have to be determined a priori. The reflectivity of such multi-layer metasurfaces with embedded Si nanoparticles and their potential limitations need to be investigated. Here we present the results on how the substrate and protective layer influence optical properties and demonstrate how dimensional and material characteristics of the structure alter light reflectivity. Additionally, we consider the impact of manufacturing imperfections, such as fluctuations of Si nanoparticle sizes and their exact placement, on the metasurface reflectivity. Finally, we demonstrate how high reflectivity of the system can be preserved under variations of the protective layer thickness, incident angle of light, and its polarization.

1. Introduction

Investigations of resonant optical properties of silicon nanoparticles have received significant attention during the last decade [1–4]. Due to the high refractive index, silicon nanoparticles can support electric and magnetic types of multipole resonances [5]. It is important to note that the respective spectral positions of the electric and magnetic multipole resonances can be controlled by specifying the particle shape, irradiation conditions, or by arranging the nanoparticles into special periodic structures [6–8]. In these cases, excitation of different multipole resonances and their overlap in specified spectral ranges can be used to monitor and control the process of light scattering, including its intensity and radiation pattern. These possibilities provide interesting applications of silicon nanoparticles for the realization of compact optical devices with tailored functional properties. It has been shown that by using 2D arrays of disk-like silicon nanoparticles it is possible to make Huygens metasurfaces [9,10]. Such metasurfaces exhibit total transmission at resonant conditions due to interference between the scattered fields generated by the resonant electric and magnetic dipole moments of nanoparticles. A similar effect (full resonant transmission) can be realized in metasurfaces consisting of spherical silicon nanoparticles [11]. The effect of full reflectance is observed when the structure is tuned only to one of the dipole resonances [12]. Destructive interference between the scattered and incident light fields prevents the beam from propagating through the structure, and so due to energy conservation, the total light field is reflected back. Using this property of high-reflectivity and varying the combinations of materials and geometric parameters, the technology is improving in areas such as wireless telecommunication, wavefront manipulation and high-quality imaging [13–16].

Crystalline silicon has a negligibly weak light absorption in the near infrared range. For this reason, metasurfaces of silicon nanoparticles have been proposed for the implementation of highly efficient optical mirrors [17]. It has been shown that periodic arrays of spherical silicon nanoparticles can demonstrate full suppression of light transmission and provide almost 100% reflection at the resonant electric or magnetic dipole conditions. In recent publications [18,19] it has been shown how an array of silicon nanospheres in a homogeneous medium can act as a high-reflective mirror at specified wavelengths. Such mirrors have a range of advantageous characteristics (e.g., ultra-compact, lightweight, and robust) that make them very attractive for precision metrology and specialized applications. In particular, these mirrors can be used in the field of modern quantum optics as a part of an optical cavity, a photodetector or other devices [20–22]. Moreover, their potential suitability is currently being investigated as an alternative high-reflective

* Corresponding author at: Institute for Gravitational Physics, Leibniz University Hannover, Callinstr. 38, Hannover 30167, Germany.
** Corresponding author.
E-mail addresses: mariia.matiushechkina@aei.mpg.de (M. Matiushechkina), a.b.evlyukhin@daad-alumni.de (A.B. Evlyukhin).

https://doi.org/10.1016/j.optmat.2023.113618
Received 9 November 2022; Received in revised form 16 February 2023; Accepted 19 February 2023
Available online 2 March 2023

coating for mirrors in next-generation interferometric gravitational wave observatories.

With the potential laser beam operation wavelength of 1550 nm, the cavity optics of the gravitational wave interferometers will be made from the materials like sapphire or silicon [23,24]. The choice of coating is still under discussion. The requirements to be fulfilled are low optical and mechanical losses. The reflectance for different mirrors can vary in the range of absolute to partial reflection. Current dielectric coatings have excellent optical and extremely good mechanical properties. However, the internal friction between the layers of different amorphous oxides, in combination with the thermal noise from each individual layer, generates one of the limiting displacement noises [25–27]. Moreover, the thickness of such coatings is in the range of 2 to 6 micrometers. We propose an alternative idea of using a metastructure, in particular a metasurface, as a coating for the optics in future gravitational wave detectors. The metasurface has several advantages: The thickness of the structure is on the nanometer scale. Moreover, high reflectance is achieved by using only one layer of nanoparticles avoiding contact between several different material layers and therefore promising lower mechanical loss.

This article reports on our work towards the development of silicon nanosphere metasurface mirror at 1550 nm wavelength for potential implementation in next-generation gravitational wave detectors. Building on our previous studies that demonstrated the absolute 100% reflection at a single wavelength of the metasurfaces located in a homogeneous and isotropic environment [19], in this article we investigate the influence of multi-layer inhomogeneous media, including substrate and protective coating, on the reflective properties of the metasurfaces. With the knowledge that the substrate material below and a material layer in-between the nanoparticle array can change the optical properties of the whole structure [28–32], we perform a detailed numerical analysis of the induced effects. The proposed design of the metasurface is taken as a periodic construction of silicon nanospheres placed on a sapphire substrate and embedded in a protective layer (PL) with a certain refractive index. We demonstrate that the presence of the sapphire substrate does not deteriorate high reflection of light from the metasurface at a fixed wavelength; however, the protective layer shifts the parameters of perfect resonant condition and therefore, has to be taken into account before the fabrication process. Detailed modeling is performed to determine the optimum dimensional parameters of the metasurface that provide high reflection of light at the wavelength of 1550 nm. Moreover, we test the robustness of the metasurface mirror to possible imperfections (deviations in the size of nanoparticles and their positions).

2. Model of the structure and physical description

2.1. Main parameters and configuration

The geometrical configuration of the structure is presented in Fig. 1 as an array of nanospheres placed on a sapphire substrate. The spheres have a fixed diameter (D) and are placed at equal distances from each other (periodicity P). They touch the substrate only at one point and can be embedded in an additional protective layer with thickness (h).

The choice of materials is motivated by the chosen wavelength of 1550 nm of the incident light, which is considered to be a linearly polarized plane wave incident perpendicular to the structure. Considering optical and mechanical properties, we selected Si as a high refractive index material for the realization of the nanoparticle array. Note that for Si, the absorption of infrared light at wavelengths around 1550 nm is negligible. Sapphire was chosen as the substrate material as one of the material candidates for use in gravitational wave detectors. In contrast to Si, sapphire has low refractive index and therefore has less impact on the metasurface behavior. A suitable material for the embedding protective layer (PL) is still under discussion. However, the necessity of using of such a layer is obvious, as the nanostructure needs

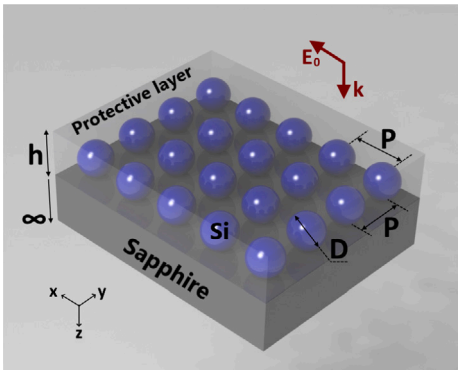

Fig. 1. Schematic view of silicon nanospheres forming a periodic structure (metasurface) on top of a sapphire substrate, embedded in a protective layer. Each nanosphere has a fixed diameter (D) and is placed with distance P (periodicity) in x- and y-directions to the neighboring spheres. The metasurface is irradiated by a plane monochromatic light wave under normal incidence with respect to the metasurface plane: $\mathbf{E}_0$ and $\mathbf{k}$ are the electric field and the wave vector, respectively.

to be shielded from any kind of damage. The minimum requirement is that it should have minimal absorption (i.e. be relatively transparent) for the light, and that its contribution to the mechanical noise should be low. One of the prospective materials to be used is fused silica with a refractive index of 1.4 at 1550 nm wavelength. In order to implement a metasurface mirror in future gravitational wave detectors, all of the materials of the mirror should exhibit high mechanical quality factor. The mechanical quality factor of sapphire is higher than 10^9 [33]. For silicon, a significant reduction of thermo-elastic noise and consequently a high mechanical quality factor have been demonstrated at temperatures of 123 K and 18 K [34]. In this article, the operation of the modeled nanostructure is considered at room temperature.

2.2. Numerical approach

The fundamental behavior of a metasurface is based on the process of Mie-scattering [35]. The theoretical description and calculation approaches for the silicon metasurface mirror in a homogeneous PDMS layer were discussed here [19]. In this article, we get closer to the realistic case, where we consider Si nanoparticles on a sapphire substrate embedded in an additional layer to protect the nanostructure from mechanical damage. The theoretical interpretation of the multiple medium model is more complicated due to the additional transmission and reflection terms induced by the Fabry–Perot effect in the sapphire substrate and the embedding layer, which are responsible for the alteration of the results for the nanoparticle structure in a homogeneous surrounding. At the same time, the physical origin of optical reflectance is still based on Mie-scattering. To model the nanostructure and to simulate its behavior under various geometrical and material parameters, including imperfection effects, we use the commercial simulation software COMSOL Multiphysics. The computational process is based on the finite element method, which allows for analysis of the system with multiple modifications. The configuration, size, material parameters and irradiation conditions used in numerical simulations are indicated in this subsection and 2.1. Parameters for imperfection simulations are provided in the following Section 3.2.

First of all, we investigate the array of Si nanoparticles (refractive index $n_{Si} = 3.48$) located in air and placed on a sapphire substrate ($n_{sub} = 1.75$). Secondly, we study the case when this nanoparticle array is embedded in a protective layer (refractive index $n_{PL} = 1.4$) with the thickness equal to the nanoparticle diameter. Fig. 2 shows the intensity reflection coefficients calculated as a function of the nanoparticle diameter (D) and the array periodicity (P) for both cases and for a normal incident plane wave with the wavelength of 1550 nm. The

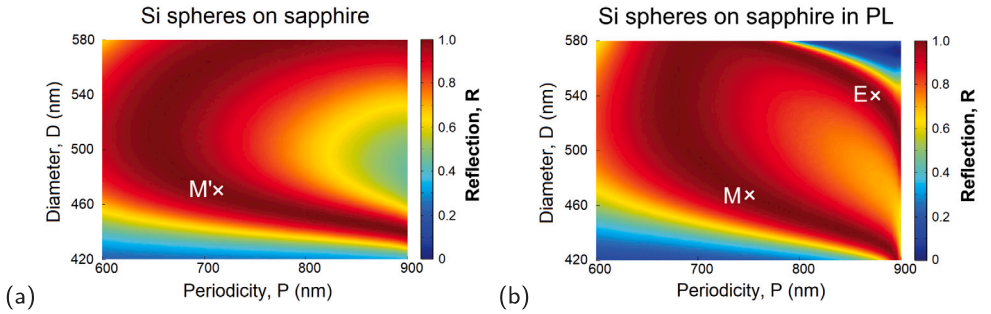

Fig. 2. Intensity reflection coefficients of metasurface calculated as a function of the nanoparticle diameter (D) and its periodicity (P). (a) Si spheres are placed on a sapphire substrate without a protective layer. (b) Si spheres are placed on a sapphire substrate and embedded in a protective layer with the refractive index $n_{PL} = 1.4$. The structure is irradiated by a plane monochromatic wave at normal angle of incidence. The marked points M'×, M× and E× indicate the parameters (D, P) for the structures discussed in the text below.

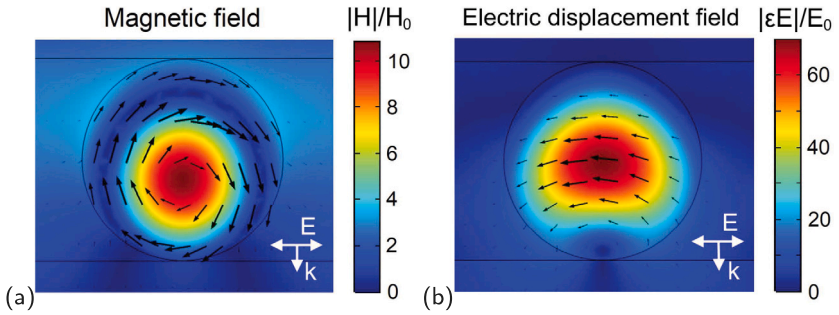

Fig. 3. Color map of (a) magnetic field distribution for M× point with $D = 468$ nm; $P = 750$ nm and (b) electric displacement field for E× point with $D = 540$ nm; $P = 874$ nm, normalized at the values of the magnetic H_0 and electric E_0 fields of the incident plane wave, respectively. Direction and magnitude of the electric current densities are shown by black arrows in both images.

maximum value of the period variation should be smaller than 885 nm (λ/n_{sub}) to exclude diffraction effects into the sapphire substrate [36]. The dark red zone corresponds to a reflection of almost 100%. From a comparison of the results in Fig. 2a and Fig. 2b, it can be seen that the inclusion of the protective layer leads only to a shift of the zone with maximum (~ 100%) reflection (dark red areas) with regard to the design parameters (diameter and periodicity).

To elucidate the physical cause of almost ideal reflection, let us consider the field distributions in metasurface nanoparticles for cases when the reflection coefficient approaches 1. Fig. 3 presents the magnetic (a) and electric (b) fields inside Si nanoparticles calculated for the parameters corresponding to the marked points M× and E× in Fig. 2b, respectively. For the point M×, the strong magnetic field is generated at the center of the Si nanoparticles (Fig. 3a), while for the other point E×, we observe at the center the strong electric displacement field (Fig. 3b). Note that such field distributions correspond to the magnetic and electric dipole resonant responses [37], respectively. Thus, we can conclude that almost ideal reflection is realized due to the resonant excitation of magnetic or electric dipole moments of Si nanoparticles. At these conditions every nanoparticle of the metasurface generates strong secondary waves which destructively interfere with incident waves in the transmission direction resulting in the suppression of total transmission and the realization of a perfect metamirror.

It is important to note that in the case of a homogeneous environment, perfect reflection can also be obtained due to resonant excitation of a certain multipole moment of metasurface nanoparticles (a detailed discussion of this question may be found elsewhere [38]). In our previous paper [19], the perfect reflection effect in the framework of the coupled dipole approximation (CDA) has been theoretically proven. In the CDA approach the reflection R and transmission T coefficients of a metasurface located in a homogeneous medium and composed of dipole nanospheres are determined by the nanosphere effective magnetic α_m^{eff} and electric α_p^{eff} dipole polarizabilities [39]

$$R = \frac{k_d^2}{4S_L^2}\left([\mathrm{Re}(\alpha_p^{\text{eff}}) - \mathrm{Re}(\alpha_m^{\text{eff}})]^2 + [\mathrm{Im}(\alpha_p^{\text{eff}}) - \mathrm{Im}(\alpha_m^{\text{eff}})]^2\right), \quad (1)$$

$$T = \left(1 - \frac{k_d}{2S_L}[\mathrm{Im}(\alpha_p^{\text{eff}}) + \mathrm{Im}(\alpha_m^{\text{eff}})]\right)^2 + \frac{k_d^2}{4S_L^2}[\mathrm{Re}(\alpha_p^{\text{eff}}) - \mathrm{Re}(\alpha_m^{\text{eff}})]^2, \quad (2)$$

where k_d is the wave number in the surrounding medium, $S_L = P^2$ is the elementary cell area defined as a square of periodicity. In [18,19], using Eqs. (1) and (2), it has been demonstrated that perfect reflection can be reached at the electric or magnetic dipole resonances.

The presence of the sapphire substrate and the protective layer do not prevent the realization of perfect reflection due to the magnetic or electric dipole resonances of Si nanospheres. The existence of the sapphire substrate results in modification of the dimensional parameters (compared to the case of a homogeneous environment) corresponding to ideal reflection. A more thorough analysis of a multi-layer medium with different refractive indices will be considered in the next section.

3. Results and discussion

3.1. Substrate and embedding layer impact

First, we consider a model when the particles are located in air and placed on dielectric substrates with different refractive indices (RI). At the condition of the magnetic dipole resonance marked as the point M'× in Fig. 2a, the changes of the substrate RI within the range from 1.65 to 1.85 do not affect the optimal metasurface period for perfect reflection (Fig. 4a). Substrates with higher refractive indices are not considered in this paper in order to exclude a discussion of diffraction effects introduced by the substrate material.

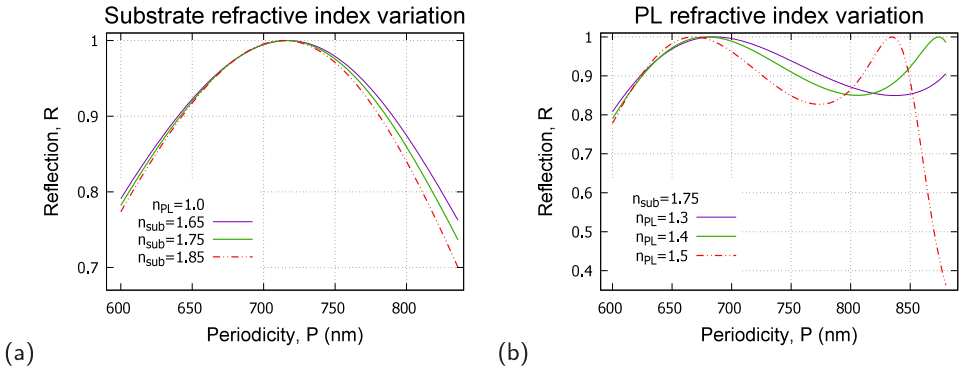

Fig. 4. (a) Influence of the substrate refractive index on the reflectivity of the metamirror. The diameter of nanoparticles is fixed at $D = 468$ nm (marked as M'× in Fig. 2a). (b) The dependence of power reflection coefficients on the periodicity for different refractive indices of the protective layer (PL) for the nanoparticle diameter $D = 540$ nm. The left and right peaks correspond to the magnetic and electric resonances, correspondingly (the latter is labeled as E× in Fig. 2b).

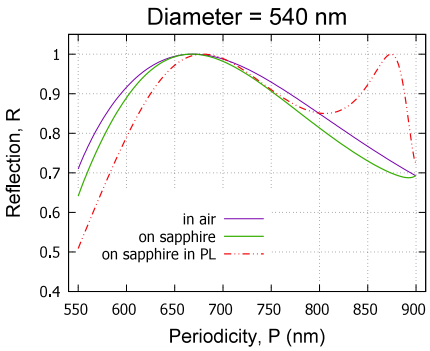

Fig. 5. Influence of the environment on the metamirror reflection for the fixed nanoparticle diameter $D = 540$ nm: nanoparticles in air (purple), placed on a sapphire substrate (green), and additionally embedded in a protective layer with refractive index $n_{PL} = 1.4$ (red).

When the particles are placed on a sapphire substrate ($n_{sub} = 1.75$) and additionally embedded in a protective layer, the sets of dimensional parameters like nanoparticle diameter and periodicity required for the realization of high reflectivity tend to be altered (see Fig. 2b). The magnetic dipole resonance is less affected by presence of the protective layer (see the perfect reflection around $P = 670$ nm in Fig. 4b), since in this case the strong magnetic field is confined inside the nanoparticles. Conversely, the electric dipole resonance depends higher on the refractive index of the surrounding material, due to the strong electric near-field interaction in the metasurface. For periodicity around $P = 850$ nm in Fig. 4b, one can see that the peak of the electric dipole resonance is strongly shifted to lower periodicity for higher refractive index of the protective layer, because with increasing refractive index the distance between the nanospheres providing the same interaction force is decreased.

Comparison of reflectances for metasurfaces in three different environments is shown in Fig. 5. The configuration when an array of silicon nanoparticles is placed on a sapphire substrate and enclosed in a protective layer (red line) has two peaks corresponding to perfect reflection. The right peak at the periodicity of 874 nm is formed by the excitation of electric dipole moment. It appears due to the strong shift of the electric dipole resonance when the protective layer is included. The left peak corresponds to the magnetic dipole resonance and observed also in the configurations when the environment is simplified to a homogeneous medium, like air, or nanospheres are placed on a sapphire substrate without a protective layer.

3.2. Analysis of imperfections

The computational accuracy allows to define how precise we can estimate the optical properties and their changes due to configuration or parameter uncertainties related to the fabrication of the metasurface and other devices [40]. The accuracy of the conducted simulations reaches 10^{-5} using a mathematical approach called Perfectly Matched Layer (PML). The PML boundary condition allows to avoid back reflection from the computational boundary of the model and not to interfere with the originally scattered field. Therefore, the limiting computational error is related to the model discretization that depends on the computational time and resources.

The fabricated metasurface will not consist of perfectly identical nanoparticles separated at perfectly identical distance from each other. Such parameters as the diameter and periodicity can fluctuate in a certain range defined by the accuracy and precision of the fabrication technology. To estimate the intensity reflection changes in case of imperfections, we explicitly consider elementary cells with $2\times2 = 4$ and $3 \times 3 = 9$ nanoparticles and randomize their parameters around corresponding perfect values in the simulation of the metasurface reflection properties (see Fig. 6a,b). We consider the case of perfect reflection at the following parameters ($D = 476$ nm, $P = 730$ nm) of the infinite metasurface structure on a sapphire substrate embedded in a protective layer with the refractive index $n_{PL} = 1.4$ (Fig. 2b). These parameters are chosen to provide a relatively broadband mirror performance, expected from a broad red zone of high reflection in Fig. 2b. Moreover, the distance between the nanoparticles is large enough to avoid their contact. That makes this set of parameters feasible in the fabrication process.

We conducted 100 simulations for different random configurations and calculated the mean value of the reflection coefficients. The standard errors of the mean for all solutions are also presented in Fig. 6. The fluctuations of nanoparticle diameters (Fig. 6a) decrease the mean value of the reflection coefficient more significantly than the fluctuations of periodicity (Fig. 6b). When diameters differ from the perfect value by less than 6%, the structure can still be considered as a highly-efficient mirror.

The metasurface is embedded in a thin layer to protect the structure against possible damage and impurities. However, the thickness of the protective layer may also have fluctuations. Driven by the question if the accuracy of the layer deposition would be relevant in future experiments, we analyzed changes of the intensity reflection coefficients for different protective layer thicknesses considering two cases presented in Fig. 7. The red curve corresponds to the resonant excitation of electric dipole moments ($D = 540$ nm; $P = 874$ nm). The blue curve corresponds to the magnetic resonant response ($D = 480$ nm; $P = 722$ nm). The dimensional parameters of Si nanospheres in both cases are taken at the conditions of perfect reflection when the thickness of

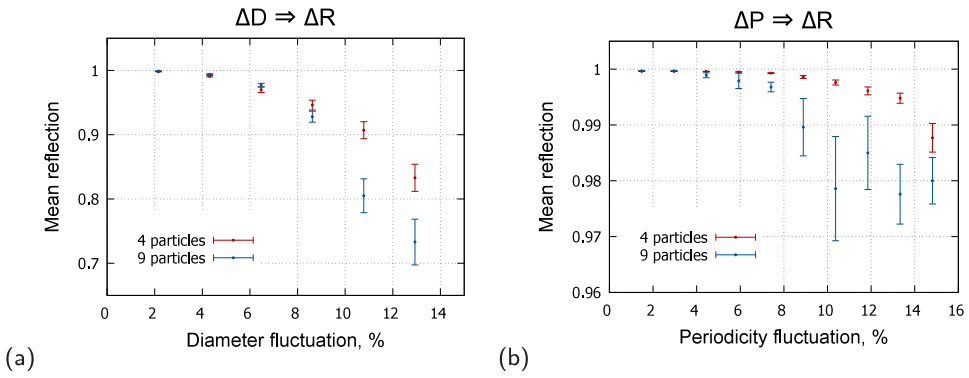

Fig. 6. The influence of (a) nanoparticle diameter fluctuations and (b) periodicity fluctuations on the mean value of power reflection coefficient. We consider the case of perfect reflection at the following parameters ($D = 476$ nm, $P = 730$ nm) of the infinite metasurface structure located on a substrate and embedded in a protective layer. Refractive indices of the substrate and protective layer are $n_{sub} = 1.75$ and $n_{PL} = 1.4$, respectively.

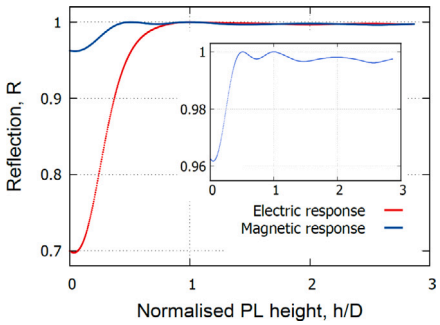

Fig. 7. Power reflection coefficients of metasurface calculated as a function of the protective layer thickness, normalized to the value of the nanoparticle diameter (h/D). The simulations are run at the conditions of magnetic and electric dipole resonances.

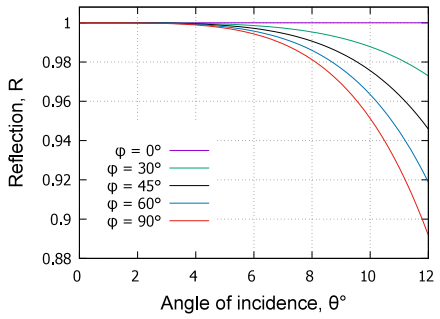

Fig. 8. Tolerable angle of incidence θ of the light beam for different polarization angles φ: $\varphi = 0°$ ($\varphi = 90°$) corresponds to s- (p-) polarization of the electric field. The parameters of metasurface: $D = 468$ nm, $P = 750$ nm. Refractive index of the substrate $n_{sub} = 1.75$, of the protective layer $n_{PL} = 1.4$.

the protective layer is equal to the nanoparticle diameter. Fluctuations in the layer thickness does not significantly decrease the intensity reflection. When the layer thickness is smaller than the nanoparticle diameter, the electric dipole moments change and a reduction of reflectivity is observed, since near-field interactions between electric dipole moments are sensitive to the surrounding medium. The magnetic dipole resonance is less sensitive due to the localization of the electric field inside the nanoparticles.

We consider now the case of a slightly oblique incidence of light on the metasurface and introduce in addition a polarization angle φ. Here the angle $\varphi = 0°$ ($\varphi = 90°$) corresponds to s-polarized (p-polarized) light with $\mathbf{E}_0$ perpendicular (parallel) to the plane of incidence (yz-plane in Fig. 1). The dependence of the intensity reflection coefficient on the angle of incidence and the polarization angle are illustrated in Fig. 8. The investigated point is chosen for the magnetic dipole resonance ($D = 468$ nm, $P = 750$ nm) marked as M× in Fig. 2b. The metasurface remains highly-reflective for all polarizations of the electric field if the angle of incidence is less than 4°. Note, that for the s-polarization the reflection remains higher than 0.999 up to 20°.

4. Conclusion

This article reports on our ongoing work towards the realization of a highly efficient silicon nanosphere metasurface mirror. The metasurface consists of silicon nanoparticles located on a sapphire substrate and embedded in a protective layer. It has been demonstrated that the optical behavior of the metasurface mirror can be described by resonant excitation of electric and magnetic dipole moments. While the substrate does not noticeably affect the metasurface reflectivity, the presence of a protective layer requires adjustment of the size parameters (diameter and periodicity) of Si nanospheres at which perfect reflection is realized. Taking into account the role of possible metasurface imperfections, it has been found that fluctuations in the nanoparticle diameter have larger influence on the metasurface reflection compared to fluctuations in periodicity. If the diameter fluctuations are larger than 6% of the ideal value, the mirror effect may be significantly reduced. It has been demonstrated that the uncertainties in the thickness of the protective layer are not critical for the realization of a perfect mirror. As a final step, deviations in the angle of incidence were considered, showing that the ideal reflection is maintained at normal incidence and at angles of incidence less than 4 degrees for all polarization directions of the incident electric field.

Funding

Deutsche Forschungsgemeinschaft (DFG), Germany (EXC 2122, Project ID 390833453) and (EXC 2123, Project ID 390837967), Villum Fonden, Denmark (Grant No. 40707).

CRediT authorship contribution statement

Mariia Matiushechkina: Writing – original paper, Numerical simulations. **Andrey B. Evlyukhin:** Methodology, Paper preparation. **Vladimir A. Zenin:** Numerical simulations, Paper preparation. **Michèle Heurs:** Supervision, Conceptualization. **Boris N. Chichkov:** Coordination, Paper preparation.

Declaration of competing interest

The authors declare that they have no known competing financial interests or personal relationships that could have appeared to influence the work reported in this paper.

Data availability

Data will be made available on request.

Acknowledgments

Authors acknowledge financial support from the Deutsche Forschungsgemeinschaft, Germany (DFG, German Research Foundation) under Germany's Excellence Strategy within the Cluster of Excellence PhoenixD (EXC 2122, Project ID 390833453) and the Cluster of Excellence QuantumFrontiers (EXC 2123, Project ID 390837967).V.A.Z. acknowledges financial support from Villum Fonden, Denmark (Grant No. 40707).

References

[1] I. Staude, J. Schilling, Metamaterial-inspired silicon nanophotonics, Nat. Photon. 11 (5) (2017) 274–284, http://dx.doi.org/10.1038/nphoton.2017.39.

[2] R.S. Savelev, O.N. Sergaeva, D.G. Baranov, A.E. Krasnok, A. Alù, Dynamically reconfigurable metal-semiconductor Yagi-Uda nanoantenna, Phys. Rev. B 95 (2017) 235409, http://dx.doi.org/10.1103/PhysRevB.95.235409, URL https://link.aps.org/doi/10.1103/PhysRevB.95.235409.

[3] X. Zhu, W. Yan, U. Levy, N.A. Mortensen, A. Kristensen, Resonant laser printing of structural colors on high-index dielectric metasurfaces, Sci. Adv. 3 (5) (2017) e1602487, http://dx.doi.org/10.1126/sciadv.1602487, arXiv:https://www.science.org/doi/pdf/10.1126/sciadv.1602487.

[4] F. Zhang, M. Pu, X. Li, X. Ma, Y. Guo, P. Gao, H. Yu, M. Gu, X. Luo, Extreme-angle silicon infrared optics enabled by streamlined surfaces, Adv. Mater. 33 (11) (2021) 2008157, http://dx.doi.org/10.1002/adma.202008157, arXiv:https://onlinelibrary.wiley.com/doi/pdf/10.1002/adma.202008157.

[5] A.B. Evlyukhin, S.M. Novikov, U. Zywietz, R.L. Eriksen, C. Reinhardt, S.I. Bozhevolnyi, B.N. Chichkov, Demonstration of magnetic dipole resonances of dielectric nanospheres in the visible region, Nano Lett. 12 (7) (2012) 3749–3755, http://dx.doi.org/10.1021/nl301594s, PMID: 22703443.

[6] P. Spinelli, M.A. Verschuuren, A. Polman, Broadband omnidirectional antireflection coating based on subwavelength surface mie resonators, Nature Commun. 3 (1) (2012) 692, http://dx.doi.org/10.1038/ncomms1691.

[7] K.V. Baryshnikova, M.I. Petrov, V.E. Babicheva, P.A. Belov, Plasmonic and silicon spherical nanoparticle antireflective coatings, Sci. Rep. 6 (1) (2016) 22136, http://dx.doi.org/10.1038/srep22136.

[8] M. Pu, Y. Guo, X. Li, X. Ma, X. Luo, Revisitation of extraordinary Young's interference: from catenary optical fields to spin–orbit interaction in metasurfaces, ACS Photon. 5 (8) (2018) 3198–3204, http://dx.doi.org/10.1021/acsphotonics.8b00437.

[9] M. Decker, I. Staude, M. Falkner, J. Dominguez, D.N. Neshev, I. Brener, T. Pertsch, Y.S. Kivshar, High-efficiency dielectric huygens' surfaces, Adv. Opt. Mater. 3 (6) (2015) 813–820, http://dx.doi.org/10.1002/adom.201400584, arXiv:https://onlinelibrary.wiley.com/doi/pdf/10.1002/adom.201400584.

[10] A. Howes, W. Wang, I. Kravchenko, J. Valentine, Dynamic transmission control based on all-dielectric huygens metasurfaces, Optica 5 (7) (2018) 787–792, http://dx.doi.org/10.1364/OPTICA.5.000787, URL https://opg.optica.org/optica/abstract.cfm?URI=optica-5-7-787.

[11] V.E. Babicheva, A.B. Evlyukhin, Resonant lattice kerker effect in metasurfaces with electric and magnetic optical responses, Laser Photonics Rev. 11 (6) (2017) 1700132, http://dx.doi.org/10.1002/lpor.201700132, arXiv:https://onlinelibrary.wiley.com/doi/pdf/10.1002/lpor.201700132.

[12] P. Moitra, B.A. Slovick, W. li, I.I. Kravchencko, D.P. Briggs, S. Krishnamurthy, J. Valentine, Large-scale all-dielectric metamaterial perfect reflectors, ACS Photon. 2 (6) (2015) 692–698, http://dx.doi.org/10.1021/acsphotonics.5b00148.

[13] S. Taravati, G.V. Eleftheriades, Full-duplex reflective beamsteering metasurface featuring magnetless nonreciprocal amplification, Nature Commun. 12 (1) (2021) 4414, http://dx.doi.org/10.1038/s41467-021-24749-7.

[14] J. Martínez-Llinàs, C. Henry, D. Andrén, R. Verre, M. Käll, P. Tassin, A Gaussian reflective metasurface for advanced wavefront manipulation, Opt. Express 27 (15) (2019) 21069–21082, http://dx.doi.org/10.1364/OE.27.021069, URL https://opg.optica.org/oe/abstract.cfm?URI=oe-27-15-21069.

[15] G. Ding, K. Chen, X. Luo, G. Qian, J. Zhao, T. Jiang, Y. Feng, Direct routing of intensity-editable multi-beams by dual geometric phase interference in metasurface, Nanophotonics 9 (9) (2020) 2977–2987, http://dx.doi.org/10.1515/nanoph-2020-0203.

[16] H. Liu, H. Xue, Y. Liu, L. Li, Generation of multiple pseudo bessel beams with accurately controllable propagation directions and high efficiency using a reflective metasurface, Appl. Sci. 10 (20) (2020) 7219, http://dx.doi.org/10.3390/app10207219.

[17] B. Slovick, Z.G. Yu, M. Berding, S. Krishnamurthy, Perfect dielectric-metamaterial reflector, Phys. Rev. B 88 (2013) 165116, http://dx.doi.org/10.1103/PhysRevB.88.165116, URL https://link.aps.org/doi/10.1103/PhysRevB.88.165116.

[18] V.E. Babicheva, A.B. Evlyukhin, Resonant suppression of light transmission in high-refractive-index nanoparticle metasurfaces, Opt. Lett. 43 (21) (2018) 5186–5189, http://dx.doi.org/10.1364/OL.43.005186, URL https://opg.optica.org/ol/abstract.cfm?URI=ol-43-21-5186.

[19] A.B. Evlyukhin, M. Matiushechkina, V.A. Zenin, M. Heurs, B.N. Chichkov, Lightweight metasurface mirror of silicon nanospheres, [Invited], Opt. Mater. Express 10 (10) (2020) 2706–2716, http://dx.doi.org/10.1364/OME.409311, URL https://opg.optica.org/ome/abstract.cfm?URI=ome-10-10-2706.

[20] P. Cencillo-Abad, J.-Y. Ou, E. Plum, N.I. Zheludev, Electro-mechanical light modulator based on controlling the interaction of light with a metasurface, Sci. Rep. 7 (1) (2017) 5405, http://dx.doi.org/10.1038/s41598-017-05906-9.

[21] C.A. Curwen, J.L. Reno, B.S. Williams, Broadband continuous single-mode tuning of a short-cavity quantum-cascade VECSEL, Nat. Photon. 13 (12) (2019) 855–859, http://dx.doi.org/10.1038/s41566-019-0518-z.

[22] J. Li, J. Li, S. Zhou, F. Yi, Metasurface photodetectors, Micromachines 12 (12) (2021) http://dx.doi.org/10.3390/mi12121584, URL https://www.mdpi.com/2072-666X/12/12/1584.

[23] R.X. Adhikari, K. Arai, A.F. Brooks, et al., A cryogenic silicon interferometer for gravitational-wave detection, Classical Quantum Gravity 37 (16) (2020) 165003, http://dx.doi.org/10.1088/1361-6382/ab9143.

[24] M. Punturo, H. Lück, Toward a third generation of gravitational wave observatories, Gen. Relativity Gravitation 43 (2) (2011) 363–385, http://dx.doi.org/10.1007/s10714-010-1010-8.

[25] E. Hirose, K. Craig, H. Ishitsuka, I.W. Martin, N. Mio, S. Moriwaki, P.G. Murray, M. Ohashi, S. Rowan, Y. Sakakibara, T. Suzuki, K. Waseda, K. Watanabe, K. Yamamoto, Mechanical loss of a multilayer tantala/silica coating on a sapphire disk at cryogenic temperatures: Toward the KAGRA gravitational wave detector, Phys. Rev. D 90 (2014) 102004, http://dx.doi.org/10.1103/PhysRevD.90.102004, URL https://link.aps.org/doi/10.1103/PhysRevD.90.102004.

[26] S. Reid, I.W. Martin, Development of mirror coatings for gravitational wave detectors, Coatings 6 (4) (2016) http://dx.doi.org/10.3390/coatings6040061, URL https://www.mdpi.com/2079-6412/6/4/61.

[27] J. Steinlechner, I.W. Martin, A.S. Bell, J. Hough, M. Fletcher, P.G. Murray, R. Robie, S. Rowan, R. Schnabel, Silicon-based optical mirror coatings for ultrahigh precision metrology and sensing, Phys. Rev. Lett. 120 (2018) 263602, http://dx.doi.org/10.1103/PhysRevLett.120.263602, URL https://link.aps.org/doi/10.1103/PhysRevLett.120.263602.

[28] F. Moreno, B. García-Cámara, J.M. Saiz, F. González, Interaction of nanoparticles with substrates: effects on the dipolar behaviour of the particles, Opt. Express 16 (17) (2008) 12487–12504, http://dx.doi.org/10.1364/OE.16.012487, URL https://opg.optica.org/oe/abstract.cfm?URI=oe-16-17-12487.

[29] N.L.D. Serhiy Z. Malynych, I.E. Moroz, Influence of substrate on the optical properties of non-aggregated silver nanoparticles, Eur. Phys. J. Appl. Phys. 2 (64) (2013) 20402, http://dx.doi.org/10.1051/epjap/2013120531.

[30] A.E. Miroshnichenko, A.B. Evlyukhin, Y.S. Kivshar, B.N. Chichkov, Substrate-induced resonant magnetoelectric effects for dielectric nanoparticles, ACS Photon. 2 (10) (2015) 1423–1428, http://dx.doi.org/10.1021/acsphotonics.5b00117.

[31] M. Hesari-Shermeh, B. Abbasi-Arand, M. Yazdi, Analysis of substrated periodic metasurfaces under normal incidence, Opt. Express 29 (2) (2021) 1694–1710, http://dx.doi.org/10.1364/OE.413103, URL https://opg.optica.org/oe/abstract.cfm?URI=oe-29-2-1694.

[32] J. van de Groep, A. Polman, Designing dielectric resonators on substrates: Combining magnetic and electric resonances, Opt. Express 21 (22) (2013) 26285–26302, http://dx.doi.org/10.1364/OE.21.026285, URL https://opg.optica.org/oe/abstract.cfm?URI=oe-21-22-26285.

[33] S. Rowan, G. Cagnoli, P. Sneddon, J. Hough, R. Route, E. Gustafson, M. Fejer, V. Mitrofanov, Investigation of mechanical loss factors of some candidate materials for the test masses of gravitational wave detectors, Phys. Lett. A 265 (1) (2000) 5–11, http://dx.doi.org/10.1016/S0375-9601(99)00874-9, URL https://www.sciencedirect.com/science/article/pii/S0375960199008749.

[34] S. Reid, G. Cagnoli, D. Crooks, J. Hough, P. Murray, S. Rowan, M. Fejer, R. Route, S. Zappe, Mechanical dissipation in silicon flexures, Phys. Lett. A 351 (4) (2006) 205–211, http://dx.doi.org/10.1016/j.physleta.2005.10.103, URL https://www.sciencedirect.com/science/article/pii/S0375960105016981.

[35] D.R.H. Craig F. Bohren, Absorption and scattering of light by small particles, ISBN: 9783527618156, 1998, http://dx.doi.org/10.1002/9783527618156.ch1, arXiv:https://onlinelibrary.wiley.com/doi/pdf/10.1002/9783527618156.ch1.

[36] V.G. Kravets, F. Schedin, A.N. Grigorenko, Extremely narrow plasmon resonances based on diffraction coupling of localized plasmons in arrays of metallic nanoparticles, Phys. Rev. Lett. 101 (2008) 087403, http://dx.doi.org/10.1103/PhysRevLett.101.087403, URL https://link.aps.org/doi/10.1103/PhysRevLett.101.087403.

[37] U. Zywietz, A.B. Evlyukhin, C. Reinhardt, B.N. Chichkov, Laser printing of silicon nanoparticles with resonant optical electric and magnetic responses, Nature Commun. 5 (1) (2014) 3402, http://dx.doi.org/10.1038/ncomms4402.

[38] V.E. Babicheva, A.B. Evlyukhin, Multipole lattice effects in high refractive index metasurfaces, J. Appl. Phys. 129 (4) (2021) 040902, http://dx.doi.org/10.1063/5.0024274.

[39] A.B. Evlyukhin, C. Reinhardt, A. Seidel, B.S. Luk'yanchuk, B.N. Chichkov, Optical response features of Si-nanoparticle arrays, Phys. Rev. B 82 (2010) 045404, http://dx.doi.org/10.1103/PhysRevB.82.045404, URL https://link.aps.org/doi/10.1103/PhysRevB.82.045404.

[40] S.N. Khonina, N.L. Kazanskiy, M.A. Butt, S.V. Karpeev, Optical multiplexing techniques and their marriage for on-chip and optical fiber communication: a review, Opto-Electron. Adv. 5 (8) (2022) 210127–1–210127–25, http://dx.doi.org/10.29026/oea.2022.210127, URL http://www.chinaoceanengin.cn//article/id/62cfc87b99d88171c95f55bd.

5.4 Perfect mirror effects in metasurfaces of silicon nanodisks at telecom wavelength

Authors: Mariia Matiushechkina, Andrey B. Evlyukhin, Vladimir A. Zenin, Boris N. Chichkov, Michèle Heurs

Journal: Advanced Optical Materials

Article Number: 12, 2400191 (2024)

DOI: 10.1002/adom.202400191

Author contribution: All authors contributed in the conceptualisation and formulation of the research goals. A.B.E. and M.M. worked on the development of methodology in design optimisation for cylindrical metasurfaces. M.M., A.B.E. and V.A.Z. conducted formal analysis and produced simulation results. M.M. with the support of A.B.E. and V.A.Z. created the initial draft. B.N.C. and M.H. managed the project and edited the draft. All authors were actively engaged in the discussion, evaluation of the results and preparation of the manuscript.

RESEARCH ARTICLE

ADVANCED OPTICAL MATERIALS
www.advopticalmat.de

Perfect Mirror Effects in Metasurfaces of Silicon Nanodisks at Telecom Wavelength

Mariia Matiushechkina, Andrey B. Evlyukhin,* Vladimir A. Zenin, Boris N. Chichkov, and Michèle Heurs*

This article explores the design and optimization of nanodisk metasurfaces for achieving high reflectivity at a defined wavelength. The telecom wavelength of 1550 nm is particularly focused, selected for its potential applications in next-generation gravitational wave detectors. At this wavelength, the research goes toward the development of thin, low-loss, high-reflective coatings, where the metasurface can be chosen as an alternative. An optimization process for the dimensional parameters of nanodisks is proposed based on a systematic tuning approach, which facilitates the realization of various configurations of high-reflective metasurfaces. The concept of the "magnetic mirror effect" is examined in detail, where the magnetic dipole resonance aligns with the anapole state. Additionally, high reflectivity at the electric dipole resonance ("electric mirror effect") and at the excitation of several multipole moments is explored, including high-order modes. This variety of configurations affords more flexibility in the phase manipulation of the reflected beam. Furthermore, the potential experimental realization of mirror effects is discussed by exploring the structure in the surrounding medium with a refractive index of $n_d = 1.4$. This research platform provides a promising tool for the fabrication of high-reflective nanodisk metasurfaces and demonstrates its applicability across various fields.

1. Introduction

The appearance of thin, lightweight, optically efficient devices to control and manipulate light has recently been widely acknowledged across diverse scientific disciplines.[1] Considerable research efforts are directed toward the development of metasurfaces capable of meeting stringent optical and mechanical requirements. This involves a diversified and in-depth exploration of nanoparticle configurations and their operational modes.[2,3]

The motivation for our metasurface design has its origin in the field of gravitational wave astronomy. Our research focus extends towards next-generation projects, such as the Einstein Telescope,[4,5] where new techniques and materials are expected to be used at the telecom wavelength (1550 nm) to increase the low-frequency sensitivity of the gravitational wave detectors. Both table-top and large-scale experiments must employ low-loss highly reflective coatings deposited on crystalline structures.[6]

Previous research demonstrated possibilities to design reflective metasurfaces made of periodically arranged silicon nanospheres on top of a sapphire substrate and provided consequent analysis of reflection sensitivity to fabrication limitations.[7,8] The design of the nanospherical metasurface has the advantage that the behavior of the system is determined by a minimum set of dimensional parameters. However, nanosphere manufacturing technology, such as laser printing,[9] faces challenges in maintaining uniform size and precise positioning for each nanoparticle. As an alternative, electron beam lithography (EBL) is considered. The EBL capabilities are constrained by the fabrication of vertical walls and, thus, are well suited for the fabrication of cylinders, cuboids, triangular prisms, etc. To circumvent

M. Matiushechkina, A. B. Evlyukhin, B. N. Chichkov, M. Heurs
Cluster of Excellence PhoenixD
Leibniz University Hannover
Welfengarten 1, 30167 Hannover, Germany
E-mail: mariia.matiushechkina@aei.uni-hannover.de; evlyukhin@iqo.uni-hannover.de

The ORCID identification number(s) for the author(s) of this article can be found under https://doi.org/10.1002/adom.202400191

DOI: 10.1002/adom.202400191

M. Matiushechkina, M. Heurs
Institute for Gravitational Physics
Leibniz University Hannover
D-30167 Hannover, Germany

A. B. Evlyukhin, B. N. Chichkov
Institute of Quantum Optics
Leibniz University Hannover
Welfengarten 1, 30167 Hannover, Germany

V. A. Zenin
Center for Nano Optics
University of Southern Denmark
Campusvej 55, 5230 Odense, Denmark

the limitations associated with the uncertainties in achieving the perfect shape of the sharp corners,[10] we choose for our investigation a cylindrical nanoparticle configuration, which is explored in this paper.

The dominant resonant effect occurring in nanocylinders is Mie resonance, based on the same mechanisms as in nanospheres. High reflectivity from nanocylinders can be observed at either electric or magnetic dipole resonances.[11] However, the relative spectral positioning of the dipole resonances for a sphere is strictly fixed, whereas the ratio of a cylinder height to its radius can alter their mutual spectral correlation.[12,13] For thin nanocylinders resembling a nanodisk shape (when their height, H, is less than the diameter, D), the magnetic dipole resonance is spectrally located in close proximity to the electric dipole resonance, whereas for tall nanocylinders ($H > D$) the resonances are spectrally spaced far apart.

The preference toward structures consisting of nanodisks ($H < D$) is motivated by achieving thinner and lighter coatings for applications in quantum metrology and gravitational wave physics. At the same time, this choice helps to mitigate the challenges associated with numerous manufacturing defects.[14,15] However, the optical properties of metasurfaces made from nanodisks require a more detailed investigation.

At certain size parameters of the nanodisks, the electric and magnetic dipole resonances, excited by external waves, spectrally overlap. If this occurs, it may lead to destructive interference between the electric and magnetic dipole backscattering (Kerker effect), and consequently to suppression of reflection.[16,17] To avoid this behavior and obtain high reflectivity, one should choose a geometry where the dipole resonances are spectrally separated.

By a large reduction in the height of a nanodisk (height is less than radius), the magnetic dipole (MD) resonance is placed in the shorter wavelength range compared to the electric dipole resonance. Another interesting point for such disk configuration is the radiationless state of the electric dipole (ED) moment, called anapole state.[18,19] The reflective properties of the metasurface in this state are completely defined by other multipole contributions. Positioning the MD resonance at this state allows to obtain ideal magnetic dipole scattering[20] and design a "magnetic mirror" with zero phase shift of reflected electric field in relation to the incident light wave.[21] This paper provides a detailed discussion of the construction method for a "magnetic mirror" tailored to the operational wavelength of 1550 nm.

Furthermore, the reflection of the mirror can also be predominantly characterized by the contribution of only the ED moment, essentially forming an "electric mirror". We will show how specific dimensional parameters of the metasurface can be easily adjusted to operate the mirror at the ED moment or any other mode, with the potential to change the phase of the reflected beam. A comprehensive discussion of all cases, accompanied by information on potential future experimental realization, will be presented in the concluding sections.

2. Analytical Approach

High-refractive-index dielectric nanoparticles support electric and magnetic multipole resonances, providing amplitude and phase manipulations with the incident light field. The shape of nanocylinders, in particular the ratio between radii and height,

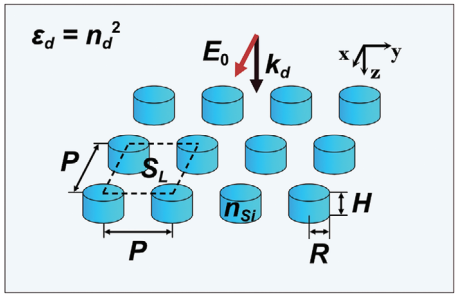

Figure 1. The infinite array of silicon nanocylinders, characterized by their height H, radius R and periodicity P in x- and y-directions. The unit cell area, defined by the square of periodicity, is denoted as $S_L = P^2$. The refractive index of nanocylinders is n_{Si}. The array is embedded in the surrounding medium with a dielectric constant $\varepsilon_d = n_d^2$, where n_d is the refractive index of medium. The structure is perpendicularly exposed to a monochromatic plane wave with a linearly polarized electric field E_0 along the x-axis.

influences the location of electric and magnetic dipole (multipole) resonances on the spectrum, spacing the resonances apart from each other or making them overlap.[12]

Let's examine a metasurface, represented as a 2D infinite periodic array composed of identical nanoparticles (**Figure 1**). The metasurface is normally irradiated by linearly polarized light, with the electric field E_0 oriented along the x axis. Within the coupled-dipole approximation theory, the electric-field reflection r and transmission t coefficients can be written as Ref. [22]

$$r = \frac{ik_d}{E_0 2S_L \epsilon_0 \epsilon_d}\left[p_x - \frac{1}{v_d} m_y\right] \tag{1}$$

$$t = 1 + \frac{ik_d}{E_0 2S_L \epsilon_0 \epsilon_d}\left[p_x + \frac{1}{v_d} m_y\right] \tag{2}$$

where k_d is the wave number in a surrounding medium, S_L is the unit cell area ($S_L = P^2$ for the square lattice, where P is the array periodicity), ϵ_0 is the vacuum permittivity, ϵ_d is the permittivity of a surrounding medium, v_d is the speed of light in the surrounding medium, p_x and m_y are the in-plane components of electric and magnetic dipole moments, respectively, induced in all particles by the incident wave. Here, the electric field E_0 is taken in the plane of the metasurface.

High reflectance is typically attained at the resonances of electric and magnetic dipole moments when they are spectrally separated from one another.[11] For this demonstration, let's present the dipole moments in the metasurface using the tensors of electric $\hat{\alpha}^{\mathrm{eff}-E}$ and magnetic $\hat{\alpha}^{\mathrm{eff}-M}$ effective dipole polarizabilities,

$$p_x = \epsilon_0 \epsilon_d \alpha_{\parallel}^{\mathrm{eff}-E} E_0 \qquad m_y = \alpha_{\parallel}^{\mathrm{eff}-M} H_0 \tag{3}$$

where $\alpha_{\parallel}^{\mathrm{eff}-E}$ and $\alpha_{\parallel}^{\mathrm{eff}-M}$ are the in-plane components of the corresponding polarizability tensors, E_0 and H_0 are electric and magnetic fields of the incident plane waves at the points of dipole locations, $H_0 = \sqrt{\epsilon_0 \epsilon_d / \mu_0} E_0$ (here μ_0 is the vacuum magnetic permeability). Note that the effective polarizabilities can differ significantly from single particle polarizabilities due to the interparticle coupling in arrays, especially under the condition of collective lattice resonances.[23] However, if the single particle

dipole resonances are realized at subdiffractional periodicity, the effect of interparticle coupling on the polarizabilities is weak in this spectral range. This results in only small spectral shifts of resonances, while the collective lattice resonances are excluded.[23,24]

Using (3), the reflection and transmission coefficients can be written as

$$r = \frac{ik_d}{2S_L}\left[\alpha_{\parallel}^{\text{eff}-E} - \alpha_{\parallel}^{\text{eff}-M}\right] \tag{4}$$

$$t = 1 + \frac{ik_d}{2S_L}\left[\alpha_{\parallel}^{\text{eff}-E} + \alpha_{\parallel}^{\text{eff}-M}\right] \tag{5}$$

Note that at the resonant wavelength λ_R, the real part of the dipole polarizability is zero, so that the polarizability is purely defined by the imaginary part.

Let's determine the conditions for achieving 100% reflectivity in a system with electric and magnetic dipole responses. From (5) and requirement $t = 0$ we obtain

$$\alpha_{\parallel}^{\text{eff}-E} = \frac{i2S_L}{k_d} - \alpha_{\parallel}^{\text{eff}-M} \tag{6}$$

and from (4) and requirement $|r| = 1$ (i.e., $r = e^{i\phi}, \phi \in [-\pi; \pi]$), the general solution is

$$\alpha_{\parallel}^{\text{eff}-M} = \frac{iS_L}{k_d}\left(1 + e^{i\phi}\right), \quad \alpha_{\parallel}^{\text{eff}-E} = \frac{iS_L}{k_d}\left(1 - e^{i\phi}\right) \tag{7}$$

It is important to note that control of the contributions of electric and magnetic dipole polarizabilities in total reflection, in principle, makes it possible to control the phase of reflection fields in the range of 0 to 2π.[25] The phase angle ϕ can be considered as the phase difference between the reflected and incident electric fields.

Three partial cases can be distinguished:

1) if $r = 1, (\phi = 0)$ then $\alpha_{\parallel}^{\text{eff}-M} = i2S_L/k_d$ and $\alpha_{\parallel}^{\text{eff}-E} = 0$

(magnetic mirror effect) (8)

2) if $r = -1, (\phi = \pi)$ then $\alpha_{\parallel}^{\text{eff}-M} = 0$ and $\alpha_{\parallel}^{\text{eff}-E} = i2S_L/k_d$

(electric mirror effect) (9)

3) if $r = \pm i, (\phi = \pm\pi/2)$ then $\alpha_{\parallel}^{\text{eff}-M} = (i \mp 1)S_L/k_d$ and

$\alpha_{\parallel}^{\text{eff}-E} = (i \pm 1)S_L/k_d$ (10)

The first two cases correspond to a single-dipole response, when the polarizability of the other dipole is negligibly small and does not contribute to reflection and transmission. Case 1) is realized due to the radiation of a magnetic dipole, resulting in the reflection of an electric field without a phase jump (the effect of a magnetic mirror). Case 2) corresponds to the effect of an electric mirror with a π-change in the phase of the reflected electric field. For case 3), the participation of both dipoles is necessary: total reflection is realized between electric and magnetic dipole resonances under special conditions $\text{Im}(\alpha_{\parallel}^{\text{eff}-M}) = \text{Im}(\alpha_{\parallel}^{\text{eff}-E}) = S_L/k_d$ and $\text{Re}(\alpha_{\parallel}^{\text{eff}-M}) = -\text{Re}(\alpha_{\parallel}^{\text{eff}-E}) = \pm S_L/k_d$. It is important to note the absorption in the system is assumed to be zero.

Thus, from the above analysis we can write down two necessary and sufficient conditions to achieve total reflection in the ED-MD approximation for the metasurfaces under consideration:

$$\text{Re}(\alpha_{\parallel}^{\text{eff}-M}) = -\text{Re}(\alpha_{\parallel}^{\text{eff}-E}), \qquad \text{Im}(\alpha_{\parallel}^{\text{eff}-M}) + \text{Im}(\alpha_{\parallel}^{\text{eff}-E}) = \frac{2S_L}{k_d} \tag{11}$$

Under these conditions, the phase ϕ of the reflected electric field is determined by the expression:

$$\tan\phi = \frac{\text{Re}(\alpha_{\parallel}^{\text{eff}-E}) - \text{Re}(\alpha_{\parallel}^{\text{eff}-M})}{\text{Im}(\alpha_{\parallel}^{\text{eff}-M}) - \text{Im}(\alpha_{\parallel}^{\text{eff}-E})} \tag{12}$$

3. Spectral Tuning of the Magnetic Mirror with the Electric-Dipole Anapole State

Let us consider case 1), when the total reflection is achieved due to the magnetic dipole resonance excited against the background of suppression of electric dipole polarizability in the anapole state, that is, at the point where $\alpha_{\parallel}^{\text{eff}-E} = 0$. This approach is justified by the fact that a significant, close to zero suppression of the electric dipole moment can only be achieved in the anapole state, which is basically the result of destructive interference between the quasistatic electric dipole and the toroidal dipole moments.[18,26] As a first step, we will show how the magnetic dipole resonance of a single silicon disk can be tuned to its electrical dipole-anapole state in the telecom spectral range for $\lambda = 1550$ nm. All numerical steps are conducted using the commercial software Comsol Multiphysics, which is based on the finite element method. The refractive index of silicon nanoparticles in Section 3 and Section 4.1 was set to be wavelength independent and equal to its value for crystalline silicon at the design wavelength: $n_{Si}(\lambda) = n_{Si}(1550) = 3.48$.[27] After this, having chosen a periodicity, we will construct a metasurface from these disks and demonstrate the effect of an ideal magnetic mirror at $\lambda = 1550$ nm precisely due to the coincidence of the magnetic dipole resonance with the anapole state.

Here, we consider an environment with a refractive index $n_d = 1$. In the final part of the paper, the results obtained will be generalized to the case of an environment with a higher refractive index.

3.1. Tuning of the Magnetic Resonance to the Anapole State for a Single Disk Particle

Single spherical nanoparticles support spectrally separated resonant optical responses, with the magnetic resonance occurring at a longer wavelength range compared to the electric resonance.[23] A similar behavior is observed for a nanocylinder with a height equal to twice the radius ($H = 2R$). To illustrate this statement, let's consider both cylindrical and spherical nanoparticles with the same radius $R = R_{sp}$, where R and R_{sp} are the radius of a cylinder and a sphere, respectively. As a starting value, R is estimated from the MD resonant condition for a sphere in Mie theory $R \approx$

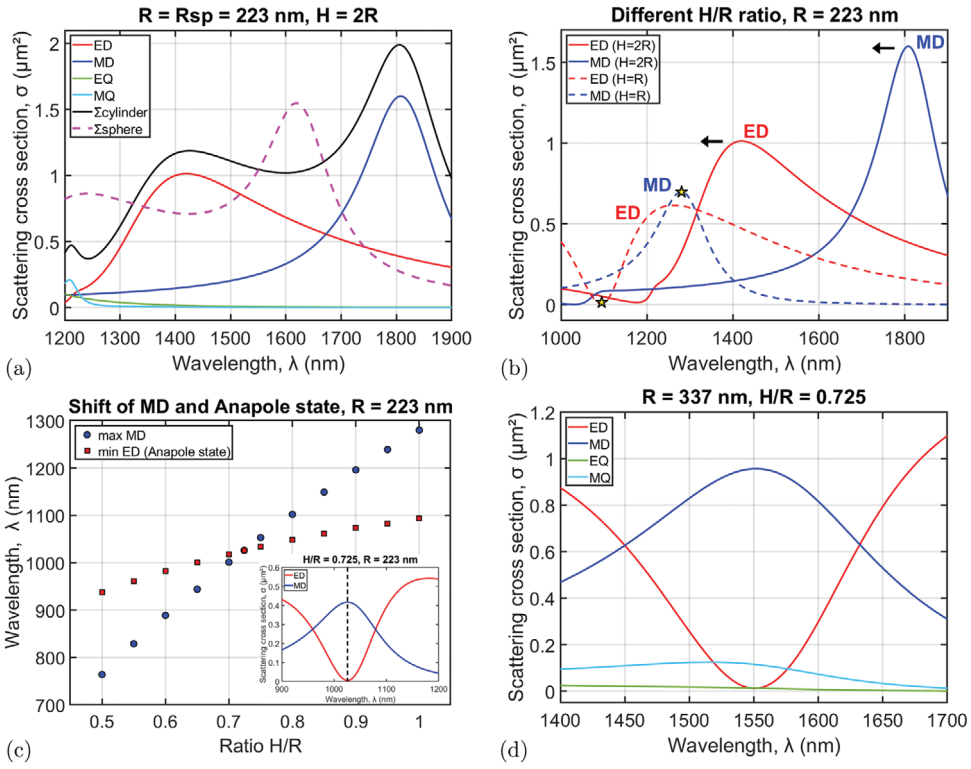

Figure 2. a) Scattering cross-section (SCS) and multipole decomposition calculated for a nanocylinder with radius $R = 223$ nm and height $H = 2R$. Shown is the comparison with the SCS of a nanosphere of the same radius ($R = R_{sp}$). b) Redistribution of the magnetic and electric dipole resonances in the spectra of SCSs by changing the height of the nanodisk at a fixed radius $R = 223$ nm (changing the aspect ratio). The dipole resonances overlap when $H \approx R$. The asterisk symbols denote the maximum of magnetic dipole contribution and the minimum of the electric dipole response (the anapole state). c) The spectral position of the MD maximum and anapole state as a function of the aspect ratio of the nanodisk. These states intersect at $H/R = 0.725$. The multipole decomposition of SCS for this point is plotted in the lower right corner of the graph. d) The alignment of the MD resonance and the anapole state to a 1550 nm wavelength by tuning the radius to $R = 337$ nm at the fixed aspect ratio of $R/H = 0.725$. All calculation is done with a constant refractive index of silicon $n_{Si} = 3.48$.

$\lambda/2n_{Si}$, where $\lambda = 1550$ nm, $n_{Si} = 3.48$, resulting in a radius of approximately 223 nm.

The total scattering cross-section (SCS), along with its multipole decomposition for a nanocylinder, are presented in **Figure 2a** by solid curves (see Appendix for the details of the calculation). The contribution of quadrupole moments (EQ, MQ) to the total scattering is found to be negligible in comparison to the electric (ED) and magnetic (MD) dipole moments. As expected, the total SCS of the nanosphere (dashed curve in Figure 2a) has similar shape as that of the nanocylinder, but blueshifted du to the smaller volume of the nanosphere.

In conclusion, for nanocylinders whose height surpasses their diameter, we operate exclusively in the distinct dipole regime described by the MD resonance at longer wavelengths.

Before further discussion, let's pre-define the terminology for nanocylinders with a height less than diameter ($H/R < 2$), calling them nanodisks.

By reducing the nanodisk height while keeping the radius constant, or in other words, by altering the height-to-radius aspect ratio (Figure 2b), both the ED and MD resonances shift toward shorter wavelengths. Notably, the MD peak shifts faster compared to the ED peak. The tendency can be explained by electric field redistribution within the particle, where MD has a peripheral distribution of polarizability currents.[13] In contrast, the ED has a concentric field inside of the nanoparticle, making it comparatively less sensitive to changes in height.

As the nanodisk height decreases, the resonances come into closer proximity. In the regime around equal height and radius ($H \approx R$), the dipole resonances overlap, leading to the resonant suppression of the backward scattering known as the Kerker effect.[11,13] Continuing the reduction in height results in the resonances drifting once more apart, with the MD peak positioned to the shorter wavelength relative to the ED one. The maximum of the MD resonance is marked by the asterisk symbol in Figure 2b. In this regime, particular attention is drawn to the anapole state, also denoted by the asterisk symbol placed on the left side from the ED peak. The anapole state features substrantial suppression of the ED contribution, thereby supporting the reflectivity solely due to the MD response.[20]

Figure 2c illustrates the shift of the anapole state and the maximum of the MD contribution with respect to the height-to-radius aspect ratio (H/R). Their intersection defines the exact ratio when the resonant maximum of the magnetic dipole moment overlaps the anapole state. Such a point corresponds to the ratio $H/R \approx 0.725$ at the wavelength of $\lambda = 1026$ nm. In order to achieve the same condition at the wavelength of interest (1550 nm), the size of nanodisk should be scaled accordingly. The multipole decomposition of SCS for the scaled disk of the radius $R = 337$ nm and

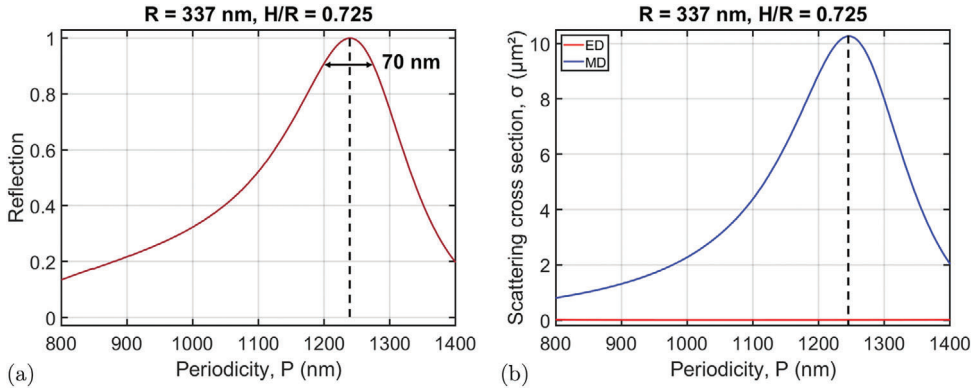

Figure 3. The behavior of the array of identical nanodisks (R = 337 nm, H/R = 0.725) at 1550 nm wavelength. a) The dependence of reflection on periodicity. Full reflection occurs around P = 1239.5 nm. The tolerance in the periodicity can be up to 70 nm for the reflection of more than 90%. b) Dipole decomposition in the periodicity range. There is no mutual contribution to the anapole state of each individual nanoparticle. The magnetic dipole has its maximum at the same periodicity P = 1239.5 nm as total reflection.

the aspect ratio $H/R = 0.725$ verifies the pure MD resonance without ED contribution at the wavelength of 1550 nm (Figure 2d). Although the MQ moment is also shifted into the telecom spectral range, its scattering cross-section is significantly smaller than for the MD moment.

3.2. Magnetic Mirror Effect

The array of nanodisks forms a metasurface characterized by its reflectivity. Magnetic mirror metasurface features high reflectance at the magnetic dipole resonance without any electric dipole excitation. Moreover, at such an operational point, the incident light beam reflects back without any phase shift in the absence of contribution from higher order modes, as seen in Equation (8).

Transitioning from the analysis of a single nanoparticle to the structured collective behavior, it is essential to account for the interparticle coupling effect. The position of nanodisks, described by periodicity P (Figure 1), has an impact on the total electric field of nanoparticles. This influence results from the mutual interactions in combination with the individual response to the incident light field.

A single nanoparticle resonating at the MD moment aligned to the anapole state at a wavelength of 1550 nm has geometric parameters of radius $R = 337$ nm and aspect ratio $R/H = 0.725$. Taking these parameters for each nanodisk of the array, we observe the change in reflection as a function of periodicity (**Figure 3a**). The full reflectance in the case of zero absorption for the non-diffractive periodicity range is obtained at $P = 1239.5$ nm.

By extracting the polarization density for a nanoparticle within the array and incorporating it into the equations for the multipole moments, and then calculating the scattering cross-section using Equation (A2) for a single nanoparticle in a homogeneous surrounding, we formally obtain information about which multipoles make a resonant contribution to the perfect reflection effect. This type of analysis has been applied to the current metasurface (Figure 3b), showing the dependency of scattering cross-section on periodicity. The plot demonstrates that the MD exhibits the same profile as the reflection curve, with its maximum resonance situated at the identical periodicity of $P = 1239.5$ nm. The electric dipole moment, on the other hand, is suppressed and remains unaffected by periodicity change.

The resonance quality factor, defined as the periodicity misalignment tolerable to exceed 90% reflection, is 70 nm.

In this section, we showed how to conduct an optimization procedure in order to find the parameters for the magnetic mirror effect at a specific wavelength. In the next section, we consider the electric mirror effect and other possible solutions for nanodisk metasurfaces.

4. Ideal Reflection of Nanodisk Metasurface with Various Phase Control

4.1. Electric Mirror Effect

The realization of a fully reflective mirror is possible not only at the magnetic dipole resonance but also at the electric one Equation (9). It's important to note that the ideal electric mirror effect is achievable in the complete absence of a magnetic response. Although such nanoparticle geometries do not allow for a radiationless state of the magnetic dipole moment, it is still feasible to tune the metasurface in such a way that the input from the MD is negligible compared to the ED moment.

We know that by reducing the radius of the nanodisk and keeping the aspect ratio the same, we reduce the volume of the nanoparticle and shift electric and magnetic resonances simultaneously to a smaller wavelength range. To get the electric mirror effect at 1550 nm wavelength, the radius of the nanodisk is varied by keeping the aspect ratio of nanoparticles and periodicity of the array the same (**Figure 4a**). The full reflection for the electric mirror effect is observed at $R = 308$ nm. To show that the following analysis is correct, the multipole decomposition is presented in Figure 4b. The resonance of ED on the plot is placed at 1550 nm wavelength, with a subtle maximum shift attributed to the influence of interparticle coupling.

The phenomenon known as the electric mirror effect is characterized by a phase shift of the reflected beam with respect to the incident light field to $\phi = \pi$, whereas the phase shift for the magnetic mirror effect is equal to zero, $\phi = 0$. The standing-wave pattern in Figure 4c shows that the π-phase shift for the

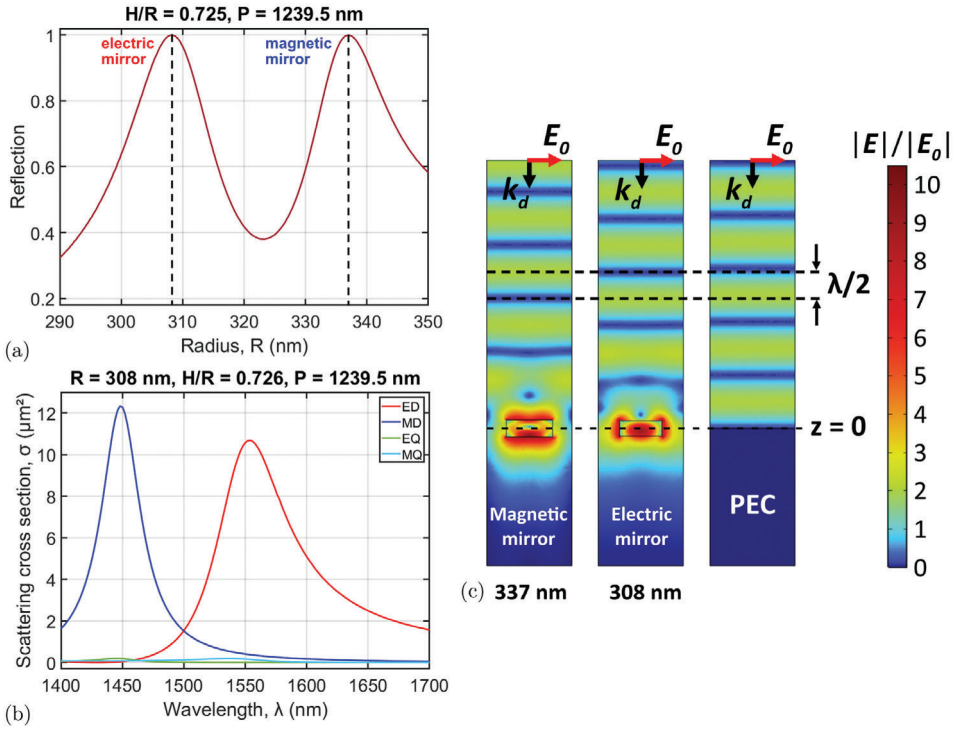

Figure 4. a) Reflection of different metasurfaces at 1550 nm wavelength versus disk radius (at fixed height-to-radius aspect ratio). The decrease of the radius leads to the transition from the mirror with magnetic effect ($R = 337$ nm, $H/R = 0.725$, $P = 1239.5$ nm) to the mirror operating at electric dipole resonance ($R = 308$ nm, $H/R = 0.725$, $P = 1239.5$ nm). b) Multipole decomposition of the scattering spectra for a particle in the metasurface with electric mirror effect. c) Visualization of the π-phase shift ($\lambda/2$, where $\lambda = 1550$ nm) in reflection between the metasurface supporting magnetic mirror effect (left panel) and the metasurface of electric mirror effect (middle panel). Their comparison with the perfect electric conductor (PEC) placed at the center of the nanoparticles.

electric mirror leads to destructive interference in the near field region. The near field of magnetic mirror due to the constructive interference has its maximum. The operation of these two mirrors differs in the phase control of the reflected beam, where the phase of the total electric field can be modulated around half of the wavelength $\lambda/2$.

Our precise numerical calculations show that the difference between the two marginal cases does not align exactly with 180°, but instead displays a slight deviation, reaching 2.5°. This discrepancy can be attributed to the influence of higher order modes in reflectivity and limitations in achieving complete elimination of the MD response. Furthermore, we conducted a comparative analysis of metasurfaces with a perfect electric conductor (PEC) positioned at the center of the nanoparticles. This comparison indicated that the effective center of reflection for these nanoparticles is displaced relative to their physical center, which results in a consequential shift of the far-field up to 20°.

4.2. Other Cases

A comprehensive overview of all potential configurations of a metasurface, with varying aspect ratios of nanodisks to achieve a high reflective state in the telecom wavelength range, is presented in **Figure** 5a. It's important to note that a general analysis of the spectral representation is essential for a proper understanding of all possible resonant states and their spectral positions relative to each other. By adjusting the dimensional parameters of the nanoparticle array, each resonant state can be tuned to a desired wavelength. In our case, the radius of the disks and their periodicity ($R = 337$ nm, $P = 1239.5$ nm) are taken from the previous optimization analysis, where the magnetic mirror was specifically designed to exhibit high reflectivity at 1550 nm wavelength. All metasurfaces are configured in the non-diffractive regime, meaning the periodicity P is smaller than the wavelength λ. For this analysis, we still consider air surrounding the structures ($n_d = 1$). The refractive index of silicon n_{Si} in the further investigation is taken as the wavelength-dependent value at room temperature according to Ref. [28].

Total reflection, represented by the red area, is observed across various nanoparticle resonances and their combinations. By choosing the specific aspect ratio of nanodisks and looking at the spectra of multipole decomposition, we can define multipole moments responsible for the optical properties of the metasurface.

In Figure 5b, we illustrate an example of a metasurface with the arbitrarily chosen aspect ratio of $H/R = 1.6$. The purple dashed line represents the reflection profile, with its corresponding axis on the right side of the graph. The scattering cross-section of multipoles is presented by solid lines with its axis on the left side. The metasurface, characterized by dimensional parameters $R = 337$ nm, $H/R = 1.6$, and $P = 1239.5$ nm, exhibits full reflection at the wavelengths of 1511 , 1636, and 1912 nm. The first point of total reflection at the lowest wavelength occurs due to the electric quadrupole moment (EQ), followed by the

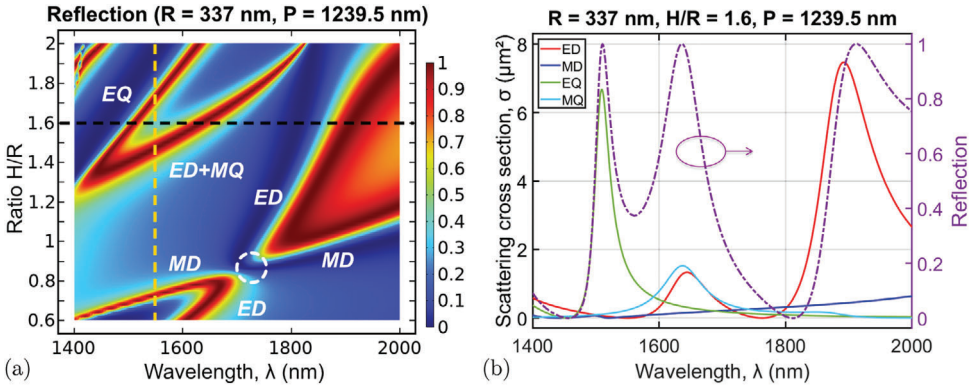

Figure 5. a) Reflection of metasurfaces with different aspect ratios for the telecom wavelength range. The 2D plot shows the relative spectral position of the dipole and quadrupole moments responsible for the high reflectivity of the metasurfaces. The dashed white circle indicates the area of high transmittance due to the overlap of the magnetic and electric dipole moments (Kerker effect). The dashed black line is a reflection spectrum presented in (b). The dashed orange line shows possible high-reflective metasurface configurations at 1550 nm wavelength. b) Multipole decomposition (left axis) and reflection (right axis) of the metasurface with $H/R = 1.6$ aspect ratio at telecom wavelengths.

second maximum resulting from the mutual contribution of electric dipole (ED) and magnetic quadrupole (MQ) moments. The last reflection maximum is attributed to ED with a small contribution of MD. By adjusting the disk's radius and periodicity while maintaining a constant aspect ratio, we can tailor each resonance to the desired wavelength.

Furthermore, Figure 5a shows that achieving total reflection at a wavelength of 1550 nm is not limited to the magnetic mirror regime corresponding to the aspect ratio $H/R = 0.725$. Total reflection is also attainable for $H/R = 1.48$ with the excitation of ED and MQ moments (dashed orange line), as well as for $H/R = 1.72$ with the dominant contribution of the EQ moment.

Within the aspect ratio range of 0.795 to 1, the overlap between ED and MD resonances precludes high reflectivity of the metasurfaces at any wavelength (the white dashed circle in Figure 5a). As mentioned above, the phenomenon, known as the Kerker effect, originates from the destructive interference of scattered light from ED and MD moments and can lead to the Huygens metasurface effect.[13,25] The reflection bandgap between the marginal points of aspect ratios $H/R = 0.795$ (dashed) and $H/R = 1$ (solid) is shown in **Figure 6**. The mutual crossover of ED and MD resonances is clearly visible. The MD resonance undergoes a more rapid spectral shift compared to the ED resonance, as detailed in the earlier sections. It is interesting to notice that the maxima of reflection in Figure 6 align with the intersection points of ED and MD resonances, rather than with the maxima of their peaks. The values of the scattering cross section at these points from both resonances are equal, resulting in a comparable contribution to perfect reflection. Extracting information about ED and MD moments and substituting it in Equations (3) and (4), we observe that these metasurface configurations are close to the third partial case Equation (10).

The next analytical step, validating the concept for practical realization, involves the consideration of a metasurface within a medium.

5. Metasurface in Medium

For practical realization, let's consider a metasurface placed in the surrounding medium with the refractive index $n_d = 1.4$ (corresponding, for example, to polydimethylsiloxane[29] and fused silica[30] materials). To ensure operation in the non-diffractive regime, the periodicity of the nanodisks must be smaller than λ/n_d. For comparison, let's assume the same nanodisk radius of $R = 337$ nm, but with the scaling periodicity of $P/n_d = 885.4$ nm, where P is the periodicity in Figure 5a.

The reflection plot in **Figure 7a** for different nanodisk aspect ratios and wavelengths demonstrates the potential to attain total reflection, analogous to the high-reflective curves observed in Figure 5a. Note that the contributions of quadrupole moments in the scattering are weak for nanodisks of this radius.

The dashed black line corresponds to a reflection profile for the metasurface with an aspect ratio of $H/R = 0.725$, which was the parameter for the magnetic mirror effect in Section (3.2). The multipole decomposition of the metasurface (Figure 7b) illustrates the position of the MD resonance maximum with respect to the anapole state. Their relative shift (absence of overlap) indicates an uneven displacement of the resonant curves due to

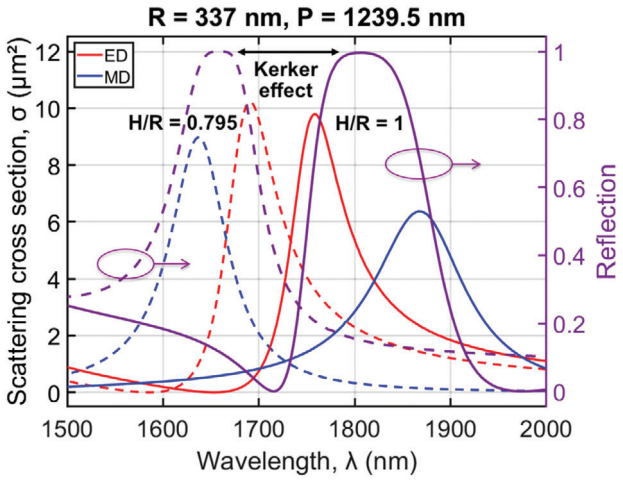

Figure 6. Scattering cross-section of electric and magnetic dipole moments (left axis) and reflection (right axis) for two metasurfaces ($H/R = 0.795$ & $H/R = 1$) as functions of wavelength.

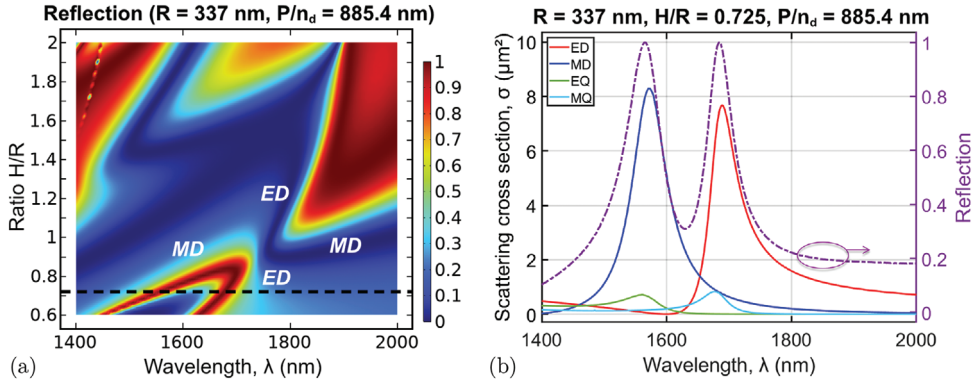

Figure 7. a) Reflection of metasurfaces embedded in a medium with refractive index $n_d = 1.4$ for different aspect ratios in the telecom wavelength range. The reflection profile at $H/R = 0.725$ is marked by the black dashed line. b) Multipole decomposition (left axis) and reflection (right axis) of the metasurface with $H/R = 0.725$ aspect ratio at telecom wavelengths. The wavelength λ is presented in free space.

the surrounding medium. The behavior originates from different field redistribution in MD and ED resonances. To obtain a magnetic mirror effect in the medium with $n_d = 1.4$, another optimization iteration is necessary, following the same steps described in the previous chapters.

The reflection profile is represented by a purple dashed line with the axis on the right side (Figure 7b). Although the observed dipole resonances don't resemble the specific cases of Equation (7) because of the contribution of the quadrupole moments, the total reflection is achievable for the general scenario.

Under fabrication considerations, the silicon nanodisk metasurface structure can be fabricated on top of a dielectric substrate, which can affect metasurface optical properties.[31,32] By covering the nanostructure with an additional matching layer with a refractive index close to that of the substrate, the metasurface can be considered in a homogeneous environment. Therefore, in the experimental realization, the near-complete reflection can be achieved in accordance with the models presented in our paper.

The additional estimations show that reflectivity can remarkably depend on polarization of oblique incident light field. However, for the gravitational wave detection application, the linearly polarized light at zero angle of incidence is of primary interest, so our research is focused on this case.

6. Conclusion

In this paper, we have discussed nanodisk metasurfaces and explored their potential operational configurations to achieve high reflectivity. We presented a concept of how to step-by-step optimize the dimensional parameters of the metasurface and tune it to the specific resonant response at the wavelength of interest.

As an example of the design, a reflective metasurface operating at the magnetic dipole moment aligned to the anapole state (magnetic mirror effect) at a wavelength of 1550 nm has been proposed. This wavelength was chosen based on the potential implementation of the technology in the research field of gravitational wave detection. Successive tuning of the aspect ratio and radius of an individual nanodisk and then the periodicity of the array demonstrated the precise optimization of the ideal reflection effect at the required wavelength. At the same time, information on the multipole contribution to the reflectivity was formally obtained from single-particle cross-section simulation with multipole decomposition. For the same wavelength of 1550 nm we were able to numerically modify the radius of the disks so that they would be resonant at electric dipole moment.

We showed various metasurface designs capable of achieving high reflection with varying phases of the reflected light field in the range of π to $-\pi$, accomplished through a combination of dipoles. Additionally, we demonstrated the potential of high reflection due to the influence of quadrupole moments. Notably, even in the scenario of the metasurface embedded in the surrounding medium with the refractive index of $n_d = 1.4$, full reflection was successfully achieved in the simulations. The considered theory and simulations are in full agreement with each other. The developed approach can be applied to the tuning of the perfect mirror effect at different wavelengths in the spectral region where the absorption in silicon is negligibly small. The results pave the way for the potential implementation of this research in future fabrication processes.

Appendix A: Multipole Decomposition of Scattering Cross-Sections

The total scattering cross-section is a sum of contributions from different multipole moments[33–35]:

$$\sigma_{\text{sca}}^{\text{total}} = \sigma_{\text{sca}}^{p} + \sigma_{\text{sca}}^{m} + \sigma_{\text{sca}}^{Q^e} + \sigma_{\text{sca}}^{Q^m} + \cdots \tag{A1}$$

where p - the electric dipole moment, m - the magnetic dipole moment, Q^e - the electric quadruple moment, Q^m - the magnetic quadruple moment.

This expression can also be written as follows:

$$\sigma_{\text{sca}}^{\text{total}} = \frac{k_0^4}{6\pi\varepsilon_0^2|\mathbf{E}_{\text{inc}}|^2}\sum_{\alpha}|p_\alpha|^2 + \frac{k_0^4\varepsilon_d\mu_0}{6\pi\varepsilon_0|\mathbf{E}_{\text{inc}}|^2}\sum_{\alpha}|m_\alpha|^2 + \\ + \frac{k_0^6\varepsilon_d}{720\pi\varepsilon_0^2|\mathbf{E}_{\text{inc}}|^2}\sum_{\alpha\beta}\left|Q_{\alpha\beta}^e\right|^2 + \frac{k_0^6\varepsilon_d^2\mu_0}{80\pi\varepsilon_0|\mathbf{E}_{\text{inc}}|^2}\sum_{\alpha\beta}\left|Q_{\alpha\beta}^m\right|^2 + \cdots \tag{A2}$$

where $\mathbf{E}_{\text{inc}}$ is the electric field of the incident wave, k_0 is the wavenumber in vacuum, ϵ_0 and μ_0 are the electric permittivity

and the magnetic permeability of free space, respectively, ϵ_d is the relative dielectric permittivity of the surrounding medium.

The exact multipole moments can be derived using the induced electric current density $\mathbf{J}^{\omega}$, distributed within the nanoparticle volume V. The indices α, β iterate over the values x, y, z.

$$p_\alpha = \frac{i}{\omega}\left\{\int_V d^3\mathbf{r} J_\alpha^\omega j_0(k_d r) + \frac{k_d^2}{2}\int_V d^3\mathbf{r}\left[3(\mathbf{r}\cdot\mathbf{J}^\omega)r_\alpha - r^2 J_\alpha^\omega\right]\frac{j_2(k_d r)}{(k_d r)^2}\right\} \tag{A3}$$

$$m_\alpha = \frac{3}{2}\int_V d^3\mathbf{r}[\mathbf{r}\times\mathbf{J}^\omega]_\alpha \frac{j_1(k_d r)}{k_d r} \tag{A4}$$

$$Q^e_{\alpha\beta} = \frac{3i}{\omega}\left\{\int_V d^3\mathbf{r}\left[3\left(r_\alpha J_\beta^\omega + r_\beta J_\alpha^\omega\right) - 2(\mathbf{r}\cdot\mathbf{J}^\omega)\delta_{\alpha\beta}\right]\frac{j_1(k_d r)}{k_d r} + 2k_d^2\int_V d^3\mathbf{r}\left[5r_\alpha r_\beta(\mathbf{r}\cdot\mathbf{J}^\omega) - \left(r_\alpha J_\beta^\omega + r_\beta J_\alpha^\omega\right)r^2 - r^2(\mathbf{r}\cdot\mathbf{J}^\omega)\delta_{\alpha\beta}\right]\frac{j_3(k_d r)}{(k_d r)^3}\right\} \tag{A5}$$

$$Q^m_{\alpha\beta} = 15\int_V d^3\mathbf{r}\left(r_\alpha[\mathbf{r}\times\mathbf{J}^\omega]_\beta + r_\beta[\mathbf{r}\times\mathbf{J}^\omega]_\alpha\right)\frac{j_2(k_d r)}{(k_d r)^2} \tag{A6}$$

k_d is the wavenumber in the surrounding medium, $j_n(k_d r)$ is the n-th order spherical Bessel function.

The simulation software Comsol Multiphysics, used in the paper for the metasurface optimization process, calculates the polarization density $\mathbf{P}$, which is related to the electric current density $\mathbf{J}^{\omega}$ by the equation:

$$\mathbf{P} = -\frac{\mathbf{J}^\omega}{i\omega} \tag{A7}$$

The information about the total scattering cross-section is applicable to the study of resonances of a single nanoparticle. In the context of metasurface investigation, our focus shifts to the relative contributions of individual multipoles. By extracting information about the polarization density $\mathbf{P}'$ of the nanoparticle within the array and incorporating this data into the equations for multipole decomposition, we can estimate the relative excitation of dipoles and quadrupoles across the spectral range.

Acknowledgements

The authors acknowledged financial support from the Deutsche Forschungsgemeinschaft (DFG, German Research Foundation) under Germany's Excellence Strategy within the Cluster of Excellence PhoenixD (EXC 2122, Project ID 390833453) and the Cluster of Excellence QuantumFrontiers (EXC 2123, Project ID 390837967).

Open access funding enabled and organized by Projekt DEAL.

Conflict of Interest

The authors declare no conflict of interest.

Data Availability Statement

The data that support the findings of this study are available from the corresponding author upon reasonable request.

Keywords

anapole, coatings, dielectric metasurface, metamaterials, mirror effect, multipole response, optical nanostructures

Received: January 21, 2024
Revised: March 7, 2024
Published online: April 20, 2024

[1] X. Zhao, Z. Sun, L. Zhang, Z. Wang, R. Xie, J. Zhao, R. You, Z. You, *Adv. Dev. Instrum.* **2022**, *2022*, 9765089.
[2] V.-C. Su, C. H. Chu, G. Sun, D. P. Tsai, *Opt. Express* **2018**, *26*, 13148.
[3] J. Hu, S. Bandyopadhyay, Y.-h. Liu, L.-y. Shao, *Front. Phys.* **2021**, *8*, 586087.
[4] Einstein Telescope Home Page, https://www.et-gw.eu/, https://www.et-gw.eu/ (accessed: October 2008).
[5] ET Science Team, Einstein Gravitational Wave Telescope Conceptual Design Study, Zenodo, https://doi.org/10.5281/zenodo.3911261 (accessed: June 2011).
[6] K. Craig, J. Steinlechner, P. G. Murray, A. S. Bell, R. Birney, K. Haughian, J. Hough, I. MacLaren, S. Penn, S. Reid, R. Robie, S. Rowan, I. W. Martin, *Phys. Rev. Lett.* **2019**, *122*, 231102.
[7] A. B. Evlyukhin, M. Matiushechkina, V. A. Zenin, M. Heurs, B. N. Chichkov, *Opt. Mater. Express* **2020**, *10*, 2706.
[8] M. Matiushechkina, A. B. Evlyukhin, V. A. Zenin, M. Heurs, B. N. Chichkov, *Opt. Mater.* **2023**, *138*, 113618.
[9] U. Zywietz, A. B. Evlyukhin, C. Reinhardt, B. N. Chichkov, *Nat. Commun.* **2014**, *5*, 3402.
[10] M. A. Mohammad, M. Muhammad, S. K. Dew, M. Stepanova, *Fundamentals of Electron Beam Exposure and Development*, Springer, Vienna **2012**, pp. 11–41.
[11] V. E. Babicheva, A. B. Evlyukhin, *J. Appl. Phys.* **2021**, *129*, 4.
[12] A. B. Evlyukhin, C. Reinhardt, B. N. Chichkov, *Phys. Rev. B* **2011**, *84*, 235429.
[13] I. Staude, A. E. Miroshnichenko, M. Decker, N. T. Fofang, S. Liu, E. Gonzales, J. Dominguez, T. S. Luk, D. N. Neshev, I. Brener, Y. Kivshar, *ACS Nano* **2013**, *7*, 7824.
[14] V.-C. Su, C. H. Chu, G. Sun, D. P. Tsai, *Opt. Express* **2018**, *26*, 13148.
[15] G. Yoon, T. Tanaka, T. Zentgraf, J. Rho, *J. Phys. D: Appl. Phys.* **2021**, *54*, 383002.
[16] M. Kerker, D.-S. Wang, C. Giles, *JOSA* **1983**, *73*, 765.
[17] W. Liu, Y. S. Kivshar, *Opt. Express* **2018**, *26*, 13085.
[18] V. Savinov, N. Papasimakis, D. Tsai, N. Zheludev, *Commun. Phys.* **2019**, *2*, 69.
[19] R. M. Saadabad, L. Huang, A. B. Evlyukhin, A. E. Miroshnichenko, *Opt. Mater. Express* **2022**, *12*, 1817.
[20] T. Feng, Y. Xu, W. Zhang, A. E. Miroshnichenko, *Phys. Rev. Lett.* **2017**, *118*, 173901.
[21] Y. Yu, Y.-Q. Li, R. Salas-Montiel, D.-Y. Qiao, *J. Appl. Phys.* **2022**, *131*, 153101.
[22] P. D. Terekhov, V. E. Babicheva, K. V. Baryshnikova, A. S. Shalin, A. Karabchevsky, A. B. Evlyukhin, *Phys. Rev. B* **2019**, *99*, 045424.
[23] A. B. Evlyukhin, C. Reinhardt, A. Seidel, B. S. Luk'yanchuk, B. N. Chichkov, *Phys. Rev. B* **2010**, *82*, 045404.
[24] B. Auguié, W. L. Barnes, *Phys. Rev. Lett.* **2008**, *101*, 143902.
[25] S. Kruk, Y. Kivshar, in *Dielectric metamaterials*, Elsevier, Amsterdam **2020**, pp. 145–174.
[26] E. A. Gurvitz, K. S. Ladutenko, P. A. Dergachev, A. B. Evlyukhin, A. E. Miroshnichenko, A. S. Shalin, *Laser Photonics Rev.* **2019**, *13*, 1800266.
[27] E. D. Palik, *Handbook of optical constants of solids*, vol. *3*, Academic Press, Cambridge **1998**.
[28] H. H. Li, *J. Phys. Chem. Ref. Data* **1980**, *9*, 561.
[29] M. R. Querry, *Optical constants of minerals and other materials from the millimeter to the ultraviolet*, Chemical Research, Development & Engineering Center, US Army Armament, **1998**.

[30] I. H. Malitson, *Josa* **1965**, *55*, 1205.
[31] J. Van de Groep, A. Polman, *Opt. Express* **2013**, *21*, 26285.
[32] V. E. Babicheva, M. I. Petrov, K. V. Baryshnikova, P. A. Belov, *JOSA B* **2017**, *34*, D18.
[33] A. B. Evlyukhin, T. Fischer, C. Reinhardt, B. N. Chichkov, *Phys. Rev. B* **2016**, *94*, 205434.
[34] R. Alaee, C. Rockstuhl, I. Fernandez-Corbaton, *Opt. Commun.* **2017**, *407*, 17.
[35] A. B. Evlyukhin, B. N. Chichkov, *Phys. Rev. B* **2019**, *100*, 125415.

5.5 Design and experimental demonstration of wavelength selective metamirrors on sapphire substrates

Authors: Mariia Matiushechkina, Andrey B. Evlyukhin, Radu Malureanu, Vladimir A. Zenin, Torgom Yezekyan, Andrei Lavrinenko, Sergey I. Bozhevolnyi, Boris N. Chichkov, Michèle Heurs

Journal: Advanced Photonics Research

Article Number: 2400116, (2024)

DOI: 10.1002/adpr.202400116

Author contribution: M.M., A.B.E. R.M., V.A.Z., B.N.C. and M.H. contributed to the creation of the design and conceptualization. M.M., V.A.Z., T.Y. worked with the numerical simulations. R.M., M.M. worked on the fabrication of the metasurfaces. V.A.Z., T.Y., M.M., A.B.E. performed the characterisation and data analysis. A.L., S.B., B.N.C., M.H. administrated the project, provided the resources and validated the results. M.M. and A.B.E. drafted the initial manuscript. R.M., V.A.Z., T.Y., A.L., S.I.B., B.N.C., M.H. edited, reviewed and approved the manuscript. All authors contributed to the formal analysis, discussed and evaluated the results.

ADVANCED PHOTONICS RESEARCH
Open Access
www.adpr-journal.com

Design and Experimental Demonstration of Wavelength-Selective Metamirrors on Sapphire Substrates

Mariia Matiushechkina, Andrey B. Evlyukhin,* Radu Malureanu, Vladimir A. Zenin, Torgom Yezekyan, Andrei Lavrinenko, Sergey I. Bozhevolnyi, Boris N. Chichkov, and Michèle Heurs*

The increasing demand for novel mirror coating designs for new generation of gravitational wave detectors is stimulating significant research interest in investigations of reflective properties of metasurfaces. Given this strong interest, this article details a systematic methodology for fabricating reflecting metasurfaces (metamirrors) designed to operate at target wavelengths of 1064 or 1550 nm. The proposed metasurfaces consist of silicon cylindrical nanoparticles placed on a sapphire substrate. First, the dimensional parameters of the structures are thoroughly selected through numerical simulations combined with material characterization. The configurations are subsequently analyzed analytically to reveal the mirror effect, which arises from the excitation of electric and magnetic dipole moments. Following this, the metasurfaces are fabricated and experimentally characterized, demonstrating reflectivity exceeding 95% around the design wavelengths, which is in good agreement with theoretical predictions. Overall, the work demonstrates the feasibility and detailed methodology for the fabrication of thin, lightweight metamirrors capable of achieving near-perfect reflectivity at the specified target wavelengths.

1. Introduction

Modern advances in dielectric nanophotonics[1–3] bring new opportunities to the development of nanoscale devices and systems for monitoring and controlling light fluxes, including control of the transmission, reflection and polarization of light,[4,5] nonlinear generation,[6–9] sensing,[10,11] laser generation,[12–14] visualization,[15–17] and others. However, achieving high efficiency of devices based on the optical properties of metasurfaces requires the use of detailed theoretical tuning methods and the practical development of experimental approaches. This, in turn, is determined by the functional requirements that apply to the final device. In this regard, systems based on metasurfaces of various configurations have become widely investigated.[18–20]

Metasurface mirrors, or metamirrors, represent a 2D analogue of metamaterials that can exhibit high reflectivity at certain wavelengths. The metasurface can be configured with an array of metallic[21,22] or dielectric[23,24] nanoparticles supporting resonant optical response[25,26] and having various geometrical configurations, including gratings,[27] bricks,[28] cylinders,[29] and so on. Moreover, the reflected light field can be manipulated to the desired phase shift,[30] polarization,[31] or different angles of reflection.[32–34]

Theoretically, the reflection effect in dielectric metasurfaces has been broadly studied during the last decade.[35–40] The

M. Matiushechkina, A. B. Evlyukhin, B. N. Chichkov, M. Heurs
Cluster of Excellence PhoenixD
Leibniz University Hannover
Welfengarten 1, 30167 Hannover, Germany
E-mail: mariia.matiushechkina@aei.uni-hannover.de; evlyukhin@iqo.uni-hannover.de

M. Matiushechkina, M. Heurs
Institute for Gravitational Physics
Leibniz University Hannover
D-30167 Hannover, Germany

M. Matiushechkina, B. N. Chichkov, M. Heurs
Laboratory of Nano and Quantum Engineering
Leibniz Universität Hannover
30167 Hannover, Germany

A. B. Evlyukhin, B. N. Chichkov
Institute of Quantum Optics
Leibniz University Hannover
Welfengarten 1, 30167 Hannover, Germany

R. Malureanu, A. Lavrinenko
Department of Electrical and Photonics Engineering
Technical University of Denmark
DK-2800 Kgs. Lyngby, Denmark

V. A. Zenin, S. I. Bozhevolnyi
Center for Nano Optics
University of Southern Denmark
Campusvej 55, 5230 Odense, Denmark

T. Yezekyan
Center for Polariton-driven Light-Matter Interactions (POLIMA)
University of Southern Denmark
Campusvej 55, 5230 Odense, Denmark

The ORCID identification number(s) for the author(s) of this article can be found under https://doi.org/10.1002/adpr.202400116.

DOI: 10.1002/adpr.202400116

phenomenon of reflection arises from the resonant excitation of dipole or higher order modes within nanoparticles,[3,41] which are inherently known as Mie resonances. The appropriate size of dielectric nanoparticles, in conjunction with their high refractive index, provides an essential amplitude and phase of the scattered electromagnetic waves. This results in destructive interference between the incident and scattered light fields in the direction of propagation, preventing light from passing through the structure and thus enabling reflection.[42,43]

In addition, the reflectivity of a metasurface is influenced by the surrounding medium, which is necessary for the practical realization of the structure. For instance, to mitigate the contribution of the underlying supportive substrate, a significant refractive index contrast between the nanoparticles and the substrate should be ensured. This contrast helps to minimize the substrate influence, allowing the reflectivity to result mainly from the resonant behavior of the nanoparticles.[44] Otherwise, the presence of a substrate may have the opposite effect of suppressing reflection.[45,46]

Considering a number of important practical properties of metasurfaces, such as compactness, lightness, strength, and high reflectivity, these structures have been proposed as an elemental basis of mirror instrumentation for gravitational wave (GW) detection.[47] Therefore, our interest lies in the design of a metamirror that is beneficial in the future generation of GW detectors, where the contribution of thermal noise has the greatest impact on the choice of materials and geometry.[48–51] The current GW detectors work at room temperature and use the laser beam at 1064 nm wavelength.[52] The operational wavelength of future GW detectors at cryogenic temperature is 1550 nm.[53] The selected promising materials for cryogenic temperature are crystalline silicon and sapphire, which exhibit low thermoelastic and Brownian noise,[54,55] in combination with low absorption at telecom wavelengths.[56]

The platform of silicon-on-sapphire (SOS) is commonly used in metasurface designs for optical sensing,[57] wavelength conversion,[58] alteration of beam propagation,[59] single-shot spectropolarimetric detection and accurate determination of thin film properties,[60] and so on. Our device, based on the resonant light reflection by a silicon metasurface on a sapphire substrate, is tailored for potential implementation in GW registration techniques, in particular, for the Einstein Telescope project,[53] where a single-layer metasurface has the advantage in terms of thermal noise at cryogenic temperatures in comparison with traditional Bragg mirrors. Sapphire substrates are already used in KAGRA cryogenic interferometers of the second-generation GW detectors.[61] Moreover, such metasurfaces can be implemented in the field of quantum metrology, where the piezoelectric property of the sapphire C-plane surface (0001) can lead to a slight change in nanoparticle periodicity and, consequently, to alteration of reflectivity.

In this article, we present the whole metasurface mirror realization process, including the stages of theoretical design, fabrication, and experimental characterization. The theoretical and fabrication stages include a number of features that must be taken into account to achieve high reflectivity at certain spectral points. The functional characteristics of the resulting mirrors are assessed by comparing experimental reflection spectra with the theoretical ones. The result of this scientific research shows how, from scratch, to develop the metasurface structures with the behavior corresponding to the predicted simulations and determines the key features of the fabrication process that affect the level of reflection. This study is an important step toward creating metamirrors with a selective reflectivity close to ideal.

2. Metasurface Design

Since the implementation of the mirror effect is focused on a specific application with pre-known spectral characteristics, the practical production of metasurfaces begins with a theoretical assessment and selection of the necessary geometrical parameters on the basis of the material parameters obtained from current experimental measurements. Therefore, the first part of the article will be devoted to this important stage. All numerical simulations are carried out using the COMSOL Multiphysics software.

2.1. Model

The target wavelengths are 1064 and 1550 nm due to their current and potential use in GW detectors. The metasurfaces are designed for both wavelengths to conduct a comparative analysis and facilitate the integration of the fabricated structures with existing optical devices.

The selected materials for metasurface realization are SOS. The high refractive index of silicon enables the design of nanoparticles with a small size and a proper fabrication distance between them. In contrast, the low refractive index of sapphire, which is approximately twice less than that of silicon, enables the sapphire substrate to have a minimum effect on the metasurface reflectivity.

One potential shape of nanoparticles that can be manufactured by existing technology, such as electron-beam lithography (EBL),[62] is a nanocylinder. The geometry is chosen with the consideration of circumventing fabrication challenges associated with defining the resolution of the corners.

The schematic of the potential metasurface on a sapphire substrate is presented in **Figure 1**. The refractive indices of silicon, sapphire, and air are designated as n_{Si}, $n_{Al_2O_3}$, and n_{air}, respectively. The geometry of periodically arranged nanoparticles is defined by the following dimensional parameters: diameter

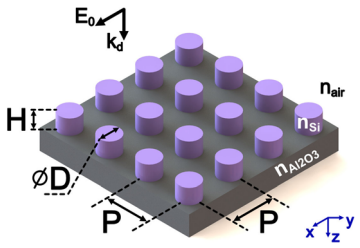

Figure 1. The design of a metasurface composed of silicon (n_{Si}) nanocylinders on top of a sapphire ($n_{Al_2O_3}$) substrate. The array of nanocylinders is characterized by parameters of diameter D, height H, and periodicity P in the x- and y-directions. The structure is illuminated in air (n_{air}) by a normally incident monochromatic plane wave with a linearly polarized electric field E_0 along the x-axis.

(D), height (H), and periodicity (P). The structure is isotropic in the x- and y-directions and illuminated by a linearly polarized monochromatic plane wave with the amplitude of the electric field E_0.

2.2. Height Selection

The initial step in metasurface fabrication involves a silicon layer deposition on top of a sapphire substrate. The thickness of the silicon layer, in other words, the height of the nanoparticles, is sufficiently constrained by operational wavelength, in our investigation by $\lambda_1 = 1064$ nm and $\lambda_2 = 1550$ nm.

In order to define the height, we refer to previous theoretical and experimental investigations of silicon nanocylinder configuration, which demonstrated that the height-to-diameter aspect ratio influences the arrangement of magnetic dipole (MD) and electric dipole (ED) resonances with respect to each other.[47,63,64] This results in the MD resonance being either at a longer or shorter wavelength range. For the aspect ratios approximately between 0.4 and 0.5, the dipole resonances spectrally overlap, resulting in the resonant suppression of the backscattered light, a phenomenon known as the Kerker effect.[64] In order to circumvent the zone of suppressed reflectivity and to create a metasurface mirror effect at a dipole resonance, preliminary estimations of nanocylinder size must be conducted.

First, we select and fix the third-dimensional parameter, namely, periodicity. The metasurface mirror operates at the subwavelength range, defined by the nondiffraction zone of the substrate. This is attributed to the substrate's higher refractive index compared to that of the superstrate, which, in our study, is air. The refractive indices of sapphire at the considered wavelengths are $n_{Al_2O_3}(\lambda_1) = 1.755$ and $n_{Al_2O_3}(\lambda_2) = 1.746$. Therefore, the border of the diffraction zone can be derived as $\lambda_d^i = \lambda_i / n_{Al_2O_3}(\lambda_i)$, where $i = 1, 2$.[65] This separation distance between the grating elements, in our case nanoparticles, evaluates the maximum periodicity for which diffraction is still absent at the operating wavelength λ_1 or λ_2. For the practical realization, the selection of periodicity is motivated by several factors. On the one hand, a larger periodicity enhances fabrication quality and permits a bigger variation range of cylindrical diameter. On the other hand, the periodicity must be smaller than the value at which diffraction zone begins in order to ensure that only the zeroth diffraction order contributes to reflection without energy leakage to other diffraction orders. As an example, let us consider the periodicities of metasurfaces that are 3% smaller than the border of the diffraction zone. These values are $P_i(\lambda_i) = 97\% \cdot \lambda_d^i$, where $P_1 \approx 586$ nm and $P_2(\lambda_2) \approx 860$ nm, accordingly.

After selecting the period of the metasurface, we proceed to determine the dimensional parameters of the building blocks (cylindrical particles). The reflection plots with varying nanoparticle height and diameter at fixed wavelengths and periodicities are presented in **Figure 2**a,b. Note that we have chosen the maximum diameter value to be less than the corresponding periodicity. The used refractive indices of crystalline silicon for these simulations are sourced from the literature:[66,67] $n_{Si}(\lambda_1) = 3.55$ and $n_{Si}(\lambda_2) = 3.48$. The total reflection, indicated by the red color, occurs either on the MD or ED resonant responses. The contribution of dipole moments to the reflection coefficient is identified by examining the electric field distribution within the nanoparticle positioned on the sapphire substrate and calculating its multipole moments.[68,69] At the point where two resonances come into close proximity, the reflection decays due to the Kerker effect. This corresponds to the area around the aspect ratio $0.4 \leq H/D \leq 0.5$, marked by the white dashed lines. The undesirable height of nanocylinders for the wavelength of 1064 nm is $H \in (170; 190)$ nm, for 1550 nm is $H \in (245; 280)$ nm. The alteration of periodicity results in a slight adjustment for these values (see details in Supporting Information).

Using the results in Figure 2, four heights (H) are specified for fabrication: 70, 130, 210, and 300 nm. It is important to note that a height of 70 nm is selected only for the structures to be resonant at 1064 nm wavelength according to Figure 2a. For this height and the wavelength of 1550 nm (Figure 2b), the diameter tuning fails to achieve high reflectivity. Note again that the smaller periodicity values only lead to a slight shift of the red reflective zone in Figure 2b toward larger cylindrical heights.

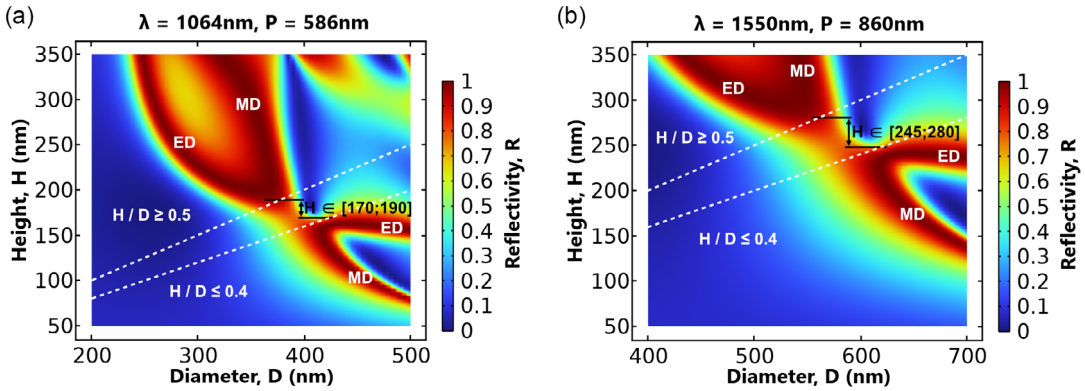

Figure 2. Reflectivity of metasurfaces on a sapphire substrate depending on the diameter and height of the nanocylinder at fixed wavelength (in vacuum) and periodicity. The white dashed lines indicate regions of low reflectivity, characterized by $(0.4 \leq H/D \leq 0.5)$. Multipole moments are determined by analyzing the calculated field distribution inside the metasurface nanocylinders located on the substrate.[44] a) The calculations are conducted at a wavelength of $\lambda_1 = 1064$ nm with a periodicity of $P_1 = 586$ nm. Undesirable nanocylinder heights are restricted to the range of $H \in [170; 190]$ nm. b) At a wavelength of $\lambda_2 = 1550$ nm and corresponding periodicity of $P_2 = 860$ nm, the prohibited nanocylinder heights fall within $H \in [245; 280]$ nm.

Table 1. The height (thickness) of poly-Si layers and their refractive indices measured by ellipsometer.

Intended height [nm]	Actual height [nm]	n@1064 [nm]	n@1550 [nm]
70	72	4.17	
130	132	4.00	3.86
210	211	4.05	3.92
300	297	4.04	3.91

The procedure described above allows us to select the heights of the cylinders and thereby determine the thickness of the silicon films that must be applied to the sapphire substrates during the fabrication of metasurfaces. The practical deposition of silicon is achieved through the low-pressure chemical vapor deposition (LPCVD) technique, which allows for the formation of poly-Si layers with a controlled height based on the deposition time. The LPCVD technique was preferred over commercial SOS samples due to its greater flexibility in selecting silicon thickness and sapphire crystal orientation. The sapphire substrates are sourced from commercially available products (https://www.siegertwafer.de/Saphir-Wafer.html) and have a thickness of 650 μm and C-plane (0001) orientation.

2.3. Size Adjustment

As a next step, the values of diameter and periodicity are carefully chosen for the fabricated poly-Si layers. The deposited poly-Si exhibits a deviation from crystalline Si in the refractive index that was used for the simulations in Figure 2. Additionally, the thickness of the fabricated poly-Si layers diverges from the intended values, attributed to the constraints in the manufacturing process. Ellipsometry serves as a valuable method for characterizing the silicon layer properties. The intended heights and measured thickness of the experimental Si layers, along with the measured refractive indices for the desired wavelengths, are provided in **Table 1**.

Operating with the actual refractive index and nanocylinder height (the layer thickness), the dimensional parameters of diameter and periodicity can be numerically selected among a wide range of possible solutions to ensure total reflection.

As an example, the results of numerical analysis for the fabricated poly-Si layer of 211 nm thickness at the wavelengths of 1064 and 1550 nm are presented in **Figure 3**, where the reflectivity as a function of the particle diameter and metasurface periodicity at fixed wavelength and particle height is shown. Several factors are taken into account when selecting the appropriate particle diameter and metasurface periodicity. 1) In the fabrication process, the range of variation in diameter is greater than that of periodicity. Therefore, the solution in the broadest high-reflectivity region for diameter (indicated by the white square) is the most favorable. 2) Additionally, to ensure good metasurface quality for the first fabrication process, the distance between nanoparticles exceeds 100 nm. Given this condition, for a highly reflective mirror at 1064 nm, parameters are chosen with a slight preference for larger periodicity (see the cross sign in Figure 3a). The parameter sets for both wavelengths are denoted by white crosses in Figure 3.

The graphs like in Figure 3 for other thicknesses are presented in the Figure S2, Supporting Information. Using numerical simulation and the above factors, metasurface parameters are determined for all poly-Si layers. The result is presented in **Table 2**.

2.4. Metasurface Resonant Behavior

Predicting the system's behavior is an essential step before its experimental realization and characterization process. The numerical analysis of metasurfaces with parameters from Table 2 is presented in **Figure 4**. Each panel provides information about reflection and ED and MD resonances of the corresponding metasurfaces. The blue lines correspond to metasurfaces with the tuned maximum reflectivity at 1064 nm wavelength, while the magenta lines correspond to metasurfaces with maximum reflectivity at 1550 nm. Vertical dashed lines of the corresponding colors mark the Rayleigh anomalies separating the diffraction and diffractionless zones for specific metasurfaces.

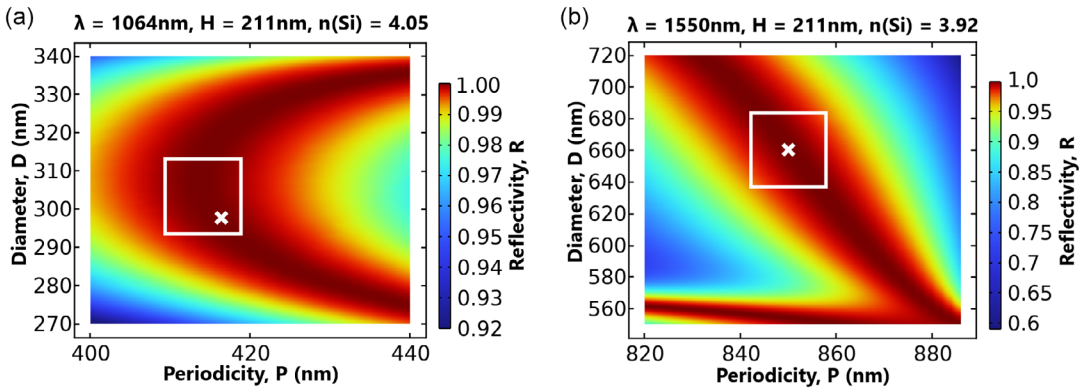

Figure 3. Diameter (D) and periodicity (P) variations in the reflectivity images for 211 nm cylinder height in order to define the optimal parameters for the metasurface fabrication. The white squares highlight the broadest regions of high reflectivity across varying diameters. The white crosses indicate the solutions (D and P) chosen for the fabrication. a) The analysis is conducted at the wavelength of $\lambda_1 = 1064$ nm, with the refractive index of poly-silicon cylinders $n_{Si}(\lambda_1) = 4.05$ and the substrate's refractive index $n_{Al_2O_3}(\lambda_1) = 1.755$. b) The structure at the wavelength of $\lambda_2 = 1550$ nm, with the refractive indices of cylinders and substrate being $n_{Si}(\lambda_2) = 3.92$ and $n_{Al_2O_3}(\lambda_2) = 1.746$, respectively.

Table 2. Diameter (D) and periodicity (P) parameters for fabrication process. The gray color indicates the parameters of $H/D \leq 0.4$; the teal color corresponds to $H/D \geq 0.5$.

Dimensional parameters of nanoparticles in nm		
	1064 nm (I)	1550 nm (II)
$H = 72$ nm	$D = 423, P = 586$	–
$H = 132$ nm	$D = 370, P = 586$	$D = 623, P = 860$
$H = 211$ nm	$D = 297, P = 416$	$D = 660, P = 850$
$H = 297$ nm	$D = 259, P = 396$	$D = 472, P = 668$

The dashed and dashed-dot red and green lines at the bottom of the reflection curves represent the absolute values of the ED $|p_x|$ and MD $|m_y|$ moments, respectively, calculated for nanocylinders in the array placed on a sapphire substrate. These values are normalized to twice the maximum value of the resonant dipole moment for each metasurface, helping to understand and elucidate the relation between the dipole resonances and the reflection resonances. It is important to note that the information about dipole moments in the diffraction zone is not presented in these figures.

Figure 4a contains information only about the structure resonant at 1064 nm wavelength due to the impossibility of designing a metasurface with a cylindrical height of 72 nm resonant at 1550 nm (Figure 2b). The resonant peak of reflection in this figure corresponds to the ED resonance and reaches 100% reflectivity at the desired wavelength. The vertical blue line around 1028 nm indicates the start of the diffraction zone extending into the spectral range of shorter wavelengths. The remaining figures can be described in an analogous manner, with the exception that both metasurfaces, resonant at 1064 and 1550 nm wavelengths, are presented on the same spectrum. It is important that all resonant reflections are directly related to the dipole resonances of the particles in the corresponding metasurface.

Comparing the quality factor of the reflective peaks for the metasurfaces with various dimensional parameters, it is apparent that the nanostructures with the highest nanocylinders of 297 nm display the broadest resonant responses. This broadening results from the resonant contributions of ED and MD resonances, which are closely spectrally positioned. Therefore, these structures are more likely to exhibit high reflection despite potential fabrication inaccuracies.

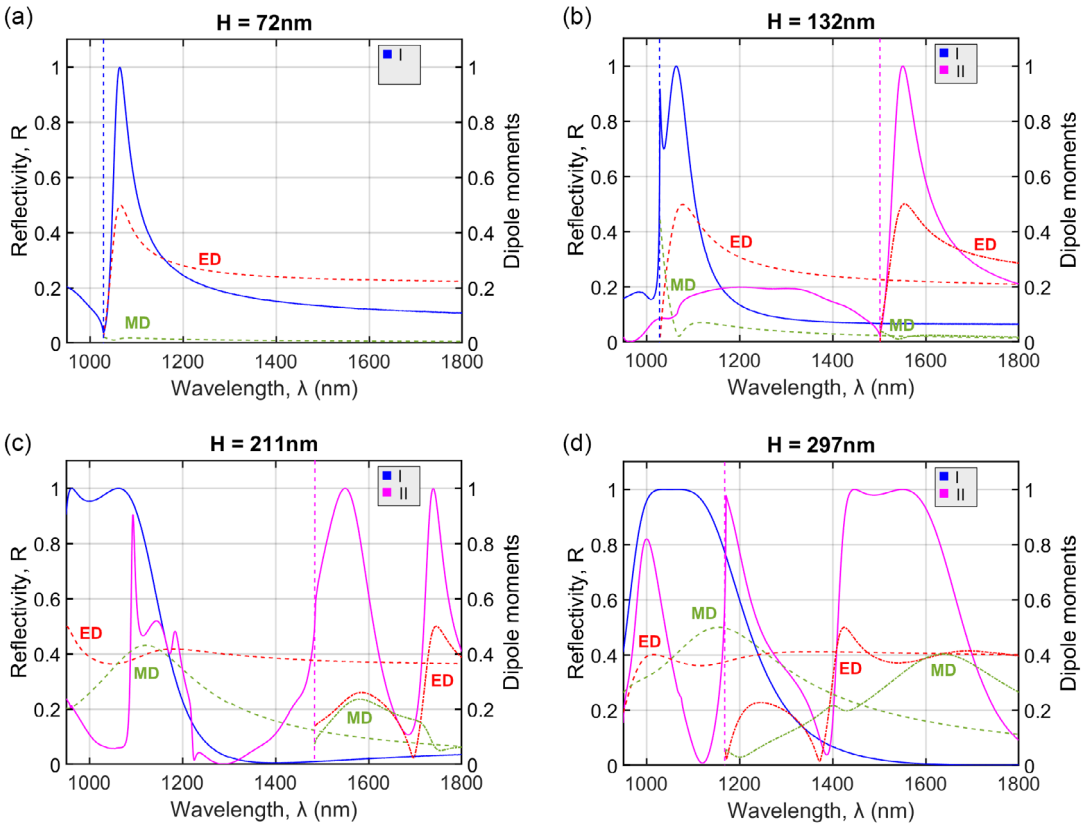

Figure 4. Reflectivity (left axis) and dipole decomposition (right axis) of the metasurfaces at infrared wavelengths. The blue and magenta lines correspond to the metasurfaces with reflectivity resonance at the wavelengths of 1064 (I) and 1550 nm (II), respectively. The red and green lines indicate the absolute values of ED ($|p_x|$) and MD ($|m_y|$) moments normalized to the twice of maximum: the dashed lines for reflection resonance at $\lambda = 1064$ nm; the dashed-dot lines for reflection resonance at $\lambda = 1550$ nm. The dimensional parameters of the metasurfaces at the wavelengths of 1064 and 1550 nm: a) $D = 423$ nm, $P = 586$ nm; b) $D = 370$ nm, $P = 586$ nm; $D = 623$ nm, $P = 860$ nm; c) $D = 297$ nm, $P = 416$ nm; $D = 660$ nm, $P = 850$ nm; and d) $D = 259$ nm, $P = 396$ nm; $D = 472$ nm, $P = 668$ nm.

3. Fabrication and Experimental Characterization of Metasurfaces

3.1. Fabrication

The fabrication of 100×100 μm^2 metasurface from a silicon layer on sapphire is conducted using a combination of the dry etching and lift-off techniques. The sequential steps of this method are presented in **Figure 5**.

The sapphire wafers, previously coated with poly-Si layers, are cut into smaller samples of the size 1.5×1.5 cm^2. A 150 nm thick layer of positive e-beam resist (AR-P 6200.09–CSAR 62) is spin-coated on top of these samples. Additionally, a conductive aluminum layer of 20 nm thickness is deposited using a thermal evaporator. This layer is applied to mitigate charging effects during the EBL process. The structures are exposed by an electron beam with a spot size of 7.5 nm and dose of 325 μC cm^{-2}. Then, the aluminum layer is removed in diluted phosphoric acid and the resist is developed for 2 min in AR600-546. The remaining resist features a layer with holes whose diameter corresponds to the diameter of the future cylinders.

The next step is the creation of a hard mask to etch the poly-Si layer. For this, a 25 nm layer of Al is deposited using e-beam evaporation. This Al layer has to be thick enough to resist during the poly-Si etch but thin enough such that there is no merging of the Al deposited on top of the resist with the one in the gaps.

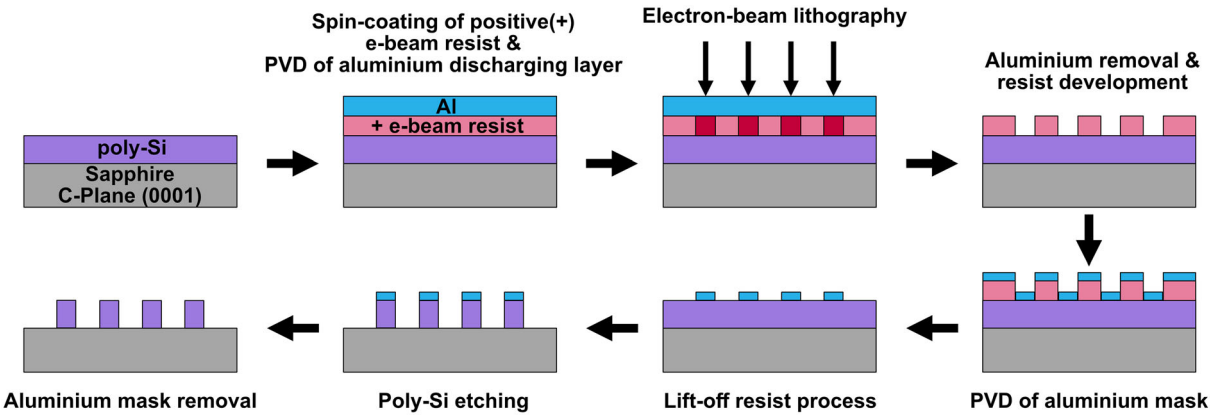

Figure 5. The fabrication steps in the lift-off lithographic technique.

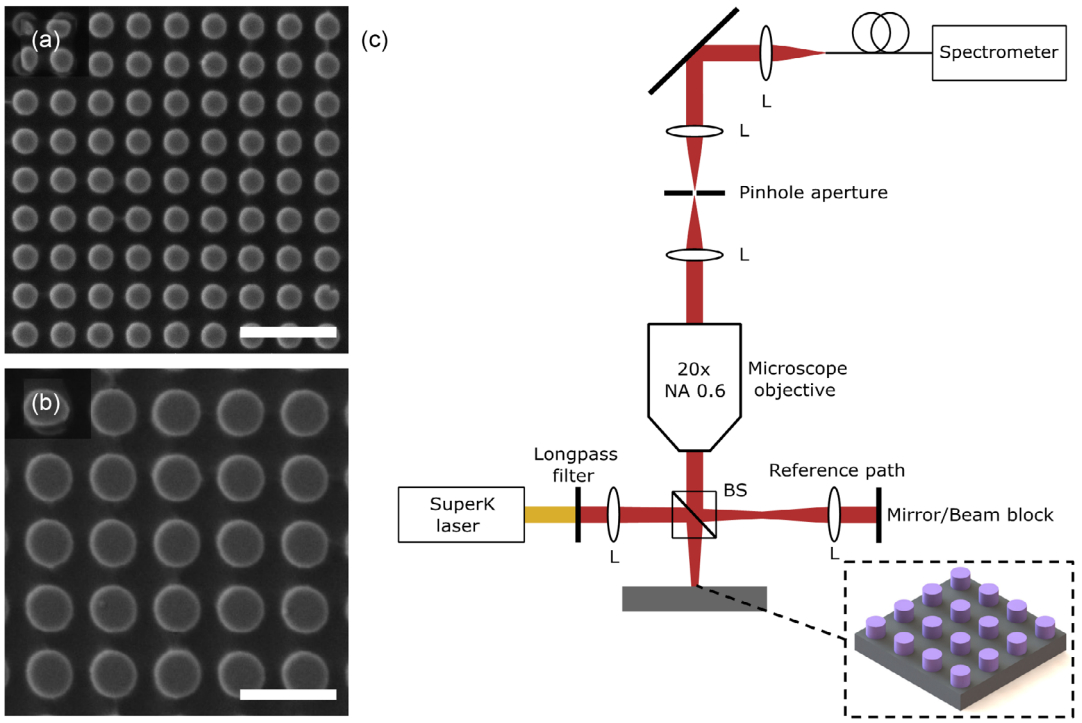

Figure 6. SEM images of fabricated nanocylinder metasurfaces with $H = 297$ nm and the following parameters: a) $D \approx 259$ nm, $P \approx 396$ nm and b) $D \approx 472$ nm, $P \approx 668$ nm. Scalebars: 1 μm. c) The experimental setup for reflection characterization.

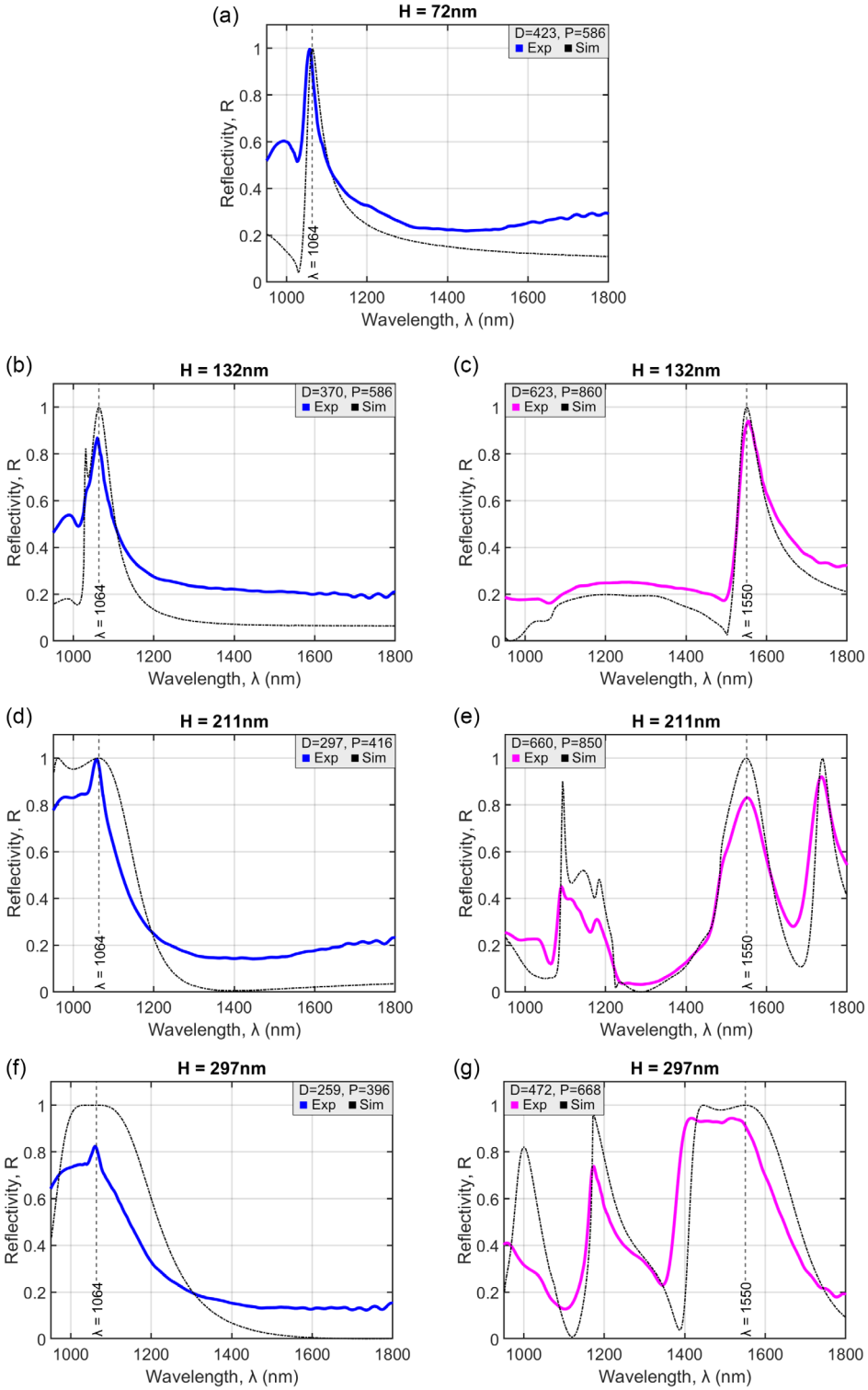

Figure 7. Reflectivity of fabricated metasurfaces compared to their theoretical predictions. The reflectivity experimentally measured for the metasurfaces designed with mirror effect at 1064 nm wavelength is represented by the blue lines in a,b,d,f); for metasurfaces with mirror effect at 1550 nm wavelength the experimental reflectivity is presented by magenta lines in c,e,g). The thickness of the lines characterizes the uncontrollable small variation of the signal during the measurements. The black dash-dotted lines correspond to the theoretical simulations (Sim). The dashed vertical lines show the spectral positions of the wavelengths, demonstrating the alignment between the experimental and theoretical reflection resonances.

We then lifted off the Al layer by removing the resist in 1165 remover. This way, the obtained hard mask is where the future cylinders will be. The final steps include the reactive ion etching of poly-silicon using C_4F_8 and SF_6 gases and the removal of the aluminum mask with phosphoric acid.

The additional details of the fabrication process are presented in Supporting Information.

3.2. Characterization Setup

Scanning electron microscope (SEM) images of the fabricated structures are shown in **Figure 6**a,b. The shape of the cylinders and their arrangement agree well with the design. However, small residuals of the aluminum mask after its removal process were found on top of the cylinders. The particularity is observed specifically in the case of the sapphire substrate. Addressing this issue will be important for future improvements in the metasurface fabrication process.

The metasurface reflectivity was characterized using the experimental setup depicted in Figure 6c. A supercontinuum laser (SuperK EXTREME from NKT Photonics) was used as a light source, where the visible part of the spectrum was filtered out by a long-pass filter. The reflection spectra were measured by Ocean Insight NIRQuest + 1.7 spectrometer with InGaAs linear array. A reference path with a mirror on a flip mount was used to minimize the influence of the spectral instability of the light source. Finally, all spectra were normalized to the reflection from a commercial mirror (protected silver mirror PF10-03-P01 from Thorlabs with reflectivity of 97% at 1064 nm, 98% at 1550 nm), placed instead of the sample. Further details of the characterization setup can be found in Supporting Information.

3.3. Experimental Results

The measured reflectivities of all metasurfaces together with their numerical simulation are presented in **Figure 7**. By comparing the experimental and theoretical reflection peaks, the very good agreement in the resonant behavior at the selected wavelengths of 1064 and 1550 nm is clearly visible.

The shape of the peaks and their quality factors match the simulations. Nevertheless, an intriguing distinction between theory and fabrication results is observed in Figure 7d,f for metasurfaces resonant at the 1064 nm wavelength. From numerical simulations, the resonant peaks are expected to be broad due to the close proximity of ED and MD resonant responses. However, in the experiment, the resonance at the MD moment appears more pronounced than at the ED moment. It may be associated with small residuals of the aluminum mask, resulting in stronger suppression of the ED resonance, which is more sensitive to the external environment, compared to the MD resonance.

It is observed that outside of the resonance conditions, the measured reflectivity spectra exceed the values predicted by simulations. This deviation can primarily be attributed to extra reflection originating from the reverse side of the samples (sapphire–air interface and from the additional glass slide used as a sample holder). Considering the refractive indices of sapphire and glass, this additional reflection contributes ≈15% of reflectivity outside of the resonance. However, at resonant frequencies, the influence of this additional reflection is almost negligible since practically all light is reflected by the metasurface side.

Overall, the reflectivity of most experimental metasurfaces shows high values at designed wavelengths, which is a good result for the first fabrication realization. Notably, some samples demonstrated near-unity reflectance at 1064 nm wavelength (Figure 7a,d). The best reflectivity at 1550 nm wavelength was found to be above 95% (Figure 7c,g). The first fabrication attempt validates the methodology used to realize metasurfaces for the specified application and shows quite good agreement with the theory. A slight reduction of the observed reflectivity can be attributed to the diffusive scattering caused by uncontrollable fabrication imperfections and challenges related to the measurement experimental setup. Future fabrication and characterization processes have to be adapted and improved to achieve a better mirror effect approaching 100%. As our research shows, there are no fundamental barriers to achieving this goal.

4. Conclusion

This article demonstrates a strategy and details of the fabrication process of metasurface mirrors operating at 1064 and 1550 nm wavelengths. It systematically outlines the selection of parameters based on operational wavelengths, material types, and the cylindrical configuration of the metasurface nanoparticles. Additionally, the article shows an estimation analysis of the expected behavior of these metasurfaces and offers a detailed description of the step-by-step fabrication process with the encountered challenges. As the final step, the characterization process is detailed along with the obtained results, which closely align with the theoretical expectations. The reflectivity of all structures exceeds 80% and, for some, reaches above 95%. Discrepancies between theoretical predictions and experimental results are primarily associated with the particular fabrication and characterization nuances, which can be refined in future work. Nevertheless, the findings from this research will undoubtedly support the substantial improvement of the sample realization process, bringing us closer to achieving total reflectivity.

The current investigation lays a foundation for future improvement and production of the metasurfaces for the implementation as an alternative or compatible mirror design in GW technology.

Supporting Information

Supporting Information is available from the Wiley Online Library or from the author.

Acknowledgements

The authors from Germany acknowledge financial support from the Deutsche Forschungsgemeinschaft (DFG, German Research Foundation) under Germany's Excellence Strategy within the Cluster of Excellence PhoenixD (EXC 2122, Project ID 390833453) and the Cluster of Excellence QuantumFrontiers (EXC 2123, Project ID 390837967). The authors from Denmark acknowledge the financial support from the Danish National Research Foundation within the Center for Polariton-driven Light–Matter Interactions (POLIMA). R.M. and A.L. also

acknowledge the support from the Independent Research Fund "Memory" project (ID 3105-00339B).

Conflict of Interest

The authors declare no conflict of interest.

Author Contributions

Mariia Matiushechkina: Conceptualization (equal); Formal analysis (equal); Investigation (equal); Software (lead); Writing—original draft (lead). **Andrey B. Evlyukhin**: Conceptualization (lead); Formal analysis (equal); Investigation (equal); Methodology (lead); Supervision (equal); Writing—review and editing (equal). **Radu Malureanu**: Conceptualization (equal); Data curation (equal); Formal analysis (equal); Investigation (equal); Resources (equal); Writing—review and editing (equal). **Vladimir A. Zenin**: Formal analysis (equal); Investigation (equal); Software (equal); Validation (equal); Visualization (equal); Writing—review and editing (equal). **Torgom Yezekyan**: Formal analysis (equal); Investigation (equal); Resources (equal); Validation (equal); Visualization (equal); Writing—review and editing (equal). **Andrei Lavrinenko**: Data curation (lead); Investigation (equal); Project administration (equal); Resources (equal); Supervision (equal); Validation (equal); Writing—review and editing (equal). **Sergey I. Bozhevolnyi**: Data curation (equal); Formal analysis (equal); Methodology (equal); Project administration (equal); Supervision (equal); Validation (lead); Writing—review and editing (equal). **Boris N. Chichkov**: Data curation (equal); Formal analysis (equal); Methodology (equal); Project administration (lead); Supervision (equal); Validation (equal); Writing—review and editing (equal). **Michèle Heurs**: Data curation (equal); Formal analysis (equal); Funding acquisition (equal); Methodology (equal); Project administration (lead); Supervision (lead); Writing—review and editing (equal).

Data Availability Statement

The data that support the findings of this study are available from the corresponding author upon reasonable request.

Keywords

coating, metamaterials, metamirrors, metasurfaces, multipole response, optical nanostructures

Received: July 18, 2024
Published online:

[1] P. Genevet, F. Capasso, F. Aieta, M. Khorasaninejad, R. Devlin, *Optica* **2017**, *4*, 139.
[2] K. Koshelev, Y. Kivshar, *ACS Photonics* **2021**, *8*, 102.
[3] V. E. Babicheva, A. B. Evlyukhin, *J. Appl. Phys.* **2021**, *129*, 4.
[4] A. Arbabi, Y. Horie, M. Bagheri, A. Faraon, *Nat. Nanotechnol.* **2015**, *10*, 937.
[5] Y. Hu, X. Wang, X. Luo, X. Ou, L. Li, Y. Chen, Y. Ping Yang, S. Wang, H. Duan, *Nanophotonics* **2020**, *9*, 3755.
[6] G. Grinblat, *ACS Photonics* **2021**, *8*, 3406.
[7] B. Sain, C. Meier, T. Zentgraf, *Adv. Photonics* **2019**, *1*, 1.
[8] K. Koshelev, S. Kruk, E. Melik-Gaykazyan, J.-H. Choi, A. Bogdanov, H.-G. Park, Y. Kivshar, *Science* **2020**, *367*, 288.
[9] P. R. Sharapova, S. S. Kruk, A. S. Solntsev, *Laser Photonics Rev.* **2023**, *17*, 2200408.
[10] F. Yesilkoy, E. R. Arvelo, Y. Jahani, M. Liu, A. Tittl, V. Cevher, Y. Kivshar, H. Altug, *Nat. Photonics* **2019**, *13*, 390.
[11] M. L. Tseng, Y. Jahani, A. Leitis, H. Altug, *ACS Photonics* **2021**, *8*, 47.
[12] S. T. Ha, Y. H. Fu, N. K. Emani, Z. Pan, R. M. Bakker, R. Paniagua-Domínguez, A. I. Kuznetsov, *Nat. Nanotechnol.* **2018**, *13*, 1042.
[13] S. Murai, G. W. Castellanos, T. V. Raziman, A. G. Curto, J. G. Rivas, *Adv. Opt. Mater.* **2020**, *8*, 1902024.
[14] A. V. Prokhorov, M. Y. Gubin, A. V. Shesterikov, A. V. Arsenin, V. S. Volkov, A. B. Evlyukhin, *Nano Lett.* **2023**, *23*, 11105.
[15] E. Engay, D. Huo, R. Malureanu, A.-I. Bunea, A. Lavrinenko, *Nano Lett.* **2021**, *21*, 3820.
[16] W. T. Chen, A. Y. Zhu, F. Capasso, *Nat. Rev. Mater.* **2020**, *5*, 604.
[17] Y. Wu, Y. Chen, Q. Song, S. Xiao, *Adv. Opt. Mater.* **2021**, *9*, 2002126.
[18] G. Yoon, T. Tanaka, T. Zentgraf, J. Rho, *J. Phys. D: Appl. Phys.* **2021**, *54*, 383002.
[19] J. Yang, S. Gurung, S. Bej, P. Ni, H. W. Howard Lee, *Rep. Prog. Phys.* **2022**, *85*, 036101.
[20] A. I. Kuznetsov, M. L. Brongersma, J. Yao, M. K. Chen, U. Levy, D. P. Tsai, N. I. Zheludev, A. Faraon, A. Arbabi, N. Yu, D. Chanda, K. B. Crozier, A. V. Kildishev, H. Wang, J. K. W. Yang, J. G. Valentine, P. Genevet, J. A. Fan, O. D. Miller, A. Majumdar, J. E. Fröch, D. Brady, F. Heide, A. Veeraraghavan, N. Engheta, A. Alù, A. Polman, H. A. Atwater, P. Thureja, R. Paniagua-Dominguez, et al., *ACS Photonics* **2024**, *11*, 816.
[21] S. Ebel, Y. Deng, M. Hentschel, C. Meng, S. Sande, H. Giessen, F. Ding, S. I. Bozhevolnyi, *Adv. Photonics Nexus* **2023**, *2*, 016005.
[22] A. S. Schwanecke, V. A. Fedotov, V. V. Khardikov, S. L. Prosvirnin, Y. Chen, N. I. Zheludev, *J. Opt. A: Pure Appl. Opt.* **2007**, *9*, L1.
[23] S. Liu, M. B. Sinclair, T. S. Mahony, Y. C. Jun, S. Campione, J. Ginn, D. A. Bender, J. R. Wendt, J. F. Ihlefeld, P. G. Clem, J. B. Wright, I. Brener, *Optica* **2014**, *1*, 250.
[24] Q. Zhang, C. Liu, G. Gan, X. Cui, *Opt. Commun.* **2017**, *402*, 226.
[25] A. B. Evlyukhin, S. M. Novikov, U. Zywietz, R. L. Eriksen, C. Reinhardt, S. I. Bozhevolnyi, B. N. Chichkov, *Nano Lett.* **2012**, *12*, 3749.
[26] A. Han, J. V. Moloney, V. E. Babicheva, *J. Chem. Phys.* **2022**, *156*, 11.
[27] Y. Huang, Q. Zhao, S. K. Kalyoncu, R. Torun, O. Boyraz, *J. Opt. Soc. Am. B* **2016**, *33*, 189.
[28] Z. Ma, S. M. Hanham, P. Albella, B. Ng, H. T. Lu, Y. Gong, S. A. Maier, M. Hong, *ACS Photonics* **2016**, *3*, 1010.
[29] C. Chen, Z. Wang, Z. Zheng, Y. Liu, W. Huang, L. Chen, *Opt. Express* **2020**, *28*, 38355.
[30] V. Asadchy, Y. Ra'Di, J. Vehmas, S. Tretyakov, *Phys. Rev. Lett.* **2015**, *114*, 095503.
[31] Z. Ma, S. M. Hanham, Y. Gong, M. Hong, *Opt. Lett.* **2018**, *43*, 911.
[32] A. M. H. Wong, G. V. Eleftheriades, *Phys. Rev. X* **2018**, *8*, 011036.
[33] N. M. Estakhri, V. Neder, M. W. Knight, A. Polman, A. Alù, *ACS Photonics* **2017**, *4*, 228.
[34] J. Cheng, S. Inampudi, H. Mosallaei, *Sci. Rep.* **2017**, *7*, 12228.
[35] V. R. Tuz, A. V. Prokhorov, A. V. Shesterikov, V. S. Volkov, B. N. Chichkov, A. B. Evlyukhin, *Ann. Phys.* **2023**, *535*, 2300111.
[36] V. R. Tuz, A. B. Evlyukhin, *Nanophotonics* **2021**, *10*, 4373.
[37] N. Yu, F. Capasso, *Nat. Mater.* **2014**, *13*, 139.
[38] J. Van De Groep, M. L. Brongersma, *Nano Lett.* **2018**, *18*, 3857.
[39] V. Asadchy, M. Albooyeh, S. Tretyakov, *J. Opt. Soc. Am. B* **2016**, *33*, A16.
[40] J. Algorri, B. García-Cámara, A. Cuadrado, J. Sánchez-Pena, R. Vergaz, *Nanomaterials* **2017**, *7*, 177.
[41] W. Liu, *Phys. Rev. Lett.* **2017**, *119*, 123902.
[42] A. B. Evlyukhin, C. Reinhardt, A. Seidel, B. S. Luk'Yanchuk, B. N. Chichkov, *Phys. Rev. B* **2010**, *82*, 045404.
[43] V. E. Babicheva, A. B. Evlyukhin, *Opt. Lett.* **2018**, *43*, 5186.
[44] M. Matiushechkina, A. B. Evlyukhin, V. A. Zenin, M. Heurs, B. N. Chichkov, *Opt. Mater.* **2023**, *138*, 113618.

[45] P. Spinelli, M. A. Verschuuren, A. Polman, *Nat. Commun.* **2012**, *3*, 692.
[46] K. V. Baryshnikova, M. I. Petrov, V. E. Babicheva, P. A. Belov, *Sci. Rep.* **2016**, *6*, 22136.
[47] M. Matiushechkina, A. B. Evlyukhin, V. A. Zenin, B. N. Chichkov, M. Heurs, *Adv. Opt. Mater.* **2024**, *12*, 2400191.
[48] R. Nawrodt, S. Rowan, J. Hough, M. Punturo, F. Ricci, J.-Y. Vinet, *Gen. Relativ. Gravitation* **2011**, *43*, 593.
[49] J. Steinlechner, *Philos. Trans. R. Soc. A* **2018**, *376*, 20170282.
[50] G. M. Harry, A. M. Gretarsson, P. R. Saulson, S. E. Kittelberger, S. D. Penn, W. J. Startin, S. Rowan, M. M. Fejer, D. R. M. Crooks, G. Cagnoli, J. Hough, N. Nakagawa, *Classical Quantum Gravity* **2002**, *19*, 897.
[51] S. Reid, I. Martin, *Coatings* **2016**, *6*, 61.
[52] J. Aasi, B. P. Abbott, R. Abbott, T. Abbott, M. R. Abernathy, K. Ackley, C. Adams, T. Adams, P. Addesso, R. X. Adhikari, V. Adya, C. Affeldt, N. Aggarwal, O. D. Aguiar, A. Ain, P. Ajith, A. Alemic, B. Allen, D. Amariutei, S. B. Anderson, W. G. Anderson, K. Arai, M. C. Araya, C. Arceneaux, J. S. Areeda, G. Ashton, S. Ast, S. M. Aston, P. Aufmuth, C. Aulbert, et al., *Classical Quantum Gravity* **2015**, *32*, 074001.
[53] H. Lück (ET Editorial Team), *Design Report Update 2020 for the Einstein Telescope* **2020**, https://apps.et-gw.eu/tds/?content=3&r=17245.
[54] A. V. Cumming, L. Cunningham, G. D. Hammond, K. Haughian, J. Hough, S. Kroker, I. W. Martin, R. Nawrodt, S. Rowan, C. Schwarz, A. A. Van Veggel, *Classical Quantum Gravity* **2014**, *31*, 025017.
[55] S. Rowan, G. Cagnoli, P. Sneddon, J. Hough, R. Route, E. K. Gustafson, M. M. Fejer, V. Mitrofanov, *Phys. Lett. A* **2000**, *265*, 5.
[56] E. D. Palik, in *Handbook of Optical Constants of Solids*, Vol. *3*, Academic Press, San Diego **1998**.
[57] W. Yang, S. Xiao, Q. Song, Y. Liu, Y. Wu, S. Wang, J. Yu, J. Han, D.-P. Tsai, *Nat. Commun.* **2020**, *11*, 1864.
[58] Y. Huang, E. K. Tien, S. Gao, S. K. Kalyoncu, Q. Song, F. Qian, E. Adas, D. Yildirim, O. Boyraz, *Appl. Phys. Lett.* **2011**, *99*, 181122.
[59] A. Arbabi, R. M. Briggs, Y. Horie, M. Bagheri, A. Faraon, *Opt. Express* **2015**, *23*, 33310.
[60] S. Wen, X. Xue, S. Wang, Y. Ni, L. Sun, Y. Yang, *Light: Sci. Appl.* **2024**, *13*, 88.
[61] T. Akutsu, M. Ando, K. Arai, Y. Arai, S. Araki, A. Araya, N. Aritomi, Y. Aso, S. Bae, Y. Bae, L. Baiotti, R. Bajpai, M. A. Barton, K. Cannon, E. Capocasa, M. Chan, C. Chen, K. Chen, Y. Chen, H. Chu, Y.-K. Chu, S. Eguchi, Y. Enomoto, R. Flaminio, Y. Fujii, M. Fukunaga, M. Fukushima, G. Ge, A. Hagiwara, S. Haino, et al., *Prog. Theoret. Exp. Phys.* **2020**, *2021*, 05A101.
[62] D. G. Baranov, D. A. Zuev, S. I. Lepeshov, O. V. Kotov, A. E. Krasnok, A. B. Evlyukhin, B. N. Chichkov, *Optica* **2017**, *4*, 814.
[63] A. B. Evlyukhin, C. Reinhardt, B. N. Chichkov, *Phys. Rev. B* **2011**, *84*, 235429.
[64] I. Staude, A. E. Miroshnichenko, M. Decker, N. T. Fofang, S. Liu, E. Gonzales, J. Dominguez, T. S. Luk, D. N. Neshev, I. Brener, Y. Kivshar, *ACS Nano* **2013**, *7*, 7824.
[65] V. G. Kravets, F. Schedin, A. N. Grigorenko, *Phys. Rev. Lett.* **2008**, *101*, 087403.
[66] M. A. Green, *Sol. Energy Mater. Sol. Cells* **2008**, *92*, 1305.
[67] H. H. Li, *J. Phys. Chem. Ref. Data* **1980**, *9*, 561.
[68] R. Alaee, C. Rockstuhl, I. Fernandez-Corbaton, *Opt. Commun.* **2018**, *407*, 17.
[69] A. B. Evlyukhin, B. N. Chichkov, *Phys. Rev. B* **2019**, *100*, 125415.

Supporting Information

Design and experimental demonstration of wavelength selective metamirrors on sapphire substrates

Mariia Matiushechkina[1,2] *Andrey B. Evlyukhin*[2,3] *Radu Malureanu*[4] *Vladimir A. Zenin*[5] *Torgom Yezekyan*[6] *Andrei Lavrinenko*[4] *Sergey Bozhevolnyi*[5] *Boris N. Chichkov*[2,3,7] *Michèle Heurs*[1,2,7]

[1]Institute for Gravitational Physics, Leibniz University Hannover, D-30167 Hannover, Germany
[2]Cluster of Excellence PhoenixD, Leibniz University Hannover, Welfengarten 1, 30167 Hannover, Germany
[3]Institute of Quantum Optics, Leibniz University Hannover, Welfengarten 1, 30167 Hannover, Germany
[4]Center for Nano Optics, University of Southern Denmark, Campusvej 55, 5230 Odense, Denmark
[5]Center for Polariton-driven Light-Matter Interactions (POLIMA), University of Southern Denmark, Campusvej 55, 5230 Odense, Denmark
[6]Department of Photonics Engineering, Technical University of Denmark, DK-2800 Kgs. Lyngby, Denmark
[7]Laboratory of Nano and Quantum Engineering, Leibniz Universität Hannover, Hannover, Germany

S1 Parameters

S1.1 Height selection

The reflectivity zone between the height-diameter aspect ratios of $0.4 \leq H/D \leq 0.5$ does not precisely correspond to the Kerker effect zone for small periodicities. The interparticle interaction manifests more strongly, resulting in the aspect ratio H/D being slightly shifted to the higher values (Fig. S1).

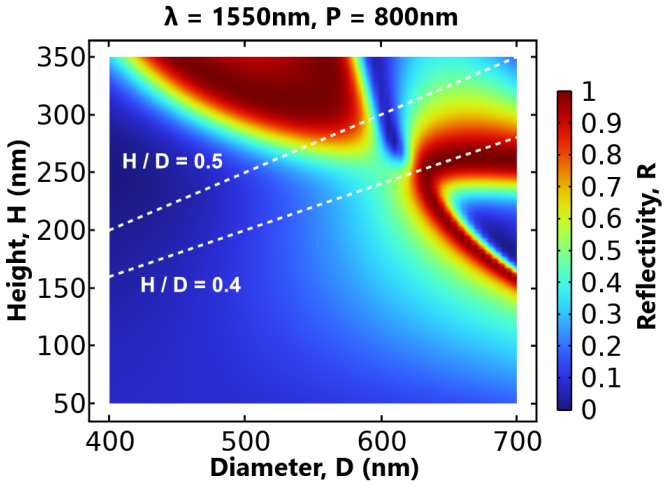

Figure S1: Reflectivity of a metasurface on a sapphire substrate as a function of nanocylinder diameter and height. The simulation is made for a periodicity of $P = 800\,\text{nm}$, the refractive indices of silicon and sapphire are $n_{Si}(1550) = 3.48$, $n_{Al_2O_3}(1550) = 1.746$, respectively. The white dashed lines indicate the height-diameter aspect ratios H/D equal to 0.4 and 0.5.

S1.2 Size adjustment

The numerical analysis of reflectivity for metasurfaces with different cylinder heights (72 nm, 132 nm, and 297 nm) is detailed in Fig. S2. This investigation aims to identify optimal parameter pairs (diameter D and periodicity P) for cylinders at these fixed heights, with incident wavelengths of 1064 and

1550 nm. The chosen fabrication parameters are indicated by white crosses. The refractive index of silicon used in the simulations is taken from the ellipsometry measurements.

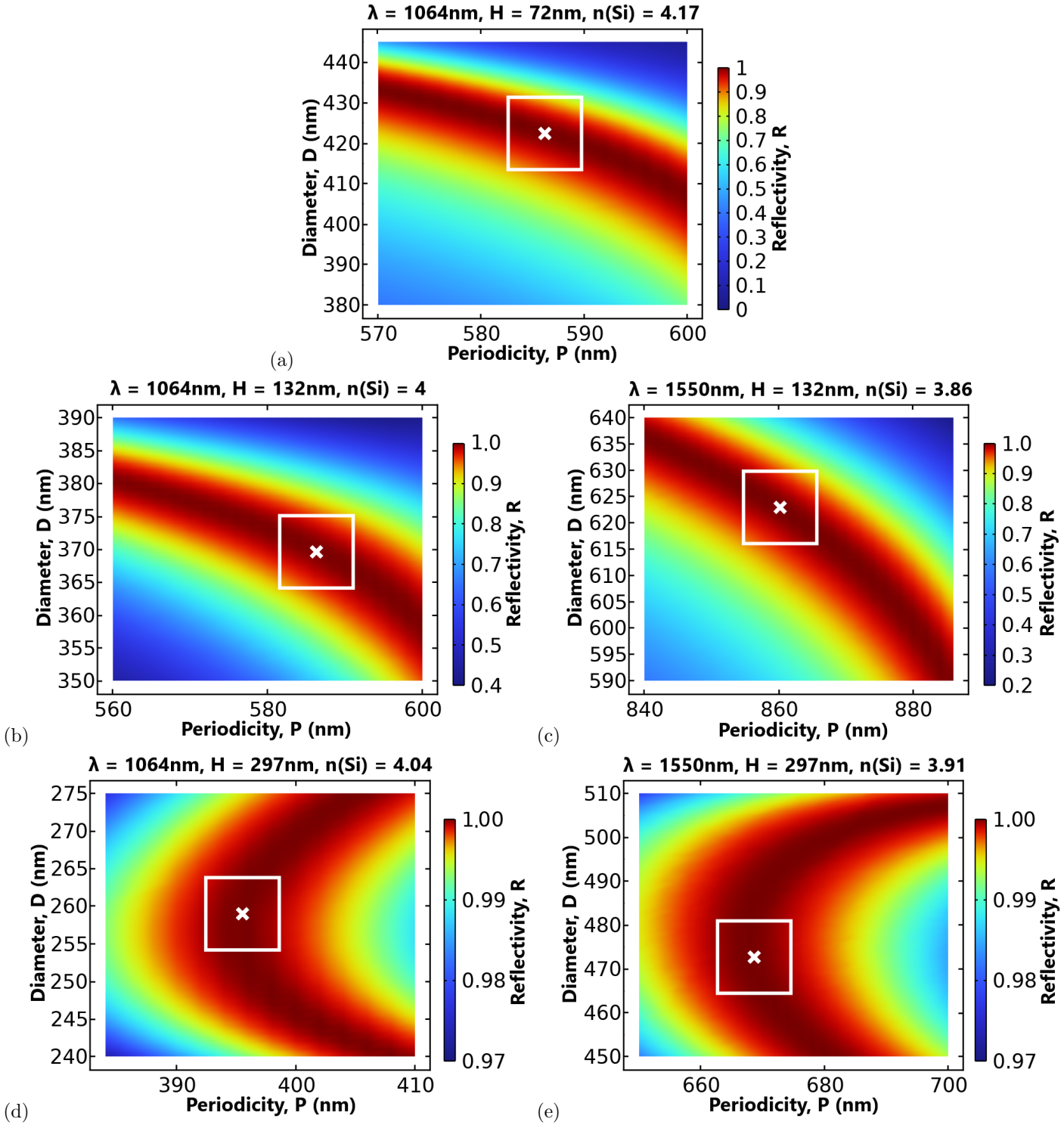

Figure S2: Reflectivity of metasurfaces with cylinder heights of 72 nm, 132 nm, and 297 nm calculated as a function of diameter D and periodicity P for 1064 and 1550 nm wavelengths. The white cross in the frame indicates the chosen solution for the fabrication process.

S2 Fabrication

S2.1 Metasurface design for electron-beam exposure

The lithographic fabrication method has several nuances related to the efficiency of exposing the necessary amount of the photoresist.

The dose factor, which is dependent on the selection of the photoresist material and its thickness, is proportional to the intensity of the electron beam and the exposure time. The dose factor impacts the quality of the structure after development. Producing several structures with different dose factors can help to optimize and reach the necessary resolution. Moreover, the diameter of the cylinders varies after the fabrication process, increasing in size to $15 - 20\,\text{nm}$. This variation is also dependent on the applied dose factor and can lead to the displacement of the resonant peaks.

Considering these aspects, several metasurfaces were fabricated with electron-beam doses varied at $325\,\mu\text{C/cm}^2$, $357,5\,\mu\text{C/cm}^2$, $390\,\mu\text{C/cm}^2$. For each dose, several designs are selected with cylindrical diameters decreased to 12, 16, 20 and 24 nm.

S2.2 Etching of poly-Si from the back side of the sapphire wafer

The low pressure chemical vapor deposition (LPCVD) process creates a layer of poly-Si on both sides of the sapphire wafer. The removal of one side of poly-Si must be implemented as an additional small step. During the etching process, we used Galden HT Low-boiling oil to ensure the thermal contact between the chip and the carrier. Subsequently, the sample undergoes the reactive ion etching, with the side to be removed positioned at the top. As a final step, the sample is cleaned from the resist using IPA and "1165" remover.

S3 Characterization

S3.1 Experimental setup and methodology of measurements

The metasurface reflectivity was characterized using the experimental setup depicted in Fig. S3 . The transmission and reflection spectra were measured by Ocean Insight NIRQuest +1.7 spectrometer with InGaAs linear array. As a light source SuperK EXTREME supercontinuum laser from NKT Photonics (ranging from 400 to 2400 nm) was used, where the visible part of the spectrum was filtered out by long-pass filter. For the sample illumination a 50:50 beam splitting cube was placed between the objective and the sample. The incident beam was loosely focused to a spot of 200 µm in size to decrease unwanted background signal. Additionally, a spatial filtering with a 500 µm pinhole in the image plane is used to collect the reflection only from the metasurface area. The beam that passes the beamsplitter directly, without the sample, is used as an intermediate reference spectrum to reduce the influence of the spectral instability of the light source during the measurements. The reflected signal from the metasurface is collected with an objective (20x, NA of 0.6). After passing through achromatic lenses and a spatial pinhole filter, the reflected light is collected into a multimode fiber and guided to the spectrometer. The measured signal was normalized to the reference mirror with high effective reflection around 97% at 1064 nm and 98% at 1550 nm (protected silver mirror PF10-03-P01 from Thorlabs).

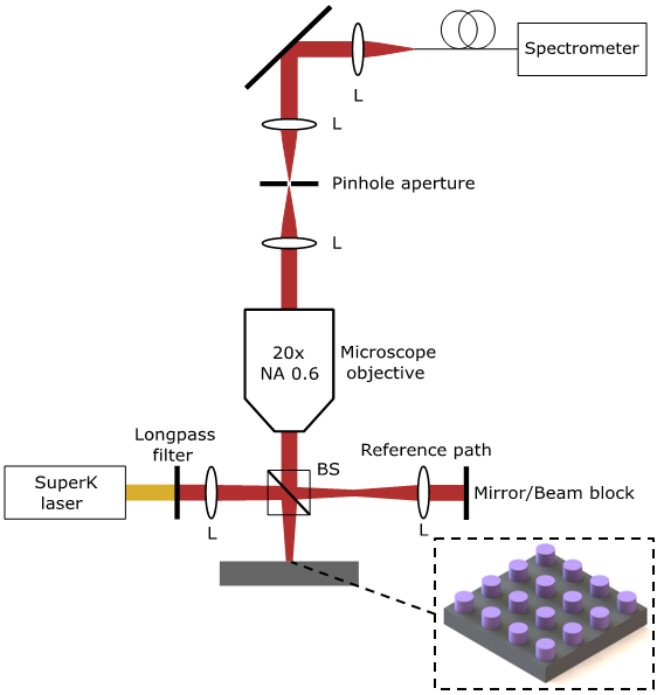

Figure S3: The experimental setup for reflection characterization.

5.6 Summary

The research described in this cumulative thesis contributes to the investigation of metasurface optical properties, with a focus on the principles of reflection. It is aimed at a potential implementation in future GWDs; the results are documented in four publications.

The scientific work begins with the study of reflectivity at 1064 nm wavelength for a metasurface consisting of Si nanospheres embedded in a homogeneous polymer layer. The theoretical analysis and numerical simulations demonstrate the potential of this metasurface to exhibit 100% reflectivity in the absence of losses. As the work progresses, the design of a metasurface on a sapphire substrate with a protective layer for Si spheres is considered, and the impacts of these additional multi-layer structures are taken into account. Advancing further, we consider a cylindrical nanoparticle array resonant at 1550 nm wavelength. Modifying the cylindrical height-to-radius aspect ratio provides control over the spectral position of the ED and MD resonant responses, thereby influencing their contributions to reflectivity. This, in turn, allows for the phase control of the reflected light field in the range of π to $-\pi$. Particular attention is given to the exploration of unconventional resonant states, such as the anapole and Kerker effects. The final stage includes the practical realisation of a poly-Si metasurface on a sapphire substrate, with experimental measurements confirming theoretical predictions. The reflectivity of realised structures reaches more than 95%, validating the correctness of the logical approach in design selection, optimisation and fabrication processes. The results highlight the potential of metasurfaces as efficient reflective mirrors at targeted wavelengths.

This research follows a logical evolution, starting from theoretical and numerical investigations of the simplest high-reflective metasurface design and concluding with the realised prototype of a wavelength-selective metamirror. The deep understanding of the principles of high reflectivity for different types of metasurfaces and the methodologies of optimisation, fabrication and characterisation possibilities, provide valuable insights for future research and the implementation of metamirrors in optical experiments.

Chapter 6

Outlook and Conclusion

6.1 Further perspectives

The study accomplished and presented in this thesis provides a foundation for future research on metasurfaces. Potential improvements could address small-scale projects, such as a more detailed investigation of design performance or optimisation of the fabrication and characterisation processes for silicon-on-sapphire metamirrors. Furthermore, the innovation and insight gained may extend beyond this work and explore metasurfaces composed of alternative materials or adapt them to new applications, including polarization and phase control. In order to organise this wide range of possibilities, the outlook is divided into three sections:

- Optimisation of metasurface mirror effect
- Noise analysis and implementation for gravitational wave detection
- Advanced applications

6.1.1 Optimisation of metasurface mirror effect

The metasurface mirror made of silicon-on-sapphire can be further investigated and improved. Future research could be directed towards enhancing reflectivity, ensuring reproducibility and stability of the fabrication results, and exploring alternative metasurface configurations that may offer refined performance.

Significant advancements can still be achieved in optimising fabrication technology. Although the first prototype of the metamirror demonstrates reflectivity greater than 95%, the results are not consistent across all fabricated structures, with some displaying higher levels of impurities. This inconsistency may be attributed to several factors.

One of these factors is the selection of material for the charge relaxation layer and fabrication mask, which, in this instance, was aluminium. Removing the aluminium from the structures presented certain challenges. The process took significantly longer than expected, requiring several hours rather than several minutes, and, in some cases, caused damage to the resist layer or led to detachment of silicon cylinders. This effect was particularly evident in structures with the thinnest poly-Si layers (72 nm and 132 nm), suggesting a potential reaction between

the aluminium and the sapphire substrate [20]. Optimisation may involve using poly-Si films thicker than 200 nm and experimentally determining the time required to remove aluminium layers of different thickness. However, this approach might not be universally applicable. A more favourable solution could be to use an alternative charge relaxation layer, such as charge dissipation polymer[114], and another mask material, such as chromium (Cr) [115, 116] or silica (SiO_2) [117].

An alternative option is to entirely avoid using the extra mask. This can be achieved either by using a negative resist or by depositing the same positive resist while exposing only the outer area of the cylinders. The development process then removes the outer regions, leaving behind resist-defined cylinders, which are subsequently used for etching. In this case, an aluminium mask becomes unnecessary.

Another critical factor in fabrication is the spacing between cylinders. A larger distance simplifies the cleaning process, improving resolution and structural purity.

To reduce absorption and surface scattering loss [21], the material for the nanocylinders should ideally be c-Si instead of poly-Si. The poly-Si material for nanoparticles was initially chosen on the basis of practical considerations, namely the accessibility of depositing poly-Si layers of any height on a sapphire substrate with the specified crystal orientation. Commercially available c-Si on sapphire has a limited variety of thicknesses and is deposited on sapphire with a crystal orientation that doesn't exhibit piezoelectric properties. Nevertheless, disregarding piezoelectric effects, the crystal layer of silicon can be etched to reach the desired thickness. This potential improvement can reduce overall losses and increase reflectivity.

In relation to characterisation possibilities, losses associated with absorption and surface scattering [22] can be calculated by measuring transmissivity of the metasurfaces [23]. For this purpose, the characterisation setup must be modified. The advancements could also involve placing the test structures in a vacuum to minimize dust accumulation or optimising the structure holder.

Further theoretical and numerical analysis of reflective metasurfaces with consequent realisation can focus on phase control of the reflected light field. The analytical discussion in the third published paper demonstrates that by using cylindrical particles in the metasurface design, it is possible to achieve different phases of the reflected light field, varying from π to $-\pi$. The marginal cases, which differ by a phase shift of π, correspond to metasurfaces exhibiting magnetic and electric mirror effects. A more extensive insight into phase control will broaden the functional capabilities of metasurfaces.

Another potential research direction could involve studying reflectivity realised by higher-order multipole moments. The numerical simulations of Figure 6.1 of the third published paper demonstrate high reflectivity achieved not only by excitation of ED and MD moments, but also

[20] It should be noted that sapphire is an aluminium oxide.

[21] The used term 'surface scattering loss' refers to classical scattering, where light is reflected at an angle due to surface roughness.

[22] In this context, it is assumed that the losses introduced by the optical components of the measuring setup can be neglected.

[23] The transmissivity graphs were measured in the initial experimental demonstration. However, the results were obtained under different conditions, making them incompatible with the reflectivity graphs. Therefore, they were not included in the main results.

by EQ and a combination of ED and MQ moments. Optimising the design for these multipole moments may lead to alternative particle configurations and dimensional parameters.

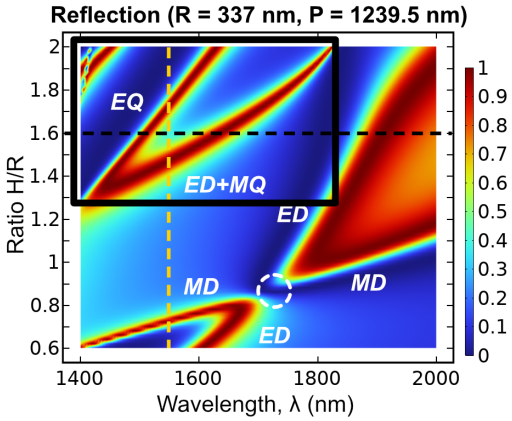

Figure 6.1.: Reflectivity of cylindrical metasurfaces with varying aspect ratios H/R at telecom wavelengths. The black box highlights cases where reflectivity is realised due to the excitation of higher-order multipole moments.

The provided examples have the substantial potential to enhance the reflectivity and enable greater functional control of silicon metasurfaces on a sapphire substrate.

6.1.2 Noise analysis and implementation for gravitational wave detection

For this thesis, the broad scope of metasurface implementation was mostly focused on an application for next-generation GW detection. The material choice for the metasurfaces and the light field parameters are selected in the investigation based on the requirements for the ET project. The research of this PhD work provides a broad accumulation of knowledge, leading to the design and realisation of the first metasurface prototype. However, lots of aspects remain unaddressed. This includes the piezoelectricity of the sapphire C-plane (0001), the effects of cryogenic temperature, the reconsideration of alternative materials, and the investigation of mechanical and optical noise sources in metasurfaces.

The initial idea for choosing the C-plane of the sapphire substrate is the potential ability of this surface to exhibit piezoelectric properties comparable to bulk piezoelectrics [55]. The poly-Si metasurfaces are fabricated on sapphire with this exact crystal orientation. The subsequent logical step would be to construct a setup that affords the opportunity to apply a voltage to the sapphire surface and observe any changes in reflectivity. The moderation of reflectivity can be potentially used in the SRM of the detector or other techniques requiring real-time reflectivity modulation.

Cryogenic temperature is considered solely for selecting metasurface materials. However, the refractive index of silicon exhibits a slight temperature dependence, changing from 3.45 at 10 K to 3.47 at 250 K for a wavelength of 1550 nm [118]. Consequently, recalculation and optimisation of the structural parameters are necessary if the metasurface is characterised or operates at cryogenic temperature.

Alternative materials have to be further considered. The ongoing discussions are progressively leaning towards the installation of silicon substrates in cryogenic temperature interferometers. This introduces the challenge of producing a silicon metasurface directly on a silicon substrate. Due to the identical refractive indices, it is essential to insulate the nanoparticles with an additional layer of low-refractive-index material, such as silica (SiO_2) [119, 120]. An alternative approach would be to fabricate the nanoparticles from a different high-refractive-index material, such as silicon nitride (SiN) [121].

The metasurface structure may also be applied to other optical components of the GWD, including the ITMs or SRM, where the reflectivity requirements are less stringent than for the ETMs. This reduces certain constraints on the perfection and fabrication precision requirements. Moreover, the metasurface structure could be integrated as the top layer on a "Bragg mirror", effectively filtering out most of the light intensity and thereby reducing thermal noise generated in the subsequent layers.

Noise characterisation plays a critical role in evaluating metasurfaces. It is incredibly important to have this characterisation for the fabricated structures, as simulations cannot account for all noise sources. The noise characterisation may include calculations of mechanical noise or side scattering at the border of the metasurface area. An interesting aspect to explore is the degree of noise introduced when dust particles are located on the lateral sides of nanocylinders rather than on their top surfaces.

6.1.3 Advanced applications

Metasurfaces have potential applications beyond GW physics. The developed technology can be extended to other optical studies, such as precision metrology in table-top experiments, or may also be relevant for innovations in solar or laser-driven systems. The properties of metasurfaces can be adapted to achieve polarization dependency or lensing effects. Their thin, flat structure enables the creation of planar optical components suitable for use on oscillating devices. Furthermore, metasurfaces can be designed to exhibit second or third-harmonic generation or retro-reflectivity. The capabilities of metasurfaces continue to expand, making them increasingly valuable for future innovations.

6.2 Conclusion

The PhD thesis covers a range of significant aspects of the investigation: theoretical analysis, modelling and numerical simulations, experimental methodology of metasurface production, fabrication technology and testing. These steps enable a versatile approach to the study of metasurfaces, evolve a deep understanding of their functional capabilities and create opportunities for their integration and future implementation in optical experiments. The results demonstrate the feasibility of designing and realising a structure with a single layer of nanoparticles that, by selecting proper dimensional parameters, could exhibit high reflectivity at the selected wavelength. This design can differ in nanoparticle shape and size, from spheres to cylinders, which can be embedded in a polymer layer, placed on a substrate, or additionally have a protective layer for nanoparticles. The research shows how an understanding of the principles of metasurface reflectivity can lead to different designs depending on the motivation requirements. The reflectivity effect is only a fraction in a pool of metasurface possibilities, but it holds valuable promise to be implemented, expanded or transferred to other fields of optics and photonics.

Bibliography

[1] R. Vaz, M. F. Frasco and M. G. F. Sales. 'Photonics in nature and bioinspired designs: sustainable approaches for a colourful world'. *Nanoscale Adv.* 2.11 (2020), pp. 5106–5129. DOI: 10.1039/D0NA00445F.

[2] A. S. Solntsev, G. S. Agarwal and Y. S. Kivshar. 'Metasurfaces for quantum photonics'. *Nature Photonics* 15.5 (2021), pp. 327–336. DOI: 10.1038/s41566-021-00793-z.

[3] K. Wang, M. Chekhova and Y. Kivshar. 'Metasurfaces for quantum technologies'. *Physics Today* 75.8 (2022), pp. 38–44. DOI: 10.1063/PT.3.5062.

[4] E. Stoja, S. Konstandin, D. Philipp, R. N. Wilke, D. Betancourt, T. Bertuch, J. Jenne, R. Umathum and M. Günther. 'Improving magnetic resonance imaging with smart and thin metasurfaces'. *Scientific Reports* 11.1 (2021), p. 16179. DOI: 10.1038/s41598-021-95420-w.

[5] E. I. Kretov, A. V. Shchelokova and A. P. Slobozhanyuk. 'Control of the magnetic near-field pattern inside MRI machine with tunable metasurface'. *Applied Physics Letters* 115.6 (2019). DOI: 10.1063/1.5099413.

[6] H. Chu, Q. Li, B. Liu, J. Luo, S. Sun, Z. H. Hang, L. Zhou and Y. Lai. 'A hybrid invisibility cloak based on integration of transparent metasurfaces and zero-index materials'. *Light: Science & Applications* 7.1 (2018), p. 50. DOI: 10.1038/s41377-018-0052-7.

[7] H. Tan, J. Deng, R. Zhao, X. Wu, G. Li, L. Huang, J. Liu and X. Cai. 'A free-space orbital angular momentum multiplexing communication system based on a metasurface'. *Laser & Photonics Reviews* 13.6 (2019), p. 1800278. DOI: 10.1002/lpor.201800278.

[8] J. Qin, S. Jiang, Z. Wang, X. Cheng, B. Li, Y. Shi, D. P. Tsai, A. Q. Liu, W. Huang and W. Zhu. 'Metasurface micro/nano-optical sensors: principles and applications'. *ACS Nano* 16.8 (2022), pp. 11598–11618. DOI: 10.1021/acsnano.2c03310.

[9] B. P. Abbott, R. Abbott, T. Abbott, M. Abernathy, F. Acernese, K. Ackley, C. Adams, T. Adams, P. Addesso, R. X. Adhikari et al. 'Observation of gravitational waves from a binary black hole merger'. *Physical Review Letters* 116.6 (2016), p. 061102. DOI: 10.1103/PhysRevLett.116.061102.

[10] The LIGO Scientific Collaboration and The Virgo Collaboration., The 1M2H Collaboration., The Dark Energy Camera GW-EM Collaboration and the DES Collaboration et al. 'A gravitational-wave standard siren measurement of the Hubble constant'. *Nature* 551.7678 (2017), pp. 85–88. DOI: 10.1038/nature24471.

[11] B. P. Abbott, R. Abbott, T. Abbott, F. Acernese, K. Ackley, C. Adams, T. Adams, P. Addesso, R. X. Adhikari, V. B. Adya et al. 'GW170817: observation of gravitational waves from a binary neutron star inspiral'. *Physical Review Letters* 119.16 (2017), p. 161101. DOI: 10.1103/PhysRevLett.119.161101.

[12] V. Savchenko, C. Ferrigno, E. Kuulkers, A. Bazzano, E. Bozzo, S. Brandt, J. Chenevez, T.-L. Courvoisier, R. Diehl, A. Domingo et al. 'INTEGRAL detection of the first prompt gamma-ray signal coincident with the gravitational-wave event GW170817'. *The Astrophysical Journal Letters* 848.2 (2017), p. L15. DOI: 10.3847/2041-8213/aa8f94.

[13] A. G. Abac et al. 'Observation of gravitational waves from the coalescence of a 2.5–4.5 M compact object and a neutron star'. *The Astrophysical Journal Letters* 970.2 (2024), pp. 1–44. DOI: 10.3847/2041-8213/ad5beb.

[14] B. F. Schutz. 'Gravitational-wave sources'. *Classical and Quantum Gravity* 13.11A (1996), A219. DOI: 10.1088/0264-9381/13/11A/031.

[15] M. Korobko, Y. Ma, Y. Chen and R. Schnabel. 'Quantum expander for gravitational-wave observatories'. *Light: Science & Applications* 8.1 (2019), p. 118. DOI: 10.1038/s41377-019-0230-2.

[16] S. Fairhurst. 'Source localization with an advanced gravitational wave detector network'. *Classical and Quantum Gravity* 28.10 (2011), p. 105021. DOI: 10.1088/0264-9381/28/10/105021.

[17] B. P. Abbott, R. Abbott, T. Abbott, S. Abraham, F. Acernese, K. Ackley, C. Adams, V. Adya, C. Affeldt, M. Agathos et al. 'Prospects for observing and localizing gravitational-wave transients with Advanced LIGO, Advanced Virgo and KAGRA'. *Living Reviews in Relativity* 23 (2020), pp. 1–69. DOI: 10.1007/s41114-020-00026-9.

[18] D. Davis, J. S. Areeda, B. K. Berger, R. Bruntz, A. Effler, R. Essick, R. Fisher, P. Godwin, E. Goetz, A. Helmling-Cornell et al. 'LIGO detector characterization in the second and third observing runs'. *Classical and Quantum Gravity* 38.13 (2021), p. 135014. DOI: 10.1088/1361-6382/abfd85.

[19] F. Acernese et al. 'Advanced Virgo status'. *Journal of Physics: Conference Series* 1342.1 (2020), p. 012010. DOI: 10.1088/1742-6596/1342/1/012010.

[20] KAGRA collaboration. 'KAGRA: 2.5 generation interferometric gravitational wave detector'. *Nature Astronomy* 3.1 (2019), pp. 35–40. DOI: 10.1038/s41550-018-0658-y.

[21] H. Vahlbruch, A. Khalaidovski, N. Lastzka, C. Gräf, K. Danzmann and R. Schnabel. 'The GEO 600 squeezed light source'. *Classical and Quantum Gravity* 27.8 (2010), p. 084027. DOI: 10.1088/0264-9381/27/8/084027.

[22] S. Goßler, A. Bertolini, M. Born, Y. Chen, K. Dahl, D. Gering, C. Gräf, G. Heinzel, S. Hild, F. Kawazoe et al. 'The AEI 10 m prototype interferometer'. *Classical and Quantum Gravity* 27.8 (2010), p. 084023. DOI: 10.1088/0264-9381/27/8/084023.

[23] R. Kirchhoff, C. Mow-Lowry, G. Bergmann, M. Hanke, P. Koch, S. Köhlenbeck, S. Leavey, J. Lehmann, P. Oppermann, J. Wöhler et al. 'Local active isolation of the AEI-SAS for the AEI 10 m prototype facility'. *Classical and Quantum Gravity* 37.11 (2020), p. 115004. DOI: 10.1088/1361-6382/ab857e.

[24] P. R. Saulson. *Fundamentals of interferometric gravitational wave detectors*. 2nd. World Scientific, 2017. DOI: 10.1142/10116.

[25] B. J. Meers. 'Recycling in laser-interferometric gravitational-wave detectors'. *Physical Review D* 38.8 (1988), p. 2317. DOI: 10.1103/PhysRevD.38.2317.

[26] LIGO Scientific Collaboration. 'LSC instrument science white paper' (2024 edition). https://dcc.ligo.org/public/0190/T2300411/001/Instrument_Science_White_Paper_2024ed.pdf [Accessed: (17.11.2024)].

[27] A. Einstein. *Investigations on the theory of the Brownian movement*. Dover Books on Physics Series. Dover Publications, 1956.

[28] S. Rowlinson, A. Dmitriev, A. W. Jones, T. Zhang and A. Freise. 'Feasibility study of beam-expanding telescopes in the interferometer arms for the Einstein Telescope'. *Physical Review D* 103.2 (2021), p. 023004. DOI: 10.1103/PhysRevD.103.023004.

[29] M. Abernathy et al. 'Einstein gravitational wave Telescope (ET) conceptual design study'. *European Commission Report No. ET-0106A-10* (2011). https://www.et-gw.eu/index.php/relevant-et-documents [Accessed: (17.11.2024)].

[30] H. Lück et al. 'Et design report update 2020'. *Design Report Update 2020 for the Einstein Telescope* (2020). https://gwic.ligo.org/3Gsubcomm/docs/ET-0007B-20_ETDesignReportUpdate2020.pdf [Accessed: (17.11.2024)].

[31] O. Anderson and H. Bömmel. 'Ultrasonic absorption in fused silica at low temperatures and high frequencies'. *Journal of the American Ceramic Society* 38.4 (1955), pp. 125–131. DOI: 10.1111/j.1151-2916.1955.tb14914.x.

[32] Y. Aso, Y. Michimura, K. Somiya, M. Ando, O. Miyakawa, T. Sekiguchi, D. Tatsumi, H. Yamamoto and K. Collaboration). 'Interferometer design of the KAGRA gravitational wave detector'. *Physical Review D—Particles, Fields, Gravitation, and Cosmology* 88.4 (2013), p. 043007. DOI: 10.1103/PhysRevD.88.043007.

[33] T. Uchiyama, T. Tomaru, M. Tobar, D. Tatsumi, S. Miyoki, M. Ohashi, K. Kuroda, T. Suzuki, N. Sato, T. Haruyama et al. 'Mechanical quality factor of a cryogenic sapphire test mass for gravitational wave detectors'. *Physics Letters A* 261.1-2 (1999), pp. 5–11. DOI: 10.1016/S0375-9601(99)00563-0.

[34] C. T. Taylor, M. Notcutt, E. K. Wong, A. G. Mann and D. G. Blair. 'Measurement of the thermal expansion coefficient of an all-sapphire optical cavity'. *IEEE Transactions on Instrumentation and Measurement* 46.2 (1997), pp. 183–185. DOI: 10.1109/19.571807.

[35] V. Braginsky, M. Gorodetsky and S. Vyatchanin. 'Thermodynamical fluctuations and photo-thermal shot noise in gravitational wave antennae'. *Physics Letters A* 264.1 (1999), pp. 1–10. DOI: 10.1016/S0375-9601(99)00785-9.

[36] R. Lifshitz and M. L. Roukes. 'Thermoelastic damping in micro-and nanomechanical systems'. *Physical Review B* 61.8 (2000), p. 5600. DOI: 10.1103/PhysRevB.61.5600.

[37] U. Gysin, S. Rast, P. Ruff, E. Meyer, D. Lee, P. Vettiger and C. Gerber. 'Temperature dependence of the force sensitivity of silicon cantilevers'. *Physical Review B* 69.4 (2004), p. 045403. DOI: 10.1103/PhysRevB.69.045403.

[38] R. Hull. *Properties of crystalline silicon*. EMIS datareviews series. INSPEC, 1999.

[39] J. Wortman and R. Evans. 'Young's modulus, shear modulus, and Poisson's ratio in silicon and germanium'. *Journal of Applied Physics* 36.1 (1965), pp. 153–156. DOI: 10.1063/1.1713863.

[40] D. McGuigan, C. Lam, R. Gram, A. Hoffman, D. Douglass and H. Gutche. 'Measurements of the mechanical Q of single-crystal silicon at low temperatures'. *Journal of Low Temperature Physics* 30 (1978), pp. 621–629. DOI: 10.1007/BF00116202.

[41] J. Degallaix, R. Flaminio, D. Forest, M. Granata, C. Michel, L. Pinard, T. Bertrand and G. Cagnoli. 'Bulk optical absorption of high resistivity silicon at 1550 nm'. *Optics Letters* 38.12 (2013), pp. 2047–2049. DOI: 10.1364/OL.38.002047.

[42] J. Agresti, G. Castaldi, R. DeSalvo, V. Galdi, V. Pierro and I. M. Pinto. 'Optimized multilayer dielectric mirror coatings for gravitational wave interferometers'. *Advances in Thin-Film Coatings for Optical Applications III* 6286 (2006), p. 628608. DOI: 10.1117/12.678977.

[43] G. M. Harry, M. R. Abernathy, A. E. Becerra-Toledo, H. Armandula, E. Black, K. Dooley, M. Eichenfield, C. Nwabugwu, A. Villar, D. Crooks et al. 'Titania-doped tantala/silica coatings for gravitational-wave detection'. *Classical and Quantum Gravity* 24.2 (2006), p. 405. DOI: 10.1088/0264-9381/24/2/008.

[44] R. Dannenberg. 'Advanced LIGO end test mass coating specification'. *LIGO Document E* 900068 (2009), p. 2014.

[45] I. W. Martin, E. Chalkley, R. Nawrodt, H. Armandula, R. Bassiri, C. Comtet, M. Fejer, A. Gretarsson, G. Harry, D. Heinert et al. 'Comparison of the temperature dependence of the mechanical dissipation in thin films of Ta2O5 and Ta2O5 doped with TiO2'. *Classical and Quantum Gravity* 26.15 (2009), p. 155012. DOI: 10.1088/0264-9381/26/15/155012.

[46] F. Y. Khalili. 'Reducing the mirrors coating noise in laser gravitational-wave antennae by means of double mirrors'. *Physics Letters A* 334.1 (2005), pp. 67–72. DOI: 10.1016/j.physleta.2004.10.078.

[47] H.-W. Pan, S.-J. Wang, L.-C. Kuo, S. Chao, M. Principe, I. M. Pinto and R. DeSalvo. 'Thickness-dependent crystallization on thermal anneal for titania/silica nm-layer composites deposited by ion beam sputter method'. *Optics Express* 22.24 (2014), pp. 29847–29854. DOI: 10.1364/OE.22.029847.

[48] P. G. Murray, I. W. Martin, K. Craig, J. Hough, R. Robie, S. Rowan, M. R. Abernathy, T. Pershing and S. Penn. 'Ion-beam sputtered amorphous silicon films for cryogenic precision measurement systems'. *Physical Review D* 92.6 (2015), p. 062001. DOI: 10.1103/PhysRevD.92.062001.

[49] R. Birney, J. Steinlechner, Z. Tornasi, S. MacFoy, D. Vine, A. Bell, D. Gibson, J. Hough, S. Rowan, P. Sortais et al. 'Amorphous silicon with extremely low absorption: beating thermal noise in gravitational astronomy'. *Physical Review Letters* 121.19 (2018), p. 191101. DOI: 10.1103/PhysRevLett.121.191101.

[50] X. Liu, T. H. Metcalf, Q. Wang and D. M. Photiadis. 'Elastic properties of several silicon nitride films'. *MRS Online Proceedings Library* 989 (2006), pp. 1–6. DOI: 10.1557/PROC-0989-A22-01.

[51] C. G. Nuñez, G. Wallace, L. Fleming, K. Craig, S. Song, S. Ahmadzadeh, C. Clark, S. Tait, I. Martin, S. Reid et al. 'Study of amorphous dielectric optical coatings deposited by plasma ion assisted electron beam evaporation for gravitational wave detectors'. *Optical Interference Coatings*. Optica Publishing Group. (2022), WB–4. DOI: 10.1364/OIC.2022.WB.4.

[52] M. Abernathy, S. Reid, E. Chalkley, R. Bassiri, I. Martin, K. Evans, M. Fejer, A. Gretarsson, G. Harry, J. Hough et al. 'Cryogenic mechanical loss measurements of heat-treated hafnium dioxide'. *Classical and Quantum Gravity* 28.19 (2011), p. 195017. DOI: 10.1088/0264-9381/28/19/195017.

[53] G. D. Cole. 'Cavity optomechanics with low-noise crystalline mirrors'. *Optical Trapping and Optical Micromanipulation IX* 8458 (2012), pp. 28–38. DOI: 10.1117/12.931226.

[54] G. D. Cole, W. Zhang, B. J. Bjork, D. Follman, P. Heu, C. Deutsch, L. Sonderhouse, J. Robinson, C. Franz, A. Alexandrovski et al. 'High-performance near-and mid-infrared crystalline coatings'. *Optica* 3.6 (2016), pp. 647–656. DOI: 10.1364/OPTICA.3.000647.

[55] A. B. Georgescu and S. Ismail-Beigi. 'Surface piezoelectricity of (0001) sapphire'. *Physical Review Applied* 11.6 (2019), p. 064065. DOI: 10.1103/PhysRevApplied.11.064065.

[56] V. G. Veselago. 'The Electrodynamics of substances with simultaneously negative values of ϵ and μ'. *Soviet Physics Uspekhi* 10.4 (1968), p. 509. DOI: 10.1070/PU1968v010n04ABEH003699.

[57] D. R. Smith, W. J. Padilla, D. C. Vier, S. C. Nemat-Nasser and S. Schultz. 'Composite medium with simultaneously negative permeability and permittivity'. *Phys. Rev. Lett.* 84 (2000), pp. 4184–4187. DOI: 10.1103/PhysRevLett.84.4184.

[58] S. Linden, C. Enkrich, M. Wegener, J. Zhou, T. Koschny and C. M. Soukoulis. 'Magnetic response of metamaterials at 100 terahertz'. *Science* 306.5700 (2004), pp. 1351–1353. DOI: 10.1126/science.1105371.

[59] W. Cai, U. K. Chettiar, H.-K. Yuan, V. C. de Silva, A. V. Kildishev, V. P. Drachev and V. M. Shalaev. 'Metamagnetics with rainbow colors'. *Opt. Express* 15.6 (2007), pp. 3333–3341. DOI: 10.1364/OE.15.003333.

[60] V. M. Shalaev, W. Cai, U. K. Chettiar, H.-K. Yuan, A. K. Sarychev, V. P. Drachev and A. V. Kildishev. 'Negative index of refraction in optical metamaterials'. *Opt. Lett.* 30.24 (2005), pp. 3356–3358. DOI: 10.1364/OL.30.003356.

[61] S. Zhang, W. Fan, N. C. Panoiu, K. J. Malloy, R. M. Osgood and S. R. J. Brueck. 'Experimental demonstration of near-infrared negative-index metamaterials'. *Phys. Rev. Lett.* 95 (13 2005), p. 137404. DOI: 10.1103/PhysRevLett.95.137404.

[62] M. W. Klein, C. Enkrich, M. Wegener and S. Linden. 'Second-harmonic generation from magnetic metamaterials'. *Science* 313.5786 (2006), pp. 502–504. DOI: 10.1126/science.1129198.

[63] A. Popov and V. Shalaev. 'Negative-index metamaterials: second-harmonic generation, Manley–Rowe relations and parametric amplification'. *Applied Physics B* 84.1 (2006), pp. 131–137. DOI: 10.1007/s00340-006-2167-4.

[64] W. Padilla and R. Averitt. 'Imaging with metamaterials'. *Nature Reviews Physics* 4 (2022), pp. 85–100. DOI: 10.1038/s42254-021-00394-3.

[65] Y. Xiong et al. 'Microscopies enabled by photonic metamaterials'. *Sensors* 22.3 (2022). DOI: 10.3390/s22031086.

[66] C. E. Gutiérrez and E. Stachura. 'Metamaterial lens design'. *J. Opt. Soc. Am. A* 33.10 (2016), pp. 2020–2026. DOI: 10.1364/JOSAA.33.002020.

[67] D. Bigoni, S. Guenneau, A. B. Movchan and M. Brun. 'Elastic metamaterials with inertial locally resonant structures: Application to lensing and localization'. *Phys. Rev. B* 87 (17 2013), p. 174303. DOI: 10.1103/PhysRevB.87.174303.

[68] N. Kundtz and D. Smith. 'Extreme-angle broadband metamaterial lens'. *Nature Materials* 9 (2010), pp. 129–132. DOI: 10.1038/nmat2610.

[69] S. A. Khan, N. Z. Khan, Y. Xie, M. T. Abbas, M. Rauf, I. Mehmood, M. Runowski, S. Agathopoulos and J. Zhu. 'Optical sensing by metamaterials and metasurfaces: from physics to biomolecule detection'. *Advanced Optical Materials* 10.18 (2022), p. 2200500. DOI: 10.1002/adom.202200500.

[70] K. Song and P. Mazumder. 'Design of highly selective metamaterials for sensing platforms'. *IEEE Sensors Journal* 13.9 (2013), pp. 3377–3385. DOI: 10.1109/JSEN.2013.2260143.

[71] R. Zhao, T. Koschny and C. M. Soukoulis. 'Chiral metamaterials: retrieval of the effective parameters with and without substrate'. *Opt. Express* 18.14 (2010), pp. 14553–14567. DOI: 10.1364/OE.18.014553.

[72] S. Oh and O. Hess. 'Chiral metamaterials: enhancement and control of optical activity and circular dichroism'. *Nano Convergence* 2 (2015), p. 24. DOI: 10.1186/s40580-015-0058-2.

[73] D. Schurig, J. J. Mock, B. J. Justice, S. A. Cummer, J. B. Pendry, A. F. Starr and D. R. Smith. 'Metamaterial electromagnetic cloak at microwave frequencies'. *Science* 314.5801 (2006), pp. 977–980. DOI: 10.1126/science.1133628.

[74] W. Cai, U. Chettiar, A. Kildishev et al. 'Optical cloaking with metamaterials'. *Nature Photonics* 1 (2007), pp. 224–227. DOI: 10.1038/nphoton.2007.28.

[75] J. Parsons, E. Hendry, J. R. Sambles and W. L. Barnes. 'Localized surface-plasmon resonances and negative refractive index in nanostructured electromagnetic metamaterials'. *Phys. Rev. B* 80.24 (2009), p. 245117. DOI: 10.1103/PhysRevB.80.245117.

[76] V. Amendola, R. Pilot, M. Frasconi, O. M. Maragò and M. A. Iatı. 'Surface plasmon resonance in gold nanoparticles: a review'. *Journal of Physics: Condensed Matter* 29.20 (2017), p. 203002. DOI: 10.1088/1361-648X/aa60f3.

[77] K. L. Kelly, E. Coronado, L. L. Zhao and G. C. Schatz. 'The optical properties of metal nanoparticles: the influence of size, shape, and dielectric environment'. *The Journal of Physical Chemistry B* 107.3 (2003), pp. 668–677. DOI: 10.1021/jp026731y.

[78] S. A. Maier et al. *Plasmonics: fundamentals and applications*. Vol. 1. Springer, 2007. DOI: 10.1007/0-387-37825-1.

[79] S. V. Boriskina, T. A. Cooper, L. Zeng, G. Ni, J. K. Tong, Y. Tsurimaki, Y. Huang, L. Meroueh, G. Mahan and G. Chen. 'Losses in plasmonics: from mitigating energy dissipation to embracing loss-enabled functionalities'. *Advances in Optics and Photonics* 9.4 (2017), pp. 775–827. DOI: 10.1364/AOP.9.000775.

[80] A. B. Evlyukhin, S. M. Novikov, U. Zywietz, R. L. Eriksen, C. Reinhardt, S. I. Bozhevolnyi and B. N. Chichkov. 'Demonstration of magnetic dipole resonances of dielectric nanospheres in the visible region'. *Nano Letters* 12.7 (2012), pp. 3749–3755. DOI: 10.1021/nl301594s.

[81] B. Lahiri, S. G. McMeekin, A. Z. Khokhar, R. M. De La Rue and N. P. Johnson. 'Magnetic response of split ring resonators (SRRs) at visible frequencies'. *Optics Express* 18.3 (2010), pp. 3210–3218. DOI: 10.1364/OE.18.003210.

[82] I. Staude and J. Schilling. 'Metamaterial-inspired silicon nanophotonics'. *Nature Photonics* 11 (2017), pp. 274–284. DOI: 10.1038/nphoton.2017.39.

[83] V. Pustynnikova, A. Musorin and A. Fedyanin. 'High-quality infrared metalenses based on germanium dimers'. *JETP Letters* 117 (2023), pp. 498–503. DOI: 10.1134/S0021364023600556.

[84] J. Tian, H. Luo, Q. Li, X. Pei, K. Du and M. Qiu. 'Near-infrared super-absorbing all-dielectric metasurface based on single-layer germanium nanostructures'. *Laser & Photonics Reviews* 12.9 (2018), p. 1800076. DOI: https://doi.org/10.1002/lpor.201800076.

[85] J. Sadasivan, S. Krishnan and J. Dontabhaktuni. 'Lattice constant and polarization-independent high transmission in tellurium-based dielectric metasurfaces'. *Journal of Optics* 25.12 (2023), p. 125401. DOI: 10.1088/2040-8986/ad024f.

[86] Y. Li, Q. Chen, B. Wu, L. Shi, P. Tang, G. Du and G. Liu. 'Broadband perfect metamaterial absorber based on the gallium arsenide grating complex structure'. *Results in Physics* 15 (2019), p. 102760. DOI: https://doi.org/10.1016/j.rinp.2019.102760.

[87] Y. Kivshar and A. Miroshnichenko. 'Meta-optics with Mie resonances'. *Opt. Photon. News* 28.1 (2017), pp. 24–31. DOI: 10.1364/OPN.28.1.000024.

[88] E. D. Palik. *Handbook of optical constants of solids*. Vol. 3. Academic press, 1998.

[89] L. F. Thompson. *An introduction to lithography*. ACS Publications, 1983. DOI: 10.1021/bk-1983-0219.ch001.

[90] J. C. Maxwell. 'VIII. A dynamical theory of the electromagnetic field'. *Philosophical Transactions of the Royal Society of London* 155 (1865), pp. 459–512. DOI: 10.1098/rstl.1865.0008.

[91] M. Chaichian, I. Merches, D. Radu and A. Tureanu. *Electrodynamics*. Springer, 2010.

[92] J. D. Jackson. *Classical electrodynamics*. John Wiley & Sons, 2021.

[93] L. Jylhä, I. Kolmakov, S. Maslovski and S. Tretyakov. 'Modeling of isotropic backward-wave materials composed of resonant spheres'. *Journal of Applied Physics* 99.4 (2006). DOI: 10.1063/1.2173309.

[94] S. Yan and G. Vandenbosch. 'Increasing the NRI bandwidth of dielectric sphere-based metamaterials by coating'. *Progress In Electromagnetics Research* 132 (2012), pp. 1–23. DOI: 10.2528/PIER12070612.

[95] R. A. Aoni, M. Rahmani, L. Xu, K. Zangeneh Kamali, A. Komar, J. Yan, D. Neshev and A. E. Miroshnichenko. 'High-efficiency visible light manipulation using dielectric metasurfaces'. *Scientific Reports* 9.1 (2019), p. 6510. DOI: 10.1038/s41598-019-42444-y.

[96] V. E. Babicheva and A. B. Evlyukhin. 'Mie-resonant metaphotonics'. *Advances in Optics and Photonics* 16.3 (2024), pp. 539–658. DOI: 10.1364/AOP.510826.

[97] C. F. Bohren and D. R. Huffman. *Absorption and scattering of light by small particles*. John Wiley Sons, Ltd, 1998. DOI: 10.1002/9783527618156.

[98] W. Hergert and T. Wriedt. *The Mie theory: basics and applications*. Springer Berlin, Heidelberg, 2012. DOI: 10.1007/978-3-642-28738-1.

[99] D. Tzarouchis and A. Sihvola. 'Light scattering by a dielectric sphere: perspectives on the Mie resonances'. *Applied Sciences* 8.2 (2018), p. 184. DOI: 10.3390/app8020184.

[100] R. Jha, R. K. Singh et al. 'Mie scattering of tightly focused beams by a core-shell nanoparticle'. *Optics Communications* 557 (2024), p. 130306. DOI: 10.1016/j.optcom.2024.130306.

[101] V. E. Babicheva and A. B. Evlyukhin. 'Analytical model of resonant electromagnetic dipole-quadrupole coupling in nanoparticle arrays'. *Physical Review B* 99.19 (2019), p. 195444. DOI: 10.1103/PhysRevB.99.195444.

[102] A. B. Evlyukhin, C. Reinhardt, A. Seidel, B. S. Luk'yanchuk and B. N. Chichkov. 'Optical response features of Si-nanoparticle arrays'. *Physical Review B—Condensed Matter and Materials Physics* 82.4 (2010), p. 045404. DOI: 10.1103/PhysRevB.82.045404.

[103] P. D. Terekhov, V. E. Babicheva, K. V. Baryshnikova, A. S. Shalin, A. Karabchevsky and A. B. Evlyukhin. 'Multipole analysis of dielectric metasurfaces composed of nonspherical nanoparticles and lattice invisibility effect'. *Physical Review B* 99.4 (2019), p. 045424. DOI: 10.1103/PhysRevB.99.045424.

[104] A. B. Evlyukhin, C. Reinhardt, E. Evlyukhin and B. N. Chichkov. 'Multipole analysis of light scattering by arbitrary-shaped nanoparticles on a plane surface'. *J. Opt. Soc. Am. B* 30.10 (2013), pp. 2589–2598. DOI: 10.1364/JOSAB.30.002589.

[105] V. E. Babicheva and A. B. Evlyukhin. 'Resonant lattice Kerker effect in metasurfaces with electric and magnetic optical responses'. *Laser & Photonics Reviews* 11.6 (2017), p. 1700132. DOI: 10.1002/lpor.201700132.

[106] V. E. Babicheva and J. V. Moloney. 'Lattice effect influence on the electric and magnetic dipole resonance overlap in a disk array'. *Nanophotonics* 7.10 (2018), pp. 1663–1668. DOI: 10.1515/nanoph-2018-0107.

[107] A. E. Miroshnichenko, A. B. Evlyukhin, Y. F. Yu, R. M. Bakker, A. Chipouline, A. I. Kuznetsov, B. Luk'yanchuk, B. N. Chichkov and Y. S. Kivshar. 'Nonradiating anapole modes in dielectric nanoparticles'. *Nature Communications* 6.1 (2015), p. 8069. DOI: 10.1038/ncomms9069.

[108] I. Allayarov, A. C. Lesina and A. B. Evlyukhin. 'Anapole mechanism of bound states in the continuum in symmetric dielectric metasurfaces'. *Physical Review B* 109.24 (2024), p. L241405. DOI: 10.1103/PhysRevB.109.L241405.

[109] A. Wold and K. Dwight. 'Electrical properties of semiconductors'. *Solid State Chemistry: Synthesis, Structure, and Properties of Selected Oxides and Sulfides*. Dordrecht: Springer Netherlands, 1993, pp. 31–46. DOI: 10.1007/978-94-011-1476-9_3.

[110] C. Kittel. *Introduction to solid state physics*. 8th ed. Wiley, 2004.

[111] I. Brodie and J. J. Muray. *The physics of micro/nano-fabrication*. Springer Science & Business Media, 2013.

[112] U. Zywietz, A. B. Evlyukhin, C. Reinhardt and B. N. Chichkov. 'Laser printing of silicon nanoparticles with resonant optical electric and magnetic responses'. *Nature Communications* 5.1 (2014), p. 3402. DOI: 10.1038/ncomms4402.

[113] H. Fujiwara. *Spectroscopic ellipsometry: principles and applications*. John Wiley & Sons, 2007.

[114] A. Arbabi, R. M. Briggs, Y. Horie, M. Bagheri and A. Faraon. 'Efficient dielectric metasurface collimating lenses for mid-infrared quantum cascade lasers'. *Optics Express* 23.26 (2015), pp. 33310–33317. DOI: 10.1364/OE.23.033310.

[115] Q. Dai, Z. Guan, S. Chang, L. Deng, J. Tao, Z. Li, Z. Li, S. Yu, G. Zheng and S. Zhang. 'A single-celled Tri-functional metasurface enabled with triple manipulations of light'. *Advanced Functional Materials* 30.50 (2020), p. 2003990. DOI: 10.1002/adfm.202003990.

[116] W. Yang, S. Xiao, Q. Song, Y. Liu, Y. Wu, S. Wang, J. Yu, J. Han and D.-P. Tsai. 'All-dielectric metasurface for high-performance structural color'. *Nature Communications* 11.1 (2020), p. 1864. DOI: 10.1038/s41467-020-15773-0.

[117] X. Yang, P. Mukherjee, M. Kim, H. Mei, C. Fang, S. Choi, Y. Tong, S. Perlowski, D. A. Czaplewski, A. M. Dibos et al. 'Atomic magnetometry using a metasurface polarizing beamsplitter in silicon-on-sapphire'. *ACS Photonics* 11.9 (2024), pp. 3644–3651. DOI: 10.1021/acsphotonics.4c00744.

[118] D. Franta, P. Franta, J. Vohánka, M. Čermák and I. Ohlídal. 'Determination of thicknesses and temperatures of crystalline silicon wafers from optical measurements in the far infrared region'. *Journal of Applied Physics* 123.18 (2018). DOI: 10.1063/1.5026195.

[119] C. Chen, Z.-y. Wang, Z.-g. Zheng, Y. Liu, W. Huang and L. Chen. 'Large-area, low-cost near-infrared meta-surface reflector based on a pixelated two-dimensional silicon disk array'. *Optics Express* 28.25 (2020), pp. 38355–38365. DOI: 10.1364/OE.412521.

[120] L. Li, J. Niu, X. Shang, S. Chen, C. Lu, Y. Zhang and L. Shi. 'Bright field structural colors in silicon-on-insulator nanostructures'. *ACS Applied Materials & Interfaces* 13.3 (2021), pp. 4364–4373. DOI: 10.1021/acsami.0c19126.

[121] C.-S. Park, I. Koirala, S. Gao, V. R. Shrestha, S.-S. Lee and D.-Y. Choi. 'Structural color filters based on an all-dielectric metasurface exploiting silicon-rich silicon nitride nanodisks'. *Optics Express* 27.2 (2019), pp. 667–679. DOI: 10.1364/OE.27.000667.

List of Figures

List of Publications

Short Author List Publications

1. L. Prokhorov et al. 'Upper limits on the mechanical loss of silicate bonds in a silicon tuning fork oscillator'. *Physics Letters A* 382.33 (August 2018). Special Issue in memory of Professor V.B. Braginsky, pp. 2186–2191. DOI: 10.1016/j.physleta.2017.07.007

2. A. B. Evlyukhin, M. Matiushechkina, V. A. Zenin, M. Heurs and B. N. Chichkov. 'Lightweight metasurface mirror of silicon nanospheres [Invited]'. *Opt. Mater. Express* 10.10 (October 2020), pp. 2706–2716. DOI: 10.1364/OME.409311

3. Y. Y. Klochkov, L. G. Prokhorov, M. S. Matiushechkina, R. X. Adhikari and V. P. Mitrofanov. 'Using silicon disk resonators to measure mechanical losses caused by an electric field'. *Review of Scientific Instruments* 93.1 (January 2022), p. 014501. DOI: 10.1063/5.0076311

4. M. Matiushechkina, A. B. Evlyukhin, V. A. Zenin, M. Heurs and B. N. Chichkov. 'High-efficiency silicon metasurface mirror on a sapphire substrate'. *Optical Materials* 138 (April 2023), p. 113618. DOI: 10.1016/j.optmat.2023.113618

5. M. Matiushechkina, A. B. Evlyukhin, V. A. Zenin, B. N. Chichkov and M. Heurs. 'Perfect mirror effects in metasurfaces of silicon nanodisks at telecom wavelength'. *Advanced Optical Materials* 12.18 (April 2024), p. 2400191. DOI: 10.1002/adom.202400191

6. M. Matiushechkina, A. B. Evlyukhin, R. Malureanu, V. A. Zenin, T. Yezekyan, A. Lavrinenko, S. I. Bozhevolnyi, B. N. Chichkov and M. Heurs. 'Design and experimental demonstration of wavelength-selective metamirrors on sapphire substrates'. *Advanced Photonics Research* 2400116 (November 2024). DOI: 10.1002/adpr.202400116

LIGO Scientific Collaboration

I have been a member of the LIGO Scientific Collaboration since May 2019, which has entitled me to be a co-author on a number of publications from the collaboration since October 2020:

1. The LIGO Scientific Collaboration, Virgo Collaboration, KAGRA Collaboration. 'A search with GEO600 for gravitational waves coincident with the first Galactic fast radio bursts from SGR 1935+2154'. *The Astrophysical Journal* (October 2024). preprint. DOI: 10.48550/arXiv.2410.09151

2. A. G. Abac et al. 'Ultralight vector dark matter search using data from the KAGRA O3GK run'. *Phys. Rev. D* 110.4 (August 2024), p. 042001. DOI: 10.1103/PhysRevD.110.042001

3. R. Abbott et al. 'Search for gravitational-lensing signatures in the full third observing run of the LIGO-Virgo network'. *The Astrophysical Journal* 970.2 (July 2024), p. 191. DOI: 10.3847/1538-4357/ad3e83

4. 'Observation of gravitational waves from the coalescence of a $2.5 - 4.5\ M_\odot$ compact object and a neutron star'. *The Astrophysical Journal Letters* 970.2 (July 2024), p. L34. DOI: 10.3847/2041-8213/ad5beb

5. R. Abbott et al. 'Search for gravitational-wave transients associated with magnetar bursts in Advanced LIGO and Advanced Virgo data from the third observing run'. *The Astrophysical Journal* 966.1 (April 2024), p. 137. DOI: 10.3847/1538-4357/ad27d3

6. C. Fletcher et al. 'A joint Fermi-GBM and Swift-BAT analysis of gravitational-wave candidates from the third gravitational-wave observing run'. *Astrophys. J.* 964.2 (March 2024), p. 149. DOI: 10.3847/1538-4357/ad1eed

7. R. Abbott et al. 'GWTC-2.1: deep extended catalog of compact binary coalescences observed by LIGO and Virgo during the first half of the third observing run'. *Phys. Rev. D* 109.2 (January 2024), p. 022001. DOI: 10.1103/PhysRevD.109.022001

8. R. Abbott et al. 'GWTC-3: compact binary coalescences observed by LIGO and Virgo during the second part of the third observing run'. *Phys. Rev. X* 13.4 (December 2023), p. 041039. DOI: 10.1103/PhysRevX.13.041039

9. R. Abbott et al. 'Search for gravitational waves associated with fast radio bursts detected by CHIME/FRB during the LIGO–Virgo observing run O3a'. *The Astrophysical Journal* 955.2 (September 2023), p. 155. DOI: 10.3847/1538-4357/acd770

10. R. Abbott et al. 'Open Data from the Third Observing Run of LIGO, Virgo, KAGRA, and GEO'. *The Astrophysical Journal Supplement Series* 267.2 (July 2023), p. 29. DOI: 10.3847/1538-4365/acdc9f

11. R. Abbott et al. 'Constraints on the cosmic expansion history from GWTC-3'. *The Astrophysical Journal* 949.2 (June 2023), p. 76. DOI: 10.3847/1538-4357/ac74bb

12. R. Abbott et al. 'Population of merging compact binaries inferred using gravitational waves through GWTC-3'. *Phys. Rev. X* 13.1 (March 2023), p. 011048. DOI: 10.1103/PhysRevX.13.011048

13. R. Abbott et al. 'Search for subsolar-mass black hole binaries in the second part of Advanced LIGO's and Advanced Virgo's third observing run'. *Monthly Notices of the Royal Astronomical Society* 524.4 (February 2023), pp. 5984–5992. DOI: 10.1093/mnras/stad588

14. R. Abbott et al. 'Model-based cross-correlation search for gravitational waves from the low-mass X-ray binary Scorpius X-1 in LIGO O3 data'. *The Astrophysical Journal Letters* 941.2 (December 2022), p. L30. DOI: 10.3847/2041-8213/aca1b0

15. R. Abbott et al. 'All-sky search for continuous gravitational waves from isolated neutron stars using Advanced LIGO and Advanced Virgo O3 data'. *Phys. Rev. D* 106.10 (November 2022), p. 102008. DOI: 10.1103/PhysRevD.106.102008

16. R. Abbott et al. 'Search for gravitational waves from Scorpius X-1 with a hidden Markov model in O3 LIGO data'. *Phys. Rev. D* 106.6 (September 2022), p. 062002. DOI: 10.1103/PhysRevD.106.062002

17. R. Abbott et al. 'Search for continuous gravitational wave emission from the Milky Way center in O3 LIGO-Virgo data'. *Phys. Rev. D* 106.4 (August 2022), p. 042003. DOI: 10.1103/PhysRevD.106.042003

18. R. Abbott et al. 'Searches for gravitational waves from known pulsars at two harmonics in the second and third LIGO-Virgo observing runs'. *Astrophys. J.* 935.1 (August 2022), p. 1. DOI: 10.3847/1538-4357/ac6acf

19. R. Abbott et al. 'Search for subsolar-mass binaries in the first half of Advanced LIGO's and Advanced Virgo's third observing run'. *Phys. Rev. Lett.* 129.6 (August 2022), p. 061104. DOI: 10.1103/PhysRevLett.129.061104

20. R. Abbott et al. 'All-sky, all-frequency directional search for persistent gravitational waves from Advanced LIGO's and Advanced Virgo's first three observing runs'. *Phys. Rev. D* 105.12 (June 2022), p. 122001. DOI: 10.1103/PhysRevD.105.122001

21. R. Abbott et al. 'Narrowband searches for continuous and long-duration transient gravitational waves from known pulsars in the LIGO-Virgo third observing run'. *Astrophys. J.* 932.2 (June 2022), p. 133. DOI: 10.3847/1538-4357/ac6ad0

22. R. Abbott et al. 'All-sky search for gravitational wave emission from scalar boson clouds around spinning black holes in LIGO O3 data'. *Phys. Rev. D* 105.10 (May 2022), p. 102001. DOI: 10.1103/PhysRevD.105.102001

23. R. Abbott et al. 'First joint observation by the underground gravitational-wave detector KAGRA with GEO 600'. *Prog. Theor. Exp. Phys.* 2022.6 (April 2022). 063F01. DOI: 10.1093/ptep/ptac073

24. R. Abbott et al. 'Tests of general relativity with GWTC-3'. *Physical Review D* (April 2022). DOI: 10.48550/arXiv.2112.06861

25. R. Abbott et al. 'Search of the early O3 LIGO data for continuous gravitational waves from the Cassiopeia A and Vela Jr. supernova remnants'. *Phys. Rev. D* 105.8 (April 2022), p. 082005. DOI: 10.1103/PhysRevD.105.082005

26. R. Abbott et al. 'Search for gravitational waves associated with gamma-ray bursts detected by Fermi and Swift during the LIGO–Virgo run O3b'. *Astrophys. J.* 928.2 (April 2022), p. 186. DOI: 10.3847/1538-4357/ac532b

27. R. Abbott et al. 'Search for intermediate-mass black hole binaries in the third observing run of Advanced LIGO and Advanced Virgo'. *Astronomy & Astrophysics* 659.A84 (March 2022). DOI: 10.1051/0004-6361/202141452

28. R. Abbott et al. 'Constraints on dark photon dark matter using data from LIGO's and Virgo's third observing run'. *Phys. Rev. D* 105.6 (March 2022), p. 063030. DOI: 10.1103/PhysRevD.105.063030

29. R. Abbott et al. 'Search for continuous gravitational waves from 20 accreting millisecond X-ray pulsars in O3 LIGO data'. *Phys. Rev. D* 105.2 (January 2022), p. 022002. DOI: 10.1103/PhysRevD.105.022002

30. R. Abbott et al. 'All-sky search for short gravitational-wave bursts in the third Advanced LIGO and Advanced Virgo run'. *Phys. Rev. D* 104.12 (December 2021), p. 122004. DOI: 10.1103/PhysRevD.104.122004

31. R. Abbott et al. 'Search for lensing signatures in the gravitational-wave observations from the first half of LIGO–Virgo's third observing run'. *Astrophys. J.* 923.1 (December 2021), p. 14. DOI: 10.3847/1538-4357/ac23db

32. R. Abbott et al. 'Searches for continuous gravitational waves from young supernova remnants in the early third observing run of Advanced LIGO and Virgo'. *Astrophys. J.* 921.1 (November 2021), p. 80. DOI: 10.3847/1538-4357/ac17ea

33. R. Abbott et al. 'Constraints from LIGO O3 data on gravitational-wave emission due to R-modes in the glitching pulsar PSR J0537–6910'. *Astrophys. J.* 922.1 (November 2021), p. 71. DOI: 10.3847/1538-4357/ac0d52

34. R. Abbott et al. 'All-sky search for long-duration gravitational-wave bursts in the third Advanced LIGO and Advanced Virgo run'. *Phys. Rev. D* 104.10 (November 2021), p. 102001. DOI: 10.1103/PhysRevD.104.102001

35. R. Abbott et al. 'All-sky search for continuous gravitational waves from isolated neutron stars in the early O3 LIGO data'. *Phys. Rev. D* 104.8 (October 2021), p. 082004. DOI: 10.1103/PhysRevD.104.082004

36. R. Abbott et al. 'Search for anisotropic gravitational-wave backgrounds using data from Advanced LIGO and Advanced Virgo's first three observing runs'. *Phys. Rev. D* 104.2 (July 2021), p. 022005. DOI: 10.1103/PhysRevD.104.022005

37. R. Abbott et al. 'Upper limits on the isotropic gravitational-wave background from Advanced LIGO and Advanced Virgo's third observing run'. *Phys. Rev. D* 104.2 (July 2021), p. 022004. DOI: 10.1103/PhysRevD.104.022004

38. R. Abbott et al. 'Observation of gravitational waves from two neutron star-black hole coalescences'. *Astrophys. J. Lett.* 915 (June 2021), p. L5. DOI: 10.3847/2041-8213/ac082e

39. R. Abbott et al. 'Constraints on cosmic strings using data from the third Advanced LIGO-Virgo observing run'. *Phys. Rev. Lett.* 126 (June 2021), p. 241102. DOI: 10.1103/PhysRevLett.126.241102

40. R. Abbott et al. 'Diving below the spin-down limit: Constraints on gravitational waves from the energetic young pulsar PSR J0537-6910'. *Astrophys. J.* 913 (June 2021), p. L27. DOI: 10.3847/2041-8213/abffcd

41. R. Abbott et al. 'GWTC-2: Compact binary coalescences observed by LIGO and Virgo during the first half of the third observing run'. *Phys. Rev. X* 11 (June 2021), p. 021053. DOI: 10.1103/PhysRevX.11.021053

42. R. Abbott et al. 'Tests of general relativity with binary black holes from the second LIGO-Virgo gravitational-wave transient catalog'. *Phys. Rev. D* 103.12 (June 2021), p. 122002. DOI: 10.1103/PhysRevD.103.122002

43. R. Abbott et al. 'Population properties of compact objects from the second LIGO-Virgo gravitational-wave transient catalog'. *Astrophys. J. Lett.* 913.1 (May 2021), p. L7. DOI: 10.3847/2041-8213/abe949

44. R. Abbott et al. 'All-sky search in early O3 LIGO data for continuous gravitational-wave signals from unknown neutron stars in binary systems'. *Phys. Rev. D* 103 (March 2021), p. 064017. DOI: 10.1103/PhysRevD.103.064017

45. R. Abbott et al. 'Gravitational-wave constraints on the equatorial ellipticity of millisecond pulsars'. *Astrophys. J. Lett.* 902 (October 2020), p. L21. DOI: 10.3847/2041-8213/abb655

Acknowledgements

My PhD journey began with the most important people in my world, with my parents and my brother. I can't express how much I love them and grateful for encouraging me to move to Germany, for supporting in pursuing my scientific studies, and for always being with me, even at a distance. (Спасибо большое мои любимые мама и папа, мой братик, за то, что поддерживали, выслушивали, переживали вместе со мной и никогда не позволяли сдаться. Не смотря на расстояние, я чувствую, что вы всегда рядом. Без вас я не смогла бы преодолеть этот путь.)

I am very thankful to Michèle for accepting me into her group. Despite my initial difficulties with English and insecurities related to moving to a new country, you gave me time to adapt and showed great patience. Thank you for the discussions and support. I have truly grown up in this group, and it couldn't be done without your help.

The people in this group are truly incredible, talented and diverse. Even though my topic was quite distinct from the research of others, you were always open to listening and offering advice and suggestions for the upcoming scientific challenges (and not just those, but bureaucratic ones as well). I've learned a lot from all of you. Thank you to Dennis and Jonas, my first office mates and my first friends in Germany; to Johnny for your sunny energy; to Lea for the emotional support; to Bernd and Roman for our work together; to Tim, Pratik and Frauke for your empathy; and to Manuel, Alex, Nenad, and the rest of the group, including the administrative staff.

Science is never done by one person, my father says, and he is absolutely right. All scientific developments, papers and research were done in a team, in the amazing team. I want to say thank you to Andrey, who has been looking after me all this time, who has taught me about metamaterials and who guided me through all the publication challenges. You were ready to discuss research with me late in the evenings or even when I had a fever, taking on the responsibility of responding to reviewers. Your care will always stay in my heart. Thank you to Boris for supporting our collaboration, wondering about our progress and going through the results. Thank you to Vladimir for being in contact and responding all these years. We've finally met each other in person only in the last year, but you have always been extremely kind, sharing your knowledge about Comsol and physics, and welcoming me to Denmark. Thank you to Torgom for the same attitude. You have been extremely nice to me in helping with the characterisation experiment. Thank you to Radu for agreeing to fabricate the structures, for supervising me in the lab, and for all our great discussions. You are a wonderful teacher! I want also to thank both professors, Andrei Lavrinenko and Sergey Bozhevolnyi, for welcoming me at DTU and SDU, for helping with the production of metasurfaces and for making the publication possible. I find myself extremely lucky to have met all of you.

And finally, to my love, Mitya, who is always by my side. It is sometimes not easy with my emotions, but you give me strength. I can't imagine what it would be without you.